The Evolution of Luminous Infrared Galaxies Through Cosmic Time

Laurence Hogan

Balliol College

University of Oxford

A thesis submitted for the degree of

Doctor of Philosophy

Trinity 2022

This thesis is dedicated to my parents
for supporting me throughout my physics journey

Acknowledgements

A DPhil cannot be completed without the support and guidance of many people. Astrophysics research is a joint effort, and although I keep referring to ‘my work’ in this thesis, it is not a solo endeavour and I would have had very few results without the feedback, discussion, and direction provided by so many. I am extremely grateful to everyone who made my life so much easier the past four years.

Firstly, I would like to thank my supervisor Dimitra Rigopoulou, for always being a source of advice, help and knowledge over the four years. She was always available to chat, offered both reassurance and guidance, and made sure everything stayed on track during a very eventful few years. Dimitra provided a welcoming environment from day one and was an excellent mentor to me throughout my time in Oxford.

Likewise, in the latter couple of years, as my DPhil pivoted towards the HARMONI mock observations work, Niranjan Thatte provided much needed assistance and advice, for which I am very thankful.

A big thanks to everyone who was part of my group in Oxford, who were always there to lend a helping hand: Miguel Pereira-Santaella, Ismael García-Bernete, Pat Roche, Almudena Alonso-Herrero and Fergus Donnan. A thank you to the simulation group: Julien Devriendt, Adrienne Slyz, and Kearn Grisdale, upon whose work chapters 4 and 5 were built and Kearn generously allowed me to use some of his material throughout these chapters. I will miss the various weekly meetings at Oxford, and the fascinating discussions we had during them.

I am grateful to all my other collaborators, and colleagues in group meetings, who offered great feedback and helped make my work and results so much better, and thanks to: Laia Barrufet, Françoise Combes, Santiago García-Burillo, Jiasheng Huang, Georgios Magdis and Axel Weiß.

A huge thanks to Andy Bunker and Mark Swinbank for reading through and examining my thesis. I learned a lot during the viva, and they both offered excellent and thoughtful feedback, which has made this thesis stronger.

Likewise, I would like to thank Martin Bureau and Anastasia Ponomareva for the excellent feedback and discussions during my first, second and third year internal vivas.

A big thanks to Ashling Gordon and the support staff, who were always available to sort things out, and making me feel welcome since I first arrived at the astrophysics department. And also huge thanks to the astrophysics department for funding my DPhil studies for the past four years.

To everyone I have shared an office with, we had a lot of craic over the years, and the DPhil would have been much duller without them. Likewise, to everyone in Balliol College and the astrophysics department, who I shared many pub trips, formal dinners, and events over the year.

I would never have made it to the DPhil stage without the friends and classmates at Trinity College Dublin and Imperial College London. We soldiered through a lot together, while also managing to enjoy the social side of university.

Also, the friends outside physics who I've grown up with and known for years. I treasured my trips back home to Ireland, and they all kept me sane when the going got tough. Also, a shout out to everyone in the Éire Óg Oxford GAA club who been a home away from home ever since I arrived at Oxford.

Finally, to my parents, to Colin and Siobhán, and little Hannah, who have probably seen more of the ups and downs than anyone, since I returned to university as a mature student. Without them I would not have made it, and I am much more grateful than they will ever know.

Abstract

(Ultra) Luminous infrared galaxies (U/LIRGs) are amongst the most powerful star forming galaxies in the universe. They play a significant role in galaxy evolution and dominate the star formation rate density at the peak of cosmic star formation, at z $\sim$ 2. Therefore, understanding the properties of luminous infrared galaxies, and how these properties evolve through cosmic time, is necessary for testing our best theories of galaxy evolution, and for pushing the current understanding of cosmic star formation.

In this thesis, I show U/LIRGs at z $\sim$ 2 have underlying mechanisms driving their huge star formation rates (SFR) that are consistent with the high redshift normal star forming population, as opposed to the merger driven star formation seen in local U/LIRGs. I show that the general properties of the U/LIRG population have changed over the past 10 Gyr and that local U/LIRGs are not necessarily analogues for high-z luminous IR galaxies. Major mergers do not appear to be a necessary condition to drive the high observed SFR, as the properties of my sample of U/LIRGs are consistent with galaxies undergoing steady state star formation.

I explore a unique sample of U/LIRGs at z $\sim$ 0.4 that form a subpopulation that straddles the region between star forming galaxies and starbursts at this epoch. This sample shows a continuous change in star formation efficiency (SFE) between these two populations, as opposed to the suggested bi-modality in SFE between normal star forming galaxies and starbursts. It seems that interactions are responsible for the boost in the SFE, and it is the SFE, as opposed to the gas fraction, that may be driving a galaxy's transition towards the starburst regime. Intriguingly, there is a possible hidden merger in one of the targets that was previously thought to be isolated based on rest frame optical observations, and also a potential CO dark ULIRG which would be a very unusual interstellar medium (ISM) for a luminous IR galaxy. These examples show how multi-wavelength observations are vital to fully understand a galaxy.

I use a new post-processing pipeline to make mock observations of a typical star forming galaxy at z $\sim$ 2. This pipeline adds mock spectra to hydrodynamical cosmological simulations, and I use the output from this pipeline to make mock High Angular Resolution Monolithic Optical and Near-infrared Integral field spectrograph (HARMONI) observations of the Hα emission line. I confirm the intrinsic physical properties of the simulated galaxy are correctly encoded into its spectrum. It is then shown how the presence of moderate dust doesn't affect the analysis of the mock observations, which is vital as U/LIRGs are ubiquitous in the high-z universe.

Having shown the post-processing pipeline correctly captures the underlying properties of a galaxy, I investigate how the observational signatures change as a galaxy progresses through a minor merger, and whether these observables can accurately predict a galaxy's stage of interaction. I show that a galaxy's position on the main sequence is not always a reliable indicator of a merging versus non-merging galaxy. Neither is the ratio of rotational velocity to velocity dispersion, although the velocity dispersion does increase throughout the minor merger. I show that the SFE, as opposed to gas fraction, is driving the boost in SFR as the minor merger progresses. The morphology indicators are affected by dust, but are still useful to categorize the galaxy correctly under moderate dust attenuation. I conclude that high spatial resolution HARMONI observations may uncover minor mergers at cosmic noon that can be missed by seeing limited observations.

This thesis helps disentangle what drives star formation in high redshift luminous infrared galaxies, explores how the SFR is linked to the global properties of galaxies, shows how these properties evolve over time and probes how accurately observations capture the intrinsic properties of a galaxy.

Declaration of Authorship

The work of this thesis is based on the following four papers:

Chapter 2 - L. Hogan, D. Rigopoulou, G. E. Magdis, M. Pereira-Santaella, I. García-Bernete, N. Thatte, K. Grisdale, J.S. Huang. *Integral Field Spectroscopy of Luminous Infrared Main Sequence Galaxies at Cosmic Noon*, 2021, MNRAS, 503, 5239.

Chapter 3 - L. Hogan, D. Rigopoulou, S. García-Burillo, A. Alonso-Herrero, L. Barrufet, F. Combes, I. García-Bernete, G. E. Magdis, M. Pereira-Santaella, N. Thatte. A. Weiß. *Unveiling the Main Sequence to Starburst Transition Region with a Sample of Intermediate Redshift Luminous Infrared Galaxies*, 2022, MNRAS, 512, 2371.

Chapter 4 - K. Grisdale, L. Hogan, D. Rigopoulou, N. Thatte, M. Pereira-Santaella, J. Devriendt, A. Slyz, I. García-Bernete. *On the Viability of Determining Galaxy Properties from Observations I: Star Formation Rates and Kinematics*, 2022, MNRAS, 513, 3906.

Chapter 5 - L. Hogan, K. Grisdale, D. Rigopoulou, N. Thatte, M. Pereira-Santaella, J. Devriendt, A. Slyz, I. García-Bernete. *On the Viability of Determining Galaxy Properties from Observations II: Observational Signatures of a Minor Merger at Cosmic Noon*, in prep.

I hereby certify that the work in this thesis is wholly my own, except where explicitly stated.

Contents

List of Figures

List of Tables

List of Abbreviations

σ_0	Intrinsic Velocity Dispersion
σ_{gas}	Gas Velocity Dispersion
Σ_{x}	Surface Density of galaxy component x
AGN	Active Galactic Nuclei
ALMA	Atacama Large Millimeter/submillimeter Array
AMR	Adaptive Mesh Refinement
AO	Adaptive Optics
BPT	Baldwin, Phillips & Terlevich (diagram)
ELT	Extremely Large Telescope
FFT	Fast Fourier Transform
FIR	Far Infrared
FMR	Fundamental Metallicity Relation
FOV	Field of View
FWHM	Full Width Half Maximum
HARMONI	High Angular Resolution Monolithic Optical and Near-infrared Integral field spectrograph
HST	Hubble Space Telescope
IFS	Integral Field Spectroscopy
IFU	Integral Field Unit
IMF	Initial Mass Function
IR	Infrared
ISM	Inter-stellar Medium
KS	Kennicutt-Schmidt (relation)
KMOS	The K-band Multi Object Spectrograph
$\mathbf{L}_{\mathrm{IR}}$	Infrared Luminosity (8 - 1000 μm)
LCARS	Light from Cloudy Added to RAMSES
LIRG	Luminous Infrared Galaxies

LTAO . . . . . Laser Tomography Adaptive Optics
$M_\odot$ . . . . Solar Mass
$M_\star$ . . . . Stellar Mass
M_{mol} . . . . . . Molecular Gas Mass
M_{gas} . . . . . . Gas Mass
MCMC . . . . Markov Chain Monte Carlo
MS . . . . Main Sequence
MZR . . . . . . Mass Metallicity Relation
NOEMA . . . NOrthern Extended Millimeter Array
OB . . . . Observation Block
PSF . . . . . . Point Spread Function
PV . . . . Position Velocity (diagram)
SED . . . . . . Spectral Energy Distribution
SFE . . . . . . Star Formation Efficiency
SFH . . . . . . Star Formation History
SFR . . . . . . Star Formation Rate
sSFR . . . . . Specific Star Formation Rate
SFRD . . . . . Star Formation Rate Density
SMG . . . . . . Sub Millimeter Galaxy
S/N . . . . . . Signal to Noise
T_{dust} . . . . . . Dust Temperature
ULIRG . . . . Ultra Luminous Infrared Galaxies
U/LIRG . . . LIRGs & ULIRGs
UV . . . . Ultraviolet
V_{rot} . . . . Rotational Velocity
VLT . . . . . . Very Large Telescope
z . . . . Redshift (not to confused with capital Z, which is metallicity)

Astronomy compels the soul to look upward, and leads us from this world to another.

— Plato *Republic*

These are small ... but those ones out there are far away.

— Fr. Ted Crilly *Father Ted*

1 Introduction

Contents

1.1 Overview

Since the dawn of civilization people have looked up at the stars and tried to make sense of our place in the cosmos. Many civilizations have come and gone in the subsequent millennia, leaving behind many sites revealing astronomical curiosity, from the Pleiades painted onto the cave walls at Lascaux to the stone circles at Nabta Playa and the passage tomb at Newgrange. Our ancestors bequeathed their curiosity of the cosmos to us, and we continue to refine and deepen our understanding of the universe. We now know the Milky Way is just one of billions of galaxies and our Sun is just a normal star located around 8kpc from the Galactic centre. But knowledge of how, why and where stars form remains key to understanding the universe and how it has changed in the past 13.7 billion years. Star formation and its interplay with gas, dust, chemical composition, existing stellar mass, morphology and the dynamical state of a galaxy allows us to understand how galaxies have evolved from cosmic dawn, approximately 13 billion years ago, to the present epoch. Observing the stars and the inter-stellar medium (ISM) in galaxies allows us to test our theories of galaxy formation and evolution and help constrain simulations. In recent decades there has been an abundance of multi-wavelength data from the ultraviolet (UV) to the radio, each giving a different insight into the underlying properties of a galaxy.

This thesis explores dusty star forming galaxies, touching on questions such as:

- What underlying mechanisms drive star formation in high-z dusty galaxies? How does this change over cosmic time?
- What is the rate at which galaxies can convert their molecular gas into stars and what global properties influence this rate?
- Can observations of the Hα emission line accurately trace the underlying physical properties of a galaxy at high redshift?
- How do observational signatures of the intrinsic properties change as a galaxy undergoes a merger, and how can we use these to disentangle what is happening within a galaxy?
- What is the impact and importance of mergers in star formation.

While no single thesis or person can answer all these questions, every astrophysicist strives to add their contribution. As Michelangelo is reputed to have said, "The sculpture is already complete within the marble block, before I start my work. It is already there, I just have to chisel away the superfluous material." In this thesis I hope to chisel my little portion of the marble. This rest of this chapter will give an overview of the salient details needed to understand the physics that follows, and more in depth explanations and analysis is provided in later chapters.

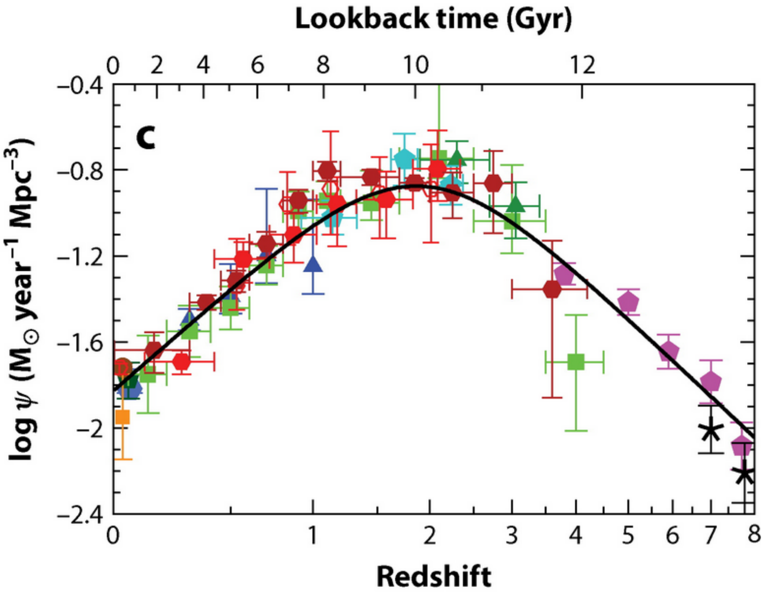

Figure 1.1: The classic Madau and Dickinson (2014) plot showing the evolution of the cosmic SFRD between z = 8 and today. The SFRD peaks at z = 1 - 3 ($\sim$ 10 Gyr ago), in an epoch that has become known as cosmic noon, before declining by over an order of magnitude to the present day.

1.2 Star Formation

Stars condense out of dense clouds of molecular gas. The rate at which they form is known as the star formation rate (SFR), and the SFR of an astronomical object is defined as the total mass that is turned into stars per unit time for said object or target. It is an inefficient process with ordinarily only $\sim$ 1 - 2 % of a molecular cloud's mass being converted into stars per dynamical free fall time of the cloud (e.g. Genzel et al., 2010, Murray, 2011).

Stars form with birth masses following a distribution known as the initial mass function (IMF). A star's mass is important as it determines its luminosity and life cycle. The relationship of mass to luminosity in main sequence stars is $L \propto M^{3.5}$, and the lifetime of a star is approximately its mass divided by its luminosity, so a star's lifetime scales with mass as $\sim M^{-2.5}$ (e.g. Kippenhahn et al., 2012). For example, the most massive stars, such as O - B stars, have effective temperatures in the range 10,000 - 60,000 K and masses greater than 3 $M_{\odot}$, with an upper limit cut-off taken to be $\sim$ 150 $M_{\odot}$, as above this mass the radiation pressure and mass loss will affect the gravitational stability of a star (the lower mass of a main sequence star is ~ 0.1 $M_\odot$ as below this mass core densities are insufficient to sustain nuclear fusion). The lifetime of a solar mass star is around 10 Gyr, so all bar the least luminous class of B stars have life times of 100 Myr or less.

The direct method of counting the number of stars in a given volume is only feasible for a handful of galaxies close to the Milky Way. Instead, astronomers use the integrated light emitted from a galaxy, which arises from the emission from stars, gas and dust within a galaxy. We can then assume a conversion factor between luminosity in a given waveband and newly formed stars, which requires models of stellar population synthesis, the IMF and the star formation history (SFH) of a galaxy. For example, the stellar continuum emission from a star is well approximated by a blackbody, so stars with effective temperatures $>$ 10,000 K dominate the UV continuum. Therefore, the UV continuum traces stars with stellar masses > 3 $M_\odot$, and with the use of an appropriate conversion factor, this makes the UV continuum a sensitive tracer of recent star formation on the timescale of 100 Myr (the UV emission is dominated by stars 100 Myr or less despite the contribution of stars a few hundred Myr in age to the near UV emission).

Another diagnostic of ongoing star formation is measuring the emission line flux arising from ionized regions surrounding massive young stars. These ionized regions comprise mainly of hydrogen gas and are known as HII regions. The Hα optical transition (n: $3 \rightarrow 2$), is the most commonly used emission line diagnostic for estimating the SFR of a galaxy. The ionization energy from the ground state of hydrogen is 13.6 eV so only stars with masses > 15 $M_\odot$ have the requisite ionizing flux to form HII regions. These massive stars have lifetimes < 10 Myr, so Hα can be considered a good tracer of the 'instantaneous' SFR within a galaxy.

As UV and Hα are strongly attenuated by dust within the ISM, estimates of the 'unobscured' SFR, from tracers such as UV or Hα emission, act as a lower bound to the SFR. The infrared (IR) emission, between 8 - 1000 μm, arises from dust that absorbs the UV radiation from massive young stars and thermally re-emits it at longer wavelengths. Therefore, the IR luminosity (L_{IR}) acts as a probe of the ‘dust obscured’ star formation. As dust absorption peaks in the UV, the IR emission traces similar timescales to the UV continuum, and measures stars that formed in the prior 100 Myr.

The visible spectrum is dominated by intermediate mass stars (0.5 - 3 $M_\odot$) and the near IR emission ($\sim$ 0.8 - 2.5 μm) is comprised mainly of long lived stars, $\leq$ 0.5 $M_\odot$), so the visible and near IR emission can be used to infer the mass of the long lived stars that form the bulk of the stellar population within a galaxy.

All these different tracers stress the importance of multi-wavelength data to accurately determine the existing stellar mass ($M_\star$) and map ongoing star formation in a galaxy, as UV or IR tracers by themselves can underestimate the SFR of a galaxy.

1.3 Cosmic Star Formation

In recent years multi-wavelength observations have determined the star formation rate per unit volume, known as the SFR density (SFRD), of the universe in the past $\sim$ 10 Gyr (Figure 1.1), i.e. the mass of new stars formed per year per unit co-moving volume. It has been found that the SFRD gradually rises from z = 8, denoted cosmic dawn, to peak between z = 1 - 3, known as cosmic noon, before declining by an order of magnitude to the current epoch (e.g. Madau and Dickinson, 2014, and references therein). This implies that most of the solar like stars that make up the bulk of a galaxy’s stellar mass were formed at high redshifts. The density of both obscured and unobscured star formation appears to follow a similar trend up to cosmic noon, with dust enshrouded star formation dominating unobscured star formation for at least the past 10 Gyr (e.g. Le Floc’h et al., 2005, Zavala et al., 2021), as shown in Figure 1.2. A similar trend is seen in active galactic nuclei (AGN) activity, which also peaks at cosmic noon, with a larger fraction AGN appearing to be dust obscured at z $\sim$ 2 than the local universe (e.g. Delvecchio et al., 2014, Vijarnwannaluk et al., 2022). In this thesis, the local universe is defined as z $<$ 0.2.

Another recent observational achievement in the field of galaxy evolution has been the tight correlation found between the SFR and $M_\star$ of a galaxy, known as the main sequence (MS) of star forming galaxies (e.g. Noeske et al., 2007, Daddi et al.,

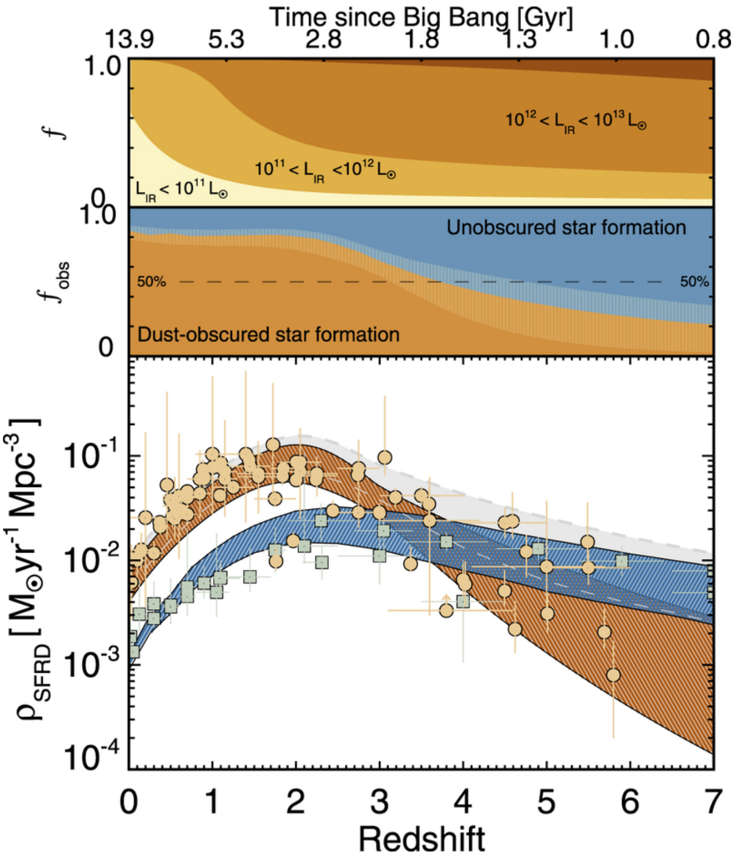

Figure 1.2: Top: The contribution of galaxies with different L_{IR} ranges to the dust obscured cosmic SFRD. **Middle:** The fractional contribution of dust obscured star formation to the total SFRD. **Bottom:** The evolution of the cosmic SFRD between z = 7 and today, showing the contribution of dust obscured and unobscured star formation. Dust enshrouded star formation appears to dominate unobscured star formation since at least z ∼ 3 (taken from Zavala et al., 2021).

2007). A galaxy's position on the SFR - $M_\star$ plane is given by the specific SFR (sSFR = SFR / $M_\star$). The sSFR can be viewed as the fractional stellar growth of a galaxy and can be used to categorize two subpopulations of star forming galaxies: normal star forming galaxies and starbursts (see Figure 1.3). Normal star forming galaxies lie within a scatter of 0.3 dex around the MS, whereas a starburst is defined as a galaxy having an SFR a factor of four or more above its expected MS SFR, based on its $M_\star$ (e.g. Whitaker et al., 2012). There is also a subpopulation of star forming galaxies with declining SFRs that lie below the MS known as green valley galaxies (e.g. Belfiore et al., 2018), that form the bridge between star forming and quiescent galaxies, a population of galaxies with little to no ongoing star formation. This thesis studies only MS and starburst galaxies, so

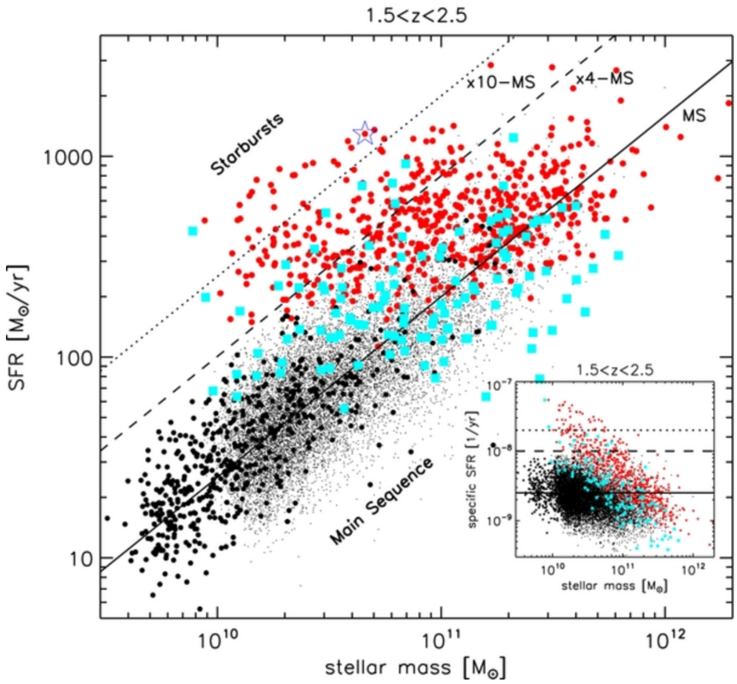

Figure 1.3: Star formation rate versus stellar mass, taken from Rodighiero et al. (2011). Most star forming galaxies appear to fall along a tight correlation which has been denoted as the main sequence, shown as a solid black line. Starbursts, a subset of galaxies with very high star formation rates, are defined as galaxies having an SFR a factor of at least four greater than the expected SFR for a MS galaxy of equal stellar mass. The red circles are PACS selected targets from the COSMOS field, the cyan squares are PACS selected targets from the GOODS-S field, the black circles are BzK selected targets from the GOODS field and the black dots are BzK selected targets from the COSMOS field (see Rodighiero et al., 2011 for details of the samples).

when I mention two populations or discuss star forming galaxies it will always be referring to MS galaxies or starbursts unless explicitly stated.

It is suggested that normal galaxies are forming stars in a quasi-steady state, fuelled from continuous in-falling gas from the intergalactic medium (e.g. Dekel et al., 2009), whereas starbursts seem to be undergoing a short-lived period of heightened star formation driven by stochastic processes such as mergers (e.g. Tacconi et al., 2008, Daddi et al., 2010. Genzel et al., 2010). Just to note, throughout this thesis the labels normal/regular star forming galaxies and MS galaxies will be used interchangeably and refer to the same population.

It appears that MS galaxies are responsible for up to 90% of the cosmic SFRD (e.g. Rodighiero et al., 2011, Sargent et al., 2012). This result also corroborates the observed normalization of the MS correlation, which increases with redshift

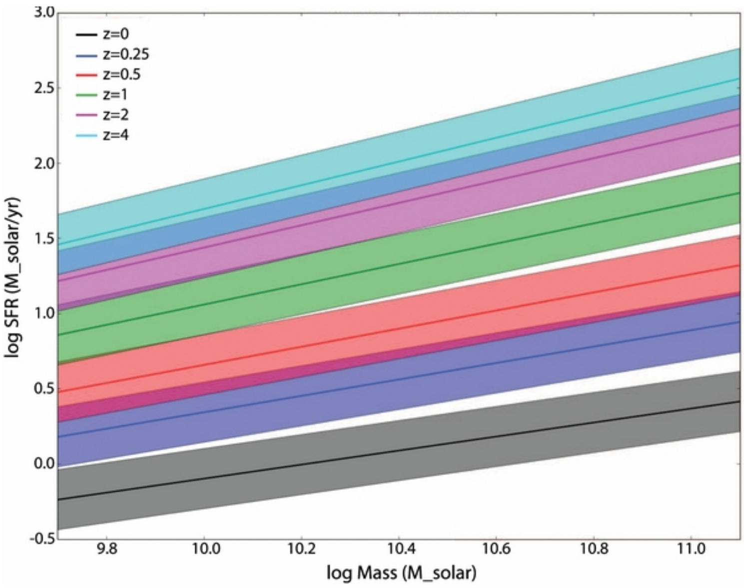

Figure 1.4: The redshift evolution of the normalization of the main sequence power law, from Speagle et al. (2014). The solid lines show the MS at a given redshift with the adjacent shaded regions showing the typical scatter. The colour codes are shown in the top left.

(e.g. Speagle et al., 2014, Pearson et al., 2018). For example, a galaxy with a given $M_\star$ at $z = 2$ has an order of magnitude greater SFR than a $z = 0$ galaxy with equivalent $M_\star$ (see Figure 1.4).

1.4 Molecular Gas and Star Formation Efficiency

The ISM is composed of multiple phases, densities and temperatures (ionized, atomic and molecular) and studying the molecular phase is important for understanding the onset of star formation. That stars formed within giant gas clouds is evidenced by the strong correlation existing between the surface density of gas within a galaxy and the surface density of SFR known as the Kennicutt-Schmidt law (KS), $\Sigma_{\rm SFR} \propto \Sigma_{\rm gas}^{N}$, with gas in local galaxies following a tight non-linear scaling law given by index $\rm N = 1.4 \pm 0.15$ (Schmidt, 1959, Kennicutt, 1998; see Figure 1.5). Shallower indices are found for the molecular gas mass surface density, $\Sigma_{\rm mol}$, with the approximately linear relationship signifying the stronger link between SFR and molecular gas within a galaxy (e.g. Bigiel et al., 2008, Bigiel et al., 2011, Schruba et al., 2011 Leroy et al., 2013, Reyes and Kennicutt, 2019).

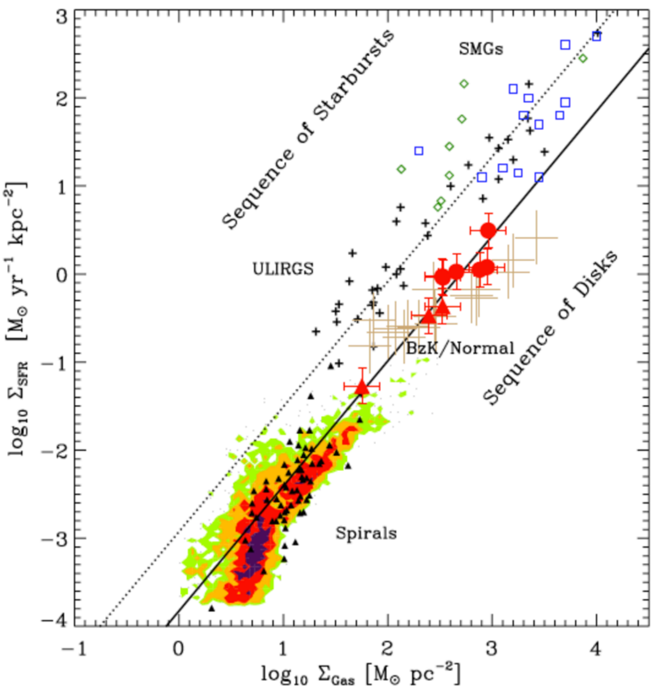

Figure 1.5: The SFR surface density as a function of gas surface density, known as the Kennicutt-Schmidt correlation, for a sample of star forming galaxies from Daddi et al. (2010). The best fit line for starbursts at both low and high-z (denoted as ULIRG and SMG on the plot) appears to be offset from the best fit line for regular star forming galaxies at both low and high-z (denoted by spirals and by Bzk/normal on the plot), which is suggestive of a bi-modal distribution.

The ratio of the SFR and the molecular gas mass (M_{mol}) gives the star formation efficiency (SFE $\equiv$ SFR / M_{mol}) of a galaxy, which tells us how quickly a galaxy can convert its current molecular gas reservoirs into stars, but does not take into account any mass recycled back into the ISM from winds and supernova remnants (e.g. Tacconi et al., 2018). MS galaxies have been observed to have lower SFE than starburst galaxies across cosmic time (e.g. Tacconi et al., 2020). The inverse of the SFE is the depletion time ($\tau_{dep} \equiv 1$/SFE), and starbursts are found to have τ_{dep} on the order of 10 Myr (e.g. Combes et al., 2011, Pereira-Santaella et al., 2021) with MS galaxies having a τ_{dep} on the order of 1 Gyr (e.g. Leroy et al., 2013, Tacconi et al., 2013). This suggests different triggering mechanisms are responsible for star formation in these two groups. Throughout this thesis SFE and τ_{dep} are used interchangeably, with a low τ_{dep} implying a high SFE and vice verse.

The apparent bi-modality of regular star forming galaxies versus the starburst population in the $M_\star$ - SFR parameter space is implicitly determined by the M_{mol} and its properties. A higher SFR can be due to higher gas fractions ($f_{gas} \equiv M_{mol}$ / $M_\star$) and/or higher SFE, with observations showing that the SFE and f_{gas} increase with distance above the MS in a given epoch (e.g. Magdis et al., 2012a, Genzel et al., 2015, Popesso et al., 2020, Tacconi et al., 2020). Both SFE and f_{gas} broadly remain constant along the MS, but it appears that f_{gas} begins to decrease at the high $M_\star$ end once the sSFR and redshift evolution are accounted for (e.g. Magdis et al., 2012b, Tacconi et al., 2018). Quiescent galaxies, which lie far below the MS and have ceased star formation, are linked with both lower SFE and f_{gas} (e.g. Piotrowska et al., 2020). It is also suggested that the KS relation shows a bi-modality between starbursts and MS galaxies (e.g. Daddi et al., 2010; see Figure 1.5), with starbursts forming a separate locus in the $\Sigma_{SFR} - \Sigma_{mol}$ plane when compared to MS galaxies.

The f_{gas} and SFE also evolve with redshift, although the molecular gas mass increases more dramatically with lookback time than the SFE, with the f_{gas} being an order of magnitude greater at z $\sim$ 2 when compared to the local universe with the SFE roughly doubling (e.g. Tacconi et al., 2018); results consistent with the evolution of the cosmic SFRD (Decarli et al., 2020, Walter et al., 2020). The molecular gas density seems to peak at z $\sim$ 1.5 before declining by an order of magnitude to today, a similar trend to the cosmic evolution of the SFRD (e.g. Lagos et al., 2011), as shown in Figure 1.6. The cosmic atomic gas and molecular gas have similar densities at z = 1.5, but the atomic gas then stays approximately constant down to the present epoch (e.g. Walter et al., 2020). The cosmic evolution of the SFRD, atomic gas density and molecular gas density reinforce the findings of the KS correlation, and is further evidence for the stronger link between SFR and molecular gas.

1.5 Dust and Metallicity

Dust and metallicity are important components of the ISM. Metals are defined as all chemical elements heavier than hydrogen and helium, and a fraction of the gas-phase metallicity is locked into dust grains ranging from tens of atoms

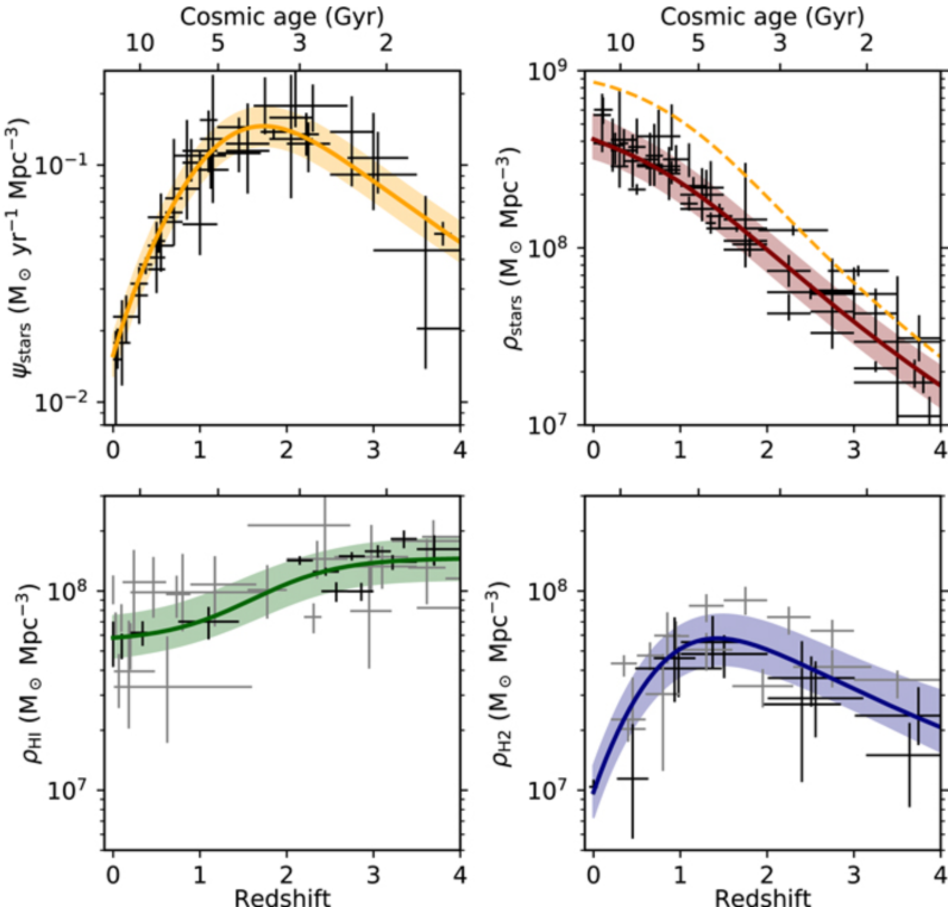

Figure 1.6: Top left: Redshift evolution of the SFR density from z = 4 to the current epoch. **Top right:** Redshift evolution of the stellar mass density. **Bottom left:** Redshift evolution of the atomic gas density. **Bottom right:** Redshift evolution of the molecular gas density. The evolution of the molecular gas density mimics the evolution of the SFR density, showing the intimate link between SFR and molecular gas (Source: Walter et al., 2020).

up to $\sim$ 0.3 μm (e.g. Draine, 2003). The ratio of dust mass to gas mass is a function of metallicity and is generally 1% or less for star forming galaxies (e.g. Galliano et al., 2018).

Dust scatters and absorbs stellar light, particularly in the UV and optical, and typically absorbs 30 - 40% of stellar light in normal star forming galaxies and re-emits it in the IR (see Figure 1.7), but can re-emit up to 99% of starlight in heavily dust obscured star forming galaxies (e.g. Galliano et al., 2018). Multi-wavelength observations now enable IR spectral energy distributions (SEDs) to be well sampled, allowing dust obscured star formation and obscured AGN to be

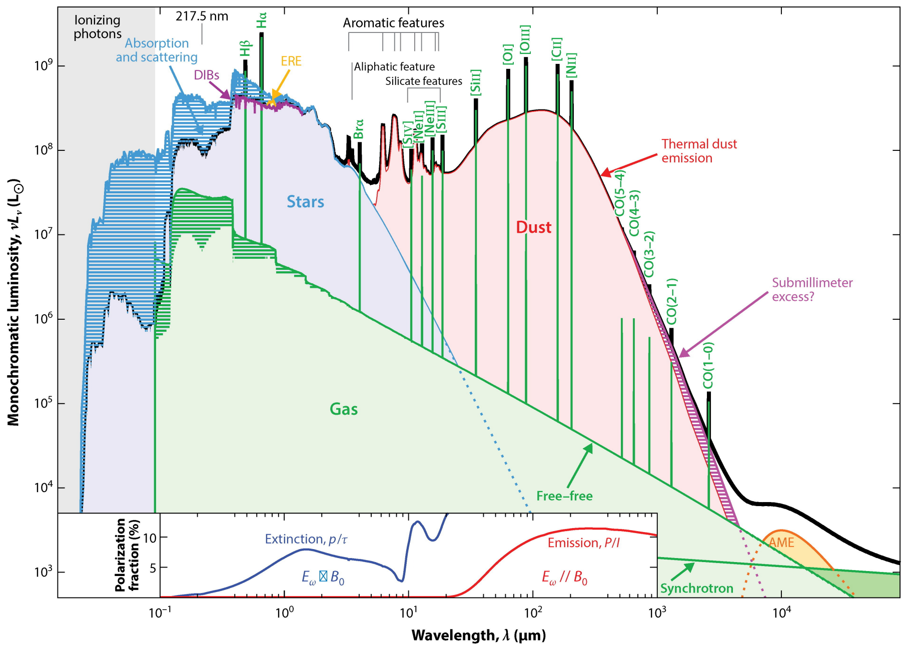

Galliano F, et al. 2018.
Annu. Rev. Astron. Astrophys. 56:673–713

Figure 1.7: The spectral energy distribution of a normal star forming galaxy, taken from Galliano et al. (2018). This shows the contribution to the SED from stars, gas and dust continuum, along with the most prominent gas emission lines. The hatched area shows the power absorbed by the dust that is re-emitted in the infrared.

studied in greater depth, which is an important development as dust obscured star formation has dominated the SFRD for at least the past 10 Gyr (e.g. Zavala et al., 2021). Observatories such as the Atacama Large Millimeter/submillimeter Array (ALMA) and the James Webb Space Telescope (JWST) are continually refining our understanding of dusty star formation over cosmic time, as prior to these observatories much of the knowledge of star formation in the $z > 4$ universe, was from rest frame UV and optical.

Dust temperatures, T_{dust}, are often found by assuming the dust emission in the IR and sub-mm takes the form of a modified blackbody (e.g. Casey et al., 2014). The T_{dust} in a typical star forming galaxy in the local universe is ~ 25 K, increasing to ~ 35 K at $z \sim 2$ (e.g. Schreiber et al., 2018). As with observables such as SFE and sSFR, MS galaxies and starbursts seem to differ in their T_{dust} with mergers tending to have $T_{dust} \sim 10$ K higher than their non merging counterparts (e.g. Elbaz et al., 2011, Clements et al., 2018). Yet, these values hide a large scatter in the observed T_{dust} of galaxies. For example, Dunne et al. (2011) find T_{dust} = 10 - 48 K after observing almost 1900 galaxies in the redshift range $0 < z < 0.5$. Therefore, a value of T_{dust} alone is not sufficient to say if a galaxy is likely to be a merger or non-merger. Also, many observations only give a single value for the T_{dust} within a galaxy, and this average value hides spatial variations in the T_{dust}.

Previous studies have found that the intensity of the radiation field heating the dust increases with lookback time, along with the concurrent rise in dust temperatures, within MS galaxies back to $z \sim 2$ (e.g. Magdis et al., 2012a, Huang et al., 2014, Béthermin et al., 2015), and an increase in T_{dust} is also seen with distance above the MS at all redshifts between cosmic noon and today (e.g. Magnelli et al., 2014). Dust temperature also appears to be positively correlated with IR luminosity (e.g. Hwang et al., 2010). Therefore, mechanisms proposed for the increase in T_{dust} include higher SFE, and/or more compact regions of star formation (e.g. Liang et al., 2019, Burnham et al., 2021). Other possibilities for the redshift evolution of T_{dust} include lower gas phase metallicities in high-z galaxies, leading to smaller dust masses and more energizing photons per unit dust mass (e.g. Sommovigo et al., 2022).

Gas phase metallicity is strongly linked to the SFH as each generation of stars enriches the metal content of the ISM, although inflows and outflows complicate this picture. A tight correlation has been found between the stellar mass and gas phase metallicity of a galaxy known as the mass-metallicity relation (MZR), in which higher stellar mass galaxies were found to have higher metallicities (e.g. Tremonti et al., 2004). This correlation seems to hold up to at least $z \sim 3$ (e.g. Onodera et al., 2016). Mannucci et al. (2010) found that gas phase metallicity also has a dependence on SFR and extended the MZR into the fundamental metallicity relation (FMR), in which galaxies follow a 3D surface with remarkably little scatter ($\sim$ 12 %).

The metal lines are regularly observed through their forbidden transitions, such as the [NII] 6583 Å in the optical band or the far IR (FIR) lines, such as [CII] 158 μm. Within the ISM electrons can be collisionally excited to sublevels with a low

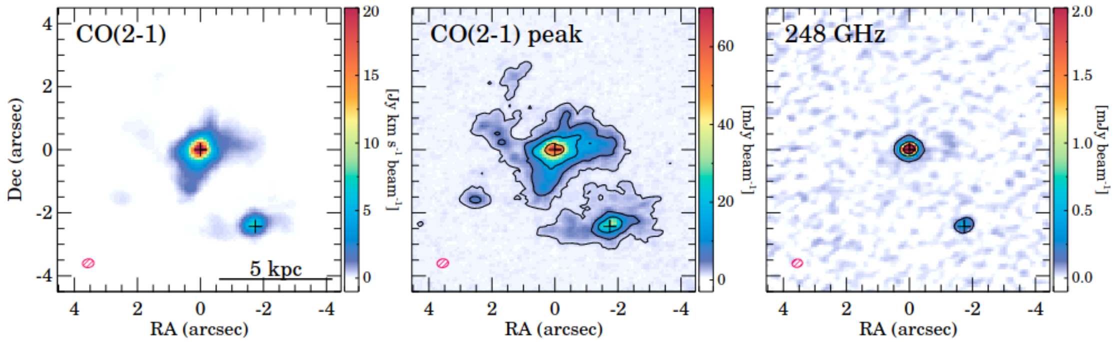

Figure 1.8: Left: CO(3-2) integrated intensity map of IRAS 12112+0305, a ULIRG found in the local universe. **Middle:** CO(3-2) peak intensity in a 10 km s^{-1} channel. **Right:** The 248 GHz continuum. These maps show the double nuclei and compact continuum emission that is typical of a local ULIRGs (taken from Pereira-Santaella et al., 2018).

probability of downward transition, but in the low densities of the ISM collisional de-excitation is rare. Therefore, although not allowed by the dipole selection rules of quantum mechanics, these sublevels can be de-excited by quadrupole transitions, which have a small but finite probability. Forbidden transitions are denoted by square brackets around the element, i.e. [NII]. As these forbidden lines have a low probability of being re-absorbed by the ISM, they act as major coolants of the ISM and are intimately linked with star formation.

Emission lines from both metals and hydrogen can be used as diagnostics to provide insight into the ISM conditions within a galaxy. Examples include dust content (Hα / Hβ), metal abundance ([NII] 6583 Å / Hα) and hardness of the radiation field ([OIII] 5007 Å / Hβ).

1.6 Luminous Infrared Galaxies Near and Far

(Ultra) Luminous infrared galaxies (U/LIRGs) are amongst the most powerful star forming galaxies in the universe. Their IR luminosities arise from thermal emission from dust heated by newly formed massive stars and AGN, with AGN being more prevalent and powerful with increasing L_{IR}. They are defined by their bolometric IR luminosity and classified as: LIRGs = $10^{11} < L_{IR} \equiv L_{8-1000\mu m} < 10^{12}$ $L_{\odot}$ and ULIRGs = $10^{12} < L_{IR} < 10^{13}$ $L_{\odot}$ (Sanders and Mirabel, 1996). They are rare in the local universe, but they dominate the SFRD at cosmic noon (e.g. Magnelli et al., 2011, Murphy et al., 2011a). This makes U/LIRGs vital probes for our understanding of star formation and no theory of galaxy evolution will be complete if it cannot explain the formation and observed properties of U/LIRGs (just to note that throughout this thesis U/LIRGs will denote both LIRGs and ULIRGs. i.e. U/LIRGs $\equiv 10^{11} < \mathrm{L_{IR}} < 10^{13}\ \mathrm{L_{\odot}}$).

Locally ULIRGs all lie above the MS and appear to be undergoing a transient starburst phase, likely fuelled by stochastic events such as gas rich major mergers (e.g. Clements et al., 1996, Rigopoulou et al., 1999), whereas local LIRGs show a more diverse range of morphological types, with minor mergers and isolated disks becoming more common with decreasing $\mathrm{L_{IR}}$ (e.g. Kartaltepe et al., 2010, Bellocchi et al., 2016, Larson et al., 2016). Their IR SEDs are dominated by the thermal emission from dust and have $\mathrm{T_{dust}}$ in the range 30-55K (e.g. Clements et al., 2018). They are very efficient at converting their molecular gas into stars (e.g. Gao and Solomon, 2004) with depletion times on the order of 10 Myr (e.g. Pereira-Santaella et al., 2021). The extent of their star forming regions is relatively compact, with sizes of 0.3 - 2 kpc (e.g. Alonso-Herrero et al., 2006, Pereira-Santaella et al., 2018), as shown in Figure 1.8. Local U/LIRGs tend to show a decrease in the [CII] 158 μm to $\mathrm{L_{IR}}$ ratio with increasing $\mathrm{L_{IR}}$ when compared to the general star forming population ('[CII] deficit problem', e.g. Luhman et al., 2003), with possible explanations including the hardness of the radiation field, compactness of the star forming regions or thermalization of the [CII] 158 μm emission line (e.g. Muñoz and Peng Oh, 2016 Díaz-Santos et al., 2017, Herrera-Camus et al., 2018, Sutter et al., 2021). Similar results have been seen in the other FIR fine structure emission lines such as [NII] and [OI] (e.g. Graciá-Carpio et al., 2011).

Although matched in luminosity, observations have shown that high redshift ($z > 1$) U/LIRGs differ from their local counterparts. Their co-moving density increases by a factor of ~ 1000 between redshifts of 1 - 2, where they are responsible for as much as 70% of the SFRD (e.g. Magnelli et al., 2011, Murphy et al., 2011a). Many authors have noted differences in the properties between high-z and low-z populations, such as the SEDs of high luminosity ULIRGs ($L_{IR} \sim 10^{13}$ $L_\odot$) at cosmic noon appearing to have mid IR and far IR SEDs closely resembling those seen in local sub-LIRGs ($L_{IR} = 10^{10}$ - 10^{11} $L_\odot$) and LIRGs (e.g. Farrah et al., 2008, Muzzin et al., 2010). They have a diverse range of morphologies even in the high luminosity range (e.g. Kartaltepe et al., 2012), with high spatial resolution studies revealing that the star-forming regions of high-z U/LIRGs are relatively extended with sizes in the range 3 - 16 kpc (e.g. Iono et al., 2009, Tacconi et al., 2013). Dynamically, high redshift U/LIRGs appear to be a mixture of mergers and disk galaxies, with spatially resolved observations revealing rotating disks at z $\sim$ 2 with SFRs in the hundreds of $M_\odot$ yr^{-1} that do not appear to be undergoing a major merger (e.g. Förster Schreiber et al., 2009, Wisnioski et al., 2015, Gururajan et al., 2022). In general, they do not exhibit the [CII] deficiency seen in local U/LIRGs, which is suggestive of softer radiation fields and more extended regions of star formation (e.g. Stacey et al., 2010, Rigopoulou et al., 2014).

At intermediate redshifts ($0.2 < z < 1$) U/LIRGs have properties that resemble both the high-z and local populations. Intermediate-z U/LIRGs appear to be a mixture of interacting and isolated objects, can have a lower dust temperatures than local U/LIRGs, but have a similar level of dust obscuration, as measured by the ratio of SFR from Hα versus SFR calculated from the IR SED (Pereira-Santaella et al., 2019). Some U/LIRGs in this redshift range have an SFE, radiation field and gas column densities that exhibit characteristics more closely resembling regular star forming galaxies than local U/LIRGs (e.g. Rigopoulou et al., 2014 Magdis et al., 2014, Lee et al., 2017), whereas other subpopulations include high luminosity starbursts (e.g. Combes et al., 2011, Combes et al., 2013). This diversity of properties, and subpopulations ranging from normal star forming galaxies to starbursts, suggest a gradual evolution in U/LIRGs between cosmic noon and the present day.

1.7 Morphology and Dynamical State of Galaxies Beyond the local Universe

In recent years, the new generation of near IR spectrographs (mounted on the 8 metre Very Large Telescope, VLT, and 10 metre Keck telescope) have allowed large surveys of the high-z universe and allowed an in-depth investigation into the morphology and kinematics of star forming galaxies at cosmic noon. Some main surveys in the past decade include the KMOS^{3D} survey (Wisnioski et al., 2015), KMOS Deep Survey (Turner et al., 2017) and KMOS Redshift One Spectroscopic Survey (KROSS, Stott et al., 2016) employing the K-band Multi Object Spectrograph (KMOS) mounted on the VLT. Surveys carried out on the Multi-Object Spectrometer For Infra-Red Exploration (MOSFIRE), on Keck, include the Survey in the near-Infrared of Galaxies with Multiple position Angles (SIGMA, Simons et al., 2016) and MOSFIRE Deep Evolution Field (MOSDEF, Kriek et al., 2015). Multi Unit Spectroscopic Explorer (MUSE) and Spectrograph for INtegral Field Observations in the Near Infrared (SINFONI), both on the VLT, have provided the Spectroscopic Imaging survey in the Near-infrared with SINFONI (SINS, Förster Schreiber et al., 2009), the Mass Assembly Survey with SINFONI in VVDS (MASSIV, Epinat et al., 2012) and the MUSE survey of Hubble Deep Field South (Contini et al., 2016).

These surveys provide data on hundreds of galaxies up to z $\sim$ 4 and spanning the stellar mass range 10^9 M$_\odot$ $< M_\star <$ $10^{11.5}$ M$_\odot$. The observations show that up to 80% of the high mass end appear to be rotation dominated and have baryon to dark matter ratios greater than unity within their effective radii, with this baryonic to dark matter ratio increasing with redshift (e.g. Wuyts et al., 2016, Genzel et al., 2017, Price et al., 2016). The disks appear to be thicker (e.g. Elmegreen and Elmegreen, 2006) and have a larger intrinsic velocity dispersion (σ_0) suggestive of a more turbulent ISM (e.g. Übler et al., 2019). After accounting for this increase in σ_0 with redshift there has been an observed correlation between the offset above the MS and velocity dispersion, with starbursts having a higher σ_0 and more turbulent disks than regular star forming galaxies (e.g. Übler et al., 2019, Perna et al., 2022). Evidence shows a stronger correlation between gravitational instabilities and σ_0 than for SFR and σ_0, suggesting a stronger link between σ_0 and mergers/interactions, as opposed to σ_0 being driven by feedback from star formation (e.g. Renaud et al., 2014, Perna et al., 2022).

Early results from a morphological study of a JWST deep field hint at disk galaxies being more abundant beyond cosmic noon than previously thought, with up to 40% of galaxies between $4.5 < z < 6$ being classified as disks (Ferreira et al., 2022), including red galaxies previously missed by the Hubble Space Telescope (HST). With JWST still in its infancy, and with multiple very high spatial resolution instruments in the pipeline, the coming years will greatly expand our knowledge of the morphological and dynamical status of galaxies, from the local universe to cosmic noon, and back to cosmic dawn.

1.8 Instrumentation

This thesis uses a variety of instruments ranging from ground based near IR observatories, radio arrays and space based photometry. The two main techniques used in the following chapters are integral field spectroscopy (IFS) and radio interferometry, and a brief description of both are provided in this section.

1.8.1 Integral Field Spectroscopy

Integral field Spectroscopy (IFS) is an observing technique that allows spectra to be captured over a two-dimensional field of view (FOV). IFS uses a device, known as an integral field unit (IFU), that allows both imaging and spectral information to be captured simultaneously. The data is usually represented as a cube with two spatial dimensions and one wavelength dimension, i.e. a stack of images with different wavelengths (see Figure 1.9). Each spatial element in the cube is known as a spaxel and each spaxel has an individual spectrum. IFS has greatly expanded our knowledge of the high-z universe as prior to its development a spectrum was captured by integrating over a single slit, so spatial information was lost. While spatial information could be gained by taking multiple measurements

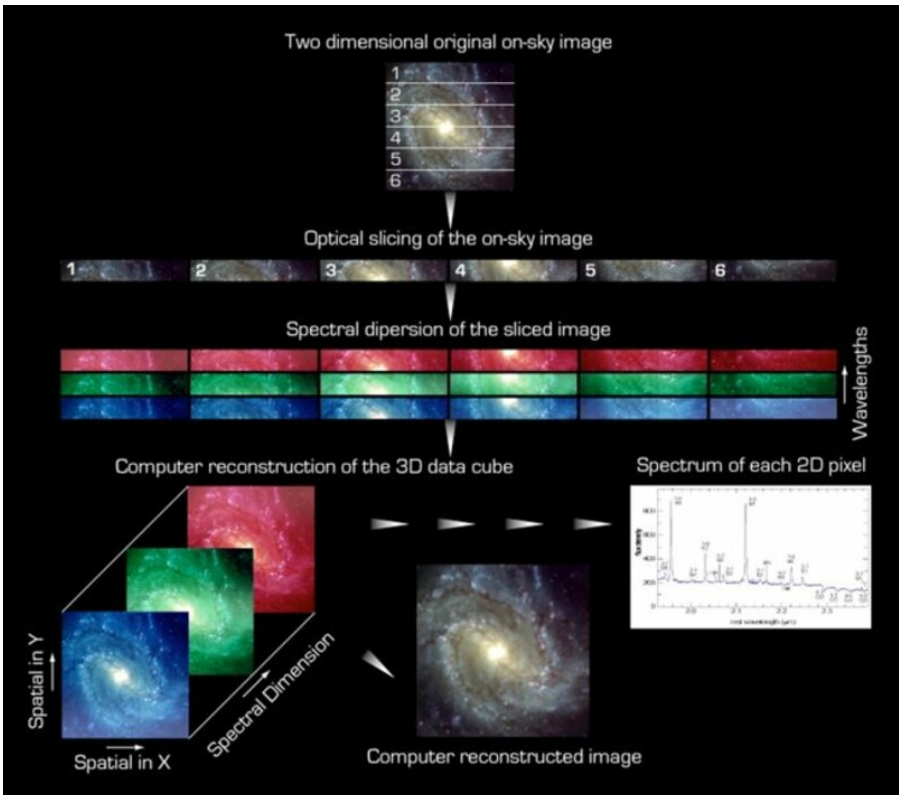

Figure 1.9: A diagrammatic explanation of the image slicer technique for IFS, which is the technique used to observe the IFU data in this thesis. The image is split into slices which form a pseudo-slit, which is fed into a spectrograph. The output data forms a cube with two spatial dimensions and one wavelength dimension (Source: European Southern Observatory website).

with the slit position altered, this was time-consuming and affected by changes in the atmosphere between observations. There are three main techniques used to divide the FOV and produce IFS data: lenslet arrays, fibre bundles and image slicers. The idea is to disperse the light from each spatial element onto a detector, whilst ensuring there is no overlap of spectra.

1. Lenslet Array: The telescope image is projected onto a lenslet array. Each lenslet essentially acts as an individual spaxel and focuses the light onto a small area on the focal plane of a spectrograph, which disperses the light. To ensure spectra do not overlap on the detector the dispersion direction is angled, and the band width is restricted. The drawback of this technique is the restriction of the band width and the inefficient use of a detector.

2. Fibres: This technique feeds light from each spaxel to an individual fibre, whose output can be arranged as a pseudo slit and input into the spectrograph. This optimizes use of the detector and allows longer spectral band passes. Fibres can also be used in conjunction with a lenslet array to allow contiguous sampling of the sky, as without a lenslet array the circular fibres leave gaps in the FOV.

3. Image slicers: This uses mirrors to rearrange the input image into slices and each is re-imaged side by side to form a pseudo-slit which is fed into the spectrograph (see Figure 1.9). This allows a contiguous FOV and maximizes use of the detector. Image slicers are mainly used on IR telescopes.

The spectrographs used to capture the data discussed in Chapter 2 and Chapter 4 use the technique of image slicing, and these instruments will be described in more detail in the relevant chapters.

1.8.2 Radio Interferometry

As the spatial resolution of a telescope is $\propto \lambda$ / D, where D is the diameter of the collecting area, to achieve high spatial resolution in the radio and sub-mm regime quickly becomes unfeasible for single dish radio telescopes. This technical problem is solved by aperture synthesis, a technique which uses an array of radio antennae and the principles of interferometry to mimic the spatial resolution of a telescope with a dish the diameter of the largest baseline length (a baseline is the vector connecting two antennae). For simplicity this method will be outlined using two antennae, which form a two element interferometer, but the same principles hold when increasing the number of receivers.

Let's assume two antennae, A and B, are located a distance, S, apart along an east - west direction and both telescopes are pointing in direction s_0 (see Figure 1.10). This setup forms a single baseline. As we are in the radio regime, we can treat the incoming radiation from an astronomical object as a plane wave. Due to the antennae separation, there is a delay ($\tau = \mathrm{S}\sin(\theta)/\mathrm{c}$, where c is the speed of

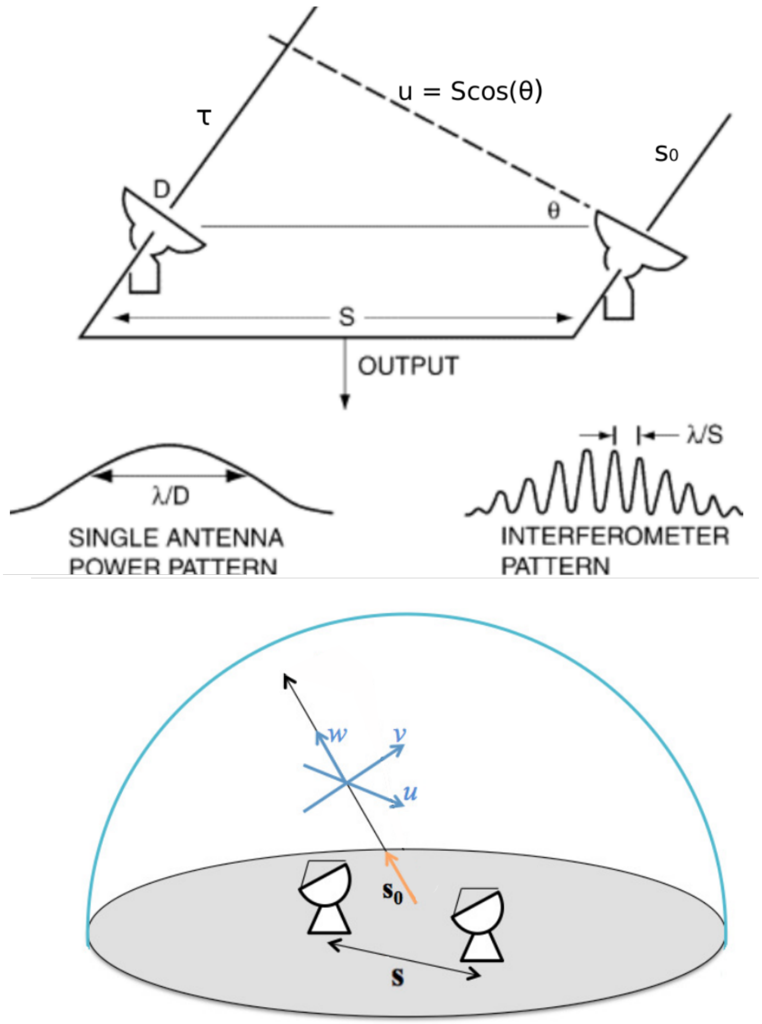

Figure 1.10: Top: A schematic of a simple two antennae interferometer as described in Section 1.8.2 (taken from Gulkis and Pater, 2003). **Middle:** Response of a single dish radio telescope (left) and an interferometer (right) to an unresolved point source. **Bottom:** A schematic of the uv plane. The w vector aligned to s_0, the direction the telescope is pointing, and the uv plane is the plane with orthogonal vectors u and v both perpendicular to w (adapted from Avison and George, 2013).

light) for the same wavefront to reach the second antennae as shown in Figure 1.10 (for simplicity let's assume one frequency). The projected length of the baseline onto this hypothetical wavefront can be written as $u = \mathrm{S}\cos(\theta)$, and together with a projected north-south vector, v, and vector w, parallel to s_0, these form an orthogonal coordinate system, as shown in Figure 1.10.

To observe a source with a radio interferometer, the signals received in both antennae are correlated (once τ has been accounted for) and the output of this correlation is known as the complex visibility, V, which is the component of the

Fourier transform of the sky brightness, T(x,y), with spatial frequency, u, in the east - west orientation. For a simple two antennae interferometer this gives one data point, V(u,v), in the uv plane, plus its complex conjugate. As the earth rotates, the baseline changes orientation and fills in a track on the uv plane (see Figure 1.11). By increasing the number of antennae to N, the number of baselines is increased to N(N-1)/2, with N(N-1) corresponding tracks. Therefore, increasing the number of antennae and/or the observation time allows us to 'fill in' more of the uv plane. Hypothetically, if we could measure V(u,v) for every point on the uv plane we would have the Fourier transform of the sky brightness, within the FOV of each antenna ($\propto \lambda$ / D). Radio interferometry works by observing multiple baselines and orientations, gradually 'filling' in the uv plane and sampling more of the Fourier transform of T(x,y). In effect, we get a 'dirty image', T_D(x,y), which is a convolution of the sky brightness, T(x,y), with the Fourier transform of the sampling function (a function, S(u,v), defined as 1 where there is a V(u,v) measurement and 0 where there is none). The Fourier transform of the sampling function gives the synthesized beam, or point spread function (PSF), of the radio image, which is analogous to the PSF in an optical telescope. To get an intensity map of the true sky brightness, we need to de-convolve the dirty map. This is generally a non-linear and computationally heavy process (e.g. CLEAN routine, Högbom, 1974), and the Fourier transform and de-convolution processes used in this thesis will be described in the relevant sections (radio imaging is also described in more detail in Appendix A.1). The quality of the intensity map is related to the uv coverage, and the full width half maximum (FWHM) of the synthesized beam is $\propto \lambda$ / b_{max}, where b_{max} is the length of the longest baseline. Therefore, the spatial resolution of a radio interferometer is $\propto \lambda$ / b_{max}, and short baselines are used to measure the large scale structure.

1.9 Thesis Motivation & Structure

This thesis explores star formation in luminous infrared galaxies across cosmic time and attempts to fill gaps in our current understanding of galaxy evolution, and the

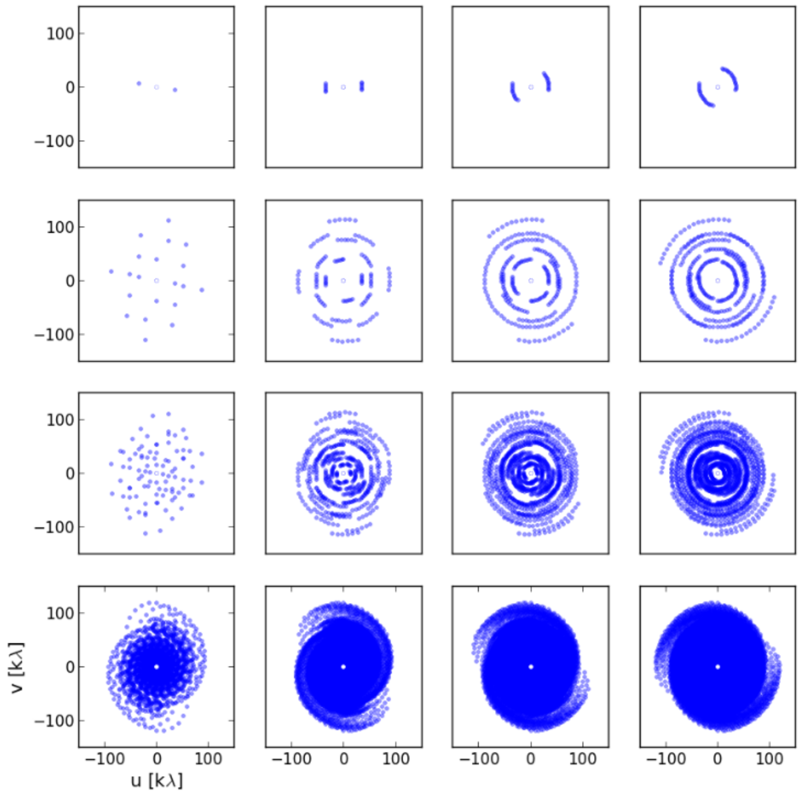

Figure 1.11: uv coverage (sampling function) of a hypothetical radio interferometer with 2, 5, 10 and 50 antennae (top to bottom). The left to right columns show the tracks created by observation times of 10 seconds, 2, 4 and 6 hours respectively (taken from Avison and George, 2013). This figure demonstrates how both an increase in antennae number and observation time 'fills in' more of the uv plane, allowing more of the Fourier transform of the sky brightness to be sampled.

.

motivation for this thesis are manifold.

As outlined in this chapter, we know that U/LIRGs at the peak of the cosmic SFRD are different from their local counterparts. This has been established from various studies that have been undertaken on z $\sim$ 2 U/LIRGs; but these tend to be either in-depth explorations of one or two galaxies, large samples focusing on a particular property (e.g. evolution of dust temperature), or surveys that focus on the general population of star forming galaxies, which happen to include a sub-sample of U/LIRGs. There is a dearth of systematic studies focusing on a sample of U/LIRGs only, and I will provide such a study in Chapter 2. This type of research is necessary, as a good reference point is needed for examining the evolution of

U/LIRGs properties from cosmic noon to the current epoch. It is also needed to ascertain what proportion of z $\sim$ 2 U/LIRGs are outliers like local U/LIRGs, and how many blend into the normal star forming population.

U/LIRGs are a relatively understudied population at intermediate redshifts, and previous observations have tended to focus on the upper or lower ends of the U/LIRG luminosity spectrum, i.e. low luminosity LIRGs or very high luminosity ULIRGs. We need to fill the luminosity gap between these subpopulations if we want to understand the properties of the U/LIRG population as a whole at intermediate redshifts, and I will provide a sample of galaxies that fill this gap in Chapter 3

Another open question in the field is establishing if star forming galaxies do indeed follow a bi-modal distribution in the SFR - $M_\star$ and $\Sigma_{\rm SFR}$ - $\Sigma_{\rm mol}$ planes. If so, what mechanisms are responsible for this bi-modality and how does a galaxy transition between these two modes? Conversely, if this bi-modality turns out to be incorrect, what are the systematic effects, or assumptions, that gave rise to this hypothetical bi-modality? Intermediate-z U/LIRGs can tackle this issue, as their luminosity range includes both MS and starbursts galaxies.

Much of our knowledge of the high-z universe is gleaned from fitting models to galaxies' emission line spectra and determining their properties. Little research has been done into whether the properties of galaxies are correctly encoded into the observed emission and absorption lines, and if high-z spectra can be modelled using the assumptions and calibrations taken from the local universe.

Even if it is established that we can correctly determine a galaxy's properties from its spectrum, current high-z observational signatures, such as the ratio of rotational velocity to velocity dispersion, are usually applied to kpc scale spatial resolution and may not be adequately capturing the underlying properties. We need to figure out at what spatial resolution observables can constrain the physical properties of a galaxy, or discriminate between merger stages of a galaxy at cosmic noon, and we need to decipher what are the best observables to use. In chapters 4 and 5, I will begin to tackle these critical issues. With the recent launch of JWST and the upcoming 30+ m class of optical and near IR telescopes, this research is vital if we want to correctly interpret their observations.

The layout of the thesis is as follows:

1. Chapter 2 describes how a sample of U/LIRGs at high redshift have similar properties to the regular star forming population found in the same redshift range. Stochastic processes, such as the mergers seen to be driving star formation in local U/LIRGs do not appear necessary to drive star formation in U/LIRGs at high-z. The majority of the sample are main sequence galaxies, are less dust obscured than local U/LIRGs and don't appear to be metal deficient, demonstrating that the properties of U/LIRGs have evolved between the peak of the cosmic SFRD and the present epoch.

2. Chapter 3 explores a unique sample of intermediate-z U/LIRGs that form a subpopulation that straddles regular star forming galaxies and starbursts. This sample suggests a continuous change in SFE between these two populations, as opposed to the hypothesized bi-modality, and the increased SFE appears to be driven by morphology and differing stages of interaction. Intriguingly, there is a possible hidden merger seen in one of the targets that was previously thought to be isolated based on rest frame optical observations, and a potential CO dark ULIRG, which is a very unusual ISM for a luminous IR galaxy, showing how multi-wavelength observations are vital to fully understand a galaxy.

3. Chapter 4 studies mock observations of a star forming galaxy at cosmic noon taken from the NewHorizon cosmological simulation. A new post-processing pipeline that adds mock spectra to hydrodynamical cosmological simulations is introduced, and I use the output from this pipeline to make mock High Angular Resolution Monolithic Optical and Near-infrared Integral field spectrograph (HARMONI) observations of the Hα emission line. I show how the intrinsic physical properties of the simulated galaxy are correctly encoded into its spectrum. It is then shown how the presence of moderate

dust doesn't affect the analysis of the mock observations, which is vital as much of the star formation in the high-z universe is dust enshrouded.

4. Chapter 5 builds on the HARMONI mock observations and takes three snapshots of a simulated high-z star forming galaxy as it undergoes a minor merger in the NewHorizon cosmological simulation. The observational signatures of the kinematics, morphology and underlying state of the ISM are extracted and I track how these change over the course of the minor merger. I will discuss what these signatures allow us to infer about the physical characteristics and merger status of the galaxy. This work will help interpret future HARMONI observations and translate the information from spatially resolved emission lines back to the underlying state of the ISM and star formation.

5. Chapter 6 gives a summary of the results and conclusions presented in this thesis and offers a brief outlook on the open questions in the field.

Unless explicitly stated in the relevant sections or captions, all the analysis, plots and tables presented in the following chapters are my own work.

Dust is beautiful ... I never knew

— Philip Pullman *His Dark Materials*

2

Luminous Infrared Galaxies at Cosmic Noon

Contents

This chapter is adapted from: L. Hogan, D. Rigopoulou, G. E. Magdis, M. Pereira-Santaella, I. García-Bernete, N. Thatte, K. Grisdale, J.S. Huang. *Integral Field Spectroscopy of Luminous Infrared Main Sequence Galaxies at Cosmic Noon*, 2021, MNRAS, 503, 5239.

2.1 Introduction

Dust obscured star formation dominates unobscured star formation at the peak of the cosmic SFRD (see Figure 1.2), so studying the main drivers of star formation in U/LIRGs at cosmic noon is necessary for our understanding of the cosmic SFH, and they are also an important probe for testing our theories of why the cosmic SFRD peaked $\sim$ 10 Gyr ago. For example, some simulations show that since z $\sim$ 6 merger driven star formation accounts for only 25% of today's stellar mass (Martin et al., 2017) and may be responsible for as little as 1% of the cosmic SFRD (Rodríguez Montero et al., 2019). As the contribution of U/LIRGs to the SFRD at cosmic noon can be as high as 70%, and they are synonymous with mergers and interactions in the local universe, they provide useful test cases to constrain theory and simulation.

Many surveys at z $\sim$ 2, for example KMOS^{3D} (Wisnioski et al., 2015), focus on the general population of star forming galaxies, which does include U/LIRGs. But it is necessary to perform a systematic study on U/LIRGs only, as we know high-z U/LIRGs have different properties to their local counterparts (see Section 1.6), and a U/LIRG only study is a good reference point for examining the evolution of U/LIRGs. For example, are they mostly isolated disks, mostly starbursts, or an equal mixture of both? Is star formation in a typical dusty galaxy as heavily dust obscured as has been observed in the intermediate-z or local U/LIRGs?

Finally, U/LIRGs in the local universe are outliers, with very different properties compared to the normal star forming population. While we know high-z U/LIRGs can still be located in the starburst regime, we need to take a sample of z $\sim$ 2 U/LIRGs to try to ascertain what proportion are outliers, and how many blend into the normal star forming population.

This chapter presents a KMOS study of a sample of eighteen U/LIRGs at cosmic noon, which I will use to examine the mechanisms driving their huge SFRs, and explore the general properties of high-z U/LIRGs.

Table 2.1: The Sample of luminous IR galaxies.

Object	RA	Dec	z
o1	03:32:22.57	-27:45:39.11	2.073
o2	03:32:38.11	-27:44:33.67	2.330
o3	03:32:46.31	-27:44:18.07	2.433
o4	03:32:19.05	-27:43:15.29	2.409
o5	03:32:36.89	-27:42:25.76	2.142
o6	03:32:33.29	-27:42:01.82	2.455
o7	03:32:28.51	-27:46:58.95	2.309
o8	03:32:29.17	-27:45:14.61	2.434
o9	03:32:36.18	-27:46:27.51	2.291
o10	03:32:33.84	-27:45:18.09	2.141
o11	03:32:47.54	-27:44:32.86	2.276
o12	03:32:28.40	-27:42:46.52	2.141
o13	03:32:35.12	-27:40:45.21	2.312
o14	03:32:23.77	-27:41:32.15	2.304
o15	03:32:36.09	-27:42:24.57	2.139
o16	03:32:48.53	-27:45:17.50	2.169
o17	03:32:40.39	-27:44:54.88	2.227
o18	03:32:23.88	-27:42:22.19	2.331
Star	03:32:31.87	-27:41:05.97	-

2.2 Observations

2.2.1 The Sample

The galaxies studied here were drawn from Herschel observations of the Great Observatories Origins Deep Survey South field (GOODS-S, Elbaz et al., 2011). GOODS-S is a well studied deep field and benefits from the availability of excellent multi-wavelength ancillary data (e.g. the ZFOURGE database of large and deep medium-band imaging survey for $z > 1$ galaxies, Straatman et al., 2016) including multiple photometric bands, stellar masses etc. The present sample (hereafter my KMOS sample) comprises eighteen targets which were selected according to the following criteria:

1. Detection in at least one of the Herschel bands to ensure the U/LIRG-like infrared luminosity of the galaxies and therefore high SFR.

2. Spectroscopic redshift or very robust photometric redshift based on at least

10 data points from broadband photometry.

3. Galaxies located in the 2 < z < 2.5 range, with this redshift chosen to allow the Hα spectral line (6563 Å) and the [NII] fine structure doublet (6549 Å and 6583 Å) to be observed by KMOS.

4. All targets have Spitzer 24 μm counterparts.

5. All targets could be simultaneously observed in one KMOS pointing.

Figure A.3, in the appendix, shows my eighteen targets are representative of the parent sample.

2.2.2 The K-band Multi Object Spectrograph

KMOS is an integral field spectrograph in operation on the VLT in the Atacama Desert in Chile. The instrument can simultaneously target up to 24 objects within a patrol field of 7.2′ in diameter (Sharples et al., 2013). KMOS uses an image slicer system, as described in Section 1.8.1. Each of the 24 IFUs has a square field of view of 2.8″ × 2.8″. This field of view is divided into 14 slices, each with 14 pixels of 0.2″ × 0.2″, which gives the FOV in each IFU a seeing limited spatial sampling of 0.2″. The spectral resolution within the K band is R = 4200 with a 2 channel FWHM.

All eighteen of my objects were prepared using the KMOS Arm Allocator (KARMA, Wegner and Muschielok, 2008), with each galaxy assigned to an IFU allowing all targets to be observed in a single pointing, ensuring atmospheric conditions are the same across the sample. Observations were taken in the K-band which has coverage of 1.934 - 2.460 μm and a channel width of approximately 3 Å.

The data is made up of twelve separate observation blocks (OBs): six on 22/23 November 2013 and six on 09/10 October 2016 [1]. The 'stare' observation mode was used, with 8 exposures per OB and an integration time of 600 seconds per exposure. One IFU was dedicated to a star to get a PSF for each OB. The seeing varied from 0.3″ - 1.3″ over the two nights, and the average seeing conditions were approximately 0.6″.

[1]OB IDs: 200297829-41, 200402165-177, 200402203-11

The raw data was reduced using the standard KMOS pipeline, part of the EsoReflex package (Davies et al., 2013, Freudling et al., 2013). The pipeline carries out dark current correction, flat field correction, wavelength calibration, telluric correction, sky subtraction and flux calibration to produce a final data cube and an associated noise cube, per OB, for each target. I took the reduced cube from each OB and combined them together to produce a final data cube per target. To ensure I accounted for any spatial offsets across the OBs I found the centre of the PSF via fitting a 2D Gaussian to the star and shifted each cube so that the centres aligned for all twelve OBs. This gives the final cubes a spatial dimension of 17 × 16 pixels. I used a weighted average rather than a simple average to account for the observations being carried out under varying seeing conditions. This weighting was calculated by finding the size in arcseconds of each of the twelve PSFs and summing these together to get a total area. I then found the fractional contribution to the total area given by each OB's PSF. The reciprocal of these fractions were then used to assign a weighting for each OB with the sum of all twelve weightings equalling one, i.e. an OB with worse than average seeing has a larger than average fractional contribution to the total area and is thus proportionally down-weighted and vice-versa for an OB with above average seeing. The PSF for the final stacked cubes was found by fitting a Gaussian to the stacked observation of the star, combined using the same weighted average, which gave the PSF a FWHM of $0.57'' \times 0.44''$.

2.3 Analysis

2.3.1 Spectra

To find the Hα and [NII] emission lines I inspected the cube at the expected Hα wavelength based on the redshift of the galaxy and scanned all adjacent channels until the emission lines were found (all these cubes had a robust photometric redshift or previous spectroscopic redshift). Once the emission lines were identified, individual apertures were applied to each data cube to distinguish between galaxy and sky emission. Two apertures were applied to each cube: the galaxy aperture and the sky aperture. The galaxy aperture was scaled to cover the extent of the

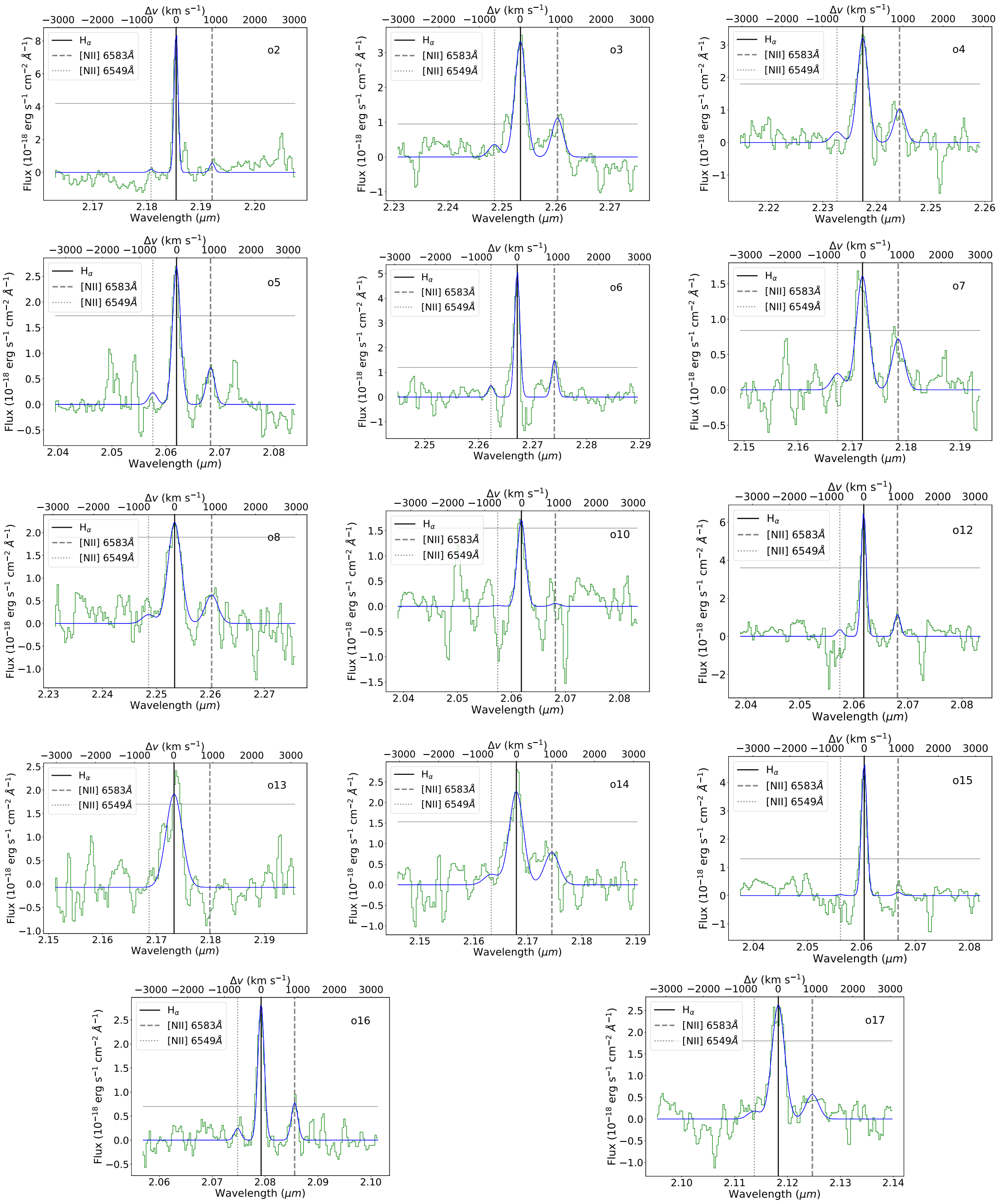

Figure 2.1: The integrated spectra for the 14 luminous IR galaxies with detected Hα emission. The best fit model, described in Section 2.3.1, is overlaid in blue and the vertical lines represent the peak of the red-shifted Hα, [NII] 6549 Å and 6583 Å lines. The grey horizontal line indicates where the S/N equals 3.

galaxy emission. The remaining spaxels were dedicated to the sky aperture, which was normalized to be the same area as the galaxy aperture.

All spaxels within the galaxy apertures were collapsed into a one dimensional spectrum and model spectra were fitted to the observed Hα and [NII] emission lines. This model involved simultaneously fitting three Gaussian profiles and a linear function to account for any continuum. The ratio of the [NII] 6549 Å / [NII] 6583 Å peak flux was preset to 0.34, as predicted theoretically (e.g. Osterbrock and Ferland, 2006) and the width of the [NII] Gaussian profiles was forced to equal the width found for the Hα emission line. All three lines were also forced to share the same line of sight velocity. The best fit was determined by applying a χ^2 minimization to the observed flux. For galaxy o13 the [NII] lines are not detected and their expected line centres coincide with a trough in the observed spectra, which affected the fitting of the model spectra. Instead, this was fitted with a single Gaussian curve, centred on the Hα line, and a linear function.

To ensure I did not miss any Hα flux, I created a sky spectrum by collapsing all spaxels within the sky aperture and compared the sky spectrum to the integrated galaxy spectrum. If any Hα emission was found in the sky spectrum, I increased the size of the galaxy aperture and repeated the above analysis. Finally, to calculate the signal-to-noise (S/N) of my spectra I used the standard deviation of the sky spectra, i.e. the standard deviation of the sky flux measured in each bin of the spectral window plotted in Figure 2.1.

Although the pipeline does basic sky subtraction by allocating a sky IFU to each object IFU, there was still some residual sky emission around the edge of the reduced cubes. To ensure these pixels did not skew the noise calculations, I clipped any pixels in the sky aperture that were greater than 3σ above or below the mean sky emission.

Hα line emission was detected in fourteen of the eighteen targets. For the four non-detections, the entire cube was scanned for an emission line. I marginally detected ($\sim 3\sigma$) the [NII] 6583 Å line in four of the galaxies. The total Hα and [NII] fluxes from the galaxies were evaluated by integrating the area under their

Table 2.2: Values found from the Hα emission line fitting. Values in italics are estimates based on upper limits as discussed in Section 2.3.1.

Object	$\lambda_{H\alpha}$[1] μm	FWHM[2] km s^{-1}	$F_{H\alpha}$[3] 10^{-17} erg s^{-1} cm^{-2}	$L_{H\alpha}$[4] 10^{42} erg s^{-1}	$SFR_{H\alpha}$[5] $M_\odot$ yr^{-1}	[NII] 6583 Å/ Hα[6]
o1	*2.017*	*267*	*< 5.46*	*< 1.72*	*<9*	
o2[7]	2.185	75 ± 9	5.13 ± 0.85	2.15 ± 0.37	12 ± 2	-
o3	2.253	310 ± 34	8.23 ± 1.12	3.83 ± 0.52	21 ± 3	0.34 ± 0.09
o4	2.237	305 ± 34	7.82 ± 1.11	3.55 ± 0.51	19 ± 3	-
o5	2.062	235 ± 21	4.61 ± ± 0.55	1.58 ± 0.19	8 ± 1	-
o6	2.267	126 ± 21	5.16 ± 1.14	2.46 ± 0.54	13 ± 3	0.29 ± 0.09
o7	2.172	355 ± 4	4.39 ± 0.36	1.80 ± 0.15	10 ± 1	0.45 ± 0.16
o8	2.254	368 ± 77	6.54 ± 1.81	3.05 ± 0.85	16 ± 5	-
o9	*2.160*	*267*	*< 3.53*	*< 1.41*	*<8*	-
o10	2.062	245 ± 22	3.07 ± 0.52	1.18 ± 0.20	6 ± 1	-
o11	*2.150*		-	-	-	-
o12	2.141	132 ± 22	6.30 ± 1.43	2.15 ± 0.49	12 ± 3	-
o13	2.173	473 ± 52	6.97 ± 0.95	2.87 ± 0.39	15 ± 2	-
o14	2.168	415 ± 43	7.22 ± 0.99	2.94 ± 0.40	16 ± 2	-
o15	2.060	145 ± 13	4.97 ± 0.57	1.69 ± 0.19	9 ± 1	-
o16	2.079	176 ± 17	3.67 ± 0.46	1.29 ± 0.16	7 ± 1	0.28 ± 0.09
o17	2.227	386 ± 39	7.83 ± 1.00	2.94 ± 0.38	16 ± 2	-
o18	*2.186*	*267*	*< 1.53*	*< 0.62*	*< 3*	-

[1] Observed peak wavelength of the Hα emission line. Errors not included as they were on the order of 1 Å and the values quoted here are in μm.
[2] The full width half maximum of the galaxy emission line, corrected for the instrumental full width half maximum.
[3] Total Hα flux of the galaxy.
[4] The total Hα luminosity of the galaxy.
[5] The star formation rate of the galaxy, uncorrected for dust attenuation, calculated from the Hα luminosity. See section 2.3.2.
[6] The ratio of Hα flux to the flux of the [NII] 6583 Å emission line.
[7] The FWHM for o2 is a lower bound due to a noise spike on the red wing of the Hα emission line, which was corrected during data reduction.

respective Gaussian curves. The total Hα flux for my KMOS sample ranges from 3.07 - 8.23 $\times$ 10^{-17} erg s^{-1} cm^{-2} and an instrument corrected FWHM of 75 - 473 km s^{-1}, with my results shown in Table 2.2. The FWHM of 75 km s^{-1} for galaxy o2 is a lower limit as a noise spike occurred on the red wing of the Hα emission line, which was corrected for in the data reduction, leading to a loss of flux on the red side of the line. Intensity maps (0th moment[2]) of the observed Hα lines of the fourteen galaxies were made by summing the intensity in all channels that span the emission line, and these are shown in Figure 2.2.

For three of the four targets with undetected Hα I estimated a 3σ upper limit for the line flux. Firstly, I fitted an aperture of 1$''$ in radius to each cube and then used the redshift of the target to find the expected peak wavelength of the Hα emission line. I found the channel that corresponds to the peak wavelength and extracted a spectrum spanning twelve channels either side (halfway between the expected H-alpha and [NII] emission lines). From this I calculated the mean and standard deviation of the spectrum. Assuming the average linewidth of my sample, 267 km s^{-1}, and a peak amplitude equalling the 3σ value, I estimated an upper limit for the Hα line flux. I could not get an upper limit for galaxy o11 due to a skyline falling in a couple of the channels of the expected Hα emission.

For the four non-detections, their L_{IR}, $M_\star$ and redshift appear within the range of the fourteen detections, so there is no correlation between these properties and the non-detections. Their rest frame UV and optical broad band fluxes (B-band to K-band) are below the sample average, so it appears that the Hα emission in these four targets may be more heavily affected by dust and/or have an intrinsically fainter surface brightness.

The analysis outlined in Section 2.2.2 was repeated, but instead of the seeing weighted averaging method, I recombined the cubes using a noise weighting scheme.

[2] 0th moment $\equiv M_0 \equiv \int I_v \, dv$,
1st moment $\equiv M_1 \equiv \dfrac{\int V_{los} I_v dv}{M_0}$,
2nd moment $\equiv \dfrac{\int (V_{los} - M_1)^2 I_v dv}{M_0}$, $\sigma = \sqrt{2ndmoment}$,
where I_v is the intensity in each channel, V_{los} is the line of sight velocity and dv is the width of each channel.

The spectra derived from both cubes agree well within error, therefore, the choice of weighting scheme does not have a significant impact on the analysis and the results reported here.

2.3.2 Star Formation Rates

Hα emission is a sensitive tracer of star formation within the past 10 Myr (see Section 1.2) as, in the absence of AGN, it is the O-type stars that provide the bulk of the requisite ionizing radiation (e.g. Kennicutt and Evans, 2012). Although I cannot exclude the presence of an AGN in my sample, the Hα / [NII] 6583 Å ratio is above one for the entire sample, which is consistent with the star forming locus of the BPT diagram (a nebular line diagnostic for classifying AGN and star forming galaxies developed by Baldwin, Phillips and Terlevich; see Baldwin et al., 1981 for details) at z $\sim$ 2 (Shapley et al., 2015). I also checked the ZFOURGE database for X-ray emission and no results came up for any of the targets.

To convert the Hα flux to a luminosity I used, $L_{H\alpha} = 4\ \pi\ D_L^2\ F_{H\alpha}$, where D_L is the luminosity distance calculated using a cosmology with values of H_0 = 70 km s^{-1} Mpc^{-1}, $\Omega_m = 0.3$ and $\Omega_\Lambda = 0.7$ (all distance measurements in this thesis will use this cosmology).

Hα is strongly attenuated by dust, so in U/LIRGs this tracer provides a lower limit for the ongoing star formation (e.g. Hopkins et al., 2001), and is a useful measure of the 'unobscured' star formation. The absorption cross-section of galactic dust strongly peaks in the UV so, assuming radiative transfer balance, the IR emission is attributable to re-processed stellar light from underlying O-type and B-type stars. This makes L_{IR} emission a probe of the star formation history within the past 100 Myr (see Section 1.2) and is also a tracer of a galaxy's 'obscured' star formation.

To determine the L_{IR} for my sample of galaxies, the available Herschel and Spitzer photometry (G. Magdis private communication) was fitted with the dust model of Draine and Li (2007) following the methodology described in Magdis et al. (2013). The L_{IR} for my sample are listed in Table 2.3, with the fits resulting in six

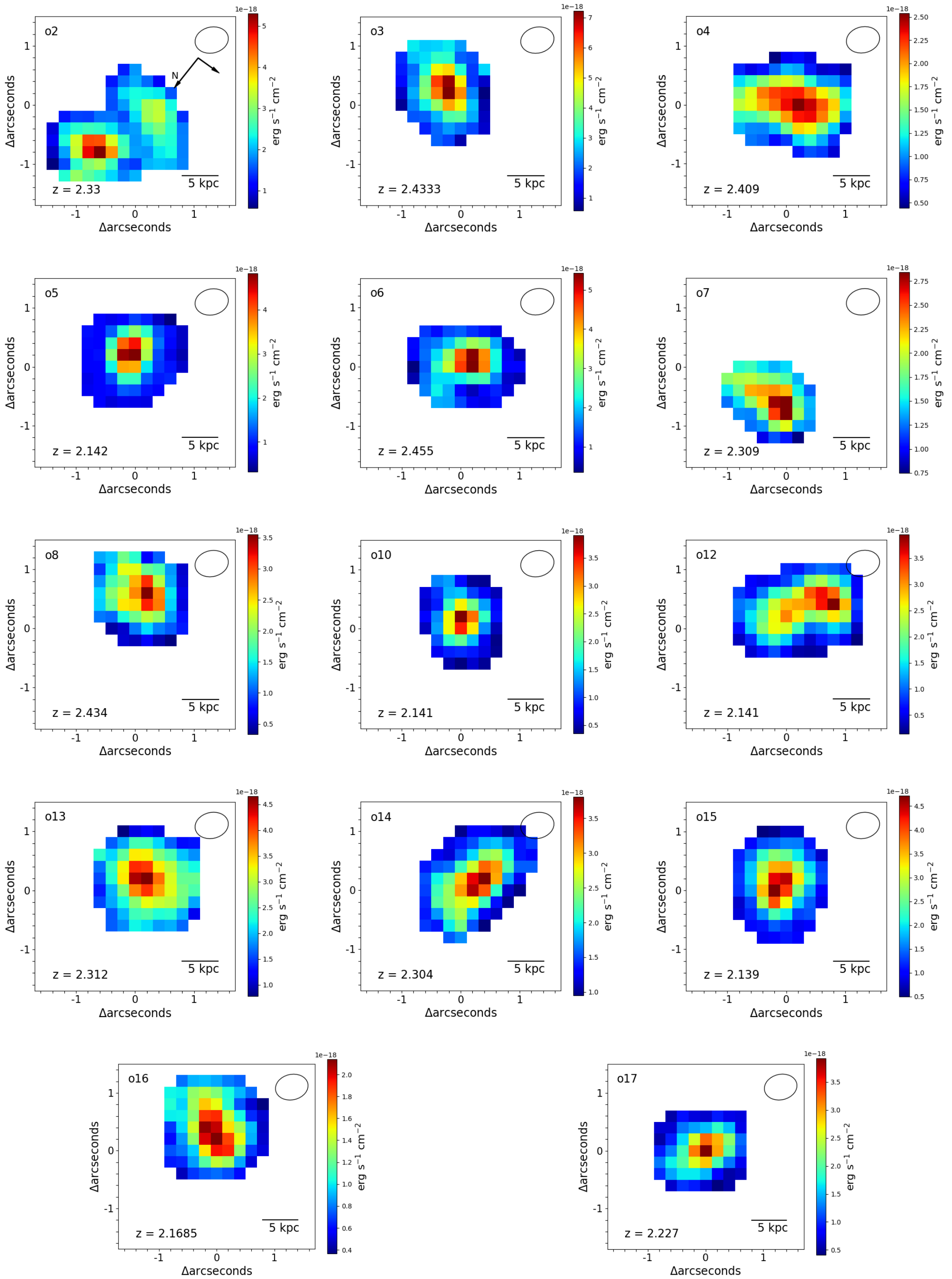

Figure 2.2: The emission maps of the Hα emission line (6563 Å) from my galaxy sample. Each pixel is 0.2″ × 0.2″ where 1″ corresponds to ∼ 8 kpc at these redshifts. The seeing is 0.57″ × 0.44″, corresponding to a resolution of ∼ 4 kpc, and the size of the PSF is shown in the top right corner. North and east are located 127 degrees anti-clockwise from the x-axis, as shown by the arrows in the emission map of galaxy o2.

of the galaxies being ULIRGs, eight are LIRGs and four could not be determined due to poor SED fits (for full disclosure, the L_{IR} and $M_\star$ in this chapter were calculated with the help of collaborators).

Taking the L_{IR} and Hα emission I can investigate the recent SFH of my sample using the following conversion factors from Murphy et al. (2011b):

$$SFR_{H\alpha} \quad (M_\odot yr^{-1}) \; = \; 5.37 \times 10^{-42} \; L_{H\alpha} \quad (erg \; s^{-1}), \tag{2.1}$$

$$SFR_{IR} \quad (M_\odot yr^{-1}) \; = \; 3.88 \times 10^{-44} \; L_{IR} \quad (erg \; s^{-1}). \tag{2.2}$$

The $SFR_{H\alpha}$ for my KMOS sample, uncorrected for attenuation, range from 6 - 21 $M_\odot$ yr^{-1} with the SFR_{IR} having values ranging from 40 - 783 $M_\odot$ yr^{-1} (see Tables 2.2 and 2.3).

2.3.3 Kinematics

To classify high-z U/LIRGs, and also to compare them to their low-z counterparts, the kinematic properties offer an excellent insight. To investigate the kinematics of the fourteen galaxies in which Hα was detected, I used GalPak^{3D} (Bouché et al., 2015) which fits a rotating disk model to the observed emission line flux. GalPak^{3D}'s Bayesian approach is well suited to recovering kinematic parameters from seeing limited galaxy observations with low S/N at increasing disk radius.

GalPak^{3D}'s model galaxy has 10 free parameters: x, y and z centroid position, flux, half-light radius, turnover radius, position angle, inclination, maximum rotational velocity and the one dimensional intrinsic velocity dispersion. The emission from this model galaxy is subsequently convolved with a PSF, specified by the user, and the best fit to the observed data is found via a Bayesian Markov Chain Monte Carlo (MCMC) approach.

For the input cube I cut around the Hα emission line to ensure no contamination from the [NII] lines on either side. The PSF was set to that calculated in Section 2.2.2 and the KMOS instrument was chosen in GalPak^{3D}'s instrumental settings, so that the algorithm properly accounted for the instrumental resolution. For

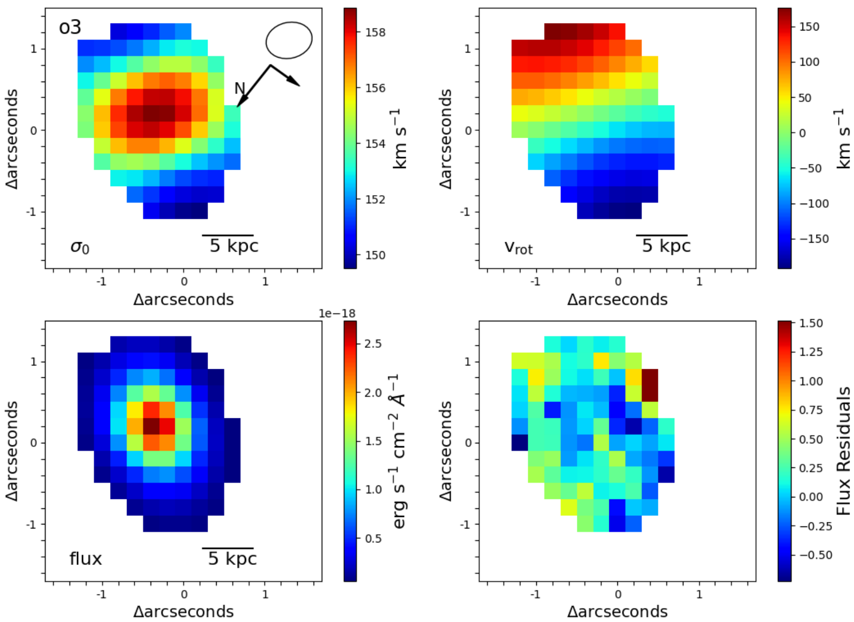

Figure 2.3: Maps of the model galaxy from GalPak^{3D}, for galaxy o3, convolved with the PSF of 0.57″ × 0.44″, but excluding background/sky. **Top left:** The intrinsic velocity dispersion across the galaxy disk. **Top right:** the projected velocity field assuming the systematic velocity of the galaxy has been set to zero. **Bottom left:** The flux arising from the model disk which is assumed to have an exponential brightness profile. **Bottom right:** The residuals of the best fit flux when compared to the observed cube. North and east are located 127 degrees anti-clockwise from the x-axis as shown by the arrows in the top left panel.

the galaxy model I assumed that the Hα emission follows an exponential radial flux profile, the rotation curves have an arctan functional form and the intrinsic velocity dispersion is isotropic and spatially constant across the disk. I set the aspect ratio (vertical scale height to effective radius) to 0.2, to account for thicker disks at high redshifts (e.g. Förster Schreiber et al., 2009, Wuyts et al., 2016) The spatial and kinematic parameters, listed in the previous paragraph, were left free for the MCMC to fit.

Six of the sample galaxies converged in the MCMC to parameters consistent with a rotating disk. The spatial and kinematic parameters found by GalPak^{3D} are shown in Table 2.4, the models are shown in Figures 2.3, 2.4, 2.5 and 2.6, and an example of how the best fit models compare to the observed maps is given

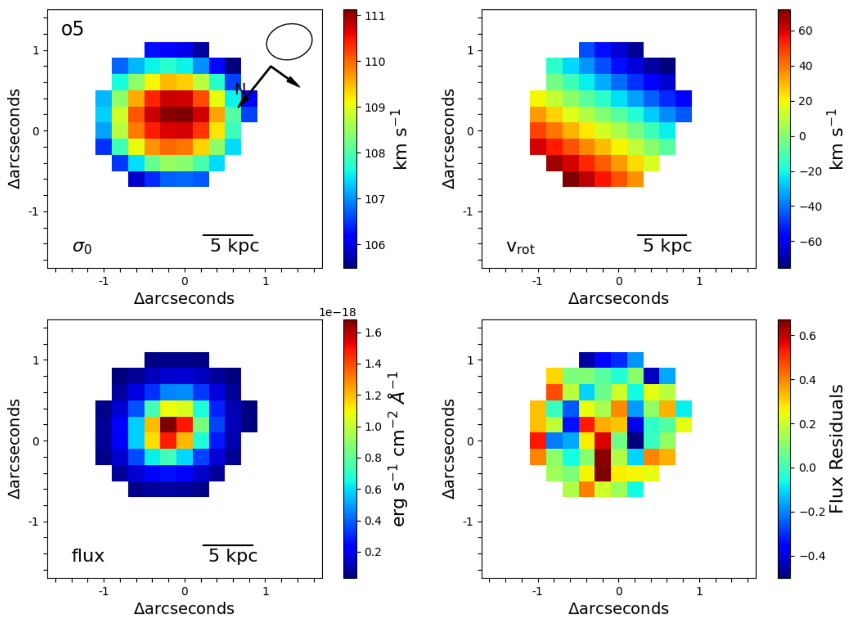

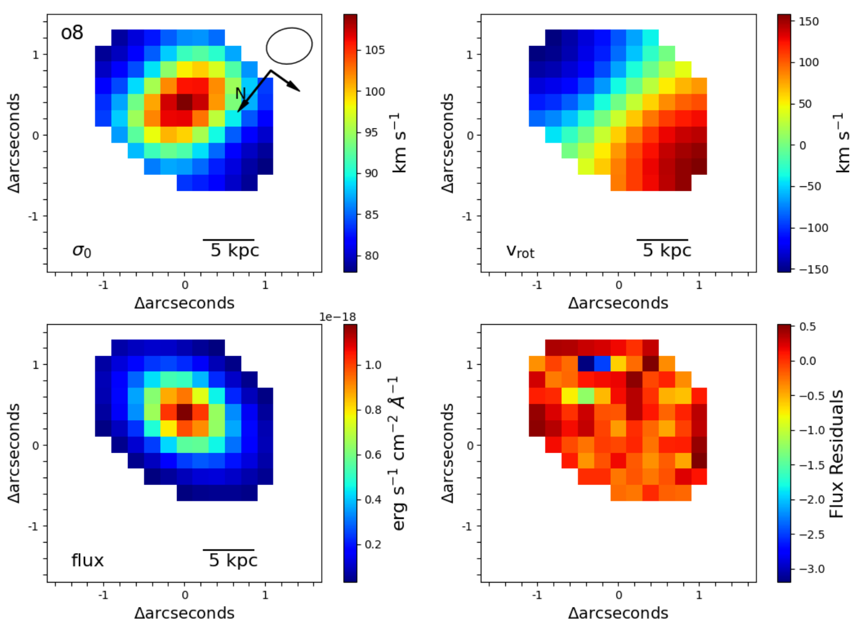

Figure 2.4: Description same as in Figure 2.3, for galaxies o5 and o8.

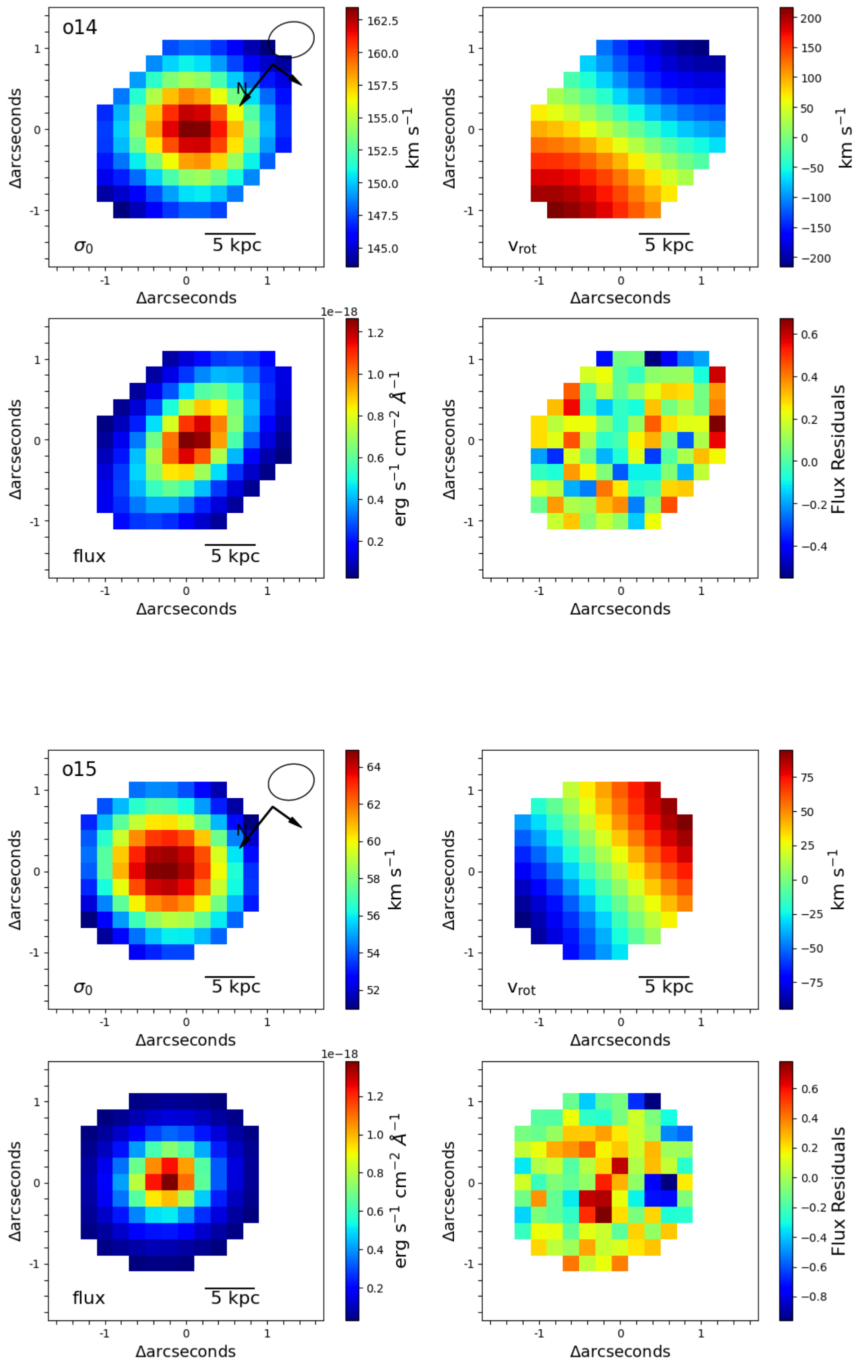

Figure 2.5: Description same as in Figure 2.3, for galaxies o14 and o15.

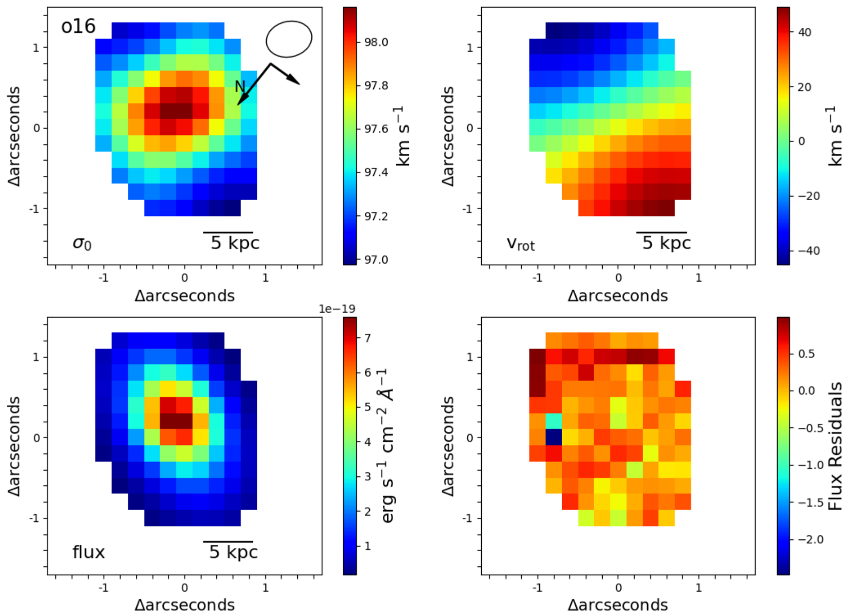

Figure 2.6: Description same as in Figure 2.3, for galaxy o16.

in Appendix A.4. I rejected model disks that converged to unphysical values, e.g. rotational velocities approaching 1000 km s^{-1} or half light radii / flux far exceeding the emission maps. Likewise, I rejected models that only converged due to a hard boundary being adopted in GalPak^{3D}, i.e. rotational velocities of 350 km s^{-1} if the hard boundary is set to 350 km s^{-1}. I rejected disks if any individual parameter didn't converge or if the model galaxy provided a poor fit to the data upon inspection of residuals cube. Galaxy o17 was omitted from this analysis, as some noisy channels in the blue wing of the emission line appeared to be affecting the best fit parameters.

To test my results' sensitivity to the assumed galaxy model, I repeated the analysis with a Gaussian radial flux profile and subsequently re-ran the analysis using GalPak^{3D}'s default aspect ratio of 0.15 and all results agreed within error.

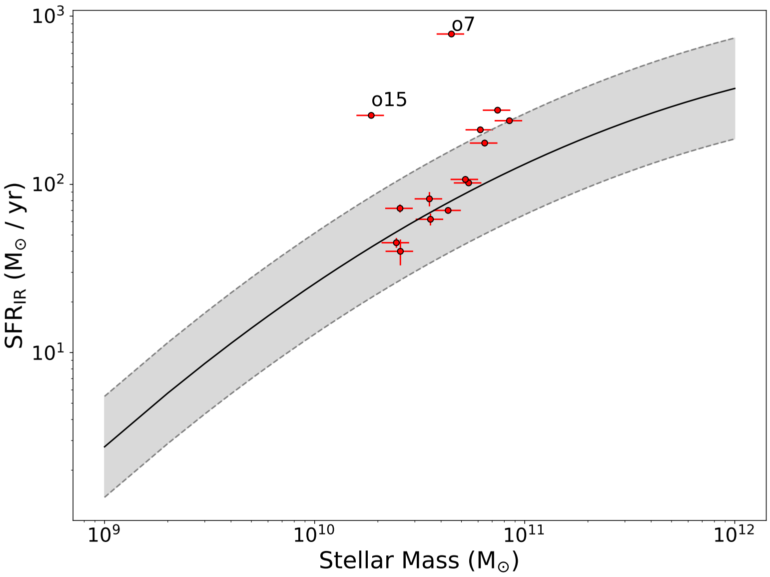

Figure 2.7: The SFR_{IR} from my sample of luminous IR galaxies plotted against the $M_\star$, with the main sequence of Whitaker et al. (2014) represented by the grey shaded region. The solid line is the main sequence at z = 2.25 and the grey region represents 0.3 dex above and below this relation. Galaxies o7 and o15 fall within the starburst regime.

2.4 The Properties of z$\sim$ 2 Luminous IR Galaxies

2.4.1 Modes of Star Formation

The location of a galaxy in the $M_\star$ - SFR plane is strongly linked to its mode of star formation. Although neither the stellar mass nor the SFR calculation rely on knowledge of what the gas is doing, the SFR is implicitly modulated by gas fraction and the SFE within the galaxy (e.g. Tacconi et al., 2018). This in turn allows the underlying mechanism driving star formation to be inferred by a galaxy's position with respect to the main sequence. To place my sample on the MS (Figure 2.7) I use the SFR_{IR} derived from the L_{IR} and the $M_\star$ derived from fitting Bruzual and Charlot (2003) models to the B, V, I, Z, Y, J and H photometry and the Spitzer Infrared Array Camera (IRAC) 3.6, 4.5, 5.8 and 8.0 μm photometric bands.

In summary, for each galaxy SED a set of models was generated using the stellar population synthesis templates of Bruzual and Charlot (2003), and the Padova stellar evolution tracks were adopted (Bertelli et al., 1994). The models were

Table 2.3: Values found by fitting an SED to the Spitzer and Herschel photometry using the dust model of Draine and Li (2007). Values in italics are estimates based on upper limits as discussed in Section 2.3.1.

Object	$\log(M_\star)$[1]	$\log(L_{IR})$[2]	SFR_{IR}[3]	$\log(\frac{SFR_{H\alpha}}{SFR_{IR}})$[4]	ΔSFR[5]	Dust Temperature[6]
	$M_\odot$	erg s^{-1}	$M_\odot yr^{-1}$			K
o1	10.78	12.07 ± 0.02	176 ± 8	< *-1.28 ± 0.02*	0.26 ± 0.02	32 ± 4
o2	10.52	-	-	-	-	-
o3	10.87	12.27 ± 0.01	276 ± 6	-1.13 ± 0.06	0.40 ± 0.01	39 ± 2
o4	10.93	12.20 ± 0.01	239 ± 6	-1.10 ± 0.06	0.30 ± 0.01	34 ± 4
o5	10.39	11.48 ± 0.03	45 ± 3	-0.73 ± 0.06	-0.06 ± 0.03	-
o6	10.55	11.62 ± 0.04	62 ± 5	-0.67 ± 0.10	-0.04 ± 0.04	-
o7	10.65	12.72 ± 0.01	783 ± 5	-1.91 ± 0.04	0.99 ± 0.01	42 ± 2
o8	10.16	-	-	-	-	-
o9	10.72	11.86 ± 0.02	107 ± 5	< *-1.15 ± 0.02*	0.08 ± 0.02	-
o10	10.73	11.84 ± 0.02	102 ± 4	-1.26 ± 0.08	0.05 ± 0.02	50 ± 2
o11	10.41	11.69 ± 0.03	72 ± 4	-	0.13 ± 0.03	-
o12	10.64	11.67 ± 0.02	70 ± 3	-0.78 ± 0.02	-0.05 ± 0.02	-
o13	10.39	-	-	-	-	-
o14	10.79	12.15 ± 0.02	211 ± 9	-1.13 ± 0.06	0.33 ± 0.02	23 ± 1
o15	10.27	12.24 ± 0.01	257 ± 4	-1.45 ± 0.05	0.78 ± 0.01	34 ± 23
o16	10.41	11.43 ± 0.07	40 ± 7	-0.76 ± 0.09	-0.13 ± 0.07	-
o17	10.55	11.74 ± 0.04	82 ± 3	-0.71 ± 0.07	0.08 ± 0.04	-
o18	10.72	-	-	-	-	-

[1] Stellar mass of the galaxy using the method described in section 2.4.1. I assume an error of 15% in any calculation that required the stellar mass.
[2] IR luminosity of my sample calculated by fitting an SED using the model of Draine and Li (2007).
[3] Star formation rate calculated from the IR luminosity. See Section 2.3.2.
[4] An estimate of the dust attenuation within the galaxy. See Section 2.4.2.
[5] The difference, in dex, between the observed SFR and the expected SFR from Whitaker et al. (2014), at the galaxy's redshift. Main sequence galaxies lie within 0.3 dex of this expected SFR.
[6] The temperature of the dust within the galaxy estimated by fitting a modified blackbody to the IR photometry. See Section 2.4.3.

constructed with solar metallicity and a Chabrier IMF (Chabrier, 2003). A Calzetti et al. (2000) starburst attenuation law was used to account for the extinction. For the parameterization of the SFH of each galaxy two simple single-component models were considered: an exponentially declining model of the form SFR(t) $\sim$ exp (-t/τ) with e-folding times of $\tau = 0.05$, 0.1, 0.5, 2.0 and 5.0 Gyr, and continuous star formation models. Finally, a χ^2 minimization technique was used to find the best-fitting model to each galaxy SED. To quantify how far each galaxy lies from the MS I used the 2 < z < 2.5 MS of Whitaker et al. (2014):

$$log(SFR_{MS}) = a + b\, log\left(\frac{M_\star}{M_\odot}\right) + c\, log\left(\frac{M_\star}{M_\odot}\right)^2, \tag{2.3}$$

where a = -19.99, b = 3.44 and c = -0.13. All but two of my sample are on the MS, as seen in Figure 2.2. The two outliers are galaxy o7, having a distance above the MS (ΔSFR) of 0.99 dex, and o15, with ΔSFR = 0.78 dex. This deviates from local U/LIRGs position with respect to the MS, and hints that star formation in a large proportion of luminous IR galaxies at cosmic noon may be similar to the regular star forming population and driven by steady state processes.

As a technical aside, the conversion factors of Murphy et al. (2011b) that I used to estimate the SFR were calibrated using a Kroupa (2001) IMF. But they yield the same results as a Chabrier IMF (e.g. Chomiuk and Povich, 2011, Kennicutt and Evans, 2012) so there is no discrepancy with the IMF used in the $M_\star$ calculation.

2.4.2 Obscured Versus Unobscured Star Formation

As my KMOS sample emits strongly at FIR wavelengths > 100 μm, a priori, I know these to be dusty star forming galaxies. Hα is strongly attenuated by dust so it is likely to underestimate the true SFR. In compact star forming galaxies, e.g. mergers, the $SFR_{H\alpha}$ can be orders of magnitude lower than IR estimates of SFR (e.g. Rodríguez-Zaurín et al., 2011). High redshift U/LIRGs tend to have more extended regions of star formation with lower SFR surface densities, so for a given IR luminosity attenuation is expected to be weaker at high-z (e.g. Buat et al., 2015).

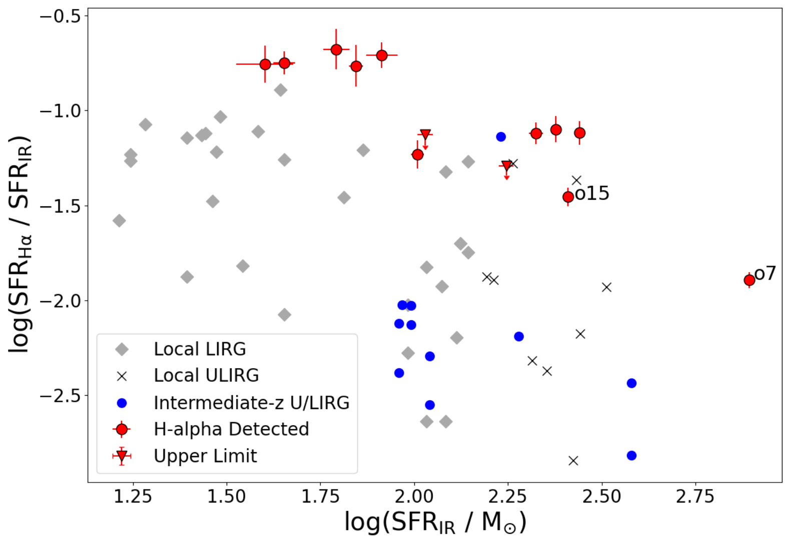

Figure 2.8: The log ratio of $SFR_{H\alpha}$ / SFR_{IR} versus log(SFR_{IR}) which is used as a proxy for dust obscuration. My sample (red) is compared to samples of intermediate-z and local U/LIRGS from Pereira-Santaella et al. (2019) and Rodríguez-Zaurín et al. (2011) respectively. The average log ratio of my sample is -1.1 ± 0.4 while the log ratio for the intermediate-z U/LIRGs, local ULIRGs and LIRGs is -2.2 ± 0.4, -2.0 ± 0.5 and -1.6 ± 0.5 respectively. Galaxy o7 and o15 are marked as both of these galaxies fall above the main sequence, and o7 is the only one of my sample to fall within the range of the local ULIRGs.

As mentioned in Section 1.2, the Hα and FIR emission arises from stellar populations with different age ranges, 10 Myr and 100 Myr respectively. If I assume a constant SFH in the past 100 Myr I can take the ratio of log($SFR_{H\alpha}$/SFR_{IR}) as a proxy for the obscured versus unobscured star formation. This allows me to investigate how dust enshrouded my sample is when compared to intermediate-z U/LIRGs in Pereira-Santaella et al. (2019) and local U/LIRGs from Rodríguez-Zaurín et al. (2011).

The average log($SFR_{H\alpha}$/ SFR_{IR}) ratio of my sample is -1.05 ± 0.39 (or -1.02 ± 0.41 when excluding the Hα upper bounds) while the value for the intermediate-z U/LIRGs is -2.2 ± 0.4, with values of -2.0 ± 0.5 and -1.6 ± 0.5 for the local ULIRGs and LIRGs respectively. My sample has similar log($SFR_{H\alpha}$/ SFR_{IR}) to local LIRGs (see Figure 2.8) with only galaxy o7, a starburst, falling within the location of local ULIRGs. This demonstrates that for the same L_{IR}, high-z

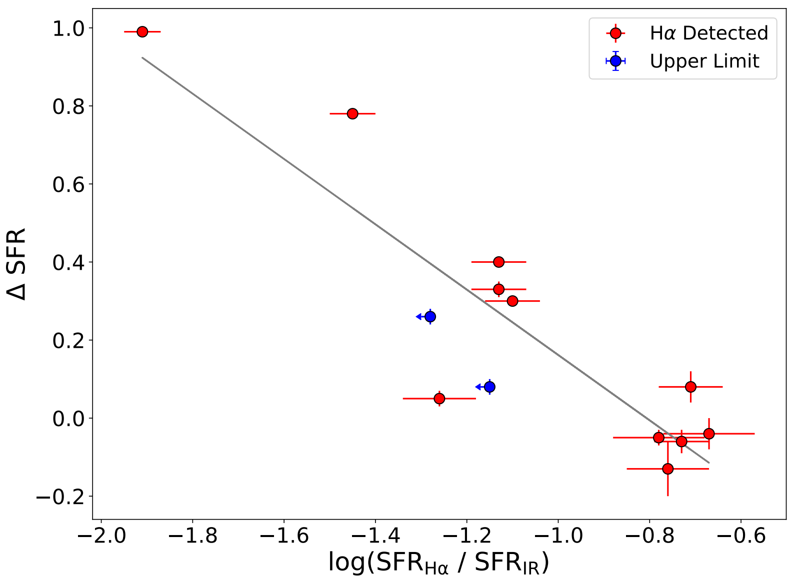

Figure 2.9: The relation between extinction, as represented by log($SFR_{H\alpha}$/ SFR_{IR}) and a galaxy's vertical offset from the main sequence of Whitaker et al. (2014), in dex, represented by ΔSFR. The linear fit has a Pearson's ρ = -0.88 (P-value $<$ 0.001) and shows that the level of obscured star formation increases with distance above the main sequence.

U/LIRGs appear to be less dust obscured than their local and intermediate-redshift counterparts. Given my selection criteria (Section 2.2.1), it may be I have selected less attenuated sources. But, as all my sources are less dust obscured than their lower z counterparts for a given L_{IR}, it holds at least a subpopulation are much less obscured than the U/LIRGs we observe in the local universe. Consequently, high-z U/LIRGs are different in their properties compared to low-z luminous IR galaxies.

Despite my sample size being relatively small, there is a statistically significant correlation between the magnitude of obscuration and a galaxy's distance from the MS, as shown in Figure 2.9, with a linear fit giving a Pearson's ρ = -0.88 and a P-value $<$ 0.001. This may reflect the dust morphology becoming more compact with distance above the MS. Galaxy o7 has a deep 1.1 mm continuum measurement in Elbaz et al. (2018), and its dust continuum is compact with an effective radius $\sim$ 1 kpc, but the rest of my sample doesn't have the requisite observations to explore this further.

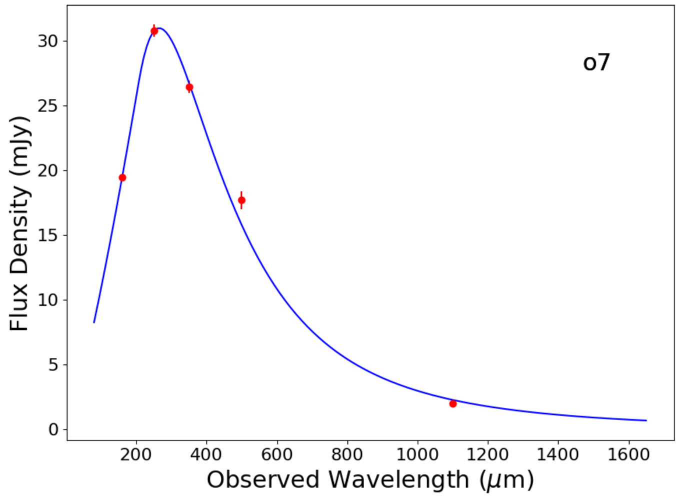

Figure 2.10: The modified blackbody, as described in Section 2.4.3, fitted to the photometry of galaxy o7. The best fit found by the MCMC is plotted in blue, and the observed flux is given by the red data points.

2.4.3 Dust Temperature

As outlined in Section 1.5, the T_{dust} of a galaxy, while not sufficient to tell a major merger from an isolated disk, can help us infer the interaction state of a galaxy when added to other observables. Dust properties within a galaxy can be deduced from the Rayleigh Jeans regime of the FIR emission (e.g. Casey et al., 2014). A single modified blackbody fitted to the FIR photometry is sufficient to determine the cold temperature of large dust grains, whereas a mixture of modified blackbodies is required to account for the warm dust of the smaller dust grains (e.g. Draine and Li, 2007).

Using the Herschel photometry, and limiting to wavelengths $> 100\ \mu$m to ensure I am sampling the peak and Rayleigh Jeans slope of the IR emission, I fit a modified blackbody to evaluate the T_{dust} for my KMOS sample. I assumed a grey-body emission model of the form:

$$F_\nu[(\nu_{obs}, T_{dust}/(1+z), \beta] = (1 - e^{-\tau})B_\nu(\nu_{obs}, T_{dust}/(1+z)), \quad (2.4)$$

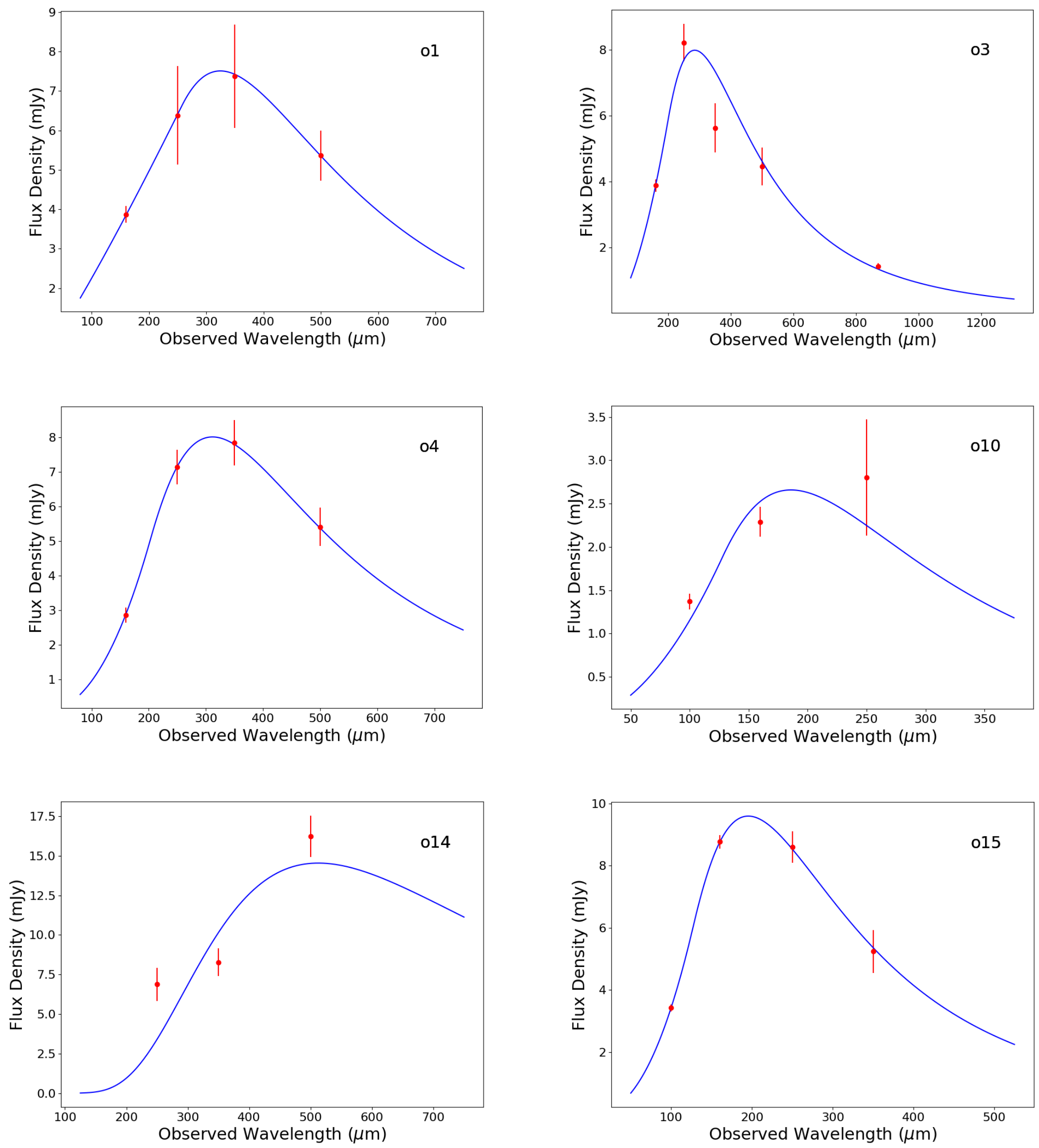

Figure 2.11: Description same as in Figure 2.10, for the six other galaxies in my sample with at least 3 photometry points > 100 μm

with

$$\tau = \left(\frac{\nu}{\nu_0}\right)^{\beta},$$

where F_ν is the flux density in Jy, β is the emissivity coefficient, ν_0 is the rest frame frequency at which the optical depth reaches unity and $B_\nu(\nu_{obs},T_{dust})$ is the blackbody function. To fit the FIR emission I adopted the MCMC approach of Dowell et al. (2013). This MCMC model uses a power law for the Wien side of the peak, $F_\nu \propto \nu^{-\alpha}$, giving the model five free parameters in total: α, β, T_{dust},

ν_0 and a normalization factor (see Dowell et al., 2013 for full details). I assumed that the dust emission is optically thin, has a single dust temperature rather than a multi-dust temperature model, and the emissivity parameter was set to $\beta = 1.5$, which is a typical value for high-z dusty star forming galaxies (e.g. Casey et al., 2014). I fit a grey-body to galaxies with three or more photometry points > 100 μm and relaxed the Wien power law condition, reverting to a standard grey-body, for those galaxies that had only three photometric data points available. Seven of the KMOS sample had the requisite photometry data and I compute a range of temperatures between 23 - 50 K, with an average value of 36 $\pm$ 8 K (see Table 2.3, and Figures 2.10 and 2.11).

Local U/LIRGs have T_{dust} $\sim$ 30 - 55 K (e.g. Clements et al., 2018) while local normal star-forming galaxies detected by the Herschel Space Observatory have colder dust with an average T_{dust} $\sim$ 20 K (Cortese et al., 2014). Dust temperatures for z $\sim$ 2 ULIRGs have been found in the range 25 - 60 K (e.g. Magdis et al., 2010, Symeonidis and Page, 2018), providing evidence that ULIRGs do not follow the same trend of T_{dust} increasing with redshift, as discussed in Section 1.5, and may be due to more extended regions of star formation in high-z ULIRGs (e.g. Swinbank et al., 2014).

On the other hand, z $\sim$ 2 galaxies lying above the MS often contain warmer dust than what is found in local ULIRGs, e.g. Miettinen et al. (2017) find T_{dust} values up to 79 K. High-z star forming galaxies hosting an AGN can have a similar range of dust temperatures as their non-AGN counterparts (e.g. Chen et al., 2021), but extremely luminous AGN such as dust obscured quasars tend to have higher temperatures, with studies showing an average $T_{dust} >$ 60K (e.g. Fan et al., 2017, D'Amato et al., 2020).

Comparing my dust temperatures to these results, I re-affirm my findings in Section 2.4.1, that the T_{dust} is consistent with MS star forming galaxies at z $\sim$ 2.

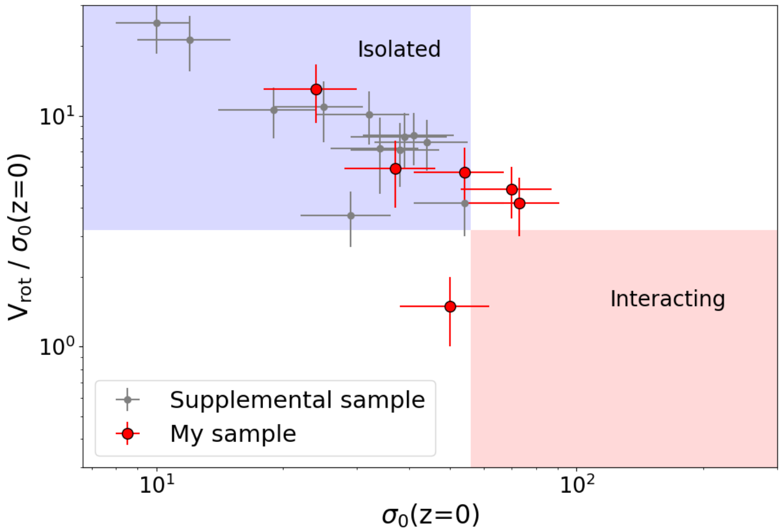

Figure 2.12: The dynamical ratio for the two sets of U/LIRGs: my sample (red) and the supplemental sample (grey). The dynamical ratio has been re-scaled using the redshift evolution in velocity dispersion in order to use the thresholds calibrated locally, as discussed in Section 2.4.4. The blue/red boxes represent typical values seen in isolated disks/interactions with threshold values of $\sigma_0 < 56$ km s^{-1} and V_{rot} / $\sigma_0 > 3.2$ for isolated disks. 3/6 of my sample appear to be isolated, with all 12 of the supplementary sample falling within the boundaries of an isolated galaxy. Galaxies falling within the white areas cannot be determined using this method and can only be categorized by relaxing one of the assumptions.

2.4.4 Dynamical Ratio

The dynamical ratio is defined as the ratio between the rotational velocity, V_{rot}, and the intrinsic velocity dispersion, σ_0, of a galaxy. The mean observed velocity dispersion increases as galaxies go from isolated, to interacting and finally merging, with a subsequent decrease in the amplitude of the rotational velocity (e.g. Bellocchi et al., 2013). Hence, high dynamical ratios correspond to isolated disks, with lower ratios signifying mergers and interactions.

As I do not have the spatial resolution and sensitivity in my KMOS observations to check if a galaxy may be undergoing a minor merger with a low mass and/or low surface brightness companion, I need a method to help infer if my targets are isolated or interacting. Pereira-Santaella et al. (2019), used the dynamical ratio to categorize intermediate-z U/LIRGs into isolated or interacting/merging galaxies by comparing their kinematics to the V_{rot} and σ_0 observed in an isolated sample and an interacting sample of local U/LIRGs. Threshold values of $\sigma_0 < 56$ km s^{-1} and V_{rot} / $\sigma_0 > 3.2$ separate the isolated subgroup from the interacting subgroup of local U/LIRGs (for full details see Pereira-Santaella et al., 2019).

To apply this method to my sample, I first need to account for the star forming ISM at high-z being more turbulent due to an increased molecular gas fraction when compared to the local universe (e.g. Bauermeister et al., 2013, Saintonge et al., 2013, Übler et al., 2019). Therefore, a $\sigma_0 > 56$ km s^{-1} at high-z can be driven purely by internal dynamic processes, and a more turbulent ISM does not always imply a recent merger or interaction. I use the redshift evolution of the intrinsic velocity dispersion to account for this increase in σ_0 as a function of redshift, allowing the threshold values ascertained in local U/LIRGs to classify my sample. I take the following relation from Übler et al. (2019), which holds for ionized gas:

$$\sigma_{0,\text{fit}}(z)/\text{km s}^{-1} = (23.3 \pm 4.9) + (9.8 \pm 3.5) \times \text{z}. \tag{2.5}$$

By plugging the redshifts of my U/LIRGs into this equation, I can find the expected intrinsic velocity dispersion for each galaxy. I then take the ratio of this with the velocity dispersion at z = 0 to find a correction factor ($\sigma_{0,\text{fit}}$(z = U/LIRG) / $\sigma_{0,\text{fit}}$(z = 0)) which gives me the expected fractional increase in σ_0 between z = 0 and the redshifts of my galaxies. I then re-scale the σ_0 found by GalPak^{3D} by this correction factor to get a velocity dispersion that can be compared to the thresholds derived from the local U/LIRGs. E.g. for galaxy o3 the expected $\sigma_{0,\text{fit}}$(z = 2.433) is 46.6 km s^{-1} which is 2.03 times higher than $\sigma_{0,\text{fit}}$(z = 0), re-scaling the observed σ_0 = 148 km s^{-1} to σ_0 = 73 km s^{-1}.

As I could only fit six of my U/LIRG sample with model disks, I choose to increase the size of my KMOS sample. I supplemented it with targets from the ESO archive (hereafter known as the supplemental sample) which satisfied the criteria, outlined in Section 2.2.1, with the addition that all archival targets are also in the ZFOURGE database to ensure the supplemental sample occupied the same region of the SFR - $M_\star$ parameter space as my KMOS sample. Twenty eight

Table 2.4: Kinematic parameters of the best fit model galaxy from $GalPak^{3D}$ for the sample of U/LIRGs.

Object	R_E[1]	i[2]	PA[3]	V_{max}[4]	σ_0[5]	σ_0(z=0)[6]	f_{gas}[7]	V_{rot}/σ_0(z=0)[8]	$\log(M_{dyn})$[9]	M_{bar}/M_{dyn}[10]
	kpc	deg	deg	km s^{-1}	km s^{-1}	km s^{-1}			$M_\odot$	
o3	3.69 ± 0.13	79 ± 4	234 ± 3	306 ± 43	148 ± 6	73 ± 18	0.62	4.2 ± 1.2	11.16 ± 0.02	0.67 ± 0.16
o5	2.33 ± 0.12	21 ± 6	1 ± 11 1	308 ± 43	103 ± 6	54 ± 13	0.47	5.7 ± 1.6	10.59 ± 0.03	0.59 ± 0.16
o8	4.01 ± 0.39	59 ± 6	88 ± 5	218 ± 48	75 ± 12	37 ± 9	0.60	5.9 ± 1.9	10.70 ± 0.06	0.36 ± 0.20
o14	6.85 ± 0.43	66 ± 3	0 ± 3	331 ± 19	138 ± 7	70 ± 17	0.61	4.8 ± 1.2	11.35 ± 0.03	0.35 ± 0.16
o15	3.16 ± 0.10	25 ± 3	157 ± 4	314 ± 45	46 ± 4	24 ± 6	0.87	13.0 ± 3.7	10.37 ± 0.02	2.99 ± 0.16
o16	5.01 ± 0.18	61 ± 3	62 ± 2	75 ± 16	97 ± 0	50 ± 12	0.42	1.5 ± 0.5	10.75 ± 0.04	0.40 ± 0.18

[1] Half-light radius of Hα emission assuming an exponential profile.
[2] Galaxy inclination.
[3] Position angle east of north to the blue-shifted major kinematic axis.
[4] De-projected maximum velocity of the asymptotically flat part of the rotation curve.
[5] Intrinsic velocity dispersion of galaxy disk.
[6] The re-scaled velocity dispersion of the galaxy at $z = 0$ assuming the redshift evolution of velocity dispersion. See section2.4.4.
[7] Estimated gas fraction of the galaxy. See Section 2.4.5.
[8] The dynamical ratio of the galaxy assuming the re-scaled velocity dispersion at $z = 0$.
[9] Dynamical mass of the galaxy. See Section 2.4.5.
[10] Fraction of the total galaxy mass comprised of baryonic matter. See Section 2.14.

galaxies (see Table 2.5) from the archive satisfied my criteria, with two of these flagged as AGN in ZFOURGE, and the FWHM of their PSFs ranged from 0.5″ - 0.94″. The archival galaxies were reduced and modelled following the same data reduction procedure as my KMOS sample (see Wisnioski et al., 2019). I note that I have identified a separate observation of galaxy o17 in the archive (GS4 35056 in Table 2.5). The reduced cube from this observation did not have the issue of the noisy sky on the blue wing channels of the Hα line that was identified in my analysis (see Section 2.3.3), so I decided to include the archival GS4 35056 cube in the supplemental sample. This cube is used for the kinematic analysis only and to avoid confusion I will continue to refer to it as part of the supplemental sample. Using GalPak^{3D} to fit the kinematics, twelve of the supplemental sample converged in the MCMC to be a rotating disk, with neither of the two AGN found to be a disk.

From the entire sample, with Hα detections, 15/41 appear to be isolated disks and this fraction increases to 17/41 if I use just the criterion of $V_{rot} / \sigma_0 > 3.2$ for the undetermined cases (see Figure 2.12). While it may seem strange that most of the galaxies that converged in GalPak^{3D} are located in the isolated disk region of the parameter space, with none falling into the interacting region, this is an artefact of fitting kinematic models to z $\sim$ 2 observations. The KMOS spectral resolution at $2 < z < 2.5$ is $\sim$ 70 km s^{-1} so galaxies with dynamical ratios below unity, i.e. low V_{rot}, may not have the requisite data points to constrain the turnover radius and rotational velocity of a fitted model galaxy. Likewise, galaxies with disturbed morphology, (e.g. galaxy o2 in Figure 2.2) can either prevent the model parameters converging, or converge to a poor fit, as GalPak^{3D} assumes a smooth rotating model disk. Factoring in the drop in S/N at increasing radii, GalPak^{3D} will be biased towards isolated disks with large rotational velocities at z $\sim$ 2. Therefore, many of the 22 galaxies in which GalPak^{3D} could not fit a model are likely to be interacting and merging, although I cannot quantify this using the above analysis.

My findings agree with previous results of interacting versus isolated disks at these redshifts. Kartaltepe et al. (2012), using HST imagery, concluded that $\sim$ 50% of galaxies appear to have some form of interaction and Molina et al. (2017)

Table 2.5: Supplementary Sample of U/LIRGs selected from the archive.

ZFOURGE ID	KMOS^{3D} ID	RA deg	Dec deg	z	$\log(M_\star)$[1] $M_\odot$	$SFR_{H\alpha}$[2] $M_\odot\ yr^{-1}$	SFR_{IR}[3] $M_\odot\ yr^{-1}$
25940	GS4 41748	53.101	-27.716	2.301	10.78	14	45
24313	GS4 38560	53.078	-27.731	2.417	10.21	13	48
19322	GS4 30548	53.078	-27.772	2.113	10.05	20	48
23965	GS4 37988	53.052	-27.734	2.201	10.24	13	49
24103	GS4 38116	53.171	-27.733	2.197	10.20	19	52
18414	GS4 28870	53.182	-27.780	2.471	9.82	21	52
28441	GS4 46432	53.112	-27.693	2.435	9.80	46	53
25583	GS4 40768	53.041	-27.719	2.303	10.14	71	61
24415	GS4 38807	53.182	-27.730	2.318	10.22	15	61
21242	GS4 33639	53.121	-27.756	2.235	10.56	19	66
26243	GS4 42235	53.135	-27.713	2.433	10.16	51	72
6000	GS4 05979	53.135	-27.882	2.393	10.28	16	75
9927	GS4 14070	53.229	-27.846	2.306	10.44	21	90
10521	GS4 15000	53.116	-27.842	2.035	10.55	15	92
22233	GS4 35056	53.168	-27.749	2.227	10.43	14	95
26492	GS4 42789	53.034	-27.711	2.254	10.61	39	97
17344	GS4 27404	53.072	-27.786	2.035	10.49	32	108
27238	GS4 44133	53.110	-27.704	2.140	10.77	21	116
23812	GS4 37745	53.183	-27.735	2.431	10.91	27	129
16282	GS4 25151	53.100	-27.794	2.223	10.59	35	130
10780	GS4 15819	53.180	-27.839	2.042	10.59	17	131
27751	GS4 45188	53.063	-27.700	2.406	10.72	15	173
25918	GS4 41438	53.019	-27.717	2.018	10.46	22	189
25326	GS4 40477	53.054	-27.722	2.061	10.91	16	219
26148	GS4 42127	53.051	-27.714	2.442	10.88	29	312
19033	GS4 30274	53.131	-27.773	2.225	11.17	65	512
25730	GS4 41181	53.107	-27.718	2.300	11.06	5	776
2466	GS4 01529	53.180	-27.921	2.122	11.30	44	782

[1] Stellar Mass of the galaxy. I assume an error of 15% in any calculation that required the stellar mass.

[3] Star formation rates calculated from the Hα luminosity from the KMOS^{3D} catalogue (Wisnioski et al., 2019).

[3] Star formation rates calculated from the IR luminosity from ZFOURGE (Straatman et al., 2016).

Table 2.6: Kinematic parameters of the best fit model galaxy from GalPak^{3D} for the supplementary sample of U/LIRGs.

ID	R_E[1] kpc	i[2] deg	PA[3] deg	V_{max}[4] km s^{-1}	σ_0[5] km s^{-1}	σ_0(z=0)[6] km s^{-1}	f_{gas}[7]	V_{rot}/σ_0(z=0)[8]	log(M_{dyn})[9] $M_\odot$	M_{bar}/M_{dyn}[10]
GS4 38560	2.76 ± 0.31	48 ± 7	78 ± 6	274 ± 46	51 ± 6	25 ± 6	0.56	10.90 ± 3.24	10.19 ± 0.05	1.21 ± 0.20
GS4 30548	2.76 ± 0.18	26 ± 3	323 ± 4	247 ± 28	22 ± 9	12 ± 3	0.67	21.33 ± 5.77	10.58 ± 0.03	0.45 ± 0.17
GS4 37988	1.97 ± 0.30	82 ± 7	52 ± 8	318 ± 35	76 ± 11	39 ± 10	0.57	8.11 ± 2.18	10.33 ± 0.07	0.94 ± 0.21
GS4 46432	1.32 ± 0.03	15 ± 2	350 ± 7	249 ± 64	70 ± 4	34 ± 8	0.79	7.25 ± 2.58	9.98 ± 0.06	1.55 ± 0.20
GS4 33639	3.36 ± 0.13	32 ± 3	274 ± 2	252 ± 27	17 ± 5	10 ± 2	0.46	25.20 ± 6.75	10.54 ± 0.02	0.97 ± 0.16
GS4 42235	3.00 ± 0.10	62 ± 2	127 ± 1	198 ± 8	38 ± 4	19 ± 5	0.69	10.61 ± 2.64	10.46 ± 0.01	0.79 ± 0.15
GS4 15000	5.18 ± 0.57	76 ± 7	16 ± 4	227 ± 30	100 ± 9	54 ± 13	0.56	4.24 ± 1.18	10.90 ± 0.05	0.51 ± 0.15
GS4 35056	1.37 ± 0.05	50 ± 3	1 ± 1	328 ± 20	63 ± 5	32 ± 8	0.62	10.15 ± 2.57	10.27 ± 0.02	1.91 ± 0.15
GS4 42789	2.60 ± 0.08	31 ± 3	42 ± 4	337 ± 18	86 ± 3	44 ± 11	0.52	7.68 ± 1.93	10.52 ± 0.01	1.29 ± 0.15
GS4 44133	2.76 ± 0.18	32 ± 5	268 ± 6	335 ± 28	78 ± 10	41 ± 10	0.49	8.21 ± 2.13	10.71 ± 0.03	1.12 ± 0.16
GS4 40477	1.50 ± 0.15	56 ± 13	160 ± 97	271 ± 52	72 ± 15	38 ± 9	0.57	7.07 ± 2.20	10.11 ± 0.05	7.28 ± 0.19
GS4 42127	2.53 ± 0.41	84 ± 7	79 ± 5	110 ± 14	60 ± 13	29 ± 7	0.64	3.74 ± 1.03	10.24 ± 0.07	6.16 ± 0.22

[1] Half-light radius of Hα emission assuming an exponential profile.
[2] Galaxy inclination.
[3] Position angle east of north to the blue-shifted major kinematic axis.
[4] De-projected maximum velocity of the asymptotically flat part of the rotation curve.
[5] Intrinsic velocity dispersion of galaxy disk.
[6] The expected velocity dispersion of the galaxy at z = 0 assuming the redshift evolution of velocity dispersion. See section2.4.4.
[7] Estimated gas fraction of the galaxy. See Section 2.4.5.
[8] The dynamical ratio of the galaxy assuming the corrected velocity dispersion at z = 0.
[9] Dynamical mass of the galaxy. See Section 2.14.
[10] Fraction of the total galaxy mass comprised of baryonic matter. See Section 2.4.5.

found 3/5 of Hα selected MS galaxies from z = <2.23> have signatures of merging based on kinemetry, a method quantifying the asymmetry in the V_{rot} and σ_0 maps allowing galaxies to be classified into ordered rotation or disturbed kinematics (Krajnovic et al., 2006).

The KMOS^{3D} survey (Wisnioski et al., 2019) finds 49 - 70% of MS galaxies ($10.00 < \log(M_\star / M_\odot) < 11.75$) at z $\sim$ 2 to be disks. The range corresponds to the different criteria used for the classification (see Wisnioski et al., 2019 for a detailed description of their criteria). When all five of their criteria are satisfied then the fraction of disk galaxies found is 49% with the value increasing to 70% when considering only two criteria. At lower redshifts, the KROSS survey found 83% of star forming galaxies at z $\sim$ 0.9 to be rotation dominated (using the definition of $V_{rot} / \sigma_0 > 1$, Johnson et al., 2018). Using the same definition, Turner et al. (2017) found that 34 $\pm$ 8% of typical star forming galaxies at z $\sim$ 3.5 are rotation dominated.

Differences in methodology and classification have been investigated by Rodrigues et al. (2017) where they find a smaller fraction of disks than Wisnioski et al. (2015), from the same KMOS^{3D} sample of 41 galaxies at z $\sim$ 1, by using a different methodology to derive the kinematic parameters, such as the σ-peak or the kinematic centre, and applying the five KMOS^{3D} survey criteria described above in Wisnioski et al. (2015). Rodrigues et al. (2017) also showed that some observations were misclassified as disks when broad-band images were investigated. Where possible, I have verified the position angle and inclination, via the Hubble Space Telescope ACS/WFC (see Figure 2.13). Where adequate S/N was available to fit isophotes to the broad-band observations, the position angle for both my KMOS and supplemental samples agree to within 30° and the inclination to within 24°, and corroborate my apparent fraction of isolated disks.

It is instructive to look at how the properties of the z $\sim$ 2 KMOS sample compares with similar luminosity samples at lower redshifts. Pereira-Santaella et al. (2019) found 10 - 25% of their intermediate-z sample to be isolated disks, while this fraction goes down to $\sim$ 5% for local U/LIRGs with $\log(L_{IR} / L_\odot) > 11.6$

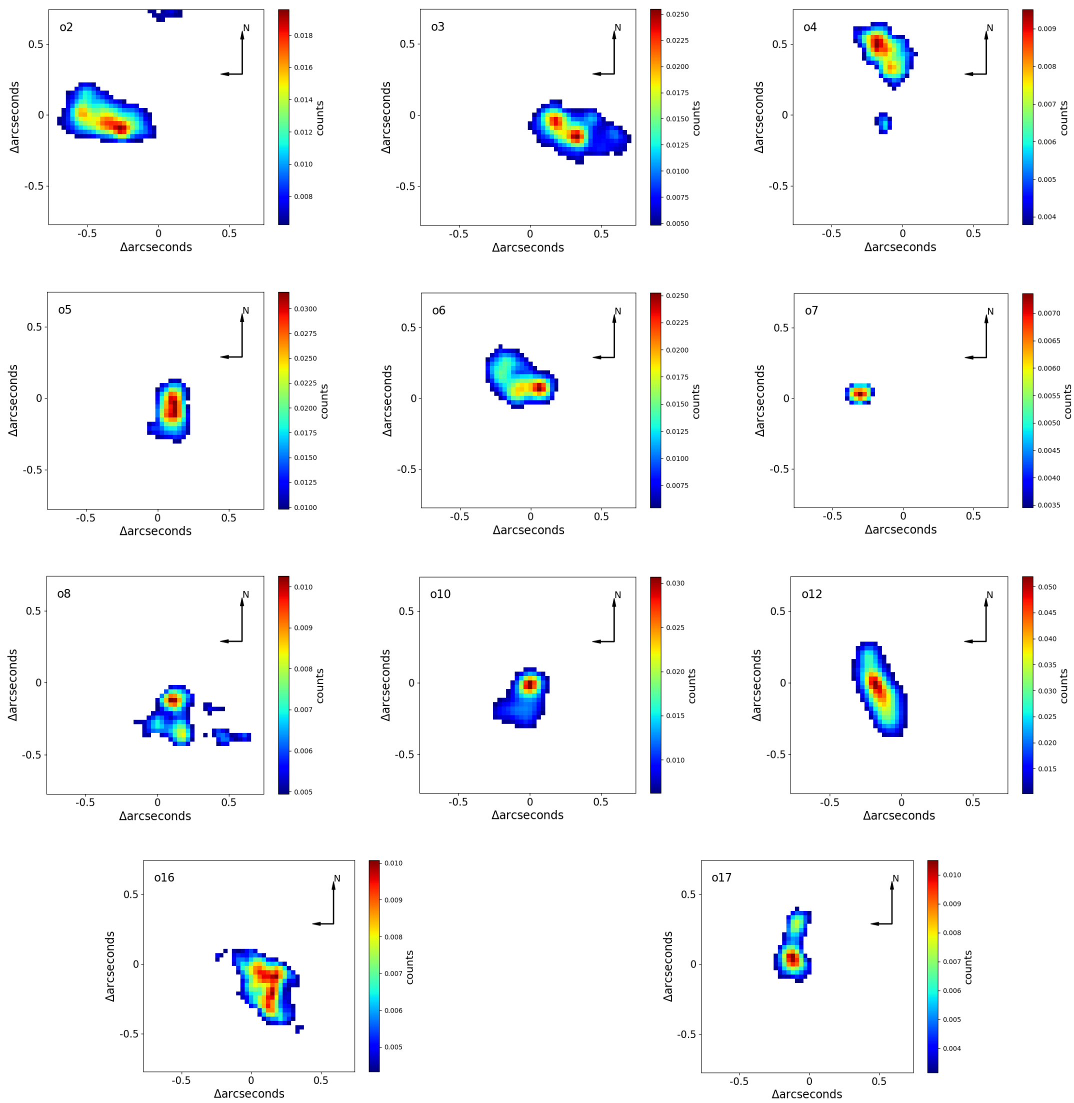

Figure 2.13: Broadband images from the ACS/WFC F814W filter on board the Hubble Space Telescope, with a 3σ threshold applied, and centred on the coordinates in Table 2.1. Three of my KMOS galaxies with Hα detections, o13, o14, o15, have not been included due to poor S/N.

(Bellocchi et al., 2013). Despite differences in sample sizes and systematic errors, the dynamical ratios suggest that the percentage of mergers and interactions in luminous IR systems decreases with look-back time.

The results presented here also agree with the evolution predicted by some cosmological simulations. The Horizon-AGN hydrodynamical simulation (Dubois et al., 2014) shows that mergers only account for 25% of stellar mass since z $\approx$ 6 meaning smooth accretion is the dominant driver of star formation through cosmic time (Martin et al., 2017). Rodríguez Montero et al. (2019), using the SIMBA simulation (Davé et al., 2019), find that mergers contribute only about $\sim 1\%$ of the SFR density at z $\sim$ 2, although they do not include the pre-merger phase in their merging sample.

2.4.5 Dynamical Mass

I can infer dynamical masses and dark matter fractions for my sample from the best-fit kinematics. Using the methodology of Price et al. (2016) the dynamical mass can be calculated from:

$$M_{\rm dyn}(R_{\rm E}) = k_{\rm eff}(R_{\rm E}) \frac{V_{\rm rms}(R_{\rm E})^2 R_{\rm E}}{G}, \tag{2.6}$$

where G is the gravitational constant, $k_{\rm eff}(R_{\rm E})$ is the effective virial coefficient, $R_{\rm E}$ is the half light radius, and $V_{rms}(R_{\rm E})$ is the root mean square velocity, defined as:

$$V_{\rm rms}(r) = \sqrt{V_{\rm rot}(r)^2 + \sigma_0^2}. \tag{2.7}$$

The effective virial coefficient is given by

$$k_{\rm eff}(R_{\rm E}) = \frac{k_{\rm disp} + k_{\rm rot}(V_{\rm rot}(R_{\rm E})/\sigma_0)^2}{1 + (V_{\rm rot}(R_{\rm E})/\sigma_0)^2}. \tag{2.8}$$

I choose $k_{\rm disp} = 5$ (e.g. Pettini et al., 2001) and set $k_{\rm rot} = 1$, (e.g. Miller et al., 2011), which are valid for a spherical potential. The effective virial coefficient term accounts for the existence of a non-negligible pressure component due to the more turbulent ISM at high-z (e.g. Förster Schreiber et al., 2009, Wuyts et al., 2016), and when $V_{\rm rot}(R_{\rm E})/\sigma_0 \gg 1$ Equation 2.6 reverts to the dynamical mass calculated from only rotational support [3].

In the absence of molecular gas observations for most of the galaxies in my sample, I estimate the gas fraction from the following:

$$f_{\rm gas} = \frac{M_{\rm gas}}{M_\star + M_{\rm gas}} = \frac{1}{\frac{M_\star}{SFR}\frac{SFR}{M_{\rm gas}} + 1} = \frac{1}{1 + (\tau_{\rm dep} \cdot sSFR)^{-1}}. \tag{2.9}$$

---

[3] $M_{\rm dyn} = V_{\rm rot}(R_{\rm E})^2\ R_{\rm E}/G$

I approximate $\tau_{\rm dep}$ by using the redshift evolution of depletion time from Wisnioski et al. (2015):

$$\tau_{\rm dep}[\rm Gyr] = 1.5 \times (1 + z)^{\alpha}, \tag{2.10}$$

I assume an α value of -1 to match that of Wisnioski et al. (2015) and Tacconi et al. (2013), and choose a pre-factor of 1.5 Gyr to represent the typical depletion time of a z = 0 MS galaxy (e.g. Saintonge et al., 2013). Re-arranging Equation 2.9 and using the $M_\star$ and SFR_{IR} I calculated for the KMOS sample and the $M_\star$ and SFR_{IR} taken from ZFOURGE for the supplementary sample (see Table 2.5, and Straatman et al., 2016 for methodology), I can deduce both a value for the M_{gas} and a value for the total baryonic mass, $M_{bar} = M_{gas} + M_\star$. I did not calculate a baryonic mass for galaxy o8 as I do not have a fitted SFR_{IR} from which to estimate the gas fraction.

By taking the ratio of baryonic mass to the dynamical mass, I can subsequently get the dark matter fraction within one R_E:

$$f_{\rm D} = 1 - \frac{M_{\rm bar}(R_{\rm E})}{M_{\rm dyn}(R_{\rm E})}. \tag{2.11}$$

To calculate the baryonic mass within one effective radius I assume that half of the stellar mass is within one $R_{\rm E}$ and a constant gas to stellar mass ratio throughout the disk, i.e. half the gas mass is also inside one $R_{\rm E}$. This is valid as high-z studies have shown gas and Hα having a similar spatial extension (e.g. Molina et al., 2019). The baryonic mass within an $R_{\rm E}$ is simply half the total baryonic mass.

It is worth noting that the dark matter fractions are subject to large uncertainties due to various assumptions, including uncertainties in the gas fraction, the uncertainties in fitting an $M_\star$ in high-z galaxies, the assumption of a spherical potential when calculating the effective virial coefficient, assuming the co-spatial distribution of ionized, molecular and stellar mass and the accuracy of the kinematic parameters recovered from seeing limited observations. With all these caveats in mind, I can attempt to determine whether both samples as a whole are baryon dominated ($f_D < 0.5$) or dark matter dominated ($f_D > 0.5$) within their effective radii.

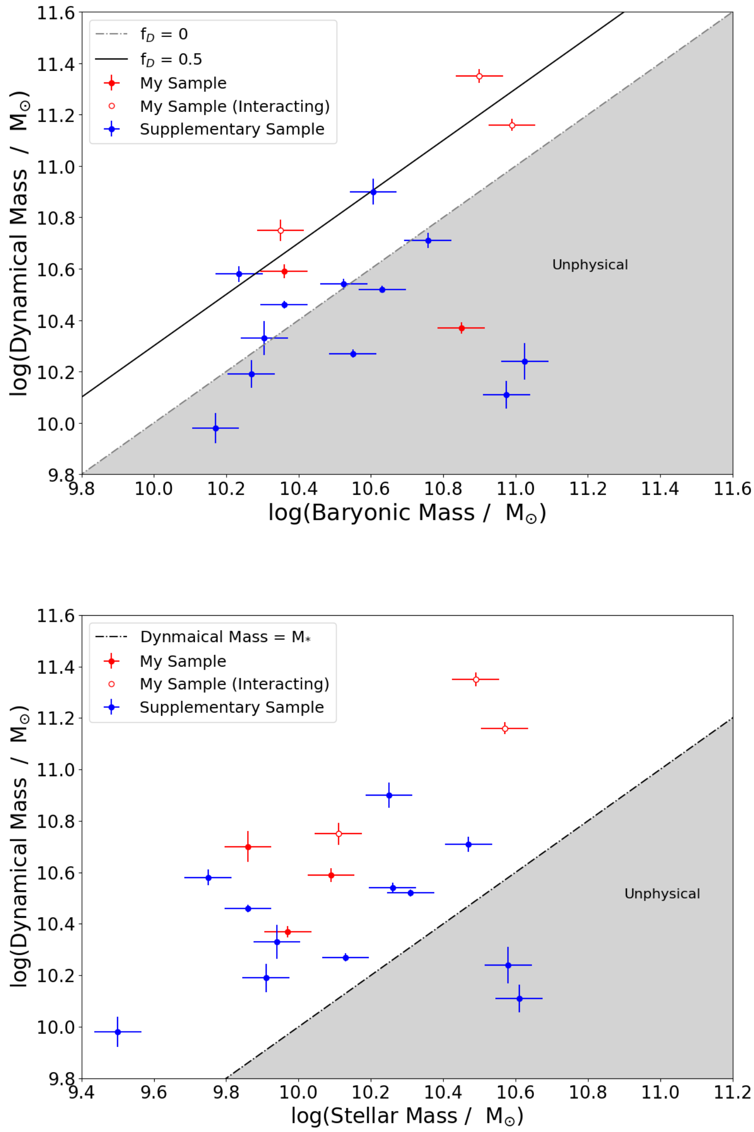

Figure 2.14: Top: Plot of the dynamical mass versus baryonic mass within one R_E. **Bottom:** Plot of the dynamical mass versus stellar mass within one R_E. The grey area represents unphysical values where the baryonic mass exceeds the dynamical mass. The dark matter fraction increases with vertical height above the dashed line, where dynamical mass equals baryonic mass, and the black solid line indicates where the dark matter fraction equals 50%. Three of the total sample fall into the dark matter dominated region (dark matter fraction > 50 %), with eight of the sample in the unphysical region. The unphysical values are mainly caused by my estimate of gas fraction, as discussed in Section 2.4.5, which can be seen when I remove the gas mass and plot just the stellar mass versus dynamical mass. Further reasons for unphysical values are discussed in Section 2.4.5. The three galaxies (o3, o14 and o16) that passed only one of the two kinematic criteria for an isolated disk in Section 2.4.4 are included and as these may be interacting they are labelled as such in the plots. The left plot only contains five data points for my KMOS sample, as I am unable to estimate a baryonic mass for galaxy o8.

Both samples span a large range of dark matter to dynamical mass fraction, f_D, from baryon dominated galaxies to unphysical values. The median value across both samples is $f_D = 0.03$ and only three appear to be dark matter dominated within one R_E (see Figure 2.14), suggesting that high-z U/LIRGs are baryon dominated within their effective radii. The ratio of stellar mass to dynamical mass is also plotted in Figure 2.14 and contains only two unphysical values, which suggests that the main reason for the unphysical dark matter fractions lies in the estimate for the gas fraction within a galaxy. For example, galaxy o15 lies above the MS so it likely has a lower τ_{dep} than that acquired from Equation 2.10, which gives a τ_{dep} of 0.48 Gyr and a gas fraction of 0.87. The f_D becomes physical when the gas fraction falls below 0.61.

In the above analysis I included the three galaxies in my KMOS sample (o3, o14 and o16) that failed one of the criteria for an isolated disk. If their high velocity dispersion is due to a perturbation from an interacting galaxy, and the disk has not yet virialized, then Equation 2.6 does not hold. Whether or not I include these three data points, the same conclusion holds: I cannot accurately measure the exact f_D for an individual galaxy, but I can state the sample as a whole is baryon dominated within one R_E.

This agrees with previous high-z research which showed that galactic disks are baryon dominated inside one R_E, displaying a range of median baryon fractions from 70% to unphysical values, i.e. > 100% (e.g. Förster Schreiber et al., 2009, Wuyts et al., 2016, Price et al., 2016, Lang et al., 2017, Genzel et al., 2017,Price et al., 2020). Tiley et al. (2019) argued that dark matter fractions of > 0.67 are found if f_D is calculated within six radial scale lengths, as opposed to an R_E. All the results are consistent as probing the dark matter fraction at larger radii probes further out into the halo where baryon fraction decreases, assuming a ΛCDM universe where the universal baryon, Ω_{bar}, to dark-matter, Ω_D, fraction is expected to be $f_b = \Omega_{bar} / \Omega_D \sim 0.2$ (Aghanim et al., 2020). My results are also in agreement with the IllustrisTNG simulation where $f_D(<R_E) = 0.29 \pm 0.11$ (Übler et al., 2021), and the NewHorizon simulation (Dubois et al., 2021) in which

Table 2.7: The metallicity values of my U/LIRGs.

Object	12+log(O/H)[1]	MZR[2]
o3	8.63 ± 0.12	8.57 ± 0.12
o5	8.60 ± 0.12	8.48 ± 0.14
o7	8.70 ± 0.16	8.52 ± 0.13
o16	8.58 ± 0.13	8.46 ± 0.14
Composite	8.46 ± 0.13	8.52 ± 0.13

[1] Metallicity of the galaxy assuming the conversion factor of Pettini and Pagel (2004).
[2] Expected metallicity of the galaxy assuming the MZR of Tacconi et al. (2018).

an analogue to o5 is baryon dominated within its R_E (this simulated galaxy will be analysed in Chapters 4 and 5).

2.4.6 Metallicity

The metal content of a galaxy can be used to constrain its SFH since gas phase metallicity is the result of enrichment of the ISM from previous star forming episodes. The ratio of [NII] 6583 Å and Hα, known as the N2 index, can be used to find the gas phase metal content of galaxies. I converted the N2 index ratios to 12 + log(O/H) using the correlation of Pettini and Pagel (2004) to compare with the metallicity predicted from the mass metallicity relation (MZR) at z $\sim$ 2. Four of my KMOS sample were marginally detected and their average N2 index is 0.34 ± 0.1. The mean N2 index value derived for my sample is lower than the 1.1 ± 0.8 derived for the intermediate U/LIRG sample (Pereira-Santaella et al., 2019) and the 0.7 ± 0.3 of local U/LIRGs (Monreal-Ibero et al., 2010, Rupke et al., 2008, Alonso-Herrero et al., 2009), as expected from the redshift evolution of the MZR (e.g. Maiolino et al., 2008).

I can also calculate the expected metallicity of a star forming galaxy at a given redshift and stellar mass using the following equation from Tacconi et al. (2018):

$$12 + log(O/H) = a - 0.087 \times (logM_\star - b)^2, \tag{2.12}$$

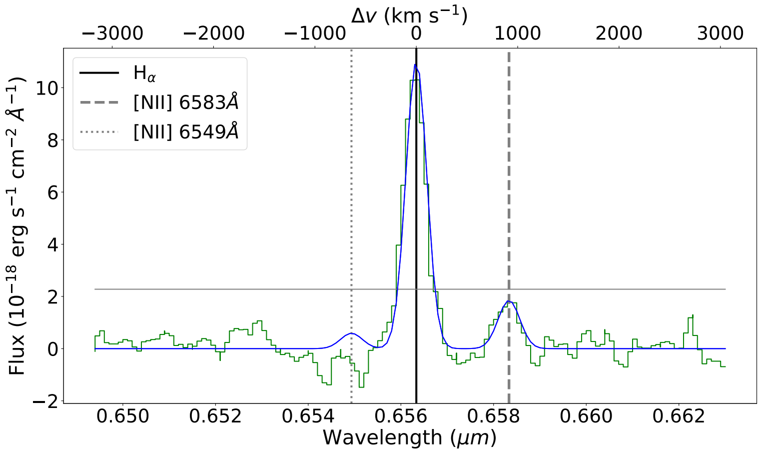

Figure 2.15: The composite spectrum for the nine galaxies without detected [NII] 6583 Å emission line. The best fit model is overlaid in blue and the vertical solid, dashed, and dotted lines represent the position of Hα, [NII] 6549 Å and [NII] 6583 Å lines. This is a marginal $\sim 2.5\ \sigma$ detection, with the grey horizontal line indicating where S/N = 3.

where

$$\begin{aligned} a =& 8.74 \pm 0.06, \\ b =& 10.4 \pm 0.05 + 4.46 \pm 0.3 \times log(1+z) - 1.78 \pm 0.4 \times (log(1+z))^2. \end{aligned} \tag{2.13}$$

Galaxies o3, o5 and o16 all fall close to the expected value of a star forming galaxy, with galaxy o7 being much more metal enriched than expected, as shown in Table 2.7. The N2 index in galaxy o7 falls in a region of the BPT diagram that could be either in the AGN or starburst regime and without an [OIII] 5007 Å / Hβ observation I cannot rule out a deeply buried AGN is skewing the N2 index higher (e.g. Kewley et al., 2013). It is also worth noting that o7 has both the highest gas phase metallicity and highest SFR in the sample which goes against the FMR (e.g.Mannucci et al., 2010, Maiolino and Mannucci, 2019), in which for a given stellar mass there is an anti-correlation between SFR and gas phase metallicity. Assuming it doesn't contain an AGN, this galaxy may be a genuine outlier from the FMR or its enhanced gas phase metallicity may be due to different conditions in its ISM, such as an elevated N/O to O/H ratio leading to an error in the N2 index to metallicity conversion factor (e.g. Shapley et al., 2015, Dopita et al., 2016). Alternative metallicity diagnostics based on IR fine structure lines (e.g. Pereira-

Santaella et al., 2017, Rigopoulou et al., 2018) may be required to shed light in the metal content of dusty star forming galaxies at high redshifts.

Of the ten targets which had Hα but no [NII] 6583 Å emission, I stacked nine of these targets to try to get a detection from a composite spectrum. Galaxy o13 was left out of this stacking, as a skyline fell in the same channel as [NII] 6583 Å. I obtained the composite spectrum by shifting the eight spectra into each galaxy's rest-frame and then averaged the flux in each channel, which had a bin size of $\sim$ 1 Å. I fit this spectrum with the same three-Gaussian model as the individual galaxies, giving a marginal 2.5σ detection, as seen in Figure 2.15.

The composite spectrum gives an N2 index of 0.17 and 12 + log(O/H) = 8.46 $\pm$ 0.06, suggesting that on average these galaxies agree with the MZR at their average redshift of 2.26 (see Figure 2.16). The disadvantage of using a stacked spectrum is the average behaviour can hide the underlying variance in the sample, so although the average metallicity agrees with the MZR this does not rule out a sub-sample being metal deficient like the local U/LIRGs.

2.5 Discussion

2.5.1 Is the SFE Consistent With MS Galaxies?

Recent studies (e.g. Elbaz et al., 2018, Franco et al., 2020, Valentino et al., 2020) have shown that position on the $M_\star$ - SFR plane may not hold in all cases when categorizing a galaxy's mode of star formation, with some massive z $\sim$ 2 MS galaxies exhibiting high SFEs and very short depletion timescales. Such objects appear to have compact star formation and are gas poor compared to their MS counterparts, and it is suggested (e.g. Dekel and Burkert, 2014, Popping et al., 2017) that these galaxies are at the end of their starburst phase and are the progenitors of massive elliptical galaxies. Conversely, case studies of starburst sub-millimetre galaxies (SMGs) have signatures consistent with rotating disks (e.g. Hodge et al., 2019, Drew et al., 2020), so distance above the main sequence does not always imply a merger. This once again highlights the importance of multi-wavelength observations to gain a complete insight into a galaxy's properties.

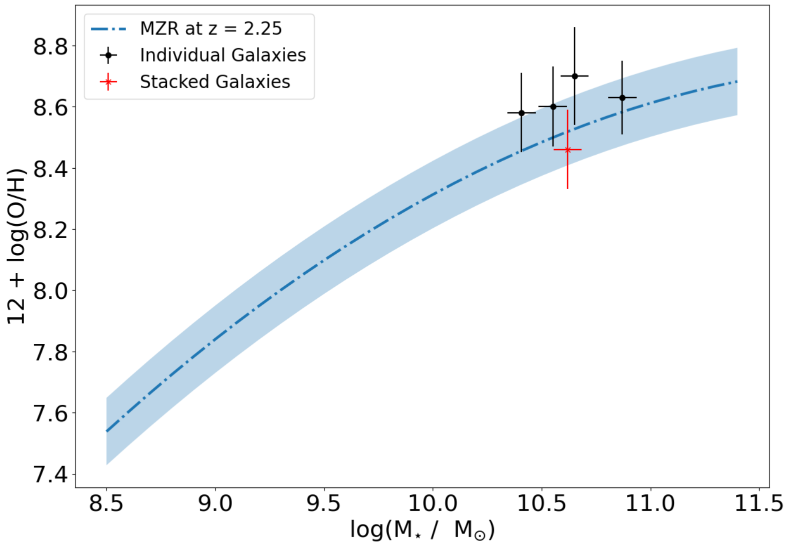

Figure 2.16: The position of my four galaxies with a [NII] 6583 Å detection, and the composite spectrum, with respect to the MZR. The track represents the values expected for a z = 2.25 galaxy taken from Tacconi et al. (2018), and the scatter in this relation is $\sim$ 0.1 dex. This plot indicates my four detections are not metal deficient, and the composite spectrum also lies within the scatter of the MZR.

To determine the $\tau_{\rm dep}$ and further explore the mode of star formation in my sample of galaxies, I searched for ancillary CO or 870 μm continuum data that would enable me to compute molecular gas masses. Four of my KMOS sample had the requisite observations in the sub-mm to infer a molecular gas mass: galaxies o3, o4, o6, and o7.

The Scoville et al. (2016) technique calculates the $M_{\rm mol}$ from a single point on the Rayleigh Jeans slope of the dust continuum and then converts to a molecular gas mass by using assumptions such as optically thin emission and conversion factors based on local galaxies. Although differing ISM conditions exist in high-z galaxies compared to local ones introduces uncertainty in this method, similar potential sources of error exist in the standard CO to $M_{\rm mol}$ conversion method of finding $M_{\rm mol}$ (e.g. Bolatto et al., 2013). These uncertainties will be left to Chapter 3, where the CO to $M_{\rm mol}$ conversion factor is applied and the pitfalls discussed.

Galaxy o3 was previously studied in Wiklind et al. (2019) in which they used the continuum method to estimate an M_{mol} of 8.57 × 10^{10} $M_{\odot}$. Using this value gives a τ_{dep} of 310 Myr which is consistent with that of a MS galaxy at cosmic noon (e.g. Tacconi et al., 2020).

Galaxy o6 has an ALMA 870 μm measurement in Tadaki et al. (2020), and they found an M_{mol} of 8.7 × 10^{10} $M_{\odot}$, allowing me to calculate a τ_{dep} of 1.4 Gyr which is higher than expected of a MS galaxy. It could not be fitted by GalPak^{3D}, and may be a dispersion dominated object. As the continuum method relies on only one data point, I need other M_{mol} tracers to confirm this τ_{dep}.

Galaxies o4 and o7 have an 850 μm continuum measurement in Cowie et al. (2018), and using the Scoville et al. (2016) technique I get an M_{mol} of 1.40 ± 0.23 × 10^{11} $M_{\odot}$ and 2.31 ± 0.17 × 10^{11} $M_{\odot}$, with gives τ_{dep} of 589 ± 97 Myr and 295 ± 22 Myr respectively. Galaxy o4 has a τ_{dep} that is typical of a MS galaxy, although o7 would have been expected to be ≤ 100 Myr based on it being a starburst. As with galaxy o6, CO data is needed to verify if this molecular gas mass is correct.

2.5.2 Drivers of Turbulence

The average velocity dispersion values of the two samples agree within error, but my KMOS sample does appear to have a consistently higher σ_0. Although the supplementary sample satisfies the selection criteria in Section 2.2.1, these targets were initially selected on their rest-frame optical emission at $2 < z < 2.5$ (Wisnioski et al., 2015), which biases the supplementary sample towards less extinguished objects when compared to my KMOS sample. This leads to a greater S/N in the outer disk regions of the supplementary sample, allowing GalPak^{3D} to probe the kinematics further out into the disk and sample σ_0 away from the central regions of high velocity dispersion. As a consistency check, the average linewidth, from a Gaussian fit, in the supplementary sample that converged in GalPak^{3D} is 268 km s^{-1} which is similar to my sample, so this shows the importance of sampling the outer disk when applying a parametric model that only fits a single σ_0 value (I will discuss velocity dispersion and how it can be used to interpret the dynamical state of a galaxy in detail in Chapter 4).

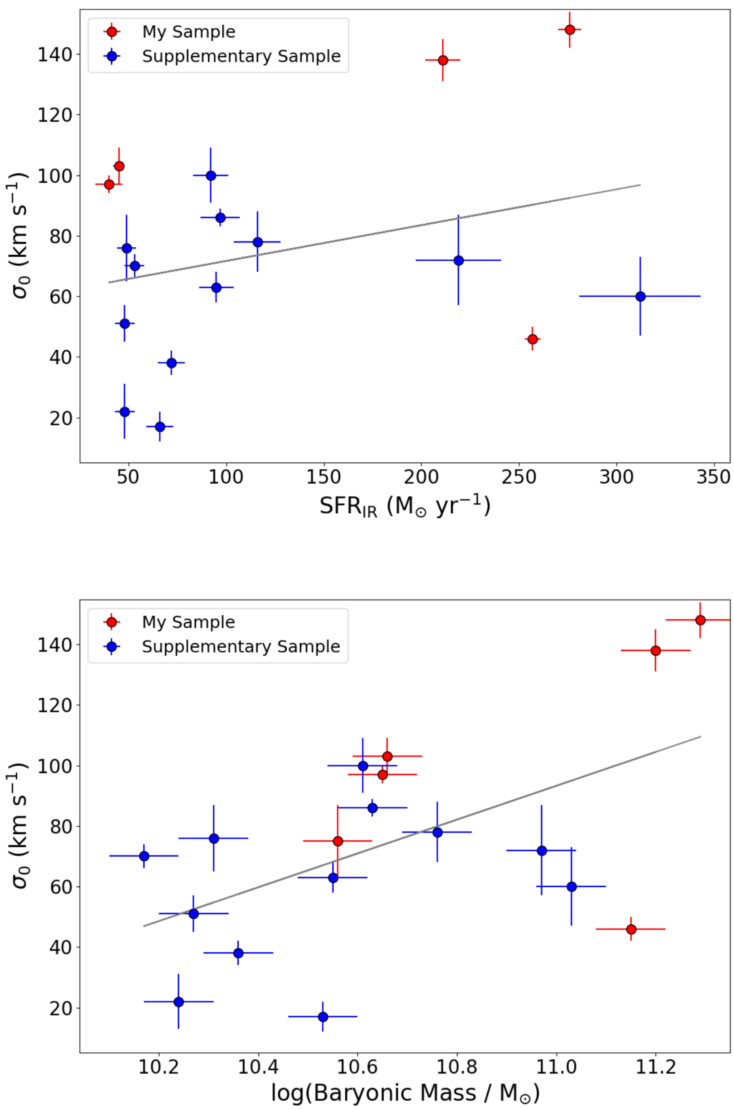

Figure 2.17: Top: Intrinsic velocity dispersion plotted against SFR. **Bottom:** Intrinsic velocity dispersion plotted against baryonic mass. There is a weak correlation for both σ_0 versus SFR and σ_0 versus baryonic mass with a Pearson's $\rho = 0.30$ (P-value $= 0.23$) and $\rho = 0.37$ (P-value $= 0.13$) for the SFR and baryonic mass respectively, although neither are statistically significant. Galaxy o8 could not be fitted with an IR SED so I do not have an SFR$_{IR}$ for this galaxy, giving only five data points in my sample for the top plot.

It is worth investigating potential non-systematic reasons for the range of velocity dispersion within both samples. Previous observational studies (e.g. Johnson et al., 2018, Übler et al., 2019) and semi-analytical modelling (e.g. Krumholz et al., 2018) indicate that turbulence in the high-z universe is driven primarily by gravitational instability as opposed to feedback from star formation. To check if the σ_0 in my sample is mainly caused by gravitationally unstable disks, I plotted σ_0 versus SFR and versus baryonic mass to gain insight into the mechanisms driving turbulence. I find weak correlations for σ_0 against baryonic mass with a Pearson's $\rho = 0.37$ (P-value = 0.13), and for σ_0 versus SFR with Pearson's $\rho = 0.30$ (P-value = 0.23), as shown in Figure 2.17, although neither are statistically significant. The weak correlation of σ_0 versus SFR may be due to the link between the SFR and baryonic mass, via the main sequence, as opposed to any causal link.

2.5.3 Are there Hidden Mergers in High-z U/LIRGs?

It is also possible that the presence of minor mergers is driving the scatter in dispersion. Such minor merger events are unlikely to be observed due to KMOS being a seeing limited instrument. Simons et al. (2019) showed, via simulations, that under seeing limited conditions at z $\sim$ 2, mergers can often be mistaken as disks under a variety of sight lines. Fensch et al. (2017) used simulations to demonstrate that mergers at z $\sim$ 2 provide an inefficient boost in SFR due to the already turbulent nature of disks at high-z, so being on the MS does not rule out potential mergers. Likewise, the dynamical ratio, which classified around 40% of the sample as isolated, may be a poor indicator of interacting galaxies when applied to seeing limited observations, as only a minor perturbation to a galaxy's kinematics would not be observable with spatial resolutions of $\sim$ 4 kpc. Very high spatial resolution may be needed to detect a merger in its initial stages or a minor merger in which the galaxy pair have a large difference in their $M_{\star}$, and this topic will be explored in detail using mock Hα observations in Chapters 4 and 5

In terms of major mergers, galaxy o7 is the only target in my sample that shows multiple signatures of being a major merger. It is the most IR luminous galaxy in my sample and clearly falls furthest into the starburst regime, with its SFR of 783 ± 5 $M_\odot$ yr^{-1}. Galaxy o15 is also denoted a starburst due to its position with respect to the MS, but isn't an outlier in terms of SFR. It lies within 1 σ of the average SFR of my sample, whereas o7 is a 3 σ outlier. Galaxy o7 has been previously studied by Elbaz et al. (2018) and Buat et al. (2019) where, using slightly different SED fitting methods, they found SFRs, (for a Chabrier IMF) of 670 ± 34 and 567 ± 28 $M_\odot$ yr^{-1} respectively, so I can be sure that its position as an outlier is not any systematic effect from the L_{IR} fit applied to my sample. Galaxy o7 also couldn't be fitted with a model disk, has a compact dust continuum, found by Elbaz et al. (2018), and has the highest N2 ratio of my sample, so adding these pieces of evidence to its huge SFR, it is likely a major merger.

2.6 Conclusion

I performed integral field spectroscopy in a sample of eighteen U/LIRGs at a redshift of $2 < z < 2.5$, which is the peak of the cosmic star formation density. I investigated the mechanisms driving their high rates of star formation and compared their properties to local and intermediate-z U/LIRGs to investigate the evolution in the dust, gas and star formation properties of U/LIRGs between the high-z universe and today. The main results are:

1. I detected Hα emission in fourteen out of eighteen galaxies, with a 3σ upper limit calculated in three of the other four. Having also fitted an IR SED to fourteen of my sample and using the SFRs calculated from the Hα and IR luminosities, I show that obscured star formation is an order of magnitude greater than the unobscured star formation within these galaxies. The average obscuration was less than intermediate and local U/LIRGs with $\log(SFR_{H\alpha} / SFR_{IR})$ = -1.05 ± 0.39.

2. Twelve of the sample are main sequence galaxies, with two being starbursts. I determined the distance of each galaxy from the MS, ΔSFR, and found a statistically significant correlation in which $\log(SFR_{H\alpha} / SFR_{IR})$ decreases

with increasing ΔSFR, demonstrating obscured star formation increases with distance above the MS.

3. Six of the Hα detections converged to a disk within GalPak^{3D}. To boost the sample size, I choose a supplementary sample of twenty eight luminous IR galaxies from the ESO archive, and twelve of this supplemental sample were found to be rotating disks. After accounting for the increase in intrinsic velocity dispersion with lookback time the dynamical ratio ($V_{rot}/\ \sigma_0$) suggest 17/41 may be isolated disks. This is a higher rate than local and intermediate redshift U/LIRGs, which have $\sim$ 5% and $\sim$ 25% respectively.

4. By quantifying the dynamical mass of my U/LIRGs I find them to be baryon dominated inside one R_E, similar to previous studies of star forming galaxies at z $\sim$ 2.

5. Far infrared photometry allowed me to fit a modified blackbody to seven of the U/LIRGs. The dust temperatures fall between 23 - 50 K, in line with dust temperatures in steady state star forming galaxies.

6. I measured the N2 ratio in four galaxies of my sample. The gas phase metallicity is in broad agreement with the mass-metallicity relation at z = 2 - 2.5, in contrast to the metal deficiency of local ULIRGs. For the remaining galaxies in the sample I stacked their spectra allowing a marginal detection of [NII] 6583 Å, and their average gas phase metallicity follows the MZR.

In summary, my high-z U/LIRGs have underlying mechanisms driving the huge SFRs that are consistent with the normal star forming population, as opposed to the merger driven star formation observed in local U/LIRGs. Even if my population is only representative of a subpopulation of U/LIRGs at cosmic noon, it still shows the general properties of the U/LIRG population have changed over the past 10 Gyr and local U/LIRGs are not necessarily analogues for high-z luminous IR galaxies. Major mergers do not appear to be a necessary condition to drive the high observed

SFR, as the observables in my sample of U/LIRGs are consistent with galaxies undergoing steady state star formation.

All changed, changed utterly:
A terrible beauty is born.

— WB Yeats *Easter 1916*

3

Main Sequence to Starburst Transition at Intermediate Redshifts

Contents

This chapter is adapted from: L. Hogan, D. Rigopoulou, S. García-Burillo, A. Alonso-Herrero, L. Barrufet, F. Combes, I. García-Bernete, G. E. Magdis, M. Pereira-Santaella, N. Thatte. A. Weiß. *Unveiling the Main Sequence to Starburst Transition Region with a Sample of Intermediate Redshift Luminous Infrared Galaxies*, 2022, MNRAS, 512, 2371.

3.1 Introduction

If star forming galaxies do indeed follow a bi-modal distribution of MS galaxies and starbursts, it poses the following questions: what mechanisms are responsible for this bi-modality, and how does a galaxy transition between these two modes? As outlined in Section 1.6, in the local universe U/LIRGs are sites of intense star formation due to mergers and interactions. At cosmic noon, they are often found within the scatter of the MS, as discussed in Chapter 2. At intermediate-z U/LIRGs straddle the MS and starbursts, making them ideal to explore the transition between both modes of star formation.

Another motivation for this research is that U/LIRGs are still a relatively understudied population at intermediate redshifts. In the local universe, U/LIRGs are well studied and drive much of our understanding of mergers. At cosmic noon U/LIRGs are of major interest due to their contribution to the peak of the cosmic SFRD. More intermediate-z observations are necessary to bridge the gap in evolution between local U/LIRGs and those at cosmic noon. We also need to better understand the properties of U/LIRGs at an epoch when the universe is undergoing a rapid decrease in SFRD.

Finally, most previous observations of intermediate-z U/LIRGs have been based either on samples of low luminosity LIRGs lying on, or just above the MS (e.g. Bauermeister et al., 2013, Lee et al., 2017) or high-luminosity ULIRGs that are undergoing a starburst phase (e.g. Combes et al., 2011, Combes et al., 2013). It is necessary to fill this luminosity gap between the 'cold' LIRGs and 'warm' ULIRGs if we want to understand the entire population at this redshift.

Exploring these three topics will allow us to gain insight into the evolution of cosmic star formation. In this chapter, I present six intermediate-z U/LIRGs observed by the NOrthern Ex-tended Millimeter Array (NOEMA) and ALMA, and establish the properties of the sample, which are located in the transition zone between regular star forming galaxies and starbursts. I will map the distribution of the molecular gas and dust, measure how efficiently they are forming stars, study their dynamics and investigate what triggers their star formation.

3.2 NOEMA and ALMA

NOEMA and ALMA are sub-mm/radio interferometers, and the principles of how these work is described in Section 1.8.2. Here follows an overview of the technical details for both instruments.

3.2.1 NEOMA

NOEMA[1] is located at 2550 m above sea level in the French Alps and currently consists of twelve antennae of fifteen meters in diameter. Baselines can range up to 750 m with four different configurations available. Three receivers non-contiguously cover frequencies in the range 71 - 276 GHz. The frequency channel spacing includes a high resolution mode of 62.5 kHz and a low resolution mode of 2 MHz (a useful approximation is 1 MHz corresponds to $\sim$ x km s^{-1} for a wavelength of x in mm). The spatial resolution ranges roughly between 0.4$''$ to 3.9$''$, depending on the exact configuration and frequency.

3.2.2 ALMA

ALMA[2] is located 5000 m above sea level in northern Chile, whose current constituent arrays are fifty twelve meter diameter antennae (known as the 12 m Array), twelve seven meter antennae packed closely together (called the 7 m Array) and four twelve meter antennae known as the Total Power Array. The arrays cycle between a variety of configurations and can have baselines up to 16 km in its most extended configuration. There are currently eight receiver bands in operation that cover a frequency range of 84 - 950 GHz non contiguously. The spatial resolution can range between 0.02 - 4.8$''$, depending on the configuration and frequency. ALMA data

[1]This work is based on observations carried out under project number W19BV and W20GC with the IRAM NOEMA Interferometer. IRAM is supported by INSU/CNRS (France), MPG (Germany) and IGN (Spain).

[2]This chapter makes use of the following ALMA data: ADS/JAO.ALMA#2016.1.00896.S. ALMA is a partnership of ESO (representing its member states), NSF (USA) and NINS (Japan), together with NRC (Canada), MOST and ASIAA (Taiwan), and KASI (Republic of Korea), in cooperation with the Republic of Chile. The Joint ALMA Observatory is operated by ESO, AUI/NRAO and NAOJ.

Table 3.1: The sample of intermediate U/LIRGs

Object	RA	Dec	z	Spatial Scale kpc arcsec^{-1}
FLS02-N	17:13:31.49	58:58:04.4	0.436	5.66
FLS02-S	17:13:31.64	58:58:01.0	0.437	5.65
CDFS1-W	03:29:04.39	-28:47:53.0	0.289	4.34
CDFS1-E	03:29:04.89	-28:47:55.5	0.291	4.36
SWIRE7	11:02:05.68	57:57:40.4	0.414	5.49
SWIRE5	10:35:57.9	58:58:46.2	0.366	5.08

cubes can contain up to 7680 frequency channels whose widths can range from 3.8 kHz to 15.6 MHz with a maximum bandwidth of 8 GHz.

3.3 Observations

3.3.1 The Sample

This study selected four systems for a total of six targets: FLS02 (2 interacting galaxies), CDFS1 (2 interacting galaxies), SWIRE5 and SWIRE7. These targets were chosen as they have previous multi-wavelength observations. The parent sample (see Figure 3.1) was first presented in Magdis et al. (2014), hereafter referred to as M14 in this chapter, and Rigopoulou et al. (2014), and was drawn from Herschel deep surveys (Oliver et al., 2012). The system names are taken from the sky surveys in which these galaxies were sourced: Spitzer Wide-area InfraRed Extragalactic survey (SWIRE), the Spitzer First Look Survey (FLS) and the Chandra Deep Field South (CDFS). The parent sample was selected based on two criteria: having 250 μm fluxes $S_{250} > 150$ mJy, and redshifts between $0.2 < z < 0.8$. The first criterion ensured the targets would be IR luminous with $\log(L_{IR} / L_{\odot}) > 11.6$. The second criterion was chosen to enable the Herschel Spectral and Photometric Imaging REceiver-Fourier Transform Spectrometer (SPIRE-FTS, Griffin et al., 2010), whose bands have a wavelength coverage of 194 - 671 μm, to observe the [CII] 158 μm emission line. No other criteria on morphologies or colours were applied, so the sample is not biased in terms of source morphology, color or other properties. The Herschel photometric and spectroscopic observations

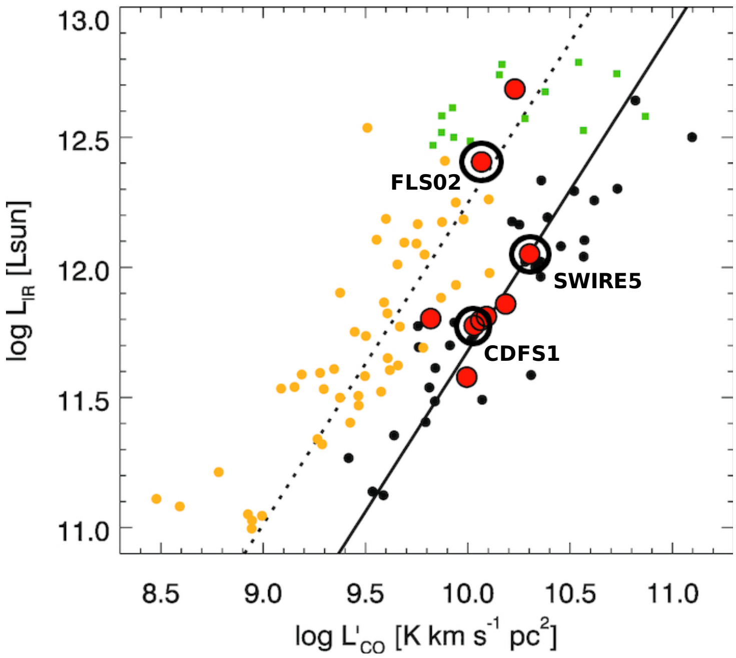

Figure 3.1: Infrared luminosity versus single dish CO(1-0) luminosity for the parent sample of intermediate redshift U/LIRGs, adapted from Pereira-Santaella et al. (2019). All galaxies in the parent sample with CO and [CII] 158 μm observations in Magdis et al. (2014) are included (red circles). The position of FLS02, SWIRE5 and CDFS1 are marked with a black ring. SWIRE7 is not included as it wasn't observed in CO in Magdis et al. (2014). The black circles are disk galaxies located at $0.3 < z < 2.5$ (Daddi et al., 2010, Geach et al., 2011, Genzel et al., 2010), the orange circles are local U/LIRGs (Solomon et al., 1997), and the green squares are starburst ULIRGs from Combes et al. (2011). The solid and dashed black lines represent the relation observed for main sequence and starburst galaxies, respectively (Sargent et al., 2014).

were complemented, in M14, with single dish CO measurements from the Institute for Radio Astronomy in the Millimeter Range (IRAM) 3 m telescope and the Atacama Pathfinder Experiment (APEX) 12 m telescope. Pereira-Santaella et al. (2019), hereafter PS19, presented I-band integral field spectroscopy observations undertaken using the SWIFT spectrograph on the 5.1 meter Hale Telescope at the Palomar Observatory (Thatte et al., 2006), which covers a wavelength band of 0.63 - 1.04 μm (see Figures 3.2 and 3.3).

The six targets have dust temperatures ranging between T_{dust} = 29 - 42 K and $\log(L_{IR} / L_{\odot})$ in the range 11.79 - 12.41. They have similar ratios of unobscured (traced by Hα) to obscured (traced by L_{IR}) star formation as the local U/LIRGs. They do not exhibit the [CII] / L_{IR} deficiency seen in local ULIRGs, except for

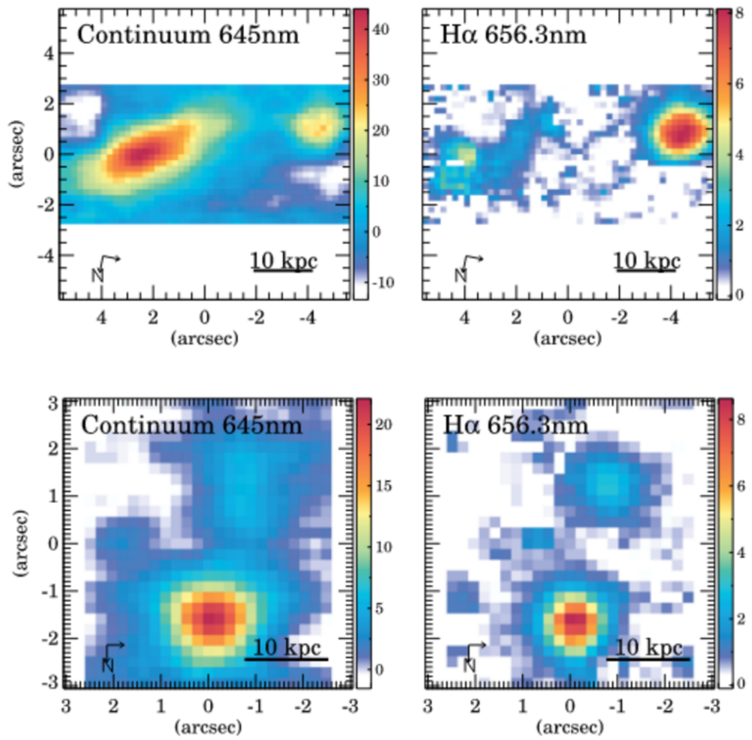

Figure 3.2: Top: Hα and rest frame 645 nm continuum for CDFS1, taken by the SWIFT telescope. The units for the continuum and emission line maps are 10^{-15} erg s^{-1} cm^{-2} μm^{-1}and 10^{-17} erg s^{-1} cm^{-2} respectively. The two arrows in the lower left-hand corner show the North and East directions. The seeing FWHM for this source was 1.4$''$/ 6 kpc. Note that north points down, opposite to my CO image of CDFS1. **Bottom:** Hα and rest frame 645 nm continuum for FLS02. The seeing FWHM for this source was 1.6$''$/ 9 kpc. Note that north points down, opposite to my CO image of FLS02. All figures taken from Pereira-Santaella et al. (2019).

FLS02, which may be indicative of softer radiation fields and more extended regions of star formation within my sources when compared to local ULIRGs (e.g. Rigopoulou et al., 2014 Díaz-Santos et al., 2017, Herrera-Camus et al., 2018). Morphology-wise, PS19 found the parent sample is a mixture of interacting and isolated disks based on the ratio of V_{rot} / σ_0. The sample straddles the region between the MS LIRGs and starburst ULIRGs at this epoch in terms L_{IR} and the L_{IR} - L'_{CO} ratio, so it is ideal for investigating the transition between MS and starburst galaxies, and its link to interaction stage. Just to note that line luminosities are denoted with a prime, L$'$, and are in units of K km s^{-1} pc^2, whereas any luminosities written without the prime, L, are in SI units, such as $L_\odot$ or erg s^{-1}, as per the previous chapter. Details of the redshifts and coordinates

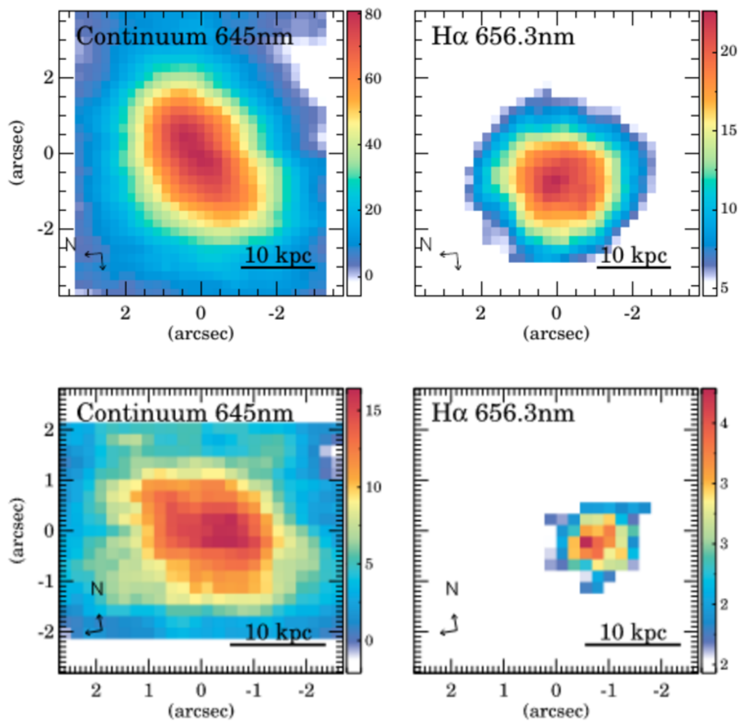

Figure 3.3: Top: Hα and rest frame 645 nm continuum for SWIRE5, with the description same as Figure 3.2. The seeing FWHM for this source was 2.7″/ 13.7 kpc. Note that north points left. **Bottom**: Hα and rest frame 645 nm continuum for SWIRE7. The seeing FWHM for this source was 2.1″/ 11 kpc. All figures taken from Pereira-Santaella et al. (2019).

targets are given in Table 3.1.

3.3.2 NOEMA Observations

NOEMA observations of the CO J $= 3 \rightarrow 2 \equiv$ CO(3-2) emission line ($\nu_{\rm rest} = 345.796$ GHz) and its underlying continuum (rest wavelength ~ 0.9 mm) were obtained for four of the targets (three systems): FLS02, SWIRE5 and SWIRE7 [3]. Ten antennae were used in the C configuration of NOEMA (A configuration is the most extended with D being the most compact, and C configuration has a longest baseline of 368 m). The observations for FLS02 took place over seven nights between 29 December 2019 and 25 February 2020, with SWIRE5 being observed on 28 March 2021 and SWIRE7 on three nights between 31 March 2020 and 04 April 2020 (details listed in Table 3.2). The FOV for these targets was $\approx$ 20-21″.

[3]projects W19BV & W20GC, PI: S Garcia-Burillo

Table 3.2: Calibrators used in data reduction

NOEMA					
Object	Date	Integration Time[1] hours	Flux Calibrator	Bandpass Calibrator	Phase/amp Calibrator
FLS02	29 Dec 2019	0.8	MWC349	3C454.3	1637+574
	02 Jan 2020	1.5	MWC349	1637+574	1637+574
	06 Jan 2020	2.2	MWC349	3C454.3	1637+574
	08 Jan 2020	1.5	MWC349	3C454.3	1637+574
	11 Jan 2020	1.1	MWC349	3C84	1637+574
	16 Jan 2020	0.8	MWC349	3C454.3	1637+574
	25 Feb 2020	1.9	MWC349	3C279	1637+574
SWIRE5	28 Mar 2021	3.8	LKHA101	3C84	1030+611
SWIRE7	31 Mar 2020	4.1	3C273	3C273	
	02 Apr 2020	1.5	1055+018	3C84	1030+611
	04 Apr 2020	1.5	0923+392	0923+392	1030+611

ALMA					
Object	Date	Integration Time hours	Flux Calibrator	Bandpass Calibrator	Phase Calibrator
CDFS1	04 Nov 2016	0.2	J0334-4008	J0522-3627	J0348-2749

[1] On source integration time.

The data was reduced using the standard pipeline in the Grenoble Image and Line Data Analysis Software (GILDAS)[4] software package. Bad visibilities were flagged and removed, and the flux, bandpass and amplitude/phase were calibrated using standard NOEMA calibrators (see Table 3.2).

Calibrated uv tables for both the continuum and the CO line were put together using the Continuum and Line Interferometer Calibration (CLIC)[5] routine and the uv tables were imaged using the MAPPING routine. The lower side bands were used to put together the continuum uv tables in order to avoid CO line emission.

For the image deconvolution, I used robust weighting, with a threshold of 1, to improve the spatial resolution of the SWIRE7 continuum map, with a natural weighting used for the continuum maps in FLS02 and SWIRE5 in order to maximize the S/N (for details of radio imaging and weightings see Appendix A.1). For the CO(3-2) data I used both robust and natural weighting. The natural weighting was used so the CO(3-2) maps have a similar beam size to the continuum maps, allowing the morphology to be compared, with the robust weighting being chosen to improve the spatial resolution when fitting the kinematics (the naturally weighted CO(3-2) cubes are used for all analysis other than fitting the kinematics). The pixel size was chosen to be $0.16''$, which corresponds to $\sim 5/6$ pixels across the synthesized beam (~ 0.8 - $1''$) for all 3 sources, and I choose a channel width of 20 km s^{-1}. The dirty cubes were cleaned using the Högbom algorithm within the CLEAN routine, and the fully reduced clean cubes were exported as FITS files for further analysis. The final cubes have a resolution of 0.72 - $1.01''$ corresponding to physical scales of ≈ 3.7 - 5.7 kpc. Details of integration times, the beam size and noise are given in Table 3.3.

3.3.3 ALMA Observations

Band 6 (211 - 275 GHz) ALMA observations of the CO(3-2) and continuum emission were obtained for CDFS1 (two interacting galaxies) using 43 antennae

[4]https://www.iram.fr/IRAMFR/GILDAS
[5]https://www.iram.fr/IRAMFR/GILDAS/doc/html/clic-html/clic.html

Table 3.3: Observation details for the sample.

Object	Integration Time[1] hours	Synthesized Beam[2] arcsec × arcsec	$\sigma_{\rm rms}$[3] mJy/beam
CDFS1	0.2	(0.31 × 0.28)[a]	0.91
FLS02	9.8	0.82 × 0.67[a]	0.55
		(1.01 × 0.78)	
SWIRE5	3.8	0.72 × 0.61	0.61
		(0.82 × 0.67)	
SWIRE7	7.1	0.90 × 0.79	0.71

[1] On source integration time.
[2] Synthesized beam for the fully reduced data.
[3] 1σ sensitivity in each 20 km s^{-1} channel.
[a] The value in brackets is the synthesized beam for natural weighting. Values without brackets are the synthesized beam for robust weighting with a threshold of 1. See Section 3.3.2 for full details.

of the 12 m Array in the C40-6 configuration [6] (C40-1 is the most compact and C40-9 is the most extended configuration and C4-0 has a maximum baseline of 1.8 km). The observations were taken on 04 November 2016, with a total on source integration time of 0.2 hours and FOV of $\approx$ 23.5″. One spectral window was centred on the expected frequency of the CO(3-2) line and the other three spectral windows were used to observe the underlying continuum.

The data was reduced using the standard pipeline in the Common Astronomy Software Applications (CASA) software package (McMullin et al., 2007). Bad visibilities were flagged and removed, and I used standard ALMA calibrators to calibrate the source.

The continuum map was created by using multifrequency synthesis mode (combines all selected channels into one image) within CASA on spectral windows that did not contain the CO(3-2) emission line. For the emission line cube I subtracted the continuum emission in each channel by using the UVCONTSUB routine to fit a 0th order polynomial continuum model to the line free channels of the uv plane.

The dirty cubes were then cleaned with the TCLEAN routine, and I used natural weighting to maximize the S/N. I choose a pixel size of 0.045″ which is $\sim$

[6]project 2016.1.00896.S, PI: D Rigopoulou

7 pixels across the synthesized beam and set the channel width to 20 km s^{-1}. All data was corrected for the primary beam response to produce the fully reduced data cubes. The reduced data has a resolution of 0.31″ which corresponds to a physical scale ≈ 1.5 kpc.

3.4 Analysis

In this analysis I assume that the main source of the continuum emission, observed at a rest wavelength $\sim$ 0.9 mm, arises from the Rayleigh-Jeans tail of the dust emission. It is difficult to rule out AGN contribution to the L_{IR}, but as the sample does not have broad components in the Hα emission line (PS19) I assume they are star formation dominated, and that the L_{IR} emission I observe is entirely attributed to star formation.

3.4.1 CO(3-2) and Continuum Emission

I created intensity maps of both CO(3-2) and continuum for the sources to study their morphology, flux and the relative positions of their peak flux. To make the CO(3-2) intensity maps, I performed a 3σ cut in each channel of the data cube and then integrated the remaining flux across the total width of the emission line. For the continuum 0th moment maps I made a 3σ cut on the continuum map. These plots are presented in Figures 3.4 and 3.5, with 3σ (and multiples of 3σ) contours of the continuum emission overlaid on the CO(3-2) maps. I also created integrated spectra by summing all spaxels within the 3σ cut, giving one flux value per channel. Linewidths are in agreement with previous measurements using a single dish observation in M14 (see Figure 3.6 for the ALMA and NOEMA integrated spectra).

For the northern source in FLS02 (hereafter FLS02-N) the continuum and CO(3-2) emission are approximately co-spatial and the centre of the continuum coincides with the centre of CO(3-2). The southern source, hereafter FLS02-S, has weaker CO(3-2) emission with a marginal $\sim$ 4σ detection in the continuum (see Figure 3.4).

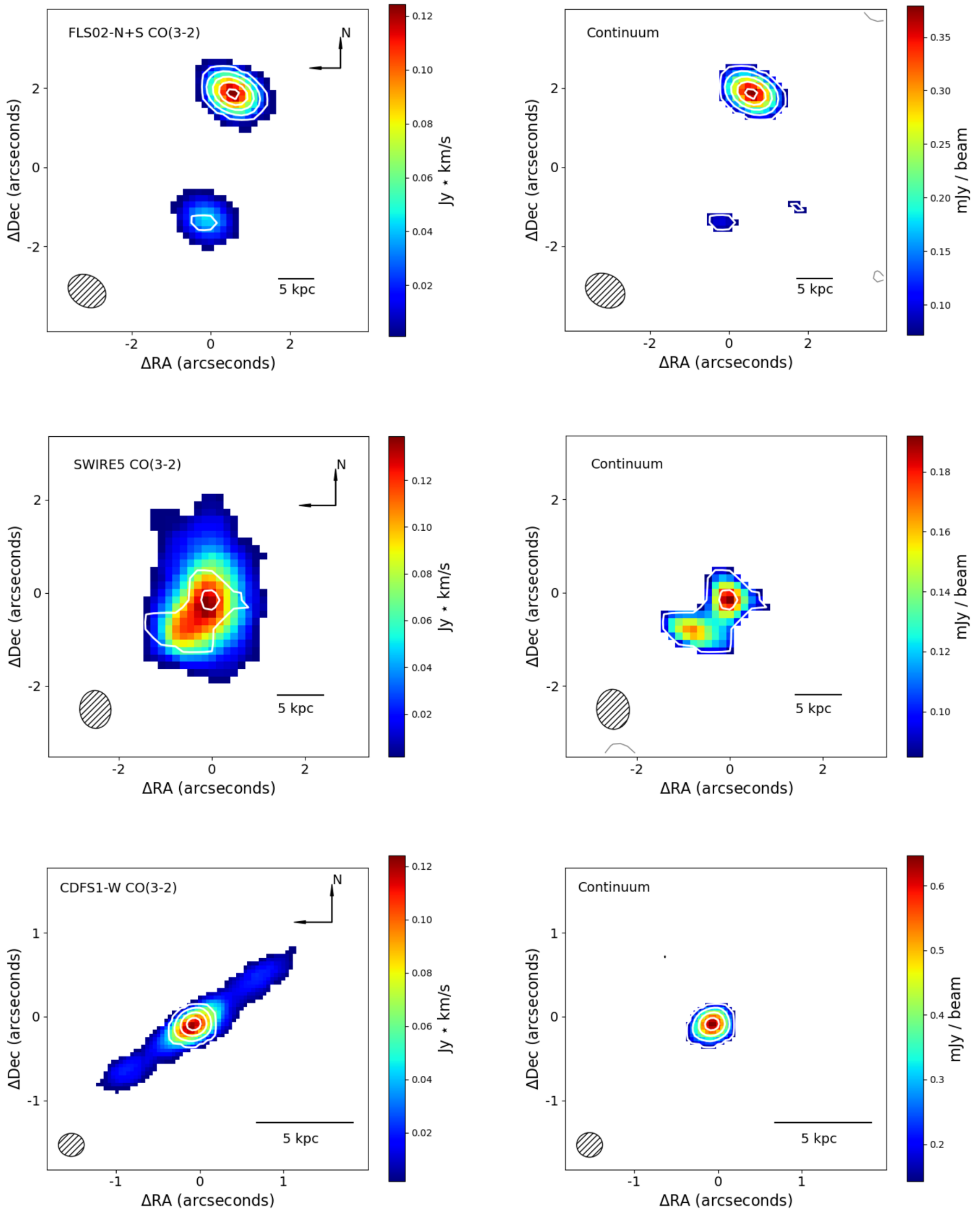

Figure 3.4: Intensity maps for my targets with CO(3-2), in units of Jy km s^{-1}, in the left column and continuum (rest wavelength $\sim$ 0.9mm), in units of mJy/beam, in the right column for FLS02 (**top row**), SWIRE5 (**middle row**) and CDFS1-W (**bottom row**). The CO(3-2) maps were made using a 3σ cut in each channel and a 3σ cut was also used on the continuum maps. Contours of the continuum emission are overlaid in white on the CO(3-2) maps to show the overlap of dust and molecular gas, with the contours representing multiples of 3σ continuum emission (i.e. 3σ, 6σ, 9σ etc.). The grey contours on the continuum plots show negative 3σ emission. The beam size is shown in the bottom left corner of each plot, and the physical size scale is shown on the bottom right. For optical maps of the same galaxies, see Figures 3.2 and 3.3.

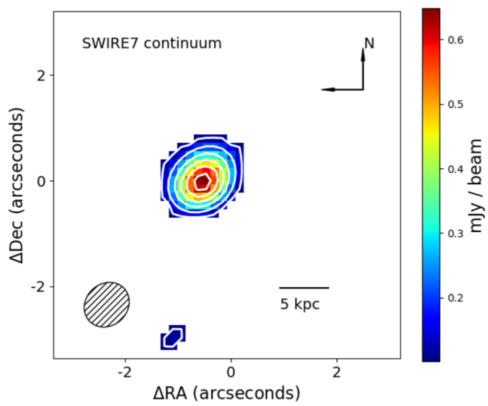

Figure 3.5: Same as Figure 3.4 except for SWIRE7 continuum. No CO(3-2) was observed in this target.

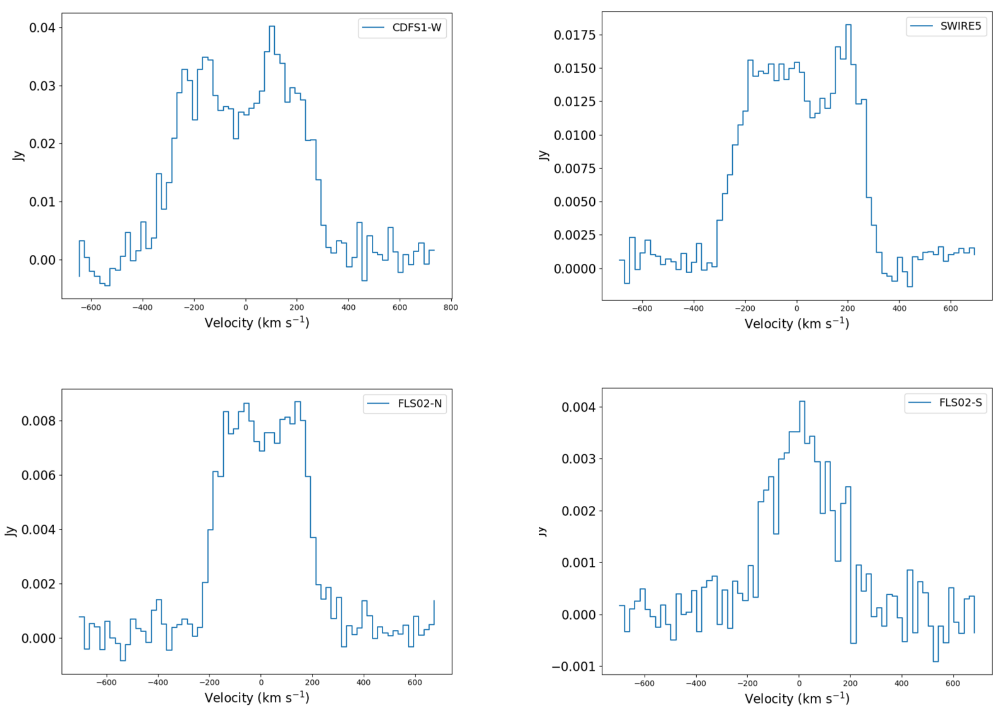

Figure 3.6: The galaxy integrated spectra of each of the targets with a CO(3-2) detection. **Top left:** CDFS1-W (ALMA). **Top right:** SWIRE5 (NOEMA). **Bottom left:** FLS02-N (NOEMA). **Bottom right:** FLS02-S (NOEMA).

Table 3.4: Observed CO(3-2) properties of my sample of intermediate-z U/LIRGs.

Object	$S_{CO}\Delta v$ (total)[1] Jy km s^{-1}	L'_{CO} (total)[2] 10^9 K km s^{-1} pc^2	$S_{CO}\Delta v$ (masked)[3] Jy km s^{-1}	L'_{CO} (masked)[4] 10^9 K km s^{-1} pc^2	$\log(L_{IR} / L_\odot)$[5]	T_{dust}[6] K	SFR_{IR}[7] $M_\odot$ yr^{-1}	12+log(O/H)[8]
CDFS1-W	13.42 ± 1.11	6.26 ± 0.52	9.71 ± 0.66	4.53 ± 0.31	11.79	29	91	9.08
FLS02-N	4.50 ± 0.33	4.93 ± 0.36	4.39 ± 0.29	4.81 ± 0.32	12.41[a]	42[a]	353	8.87
FLS02-S	1.34 ± 0.18	1.47 ± 0.20	1.34 ± 0.18[b]	1.47 ± 0.20[b]	-	-	27	8.82
SWIRE5	13.36 ± 0.87	10.18 ± 0.66	8.94 ± 0.56	6.81 ± 0.43	12.06	33	170	8.77
SWIRE7	<0.26[c]	<0.26[c]	<0.26	<0.26	12.10	36	190	-

[1] The total CO(3-2) flux density of the galaxy.
[2] The total CO(3-2) line luminosity of the galaxy.
[3] The flux density within the masked region of each galaxy as explained in Section 3.4.2.
[4] The CO(3-2) line luminosity within the masked region.
[5] The IR luminosity from Magdis et al. (2014).
[6] The dust temperature from Magdis et al. (2014).
[7] The IR star formation rate from Pereira-Santaella et al. (2019).
[8] The gas phase oxygen abundance obtained from the N2 ratio presented in Pereira-Santaella et al. (2019).
[a] The $\log(L_{IR} / L_\odot)$ of 12.41 and T_{dust} of 42 K is for the total FLS02 system. The decomposition of the LIR into SFR for the individual galaxies of FLS02 is explained in Section 3.4.3.
[b] Masked region is equal to the total CO(3-2) region for FLS02-S as explained in Section 3.4.3.
[c] SWIRE7 undetected in CO(3-2) so the upper limit is calculated from the masked region.

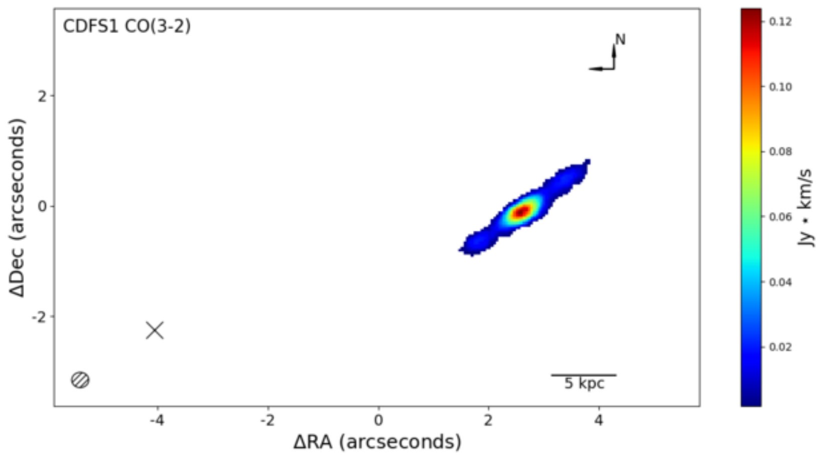

Figure 3.7: CO(3-2) intensity map of the CDFS1 system, in units of Jy km s^{-1}, with the expected position of the undetected CDFS1-E marked with an X. The beam size is plotted in the bottom left corner with the physical scale shown in the bottom right. Note this is not the full FOV of ALMA.

The SWIRE5 CO(3-2) and continuum emission maps reveal very different morphology, with the star forming region smaller in extent than the molecular gas and the dust continuum appears to have two peaks which are separated by $\sim$ 7 kpc (see Figure 3.4).

In CDFS1, the western source, CDFS1-W, has a disk like structure in CO(3-2) with a more compact continuum located in the central region of the disk (see Figure 3.4). Neither CO(3-2) nor continuum are observed in CDFS1-E despite this galaxy having a Hα detection in PS19. Figure 3.7 shows its expected position with respect to CDFS1-W and Figure 3.2 shows the Hα detection of CDFS1-E (note that north points down in the optical image).

No CO(3-2) was detected in SWIRE7, but there is a 20σ detection of the dust continuum (see Figure 3.5). In Figures 3.2 and 3.3 I have included the optical images of all four systems, from PS19, for comparison with the CO(3-2) and sub-mm continuum. The morphology and its link to both the triggers of star formation and the SFE within a galaxy will be discussed in more detail in Section 3.5.2.

3.4.2 Molecular Gas Mass

The CO(3-2) transition is 33 K above the ground state and has a critical density of $> 10^4$ cm^{-3} at temperatures < 20 K, so it traces the molecular clouds within the ISM from which stars are formed (e.g. Rigby et al., 2016). Local observations have established the integrated flux from the low-J CO transitions is proportional to the gas within a galaxy and in order to estimate the M_{mol} from the line luminosity, $L'_{CO(3-2)}$, the use of an appropriate α_{CO} conversion factor is required (e.g. Bolatto et al., 2013). This factor is dependent on the density of molecular clouds, the Rayleigh-Jeans brightness temperature and inversely proportional to the metallicity within a galaxy.

Firstly, I convert the CO(3-2) flux density from the intensity maps to the integrated line luminosity using the following equation from Solomon et al. (1997),

$$L'_{\mathrm{CO(J\,-\,J-1)}} = 3.25 \times 10^7 \cdot S_{\mathrm{CO}}\Delta \mathrm{v} \cdot \nu_{\mathrm{obs}}^{-2} \cdot \mathrm{D_L^2} \cdot (1+\mathrm{z})^{-3} \tag{3.1}$$

where $S_{CO}\Delta v$ is the integrated flux density in Jy km s^{-1}, ν_{obs} is the observed frequency in GHz, D_L is the luminosity distance in Mpc, z is the redshift of the source and the line luminosity is in units of K km s^{-1} pc^2.

To choose an appropriate α_{CO}, I account for metallicity by adopting a metallicity dependent conversion factor described in Genzel et al. (2012) and Genzel et al. (2015):

$$\alpha_{\mathrm{CO(3-2)}}(Z) \;=\; \alpha_0 \cdot \chi(Z) \cdot R_{1-3} \quad (\mathrm{M_\odot/(K\ km\ s^{-1}\ pc^2)}) \tag{3.2}$$

where α_0 is the unscaled $J = 1 \rightarrow 0$ conversion factor, $\chi(Z)$ is the metallicity dependent scaling factor and R_{1-3} is the ratio of the $L'_{CO(1-0)}$ to $L'_{CO(3-2)}$ which is required to correct for the lower Rayleigh-Jeans brightness temperatures in higher J transitions. I choose the metallicity dependent scaling factor of Genzel et al. (2015):

$$\chi(Z) = 10^{-1.27\times(12+\log(\mathrm{O/H})-8.67)} \tag{3.3}$$

where 12 + log(O/H) is the gas phase oxygen abundance. The constant of 8.67 ensures Equation 3.2 reverts to α_{MW} when the gas phase oxygen abundance equals the solar abundance.

I assume α_0 equals the Milky Way conversion factor $\alpha_{\rm MW} = 4.36 \pm 0.9$ M$_\odot$ / (K km s^{-1} pc^2), including the correction for Helium, and R$_{1-3}$ = 1.9 (Lamperti et al., 2020), which is a typical value seen in star forming galaxies. For the metallicity of the sample, I use the sample's [NII] 6583 Å / Hα ratios reported in PS19 and converted these to 12 + log(O/H) using the Pettini and Pagel (2004) correlation. For SWIRE7, I set χ(Z) = 1 as it had no [NII] 6583 Å detection in PS19. The values I obtain for $\alpha_{\rm CO(3-2)}(Z)$ are shown in Table 3.5. Thus, the molecular gas mass in each target is found by

$$M_{\rm mol} = \alpha_{\rm CO(3-2)}(Z) \cdot L'_{\rm CO(3-2)} \tag{3.4}$$

One caveat when choosing a conversion factor is that local ULIRGs typically have an $\alpha_{\rm CO}$ factor which is about five times lower than that of the Milky Way, with a value of $\approx$ 0.8 M$_\odot$ / (K km s^{-1} pc^2) for the CO(1-0) transition (e.g. Downes and Solomon, 1998). The intermediate-z sample of U/LIRGs have different ISM conditions compared to those of local ULIRGs (as discussed in M14) and are in an earlier stage of interaction (PS19). Therefore, the metallicity dependent $\alpha_{\rm CO(3-2)}$(Z) is the most appropriate conversion factor for the sample. I discuss how the lower $\alpha_{\rm CO}$ would affect my results in Section 3.5.1.

It is worth emphasizing that my choice of metallicity scaling factor is quite conservative. Genzel et al. (2015) uses two metallicity scaling functions (see equations 6 and 7 of Genzel et al., 2015) and takes the geometric mean of both as the final scaling factor. I chose Equation 3.3 to be my scaling factor as it gave me the lowest $\alpha_{\rm CO(3-2)}(Z)$. If I chose the geometric mean, as in Genzel et al. (2015), then the $\alpha_{\rm CO(3-2)}(Z)$ would be $\sim$ 15% higher on average, with a corresponding increase in M$_{\rm mol}$.

Finally, M14 estimated the M$_{\rm mol}$ using the dust to gas mass ratio technique (see M14 and references therein) and inferred an $\alpha_{\rm CO}$ consistent with local star forming galaxies for the sample (except for FLS02), further corroborating my choice. FLS02 was classified as an AGN in M14, due to its observed [CII] deficiency, and M14 calculated the average $\alpha_{\rm CO(1-0)}$ for [CII] deficient galaxies as 1.5, roughly twice

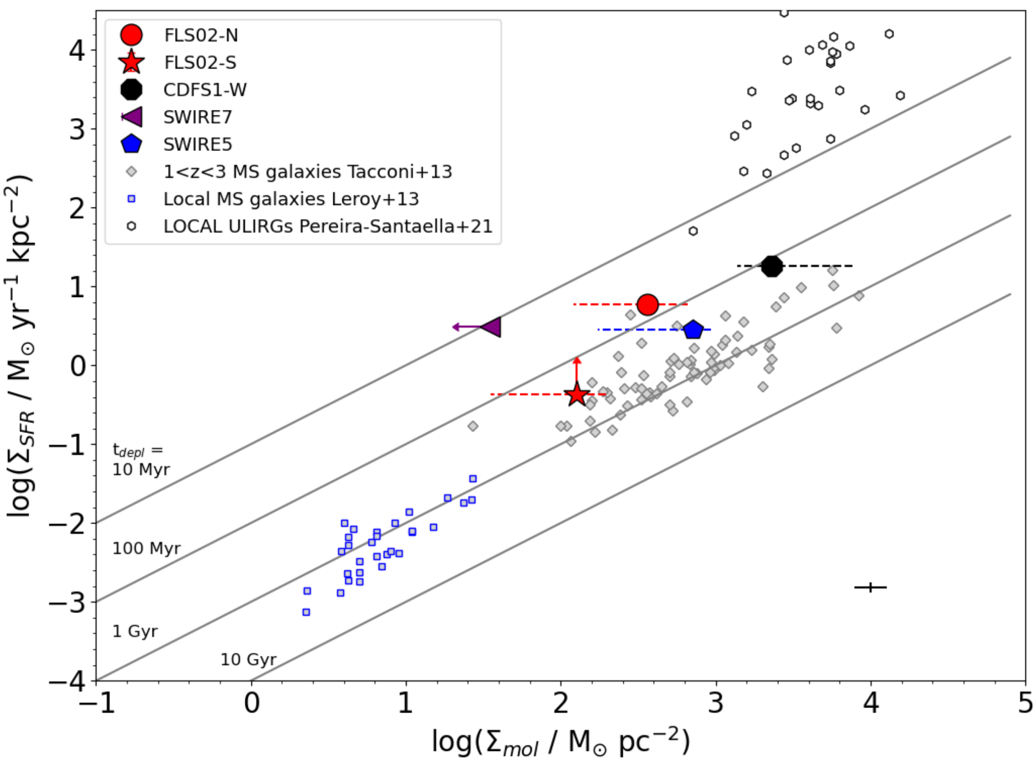

Figure 3.8: Gas surface-density, $\Sigma_{\rm mol}$, versus star-formation surface-density, $\Sigma_{\rm SFR}$, for my sample of U/LIRGs. They are compared to values for high-z star forming galaxies (grey diamonds, Tacconi et al., 2013), local ULIRGs (white hexagons, Pereira-Santaella et al., 2021) and local star forming disk galaxies (blue squares, Leroy et al., 2013). It can be seen that my sample of U/LIRGs have longer depletion times when compared to local ULIRGs, but shorter depletion times when compared to normal star forming galaxies, indicating the intermediate-z U/LIRGs falls in the transition region between starburst and main sequence galaxies. The dashed lines show how changing the $\alpha_{\rm CO}$ affects the $\Sigma_{\rm mol}$ when taking the extreme $\alpha_{\rm CO(1-0)}$ values: the local ULIRG conversion factor of 0.8 $M_\odot$ / (K km s^{-1} pc^2) and the Milky Way value of 4.36 $M_\odot$ / (K km s^{-1} pc^2). The cross in the bottom right corner shows the typical size of the error bars.

the ULIRG value, and would give an $\alpha_{\rm CO(3-2)}(Z) \sim 3$, using my choice of R_{1-3} scaling. Subsequent evidence, such as a narrow Hα and [NII] 6583 Å emission lines and polycyclic aromatic hydrocarbons features consistent with composite objects (infrared spectrograph data from Houck et al., 2007), suggest that the source is not an AGN dominated object. Hence, I argue the metallicity scaled $\alpha_{\rm CO}$(Z) is the most pertinent choice for FLS02.

3.4.3 Star Formation Efficiency

A galaxy's star forming efficiency can be calculated from its surface density of SFR and molecular gas (SFE = $\Sigma_{\rm SFR}/\Sigma_{\rm mol}$). To get the surface density, I first found the spatial size of the star forming region, $A_{\rm cont}$, within each U/LIRG by assuming that the continuum flux arises from the dust and that it traces the full extent of obscured star formation within the galaxy ($SFR_{\rm IR}$). As the sources are resolved, I measured this area directly from the 0th moment maps by multiplying the area of each pixel by the number of pixels with S/N $> 3\sigma$ (see Figure 3.4). To determine the SFR in each of the targets, I take the $L_{\rm IR}$ - $SFR_{\rm IR}$ conversion factor from Equation 2.2 and apply this to the $L_{\rm IR}$ from M14. As the sources are heavily dust obscured (PS19) I assume the $SFR_{\rm IR} \approx$ total SFR.

As discussed in Section 3.4.1, the morphology of the continuum and CO emission is different across the sample. To accurately determine the $\tau_{\rm dep}$ I use only CO(3-2) that overlaps with the $SFR_{\rm IR}$. To do this, I placed a mask on the emission line cube that ensured only CO(3-2) flux that arises within $A_{\rm cont}$ is extracted. This mask corresponds to the outer white contour in Figure 3.4. All flux outside this contour is not used for the SFE calculation. To integrate the masked CO(3-2) flux I narrowed the velocity window to include only channels containing line emission and applied no threshold within the masked region to ensure I missed no flux. The surface density for the molecular gas was then calculated using $\Sigma_{\rm mol} = M_{\rm mol}$ / $A_{\rm cont}$ and the SFR surface density was found via $\Sigma_{\rm SFR}$ = $SFR_{\rm IR}$ / $A_{\rm cont}$.

I estimated an upper limit for $M_{\rm mol}$ in SWIRE7 by finding a 3σ upper limit for $S_{\rm CO}\Delta$v. This was calculated from $3\sigma/\text{beam} = 3\sqrt{N}\delta v\sigma_{\rm rms}$, where N is the number of channels, δv is the channel width in km s^{-1} and $\sigma_{\rm rms}$ is the noise per channel. I assumed a linewidth of 300 km s^{-1} and multiplied the 3σ/beam by the square root of the number of beams within $A_{\rm cont}$ of SWIRE7 to get the upper limit. For FLS02-S there is a marginal ($\approx 4\sigma$) unresolved continuum detection, so I assumed $A_{\rm cont}$ is equal in size to the CO(3-2) emitting region.

My results are listed in Tables 3.4 and 3.5, and plotted in Figure 3.8. The sample shows a $\tau_{\rm dep}$ of 11 - 301 Myr, with $\tau_{\rm dep}$ of 62 - 301 Myr if I exclude SWIRE7, as

Table 3.5: Surface density details for the sample of intermediate-z U/LIRGs

Object	$\alpha_{CO(3-2)}(Z)$[1] $M_\odot$ / (K km s^{-1} pc^2)	M_{mol} (total)[2] 10^{10} $M_\odot$	M_{mol} (masked)[3] 10^{10} $M_\odot$	A_{cont}[4] 10^7 pc^2	$\log(\Sigma_{CO}$ / $M_\odot$ $pc^{-2})$[5]	$\log(\Sigma_{SFR}$ / $M_\odot$ yr^{-1} $kpc^{-2})$[6]	τ_{dep}[7] Myr
CDFS01-W	2.51 ± 0.52	1.57 ± 0.35	1.14 ± 0.25	0.48	3.37 ± 0.09	1.27	125 ± 30
FLS02-N	4.56 ± 0.94	2.25 ± 0.49	2.20 ± 0.48	6.04	2.56 ± 0.09	0.77	62 ± 15
FLS02-S	5.42 ± 1.12	0.80 ± 0.20[a]	0.80 ± 0.20	6.35[a]	2.10 ± 0.1	-0.38	301 ± 80
SWIRE 5	6.27 ± 1.29	6.38 ± 1.38	4.27 ± 0.92	6.02	2.85 ± 0.09	0.45	251 ± 60
SWIRE7	8.28 ± 0.18	<0.21[b]	<0.21	6.12	<1.54	0.49	< 11

[1] The conversion factor from $L'_{CO(3-2)}$ to molecular gas mass as described in Equation 3.2. This value includes a factor of 1.9 to go from $L'_{CO(3-2)}$ to $L'_{CO(1-0)}$.
[2] The total molecular gas mass within the galaxy
[3] The molecular gas mass inside the masked region, as described in Section 3.4.2
[4] The area of the continuum, assuming a 3σ cut.
[5] The molecular gas mass surface density.
[6] The star formation rate surface density. I assume an error of 10% for each target.
[7] The depletion time of the molecular gas reservoirs within each galaxy.
[a] The masked region is equal to the total CO(3-2) region for FLS02-S as explained in Section 3.4.3.
[b] SWIRE7 is undetected in CO(3-2) so the upper limit is calculated from the masked region as explained in Section 3.4.3.

the source was not detected in the CO(3-2) emission line. This is higher than the $\tau_{\rm dep}$ = 1 - 15 Myr found for local ULIRGs (Pereira-Santaella et al., 2021), but lower than the values found for the regular star forming population at both low and high redshifts which are on the order of 1 Gyr (e.g. Leroy et al., 2013, Tacconi et al., 2013). This demonstrates that my sample of U/LIRGs, which fall within the transition region between starbursts and MS galaxies, also fall between the loci of major mergers and regular star forming galaxies on the KS relation. Figure 3.8 also shows how the $\Sigma_{\rm mol}$ values of the intermediate-z U/LIRGs are similar to those of gas rich MS galaxies at high-z. However, the intermediate-z U/LIRGs have a higher SFE as indicated by the sample having, on average, a larger $\Sigma_{\rm SFR}$ for a given $\Sigma_{\rm mol}$.

It is worth noting that the $\rm SFR_{IR}$ has been computed from the $\rm L_{IR}$ and the latter was obtained by fitting the photometry from the Spitzer and Herschel Space Telescopes. For that reason, I am constrained by the resolution afforded by the Herschel SPIRE bands, which is ≈ 20 arcseconds (Griffin et al., 2010). Hence, the $\rm L_{IR}$ reported for the two interacting systems, FLS02 (centres separated by $\approx 4''$) and CDFS1 (separated by $\approx 7''$), corresponds to the entire system and, cannot be calculated for each of the two galaxies independently. Since CDFS1-E is not observed in either continuum or CO(3-2), it is not included in this analysis, and I assume that all the $\rm SFR_{IR}$ arises from CDFS1-W. For FLS02 I measure the total continuum flux from both sources and find each galaxy's fractional contribution to the total flux. This apportions the $\rm SFR_{IR}$ = 380 $\rm M_\odot\ yr^{-1}$ for the system into 353 $\rm M_\odot\ yr^{-1}$ for FLS02-N and 27 $\rm M_\odot\ yr^{-1}$ for FLS02-S.

My motivation for using the $\rm A_{cont}$, i.e. the 3σ cut on the continuum, to calculate the surface densities, is to ensure maximum overlap between star forming regions and molecular gas. If instead I assume a larger area which includes regions with CO(3-2) flux but no continuum emission, the average $\tau_{\rm dep}$ increases. This is due to the CO(3-2) emitting region being larger than the continuum emitting region, as seen in Figure 3.4. Therefore, $\Sigma_{\rm SFR}$ decreases faster than $\Sigma_{\rm mol}$ as the $\rm SFR_{IR}$ stays constant when I make the area greater than $\rm A_{cont}$ (I assumed all $\rm SFR_{IR}$

arises from within the 3σ continuum cut), whereas I increase the measured CO(3-2) flux, even if each additional pixel has a lower surface density than the average I calculated in Table 3.4. Depending on how I select this larger region, e.g. a 3σ or 5σ cut on the CO(3-2) maps (which is equivalent to choosing a lower σ threshold on the continuum maps), the average $\tau_{\rm dep}$ of the sample only increases by at most 40 Myr and therefore my conclusions remain unchanged. The sample is still far below the typical $\tau_{\rm dep}$ of 1 Gyr in normal star forming galaxies (e.g. Leroy et al., 2013, Tacconi et al., 2013).

Similarly, the (de)convolved source size also does not affect my results, as the beam sizes for the continuum and line emission are similar, and any CO(3-2) flux smeared outside $A_{\rm cont}$ will only marginally change the $\Sigma_{\rm mol}$ and $\tau_{\rm dep}$. As a test for this, I assumed that the total integrated galaxy flux (see column 3 in Table 3.4) arises from within $A_{\rm cont}$ and found that the increase in $\Sigma_{\rm mol}$ changes the average $\tau_{\rm dep}$ by less than 40 Myr, demonstrating the robustness of my findings.

3.4.4 Kinematics

Due to its critical density, the CO(3-2) emission line is considered an important tracer of the physical condition and kinematics of the star forming gas (e.g. Wilson et al., 2008, Iono et al., 2009). To fit a kinematic model to the CO(3-2) emission line I used the ^{3D}BAROLO code, which fits a 3D tilted ring model to emission line data cubes (Di Teodoro and Fraternali, 2015). I used the SEARCH algorithm within ^{3D}BAROLO to mask the galaxy from the background. This algorithm is a source finder that works by first making a 5σ cut across all channels and then assumes that all 3σ emission in adjoining channels/pixels are part of the same source (Whiting, 2012).

The model ^{3D}BAROLO disk requires the following parameters: x and y positions, systematic velocity, rotational velocity ($V_{\rm rot}$), velocity dispersion ($\sigma_{\rm gas}$), radial velocity, position angle (PA), inclination, scale height of disk and gas surface density. The best fit model is degraded to the same resolution as the input cube by

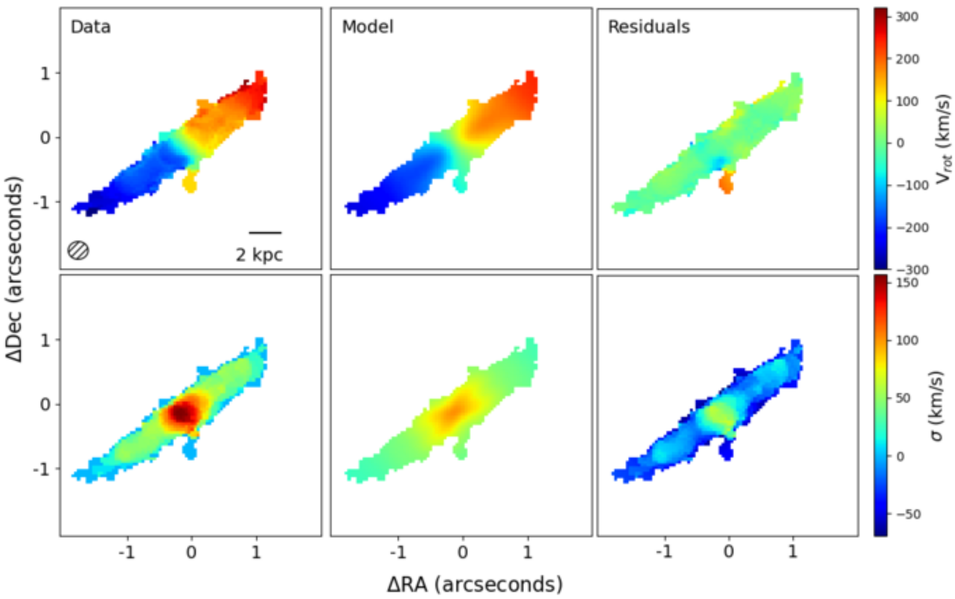

Figure 3.9: Moment maps from the observations and best-fit rotating disk model, found by ^{3D}BAROLO, for CDFS1-W. **Top left:** The observed 1st moment map. **Top middle:** 1st moment map from the best-fit model. **Top right:** The residual map made by subtracting the best-fit model from the observed map. **Bottom left:** The observed 2nd moment map. **Bottom middle:** The best-fit 2nd moment map. **Bottom right:** The residual map for the velocity dispersion. The beam size and physical scale bar are shown in the top left plot. Details of the kinematic modelling are given in Section 3.4.4.

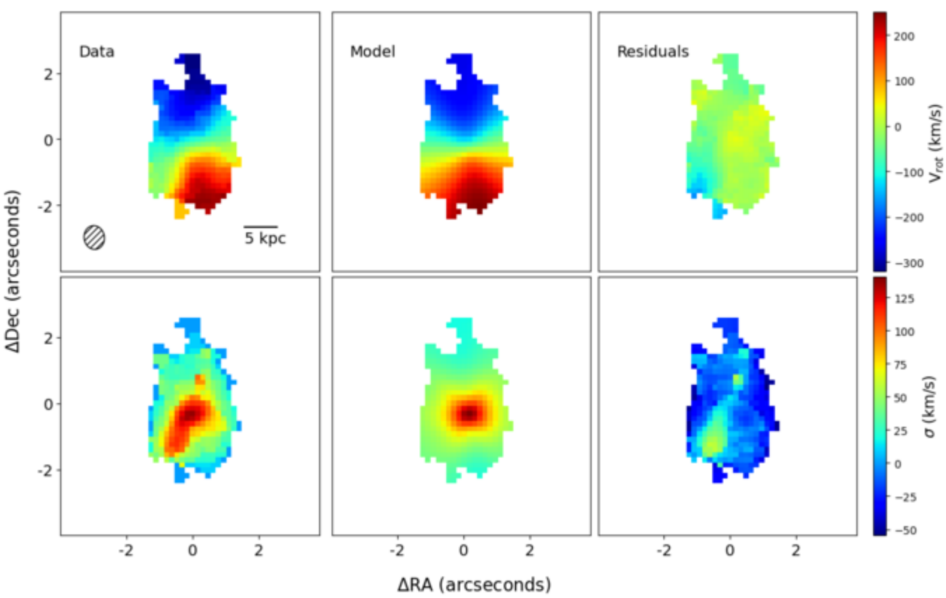

Figure 3.10: Details the same as in Figure 3.9, but for SWIRE5.

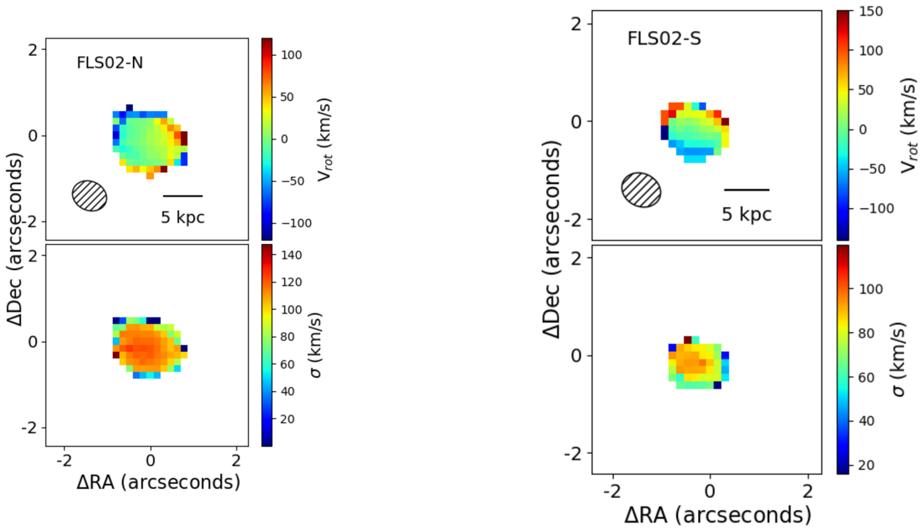

Figure 3.11: Left: The top panels show the 1st moment maps and bottom panels show the 2nd moment maps for FLS02-N. **Right:** Same maps for FLS02-S. A ^{3D}BAROLO model disk could not be adequately fitted to this data due to insufficient resolution. Both galaxies show hints of a velocity structure consistent with a rotating disk, but I need higher resolution imaging, to resolve the velocity dispersion and to have more resolution elements across the disk, to fully analyse the kinematics.

convolving it with a 2D Gaussian that has the same width and PA as the observed synthesized beam of the input cube.

I chose the peak of the continuum as the centre point of each galaxy, set the radial velocity to zero, assumed a thin disk for the scale height, fixed the systematic velocity to zero, i.e. I fit the kinematics in the rest frame of the galaxy, and left the gas surface density to be estimated by the algorithm. I let the code make initial guesses for the PA and inclination, and then left them fixed at that value. The V_{rot} and σ_{gas} were left as free parameters for the code to fit. For the ring size I choose $0.3''$ - $0.4''$ to maximize the number of rings when fitting each source, while also ensuring an adequate number of spaxels within each ring to enable a good fit. All other settings within the algorithm were left as default (see Di Teodoro and Fraternali, 2015 for full details of the model settings).

To determine the best fit model, I compared the output model's 0th, 1st and 2nd moment maps to the observed 0th, 1st and 2nd moment maps. If the PA and inclination greatly differed from the observed moment maps, I manually adjusted

Table 3.6: Kinematic details from the best fit thin disk model of ^{3D}BAROLO

Object	PA[1] degrees	Inclination[2] degrees	V_{rot}(outer ring)[3] km s^{-1}	σ_{gas}(max)[4] km s^{-1}
CDFS1-W	306	79	259 ± 14	42 ± 10
SWIRE5	188	50	346 ± 46	42 ± 6

[1] Position angle of the major axis on the receding side of the galaxy, taken anticlockwise from north. There are no errors as this value was not allowed to vary.
[2] Inclination angle of the galaxy with respect to the observer, with 0° being face-on. There are no errors as this value was not allowed to vary.
[3] The inclination corrected rotational velocity in the outer ring of the best fit ^{3D}BAROLO model.
[4] Maximum velocity dispersion in the best fit ring model of ^{3D}BAROLO.

these values to match those of the observed maps, and re-ran the algorithm to find the V_{rot} and σ_{gas}. In the four targets that have CO(3-2) emission line detections, FLS02-N and FLS02-S show signatures of disturbed disks and were impossible to be adequately fitted with a ^{3D}BAROLO model; whereas CDFS1-W and SWIRE5 show ordered rotation and were fit with a model disk. The observed moment maps, best fit model moment maps, plus the residual maps are shown in Figures 3.9, 3.10 and 3.11, respectively, with the position velocity (PV) diagrams, along the major kinematic axis, of the fitted galaxies shown in Figures 3.12 and 3.13. The best fit parameters that ^{3D}BAROLO was able to estimate/vary are given in Table 3.6. These will be discussed in more detail in Section 3.5.2.

Note that, previous chapters used σ_0 for velocity dispersion and here I am using σ_{gas}. I defined σ_0 as the intrinsic velocity dispersion, which gave a single value for each galaxy. I use σ_{gas} when I can resolve the gradient of the velocity dispersion, so they are measuring slightly different things. If I again assume σ_0 is isotropic and spatially constant across the disk, as I did in Chapter 2, I could find a value for σ_0 by fitting a parametric model to the σ_{gas} and taking the asymptotic value (similar to finding one value for V_{rot} by assuming a parametric model for the rotation curve).

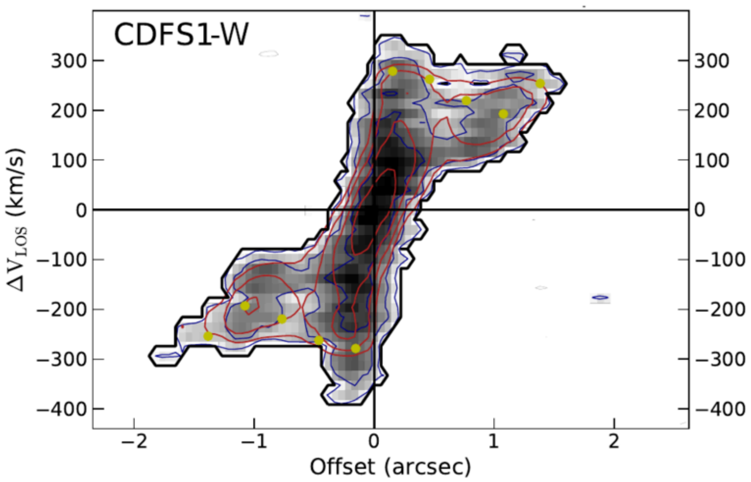

Figure 3.12: Position velocity diagram along the major kinematic axis of CDFS1-W. The black contours show the observed galaxy, with the red overlaid contours representing the model galaxy from ^{3D}BAROLO. The yellow points are the projected V_{rot} calculated for each ring (V_{LOS}) in the model disk. There seems to fast moving gas within the inner $0.5''$ of the disk with projected velocities up to ≈ 400 km s^{-1}, which may be suggestive of an outflow.

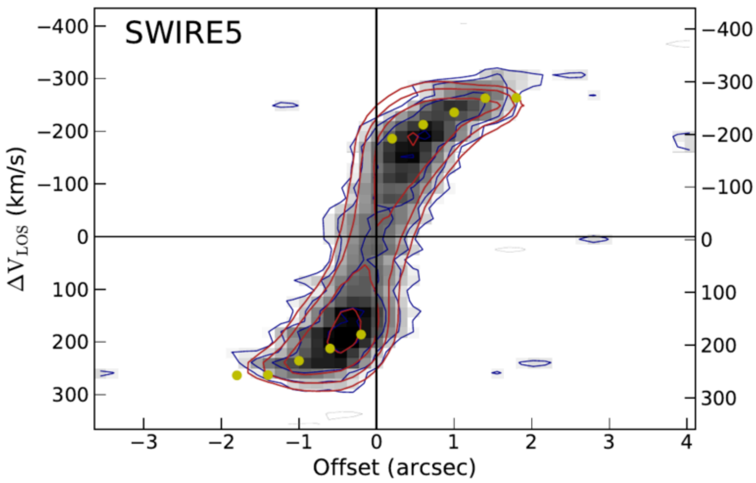

Figure 3.13: Position velocity diagram along the major kinematic axis of SWIRE5, with the black contours show the observed galaxy, with the red overlaid contours representing the model galaxy from ^{3D}BAROLO. The yellow points are the projected V_{rot} calculated for each ring (V_{LOS}) in the model disk.

3.5 Discussion

3.5.1 Molecular Gas and SFR at $0.2 < z < 0.65$

Section 1.4 discussed how distance above the MS is linked to both an increased f_{gas} and to the SFE of the gas. To explore this at intermediate-z, it is instructive to compare my results with other U/LIRG samples, at similar redshifts, from the literature. Combes et al. (2011) presented CO observations for a sample of ULIRGs at $0.2 < z < 0.6$ which were previously detected at 60 μm from IRAS and ISO observations. These ULIRGs are undergoing starbursts and have higher dust temperatures than my sample (T_{dust} = 37 - 60K with an average of 48K), and I will refer to these as 'warm' ULIRGs. Lee et al. (2017) investigated a sample of LIRGs, at $0.25 < z < 0.65$, that have lower luminosities than my sample, with $\log(L_{IR} / L_{\odot}) = 11.2 - 11.6$, and are located on, or just above, the upper boundary of the MS (hereafter referred to as 'cold' LIRGs). They are predominately disk like galaxies, with only three showing irregular morphologies that may be related to an ongoing or past merger.

Molecular gas masses and SFEs have been determined in both the cold LIRG and warm ULIRG samples (Combes et al., 2011, Lee et al., 2017), and these results along with my sample are plotted in Figure 3.14. The SFE in Combes et al. (2011) was presented in units of $L_{\odot}$ / $M_{\odot}$, so I converted it to SFR / $M_{\odot}$ by using the conversion factor of Murphy et al. (2011b). For the α_{CO} conversion factor Combes et al. (2011) choose the value of 0.8 $M_{\odot}$ / (K km s^{-1} pc^2) that is used in local ULIRGs and Lee et al. (2017) applied the Milky Way value of 4.36 $M_{\odot}$ / (K km s^{-1} pc^2). All three samples have similar M_{mol} so the amount of molecular gas available to form stars is not causing the differing L_{IR}. When comparing the SFE of the three samples, it is likely that the increase in L_{IR} is being driven by the SFE of the molecular gas. There is a statistically significant strong positive correlation for log(SFE) - $\log(L_{IR})$ of the three samples, with a Pearson's $\rho = 0.91$ (P-value < 0.001).

These results show that U/LIRGs located in the transition region between starbursts and MS galaxies in terms of dust temperature and L_{IR} also populate the transition region based on SFE, with an average τ_{dep} of 150 Myr compared to $\tau_{dep} \approx 18$ Myr for warm ULIRGs and ≈ 1 Gyr for cold LIRGs. If I expand the comparison to include the slightly higher redshift samples, Freundlich et al. (2019) find an average τ_{dep} of 0.84 Gyr for star forming galaxies at $0.5 < z < 0.8$ (mean $\alpha_{CO} = 4.0$ $M_\odot$ / (K km s^{-1} pc^2) based on using the geometric mean metallicity scaling factor from Genzel et al., 2015) and Combes et al. (2013) measured an average $\tau_{dep} \approx 15$ Myr for starbursts at $0.5 < z < 1$ ($\alpha_{CO} = 0.8$ $M_\odot$ / (K km s^{-1} pc^2)), both of which are consistent with the values at slightly lower redshifts.

Interestingly, Lee et al. (2017) found a stronger correlation between distance above the MS and increased f_{gas}, than between distance above the MS and SFE. With these findings in mind, it is possible, that an increase in just the f_{gas} is sufficient to push a galaxy's SFR above the MS and into the transition region. However, a concurrent increase in SFE is required for a galaxy to approach the starburst regime, and I will investigate what may be triggering this heightened SFE in Section 3.5.2.

Note that the values of SFE from various surveys and samples depends on the methodology of calculating the M_{mol}. Hence, the SFE is implicitly determined by the choice of α_{CO}. As mentioned in Section 3.4.2, local ULIRGs have an α_{CO} up to five times smaller than the Milky Way. If I were to use the low-z ULIRG value of 0.8 $M_\odot$ / (K km s^{-1} pc^2) for CO(1-0) (Downes and Solomon, 1998) the τ_{dep} for my sample would be between 2 - 84 Myr (21 - 84 Myr if I remove SWIRE7). These τ_{dep} values, from the four detections, are all greater than the average of 18 Myr (median of 12 Myr) determined for the warm ULIRGs. Due to the differing ISM conditions and merger stage in my sample compared to the local ULIRGs (M14, PS19) I stress that my choice of $\alpha_{CO(3-2)}(Z)$ is fully justified.

I reiterate that I was conservative in the choice of metallicity scaling factor. As discussed in Section 3.4.2, I picked the scaling factor that gives me the smallest $\alpha_{CO(3-2)}(Z)$ and if I used the exact methodology of Genzel et al. (2015) and take

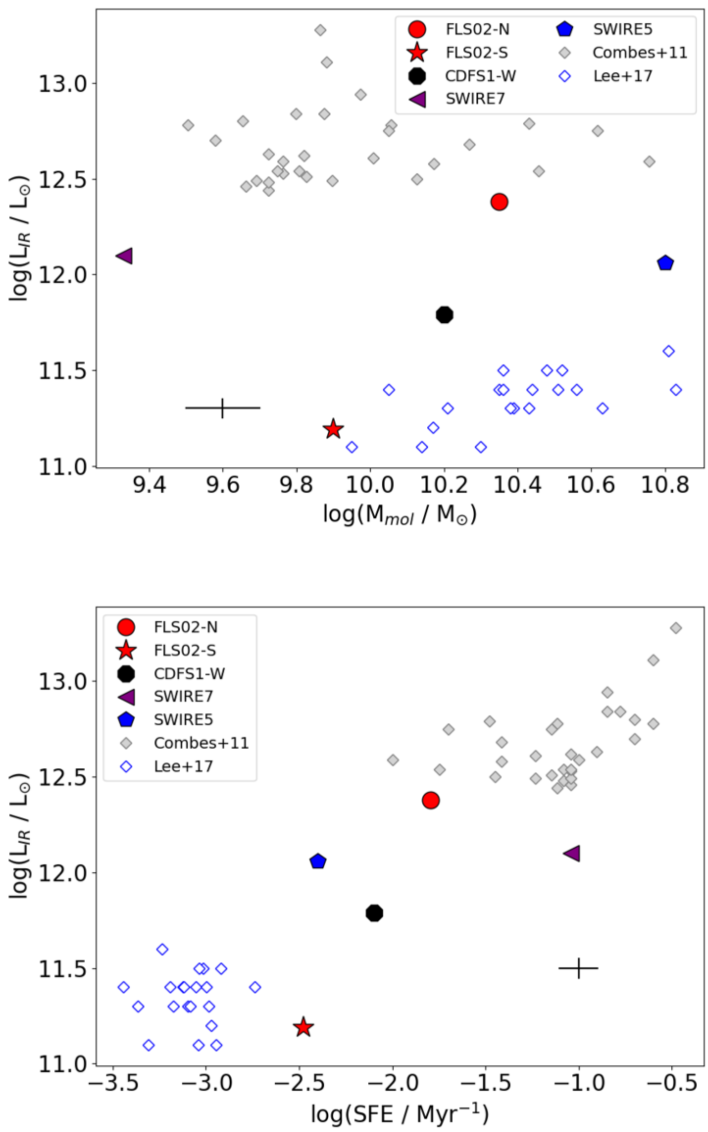

Figure 3.14: Top: The total molecular gas mass versus the IR luminosity, L_{IR}. **Bottom:** The star formation efficiency versus the IR luminosity. This is compared to cold LIRGs (blue diamonds, Lee et al., 2017) and warm ULIRGs (grey diamonds, Combes et al., 2011) from the same redshift. SWIRE7 was undetected in CO(3-2) and its M_{mol} and SFE are estimated from a 3σ upper limit. The cross on both plots show the typical size of the error bars. These plots show that all three samples have similar M_{mol} reservoirs but they are forming stars at different rates of efficiency, indicating that higher SFRs are being driven by increased SFE as opposed to a larger M_{mol} budget.

the geometrical mean of two scaling factors, then I would get a larger M_{mol}, with a corresponding slight increase in τ_{dep}, so the conclusions of this section are robust.

From Figure 3.14 it is clear the cold LIRGs and warm ULIRGs occupy two different areas on the L_{IR} - SFE plane and appear to be bi-modal. Similarly, the local ULIRGs and MS galaxies occupy different regions of the Σ_{SFR} - Σ_{mol} plane, as seen in Figure 3.8. It is possible this bi-modality of the KS relation may be due to selection effects as we move beyond local galaxies. MS galaxies make up an estimated 90% of the star formation density between z = 0 - 2.5 (e.g. Tacconi et al., 2020), so most observations should fall on the locus of star forming galaxies on the KS relation. When studying starbursts at higher-z we are biased towards the brightest targets which are easiest to detect and these bright objects are more likely to be associated with gas rich major mergers. The stochastic nature of mergers and limited time window to catch galaxies in an early interaction stage may mean that we currently do not have a large enough sample of galaxies that are transitioning between low and high SFE. With my sample of U/LIRGs, that straddles the transition region between regular star forming galaxies and starburst galaxies, the SFE seems to show a more continuous change. Shangguan et al. (2019) studied local LIRGs in various stages of interaction and argued that they filled the gap between local MS galaxies and local starbursts, suggesting a gradual change in SFE. However, studies such as Kennicutt and De Los Reyes (2021) tentatively re-affirmed the bi-modality of the KS relation based on local starbursts and MS galaxies. As my sample is small, I cannot draw any strong conclusions either way, but it reveals the necessity of future observations to fully explore this open issue.

3.5.2 Triggers of Star Formation

Both morphology and kinematics provide important information on the mechanism that is triggering star formation within a galaxy. To investigate why my sample of U/LIRGs are less efficient at forming stars than the starburst ULIRGs of Combes et al. (2011) but more efficient than the cold LIRGs of Lee et al. (2017), despite all having similar M_{mol}, requires careful analysis of the kinematics within the targets.

Local starbursts are associated with gas rich major mergers, with minor mergers and disk like morphology becoming more common with decreasing IR luminosity (e.g. Kartaltepe et al., 2010, Bellocchi et al., 2016, Larson et al., 2016). Merger fraction has also been seen to increase with distance above the MS (e.g. Pearson et al., 2019). In terms of the gas, it has been observed locally that both M_{mol} and SFE are increased during galaxy interactions (e.g. Pan et al., 2018).

In terms of the availability of molecular gas to form stars, galaxies can have the same M_{mol} reservoirs but a different SFR due to stabilization by a compact and massive bulge preventing the gas disk fragmenting and collapsing into stars (e.g. Martig et al., 2009). This can be explained in terms of the Toomre Q parameter (Toomre, 1964):

$$Q_{\rm gas} \propto \frac{\sigma_{\rm gas}\kappa}{G\Sigma_{\rm gas}} \tag{3.5}$$

where κ is the epicylic frequency[7] and G is the gravitational constant (a Toomre $Q_\star$ can also be calculated for the stellar disk). A Toomre Q > 1 denotes a stable disk, with Q < 1 and Q $= 1$ indicating an unstable and marginally stable disk, respectively. As the rotational velocity, and hence κ, is a function of the depth of the gravitational potential well, a bulge increases the rotational velocity in the inner disk and in turn pushes Q above 1 (e.g. Martig et al., 2009). If the bulge is formed via an inflow of gas and a concurrent burst of star formation, the $\Sigma_{\rm gas}$ will decrease in conjunction with the increase in rotational velocity, further increasing Q (e.g. Forbes et al., 2014).

Various simulations seem to demonstrate that interactions can boost a galaxy's SFE and transition it into a starburst (e.g. Moreno et al., 2019, Moreno et al., 2021). Interestingly, Segovia-Otero et al. (2022) and Renaud et al. (2022) argue that mergers can only boost the SFR once a galaxy disk has settled into relatively coherent flows as turbulent disks at high-z prevent much of the gas compressing into dense molecular clouds, so it may be intermediate-z is the best epoch to explore

[7] $\kappa = \sqrt{r\frac{d\Omega}{dr} + 4\Omega^2}$, where $\Omega(r)$ is the angular velocity at radius r.

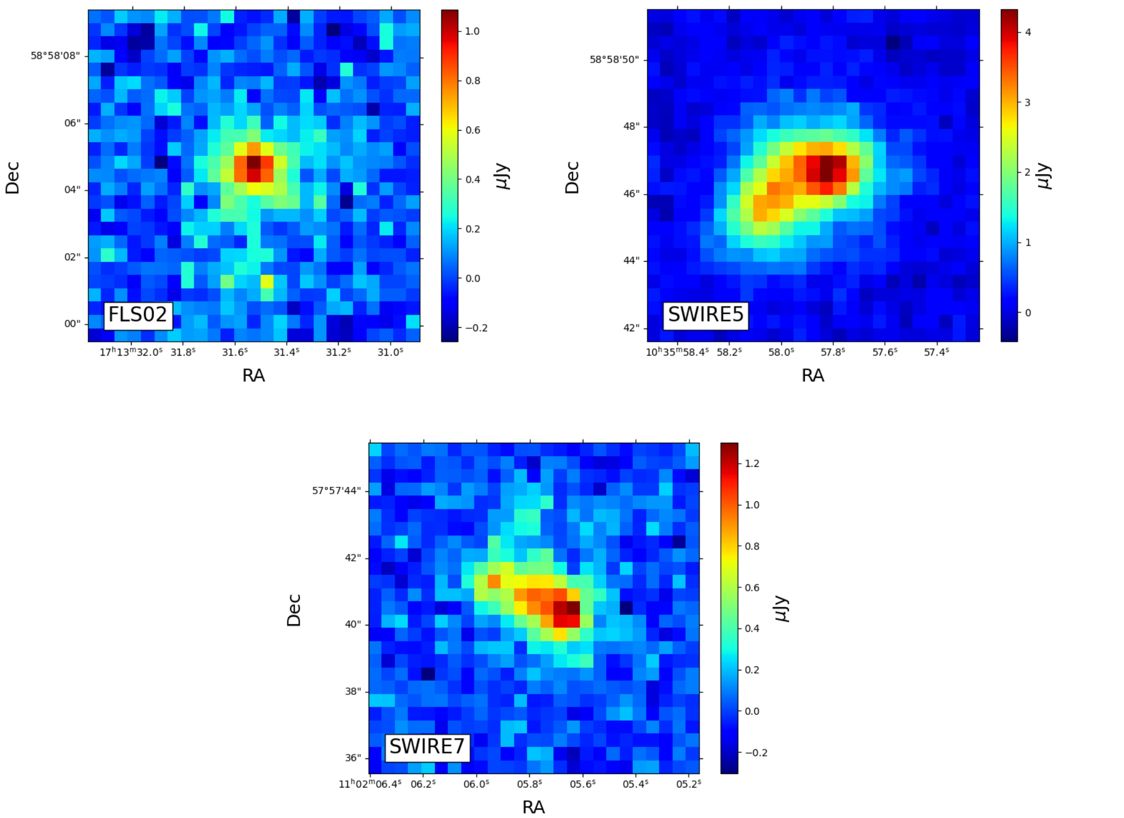

Figure 3.15: SDSS I-band (rest frame optical emission) imaging for FLS02 (**top left**), SWIRE5 (**top right**) and SWIRE7 (**bottom**). The pixel scale is $\sim 0.4''$, which corresponds to a physical scale of ~ 2 kpc. No sigma cut has been made on these images due to the relatively poor S/N. FLS02-S is undetected, and both SWIRE5 and SWIRE7 show an asymmetry consistent with interacting galaxies.

the transition between MS and starburst. With these results in mind, I try to determine how morphology and merger status is affecting SFR and SFE in my sample. I supplement the ALMA and NOEMA observations with Sloan Digital Sky Survey (SDSS, Blanton et al., 2017) I-band imaging (rest frame R-band), which has a pixel scale of $\sim 0.4''$. CDFS1 is not covered by SDSS. These I-band images are shown in Figure 3.15

CDFS1-W

Despite CDSF1-W being separated by only ≈ 30 kpc from CDFS1-E, it has a clear rotating disk structure with little signs of disturbed rotation, so it must be at an early stage of interaction (see Figure 3.9). This source has the lowest $\mathrm{SFR_{IR}}$

in my sample with 91 $M_{\odot}$ yr^{-1}, but does have the most compact star forming region with all obscured star formation located within the central $\approx$ 3 kpc of the disk. No obscured star formation is arising from the outer disk, therefore I suggest that the galaxy undergoes inside out star formation (Tacchella et al., 2018). There is a signature of fast moving gas located in the central regions where star formation is taking place, as shown in the position velocity diagram in Figure 3.12 with gas approaching 400 km s^{-1}. Outflows are ubiquitous in local U/LIRGs (e.g. García-Burillo et al., 2015, Pereira-Santaella et al., 2018) and follow-up high spatial resolution observations of CDFS1-W are needed to confirm if this fast moving gas is indeed an outflow.

Interestingly, if the CDFS1 system was observed only in CO(3-2) I would have classified CDFS1-W as an isolated galaxy, as CDFS-E is undetected by ALMA. The 0th, 1st and 2nd moment maps (Figures 3.4 and 3.9) show a relatively symmetric disk with ordered rotation and a V_{rot} / $\sigma_{gas} > 6$, so all signatures point towards an isolated disk secularly forming stars. Optical images identify CDFS-E and prove that the CDFS1 system is a pair of interacting galaxies, highlighting the importance of multi-wavelength observations in getting an accurate picture of a galaxy system. Chapters 4 and 5 will explore this topic in more detail.

FLS02

The FLS02 system has the largest SFR_{IR} in my sample, at 380 $M_{\odot}$ yr^{-1}. The velocity fields of both sources seem to show a disturbed velocity gradient, with an unresolved velocity dispersion profile (Figure 3.11). The pair of galaxies are separated by $\approx$ 20 kpc and the peak of the emission lines are offset by $\approx$ 150 km s^{-1}. This implies a more advanced merging stage than CDFS1. FLS02-N also has the shortest depletion time, τ_{dep} = 62 Myr, in the sample, which is consistent with it being in a later interaction stage when compared to the other targets. Yet, both galaxies in FLS02 evince signatures of being rotating disks, which may explain why they are located in the transition region and do not yet have the SFE of a starburst. Higher spatial resolution observations are needed to properly probe the velocity structure and determine what is triggering the high SFR.

SWIRE5

SWIRE5's morphology and kinematics are an interesting case, as it appears to be an isolated disk with a clear velocity gradient along a single axis (Figure 3.10). But, inspection of both the 0th, 1st and 2nd moment maps and the residual maps from the best fit disk model have an excess of CO(3-2) flux, southeast of the galaxy centre, than would be expected from a rotating disk (see Figure 3.16) causing an irregular morphology. This excess flux is co-spatial to a secondary peak in the continuum, a region of high velocity dispersion and a small deviation between the modelled and observed velocity field. If I select a region similar in size to the second peak in the continuum, as plotted in the bottom row of Figure 3.16, there seems to be a velocity gradient along the major axis, when compared to the best fit model disk. The I-band SDSS image (Figure 3.15) has a similar asymmetry to the CO(3-2) map with a possible second nucleus, consistent with the two peaks observed in the sub-mm continuum.

PS19 made moment maps and fit kinematics to the SWIRE5 Hα emission line (see Figure 3.3). The 0th moment map of the Hα line does not display a similar asymmetry in the flux map, but the velocity dispersion shows similar high values in the south-east region of the galaxy. These observations were taken by the SWIFT telescope and due to the poor seeing the FWHM for SWIRE5 was 2.7$''$, which gives a spatial resolution of $\sim$ 14 kpc. As the 2 peaks observed in the continuum are $\sim$ 8 kpc apart, I cannot say whether the Hα emission has a similar distribution to the NOEMA sub-mm continuum and CO(3-2) emission and the SDSS I-band emission.

This disturbance may be an unresolved region of clumpy star formation caused by disk instabilities (e.g. Behrendt et al., 2019) or another possibility is that we are seeing interacting galaxies hiding behind each other and appearing as one, such as that potentially uncovered in optical images of a low-z system in Mazzilli-Ciraulo et al. (2021) . The possible hidden merger in Mazzilli-Ciraulo et al. (2021) was taken

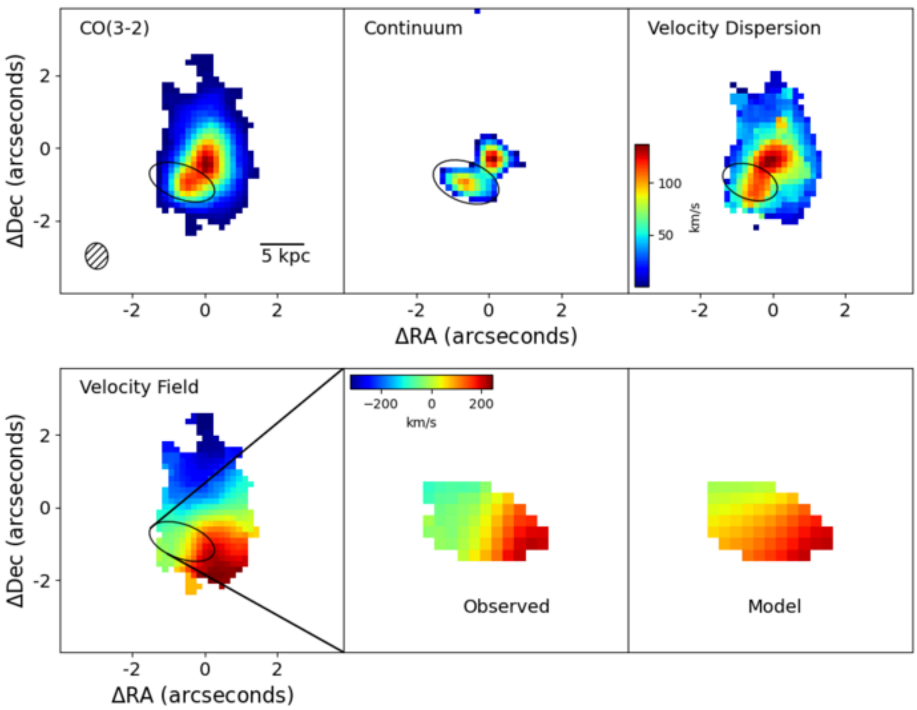

Figure 3.16: SWIRE5 shows an excess CO(3-2) flux (**top left**), southeast of the galaxy centre, than would be expected from an isolated disk as indicated by the black ellipse. This corresponds to a second peak in the continuum (**top middle**) and a larger than expected gas velocity dispersion (**top right**). There is also a slight deviation between the observed velocity field (**bottom left & middle**) and the modelled velocity field (**bottom right**). Without higher spatial resolution data, it is not clear what is causing this asymmetry. Possibilities include a hidden minor merger or a large disk instability.

from a sample of galaxies with double peak emission line profiles (Maschmann and Melchior, 2019, Maschmann et al., 2020) some of which have been put forward as harbouring hidden minor mergers. SWIRE5 has an asymmetric double peak line profile, as shown in Figure 3.6, which is additional circumstantial evidence for a hidden minor merger. Conversely, the $\tau_{\rm dep}$ of 251 Myr suggests that if there is a hidden minor merger it has not boosted the SFE of the gas, compared to the known interacting galaxies in my sample, although the $\tau_{\rm dep}$ is much higher than isolated disks, such as the LIRGs of Lee et al. (2017) with typical values of 1 Gyr. In either eventuality, this disturbance is co-spatial with a region of ongoing obscured star formation, so whatever underlying mechanism is causing the asymmetry in the CO(3-2) emission is likely triggering the star formation.

SWIRE7

Although undetected in CO(3-2), SWIRE7 does have an SDSS I-band observation, as shown in Figure 3.15, that helps infer what may be triggering its huge SFR (190 $M_\odot$ yr^{-1}). The rest frame optical continuum, in the I-band, appears to have an asymmetric flux, with an elongation along the east-west direction, a strong peak in the west and hints of a second peak in the east. The west peak corresponds to the sub-mm emission observed by NOEMA. None of the SDSS bands have the required S/N or spatial resolution to explore this further. The rest frame optical continuum from SWIFT and sub-mm continuum from NOEMA also don't have the requisite spatial resolution to add further details, but the SDSS morphology is strongly suggestive of an ongoing interaction, which is also consistent with SWIRE7 having the second highest SFR in my sample. Interestingly, PS19 found a V_{rot} / $\sigma_{gas} \sim 3$ for this galaxy, so if it is a merger, it suggests that applying the dynamical ratio to seeing limited data can miss an ongoing merger.

To conclude, all galaxies in the intermediate-z sample display at least partial signatures of being interacting and/or deviate from a model isolated disk galaxy, which may explain why their SFE is greater than cold LIRGs (predominately disk like galaxies based on morphology, as discussed in Lee et al., 2017) at similar redshifts. None of the four appear to reveal signatures of major mergers, so it is likely that the gradual rise in SFE, from the least luminous LIRGs to the highest luminosity ULIRGs at intermediate redshifts, is associated with the degree of isolation versus interaction.

3.5.3 CDFS1-E & SWIRE7 Non-Detections

The next most abundant molecule in a galaxy after H_2 is CO, whose low rotational excitation energy and critical density have made it the traditional M_{mol} tracer (e.g. Carilli and Walter, 2013, Combes, 2018). However, CO can fail to track the total H_2 reservoir in certain environments, such as the metal poor ISM of dwarf galaxies, where the requisite metals are not available to shield the CO gas from UV photons

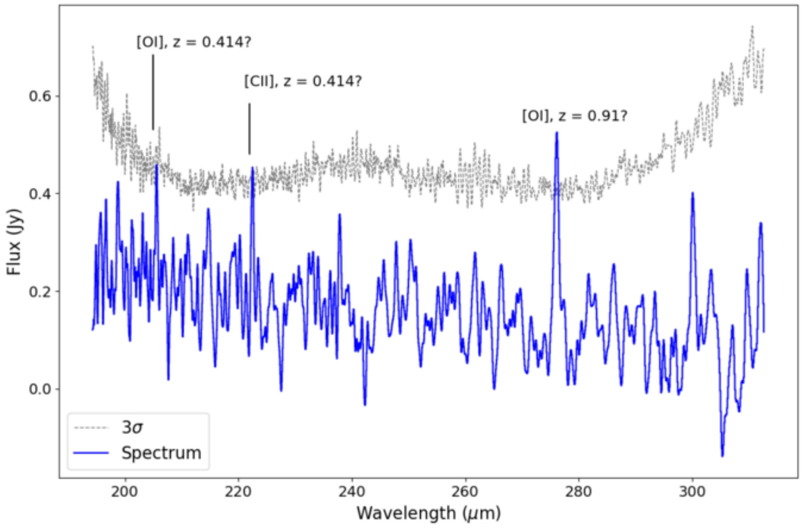

Figure 3.17: The spectrum of SWIRE7 taken by SPIRE-FTS. This galaxy was undetected in CO(3-2) but has a robust detection of an emission line at 927.8 nm in PS19 which is assumed to be the Hα line at z = 0.414 (see Section 3.5.3 for full details). There are marginal 3σ detections at 222 and 205 μm, which agree with both [CII] 158 μm and [OI] 145 μm lines at z = 0.414, corroborating PS19's Hα detection. But the possible line at 277μm fits with [OI] 145 μm at z = 0.91 and PS19's detection being Hβ, albeit it is unlikely a strong Hβ detection would be observed in a ULIRG at z = 0.91.

leading to photo-dissociation (e.g. Papadopoulos et al., 2002, Wolfire et al., 2010). H_2 has a greater capacity for self-shielding from UV photons so a non-negligible amount of molecular gas may be available to form stars, despite being deficient in CO, and this has been dubbed CO-dark gas (e.g. Krumholz et al., 2011).

Although CDFS1-E is observed in Hα in PS19, it is not detected in either CO(3-2) or continuum. This galaxy has the lowest metallicity amongst all the galaxies in PS19, so it is possible that CDFS1-E is a CO-dark dwarf galaxy, and that the large L_{IR} is arising entirely from CDFS1-W, which is the assumption I made when calculating the SFE of CDFS1-W.

SWIRE7 poses more of a challenge as it has a strong ($\approx 20\sigma$) detection in the continuum despite having no CO(3-2) detection. PS19 has a robust detection of an emission line at 927.8 nm with the most likely identification being Hα at z = 0.414. Having re-examined the SPIRE-FTS spectrum presented in M14 there are possible 3σ detections of both [CII] 158 μm and [OI] 145 μm lines at the expected wavelength, observed at 222 and 205 μm respectively, as shown in Figure 3.17. The other possibility is that PS19's observed emission line is Hβ at z = 0.91, with the $\approx 3\sigma$ peak at 277μm being the [OI] 145 μm line. This does not fit with the 222 and 205 μm lines and a strong detection of Hβ in a z = 0.91 ULIRG seems unlikely. Also, the magnitude of SWIRE7 in the five SDSS bands appears similar to FLS02, and the SDSS database gives it a photometric redshift of 0.4 - 0.6 [8], which is further circumstantial evidence for the redshift determination of z = 0.414.

It may be that this galaxy has a metal poor ISM, corroborated by the lack of [NII] 6583 Å detection in PS19. However, the SFR_{IR} of 190 $M_\odot$ yr^{-1} does not agree with a classification as a dwarf galaxy. Alternatively, the continuum detection may be due in part to thermal free-free emission from electrons scattering in the HII regions (e.g. Condon and Ransom, 2016), as opposed to being the tail of the Rayleigh-Jeans continuum, which would partly explain the 20σ continuum detection despite being a metal poor object.

Recently, possible cases of CO-dark gas have been observed in two intermediate-z LIRGs which have been detected in [CI] and dust continuum but are deficient in CO (Dunne et al., 2021). Although I do not have a [CI] detection, if the marginal detection of [CII] is correct then the galaxy may not be carbon deficient but may have some mechanism in the ISM that is rapidly dissociating CO into [CI] and [CII] (e.g. Bisbas et al., 2017).

If SWIRE7 is a true CO-dark ULIRG, and not a galaxy whose redshift is incorrect, then it poses a challenge to the understanding of the ISM within dusty star forming galaxies, so follow up observations are required.

3.6 Conclusion

In summary, I have analysed CO(3-2) observations, from NOEMA and ALMA, of four systems located at $0.28 < z < 0.44$. The sample straddles the transition region between regular star forming galaxies and starbursts, and also fills the gap between previous studies of low luminosity LIRGs and high luminosity ULIRGs at

[8] http://skyserver.sdss.org/dr7/en/tools/explore/obj.asp?id=587732581518410407

this epoch. Due to their unique location, I was able to explore both the cosmic evolution of star formation and the apparent bi-modality of MS and starbursts. The main results of this chapter are:

1. My sample of intermediate-z U/LIRGs fall between the loci of MS galaxies and starbursts on the KS relation, suggesting that galaxies in the transition region between starbursts and MS galaxies also populate the transition region on the $\Sigma_{\rm CO}$ - $\Sigma_{\rm SFR}$ plane.

2. The sample have $\tau_{\rm dep}$ on the order of 100 Myr, and compared to U/LIRGs at a similar redshift, the depletion time is lower than 'cold' LIRGs, with a $\tau_{\rm dep}$ on the order of 1 Gyr, but higher than 'warm' starburst ULIRGs, with $\tau_{\rm dep}$ of approximately 10 Myr. All three U/LIRG samples have similar $M_{\rm mol}$ budgets, and a strong positive correlation between log($L_{\rm IR}$) and log(SFE) suggests it is an increasing SFE that is driving the increasing SFRs, as opposed to larger $f_{\rm gas}$.

3. Only four of the six targets had a CO(3-2) detection: CDFS1-W, FLS02-N&S and SWIRE5. The two non-detections, CDFS1-E and SWIRE7, were previously detected in optical images and Hα emission. While CDFS1-E may be a metal poor dwarf galaxy, SWIRE7 may be a CO dark ULIRG which would challenge our understanding of the ISM in dusty star forming galaxies.

4. The location of my sample on the log($L_{\rm IR}$) and log(SFE) plane points to a gradual change in SFE as a galaxy transitions between MS and starburst. All of my sample are either confirmed interacting pairs or exhibit possible signatures of merging. It may be that interactions are necessary to boost the SFR into a starburst phase, as higher $f_{\rm gas}$ may not be sufficient.

In summary, my sample of transitioning U/LIRGs fill the gap between main sequence galaxies and starbursts on the KS relation. If the suggested bi-modality in star forming galaxies is correct, then this research may indicate that, while a higher $f_{\rm gas}$ is a necessary condition to transition, it also requires a boost to SFE; and it appears this rise in SFE is being driven by mergers and interactions. Chapter 5 will touch on this topic using mock observations of a minor merger and discuss how SFE changes throughout three snapshots.

I also demonstrated that sampling the full range of L_{IR} between 10^{11} - 10^{13} $L_\odot$ is necessary to understand the U/LIRG population at a given epoch. Prior to my sample, the intermediate-z U/LIRGs occupied two separate regions of the SFE versus L_{IR} parameter space. While my sample is small, it fills in the gap and hints that the U/LIRG population may have a continuous SFE.

Finally, my sample sheds some more light on the gradual evolution in the properties of U/LIRGs across cosmic time. We see no signature of major mergers, albeit the sample is small. But all appear to be in early stages of interaction, whereas U/LIRGs with a similar luminosity range at cosmic noon, can show observational signatures of being isolated, as discussed in Chapter 2.

We know what we are, but know not what we may be.

—William Shakespeare *Hamlet*

4

On the Viability of Determining Galaxy Properties from Observations

Contents

This chapter is adapted from: K. Grisdale, L. Hogan, D. Rigopoulou, N. Thatte, M. Pereira-Santaella, J. Devriendt, A. Slyz, I. García-Bernete. *On the Viability of Determining Galaxy Properties from Observations I: Star Formation Rates and Kinematics*, 2022, MNRAS, 513, 3906.

4.1 Introduction

Observing photons from distant galaxies has been our primary means of gaining insight into the high-z universe, and in recent years this has been supplemented with the growth of increasingly detailed simulations. Invariably, all physical properties derived from observation, such as those found in the previous chapters, require further assumptions such as a conversion factor, e.g. the SFR and M_{mol}, or fitting models to the observed flux, e.g. T_{dust} from the FIR fluxes, or the $M_\star$ found by spectral synthesis modelling. Key to translating observations into knowledge of the high-z universe is determining how accurately a galaxy's properties are encoded into the emission and absorption lines and if high-z spectra can be modelled using the assumptions and calibrations taken from the local universe.

One method of testing this is to create mock observations of galaxies and check if the tools astrophysicists use to extract information can recover the underlying physics that went into producing the simulated galaxies. In this chapter, I will utilize Light from Cloudy Added to RAMSES (LCARS), a new post-processing pipeline introduced in Grisdale et al. (2021), that adds photons to RAMSES based simulations. I will use LCARS, combined with a HARMONI mock observation simulator, to make mock IFS cubes of the Hα and Hβ emission lines and check how much of the underlying properties of the simulated galaxy I can recover.

Another motivation for this research is to test observables in the high-z universe in preparation for the unprecedented spatial resolution that HARMONI will offer. Much of the current high-z observational signatures, such as V_{rot} / σ_{gas}, have been applied to lower spatial resolution, so we cannot assume the same tools are appropriate to use on much higher spatial resolution data, and it may be that they break down when used on HARMONI observations. HARMONI will open a new window to the high-z universe, and mock observations are an excellent tool to study how we can use observables to discriminate between different models, and stages of a galaxy's evolution, at cosmic noon.

For full disclosure, all the simulation work is entirely Kearn Grisdale's, along with the properties of the galaxy extracted directly from the simulation. The post-LCARS mock observations and analysis in this chapter is my own work, and our joint results have been published in Grisdale et al. (2022), hereafter G22. I will provide the necessary details of the simulation in order to follow my research, but I will point to G22 throughout if the reader would like further information. Some figures in this chapter, which compare my data with the simulation, are taken directly from G22. These have a slightly different syntax to that used in this thesis. This difference is explained in the relevant captions, but the meaning should be clear, e.g. G22 uses v_θ instead of V_{rot}.

4.2 HARMONI

The next generation of near IR spectrographs mounted on the focal plane of the new 30+ meter class of telescopes will provide unequalled spatial resolution of galaxies at cosmic noon. HARMONI (Thatte et al., 2014) is the single-field optical and near IR spectrograph that will be mounted on the Extremely Large Telescope (ELT), and will be located in Cerro Armazones Antofogasta in Chile. The $\sim$ 39 m mirror, 0.45 - 2.45 μm wavelength coverage, and adaptive optics (AO) assisted observations will allow rest frame optical and UV emission to be probed at physical scales $\sim$ 100 pc at z $\sim$ 2. The range of spaxel scales are 4, 10, 20 and 30 $\times$ 60 mas, with a FOV up to 9$''$ for the largest spaxel scales. The spectral resolution ranges from R = 3500 - 20000, depending on the wavelength. The spectral resolution and spaxel scales, along with AO pushing the spatial resolution close to the ELT diffraction limit of $\sim$ 10 mas, will allow the dynamical status of the high-z ISM to be probed in unparalleled resolution. Observing the internal structure of high-z galaxies on these scales will allow us to study star forming clumps and resolved stellar populations in great detail and will enhance our understanding of cosmic star formation and galaxy evolution.

In preparation for this upcoming instrument, a quantitative HARMONI observation simulator was developed to help put together key science cases. HSIM[1] (Zieleniewski et al., 2015) allows users to probe how astronomical objects will look when observed with HARMONI, across a variety of integration times, atmospheric conditions, spaxel scales, PSFs, gratings and detector systematics. The simulator takes an input FITS cube of an astronomical object and adds detailed models of the sky, a wavelength dependent PSF, telescope and instrumental effects to produce a realistic fully reduced and calibrated mock IFS cube (more details are given in Appendix A.2).

4.3 Data

4.3.1 NewHorizon

NewHorizon (Dubois et al., 2021) is a high resolution hydrodynamical cosmological simulation based on the adaptive mesh refinement (AMR) code RAMSES (Teyssier, 2002). NewHorizon is a re-simulation of a sub-volume of Horizon-AGN (Dubois et al., 2014), which is a sphere of 10 Mpc co-moving radius. AMR allows new levels of refinement to be unlocked as the simulation undergoes cosmological expansion, in order to keep the spatial resolution close to 35 pc.

A full description of the initial conditions and the treatment of SFR, metallicity, black holes, AGN and feedback within the simulation can be found in Dubois et al. (2021), and also in Park et al. (2019), Grisdale et al. (2021) and G22. The salient details are that the simulation includes an equilibrium chemistry model for H and He that allows radiative cooling of the primordial gas down to $\sim 10^4$ K. Metal enriched gas (metals in the simulation are treated as a single entity, Z, and this is not split into its constituent metals) can cool down to 0.1 K using cooling rates tabulated from Dalgarno and McCray (1972) and Sutherland and Dopita (1993). Stars can form out of this gas when a hydrogen density of > 10 H cm^{-3} is reached and the rate of star formation follows the Schmidt law (Schmidt, 1959), with an efficiency determined from the local gravo-turbulent conditions (Kimm et al., 2017).

[1] https://harmoni-elt.physics.ox.ac.uk/Hsim.html

The star particles have a $M_\star \geqslant 10^4$ $M_\odot$ and follow a Chabrier IMF (Chabrier, 2003) with a mass range of 0.1 - 150 $M_\odot$. Dark matter is modelled as collisionless particles with a mass resolution of 10^6 $M_\odot$. When star particles reach 5 Myr old they undergo a supernova explosion and return 31% of the $M_\star$ of a star particle, and a metal yield of 0.05, back into the surrounding ISM (Kimm and Cen, 2014). Supernovae also input momentum into the surrounding ISM whose value is $\propto 10^5$ km s^{-1} $\times$ $(10^{51})^{16/17}$ erg and scaled as function of metallicity and hydrogen density (Thornton et al., 1998 and Geen et al., 2016). Massive black hole particles are included in the simulation, which have a seed mass of 10^4 $M_\odot$, and form in cells when both gas and stellar densities are above the threshold for star formation, the stellar velocity dispersion is above 20 km s^{-1} and the particle is at least 50 co-moving kpc away from another massive black hole. The black hole particles grow at the Bondi - Hoyle - Lyttleton rate (see Equations 5 and 6 in Dubois et al., 2021) and by black hole coalescence when they get closer than four spatial resolution elements ($\sim$ 150 pc). Mass, momentum and energy feedback is also injected into the surroundings via jets (radio mode, Dubois et al., 2010) or thermal energy (quasar mode, Teyssier, 2002) and the power is a function of the accretion rate.

Importantly, on the fly radiative transfer is not included in NewHorizon, and post-processing techniques need to be applied to study the spectra of galaxies within the cosmological simulation.

4.3.2 LCARS

LCARS is a new post-processing pipeline, introduced in Grisdale et al. (2021), that adds photons to RAMSES based simulations. Full details can be found in Grisdale et al. (2021) and GR22, and an overview of the pipeline is discussed in this section.

LCARS takes the physical properties of the stars, gas and metallicity of the NewHorizon simulated galaxy and adds radiative transfer simulations from the spectral synthesis code CLOUDY (Ferland et al., 2013) to determine the shape and magnitude of emission lines within the galaxy. CLOUDY runs the radiative transfer by modelling the ionization, chemical, and thermal state of gas and dust

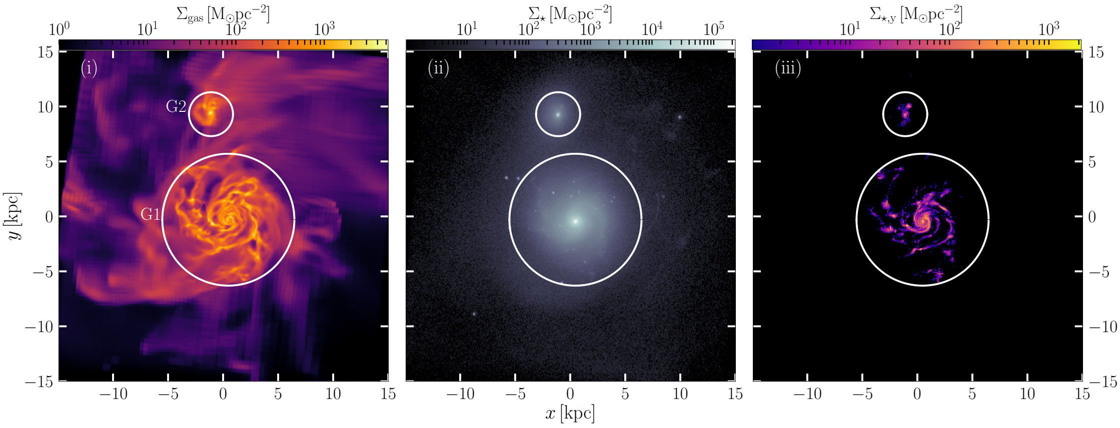

Figure 4.1: Surface density maps taken directly from NewHorizon. The large circle shows the extent of the primary galaxy (g1), with a radius of 6kpc, while the small circle denotes the minor galaxy partner (g2), with a radius of 2 kpc. **Left:** The gas surface density. **Middle:** Stellar surface density. **Right:** The surface density of stars < 10 Myr old. This figure is taken from G22 which use uppercase G for the galaxy, i.e. G1 instead of g1.

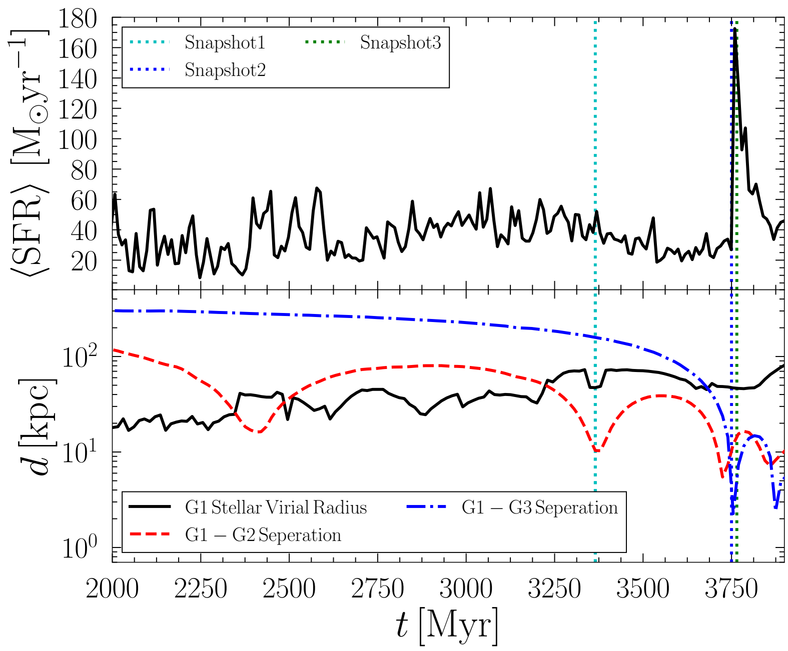

Figure 4.2: Top: Evolution of g1's mean SFR per 10 Myr bin. **Bottom:** Evolution of the separation between g1 and its two satellite galaxies (described in Chapter 5). The dashed vertical lines indicate the three snapshots taken of this galaxy and input into LCARS, with snapshot 1 being analysed in this chapter (snapshot 2 and 3 are discussed in Chapter 5). This figure is taken from G22 which use uppercase G for the galaxy, i.e. G1 instead of g1.

Table 4.1: Properties of the galaxy selected from NewHorizon.

Object	g1[1]	g2[2]
$\log(M_\star / M_\odot)$[3]	10.7	9.4
$\log(M_{gas} / M_\odot)$[4]	10.3	9.3
$\log(M_{baryon} / M_\odot)$[5]	10.9	9.6
$\log(M_{DM} / M_\odot)$[6]	10.7	9.3
$\log(M_{total} / M_\odot)$[7]	11.4	9.8
SFR [$M_\odot$ yr^{-1}][8]	38	2
Radius (kpc)	6	2

[1] Main galaxy.
[2] Minor companion.
[3] Stellar mass.
[4] Gas mass.
[5] Baryonic mass.
[6] Dark matter mass.
[7] Total mass.
[8] Average star formation rate in the previous 10 Myr.

that is exposed to a radiation field (AGN, star, etc.). It then outputs an estimate of the emission lines plus the underlying continuum.

All stars within a given cell of the simulation are combined into a single 'super' star particle located at the centre of each cell. The SED of the super star particle is found by summing the individual SEDs of each constituent star particle, employing the SED templates of STARBURST99 (Leitherer et al., 1999). A unique CLOUDY simulation is run for each super star particle, and the emission lines and continuum output by CLOUDY are used to construct a spectrum for each cell. A background radiation field that mimics the cosmic radio to X-ray background is also included in each CLOUDY simulation.

To determine the shape of the emission lines, LCARS assumes the intensity is distributed as a Gaussian, with the area of this Gaussian equalling the total line intensity output by CLOUDY. The width of each emission line is determined by a combination of the thermal motions and gas dispersion within the cell, taken directly from NewHorizon. The peak wavelength of the emission line is determined by the bulk line of sight velocity of the gas within the cell. This line of sight velocity is imposed by a hypothetical observer, whose position is a free parameter in LCARS, i.e. any PA and inclination can be chosen by the user, depending on their science case.

If the Strömgren sphere for a super star particle in a given cell is larger than the cell size, then the fraction of the Strömgren sphere that overlaps with the neighbouring cells is added to the neighbouring cells' radiation fields to mimic diffuse emission within a galaxy. For cells that do not contain stars, the gas properties are combined with an incident radiation field set by the cosmic background radiation field and any diffuse emission from neighbouring cells.

Dust is added to LCARS spectra by assuming a constant dust to gas phase metallicity ratio (Richardson et al., 2020). This ratio is a free parameter specified by the user, so can be scaled depending on whether the user wants to simulate a moderate or extreme dust attenuation. Extinction is then applied to each cell's spectrum via:

$$I_{\mathrm{E}}(\lambda) = I(\lambda) e^{-\frac{A_{\mathrm{V}} E(\lambda)}{2.5}} \tag{4.1}$$

where I_{E} is the extinction corrected intensity, I(λ) is the intensity calculated by CLOUDY, E(λ) is the dust extinction curve of Fitzpatrick (1999) and A_{V} is calculated by

$$A_{\mathrm{V}} = 1.086 \frac{3 f_{\mathrm{d}} \Sigma_{\mathrm{Z}} Q_{\lambda}}{4 \rho_{\mathrm{d}} \sqrt{a_1 a_2}} \tag{4.2}$$

where Σ_{Z} is the column density of metals between the observer and emitting cell, taken from NewHorizon, $Q_{\lambda} = 1.5$ is a constant extinction coefficient, $\rho_{\mathrm{d}} = 3$ g cm^{-3} is the typical density of a dust particle, $a_1 = 0.005$ μm is the smallest size of a dust grain, $a_2 = 1$ μm is the largest size and f_{d} is the ratio of dust to gas phase metallicity discussed above (see Richardson et al., 2020 for further details).

The final spectrum is produced by summing the spectra, having been corrected for extinction, in all cells along the chosen line of sight. Finally, the spectra are redshifted to match the redshift of the chosen galaxy within NewHorizon, and the flux is scaled to the appropriate luminosity distance. The final products delivered by the pipeline also include a cube without dust extinction, allowing users to explore the impact, if any, dust has on the observed spectral lines of their chosen target.

It should be highlighted that although a screen model is used for dust, each cell within the simulation has its own unique screen of dust. This is because the dust screen is a function of the column density of metallicity (Equation 4.2), and each cell in the simulation has a different column density of metals between the cell and the observer. For example, in a given line of sight a cell at the back of a galaxy goes through a larger column density of metals compared to a cell at the front of the galaxy. Likewise, different lines of sight have different metallicity column densities. As each cell in NewHorizon has a metallicity value, LCARS can capture spatial variations in the density of dust at a scale of $\sim$ 35 pc, if the highest level refinement in NewHorizon is selected. Therefore, the method mimics a mixed dust model, and LCARS can accurately model how the geometry of the galaxy is affected by dust extinction.

Although there are black holes in the cosmological simulation, we do not include any SED templates from AGN in this run of LCARS. All the emission lines in the current iteration of LCARS arise from radiation fields produced by stars, and the only effect black holes have on the spectra is the impact they have on the bulk velocity and velocity dispersion in each cell of the simulation, which in turn determines the shape of the emission lines in each cell, as discussed above.

LCARS can currently calculate IFS cubes for over 80 emission lines simultaneously, and it outputs line only cubes, continuum only cubes and complete cubes, which are line plus continuum.

4.3.3 Mock Observations

We selected a galaxy from NewHorizon that was a close match to the SFR, $M_\star$, redshift and dynamical status of galaxy o5 in Chapter 2 (see Table 4.1). Galaxy o16 is also a close match in SFR and $M_\star$ (see Figure 4.3) but this object was found to be dispersion dominated in Section 2.4.4 and our aim for this project was to study a high-z analogue to a disk galaxy (V_{rot} / $\sigma_{gas} > 1$). The simulated galaxy is on

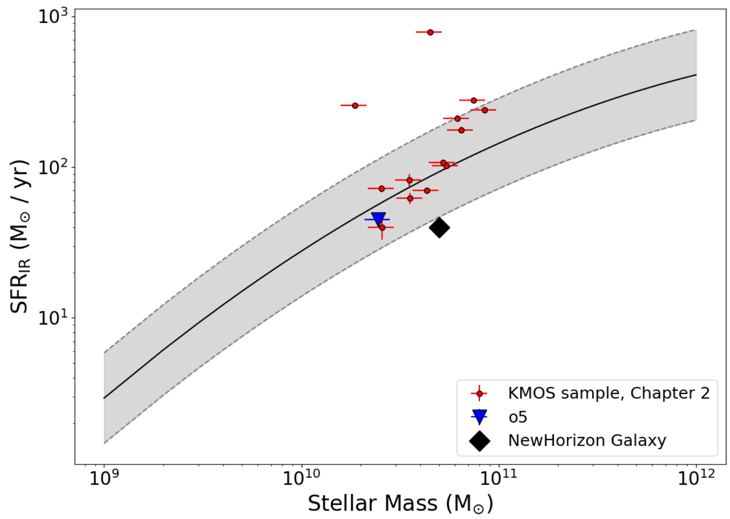

Figure 4.3: The position of the galaxy selected from NewHorizon (black diamond) with respect to the main sequence of Whitaker et al. (2014). The red circles show the position of the KMOS sample presented in Chapter 2. The blue triangle shows the position of galaxy o5, which motivated the choice of the NewHorizon galaxy.

the MS, exhibiting typical properties of a star forming galaxy at cosmic noon, with an $M_\star \approx 5.5 \times 10^{10}$ $M_\odot$ and an SFR of 38 $M_\odot$ yr^{-1}. Co-incidentally this galaxy (which I will refer to as g1 throughout this chapter) happened to be undergoing an interaction with a second galaxy (g2) with a mass ratio of $\sim$ 20:1, and their nuclei are approximately 10 kpc in separation at $z = 2$, the redshift in the simulation at which we selected the galaxy (as this galaxy evolves in the simulation a third galaxy, g3, interacts with the system and that will be the focus of Chapter 5).

Once the galaxy has been through LCARS I created mock observation cubes using HSIM. As the galaxy is located at $z = 2$, the Hα falls close to the edge of the K-band grating at this redshift. To ensure a better outcome we moved this galaxy to $z = 2.2$. This changes the observed wavelength of the emission lines (Hα shifts to 2.1 μm), the luminosity distance and angular size of the galaxy. These re-scalings are accounted for in LCARS and do not change the results or conclusions of this chapter.

I made mock observations of the complete Hα and Hβ emission line cubes, i.e. cubes with line plus continuum emission. Details of the settings I used are given in Table 4.2 and the mock data was created using HSIM version 3.03. I have gone for long observation times to maximize S/N in the outer disk of the galaxy. The settings of most relevance to the results and discussion that follows are: I use the laser tomography adaptive optics (LTAO) mode giving us a point spread function (PSF) of $\sim$ 27 mas, and I chose a spaxel scale of 20 mas. The 20 mas spaxel scale was chosen as the LCARS input cube has a spaxel size of $\sim$ 10 mas. This is not the maximum resolution that LCARS and NewHorizon can achieve, but I did not require $\sim$ 50 pc resolution, as this would greatly increase computation time, and the $\sim$ 100 pc resolution is sufficient for this research. I make mock observations of the cubes with and without dust, so I can check how the presence of dust affects the observations and analysis (a collapsed image from a fully reduced data cube is shown in Figure 4.4).

The Hα output cubes have a field of view of $\sim 3.5'' \times 3.5''$ with corresponds a physical size of $\sim$ 30 kpc $\times$ 30 kpc (note this is the FOV of the LCARS cube and not the exact FOV of HARMONI). The spectral window is $\sim$ 3000 km s^{-1} with a spectral channel of $\sim$ 20 km s^{-1}. Although the PSF of my observations is $\sim$ 27 mas, due to the 20 mas spaxel scale and undersampling effects, the effective spatial resolution of the data is 40 mas.

The integration time of 5 hours and 10 hours for the cubes with and without dust respectively were selected to maximize the S/N in the outer and diffuse regions of the disk without the need to re-bin data. This was a deliberate choice, as the goal of this research was to check if the properties of a galaxy are imprinted onto its spectrum, and the aim wasn't to test the observing limit of HARMONI at cosmic noon. Much of the analysis described in this chapter can be adequately recovered with integration times of 30 minutes, and I will delve further into this topic in Section 4.6.3.

4.4 Mock Observations Analysis

One aim of this project is to check if observing the Hα and Hβ emission lines allow me to accurately recover the true properties of the simulated galaxy. To do this,

Table 4.2: HSIM v3.03 settings used for my mock observations.

Parameter	Setting
Integration Time	900s
Number of Integrations (without extinction)	20
Number of Integrations (with extinction)	40
Band - Hα	K
Band - Hβ	H
Spaxel Scale	20 × 20 mas
Adaptive Optics Mode	LTAO
Atmospheric Seeing	0.57″
Airmass	1.1
Moon Illumination	0
Telescope Temperature	280 K
Atmospheric Differential Refraction	True
Detector Systematics	False
Jitter	3 mas
Noise Seed	10

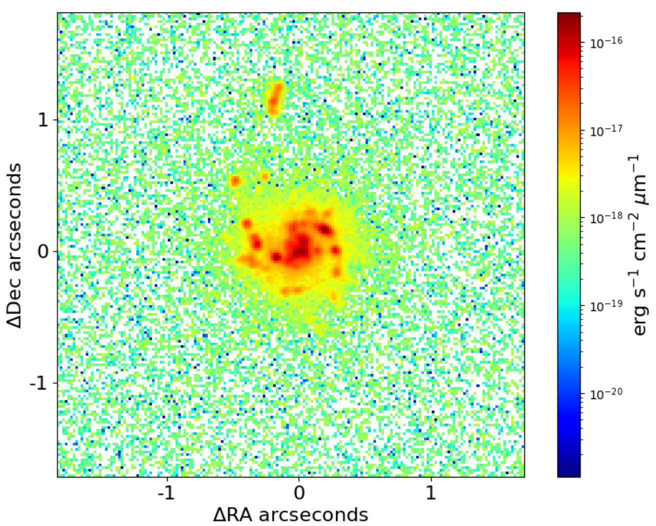

Figure 4.4: The collapsed (partial) K-band observation described in Section 4.3.3, which includes the Hα emission plus continuum. All analysis is performed on continuum subtracted cubes, and this figure is to show the output from HSIM, and demonstrate the detail in a K-band observation with HARMONI, using a 20 mas plate scale.

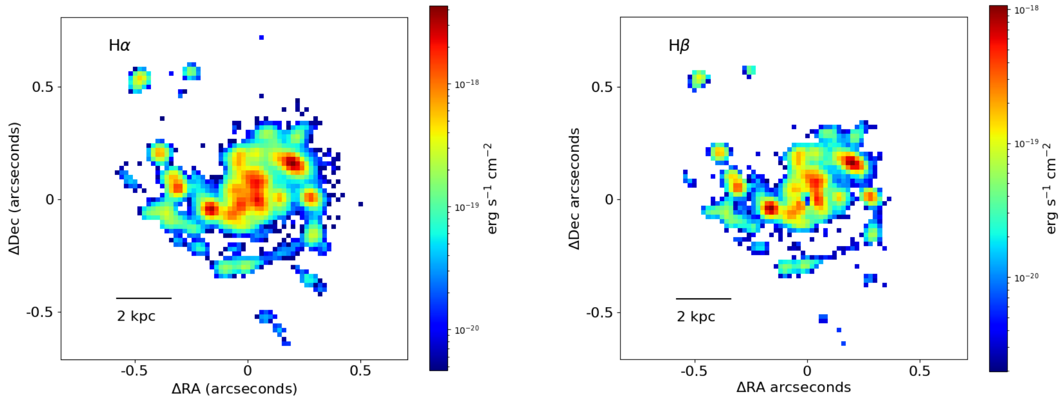

Figure 4.5: Left: Intensity map of the Hα emission line for g1. **Right:** Intensity map of the Hβ emission line for g1. I performed a continuum subtraction on the cube and then made a 5σ cut on each channel before integrating across the emission line. A scale bar is shown in the bottom left of both plots for reference. Note that I am using two different colour scalings, as using the same colour scaling for both reduced the contrast of the Hβ features, making the structure in the two maps more difficult to compare.

I choose tools and procedures commonly used in analysing real observations. In this, and the following chapter, I will refer to properties taken directly from the NewHorizon simulation as the 'true', 'correct' or 'intrinsic' values and the post-HSIM values as the 'observed properties'. I will concentrate on the main galaxy, g1, throughout this analysis.

4.4.1 Moment Maps of Line Emission

I created intensity maps for my observed galaxy to compare the observed morphology and distribution of star formation with the simulation. To make the intensity map of the emission lines I first performed a continuum subtraction on each spaxel of the cube. As the continuum is flat, to first order (in erg s^{-1} cm^{-2} Å^{-1} arcsecond^{-2}), in the IFS cubes I select the first 20 channels, which are free of line emission, and take the average continuum in each spaxel across these channels. I then subtract the average continuum from each channel in the cube. Comparing the continuum subtracted cube with the line only cube, the difference in line emission is $< 1\%$ so the constant continuum assumption is adequate. I then made a 5σ cut in each channel of the data cube and integrated the remaining flux across the total width of the emission line. The stringent 5σ was chosen as I have very high S/N data due to my choice of long integration times.

Figure 4.5 shows that the Hα and Hβ have a clumpy star forming structure and the spiral arms are clearly visible. Continuous line emission can be traced out to a radius of $\sim$ 4kpc. The S/N rapidly diminishes beyond this radius, although some star forming clumps can be observed out to $\sim$ 6 kpc. The radius of the galaxy taken from the simulation is 6kpc, which is the maximum extent of the stars that formed within the galaxy in the past 10 Myr in the simulation, so the mock observations are capturing the maximum extent of the star forming regions. The intensity maps have a spatial resolution of $\sim$ 300 pc, assuming a spatial resolution of 2 pixels. The morphology of the observed intensity maps is in excellent agreement to the map of stars formed within the last 10 Myr taken directly from NewHorizon (rightmost map in Figure 4.1). The observations are taken with the 20 mas spaxel scale and have relatively coarse spatial resolution compared to the maximum spatial resolution achievable by HARMONI, yet much of the internal structure can be recovered and regions of ongoing star formation resolved (a seeing limited instrument has a spatial resolution on the order of a few kpc depending on the atmospheric conditions, so 1 kpc clumps are unresolved).

Rest frame optical images show that high-z star forming galaxies can host giant star forming clumps on scales of 100 pc - 1 kpc with typical $M_* = 10^7$ - 10^9 $M_\odot$ (e.g. Förster Schreiber et al., 2011, Guo et al., 2012), and clumpy structure has also been seen at high-z in the molecular gas (e.g. Swinbank et al., 2015). Local turbulent disk galaxies with high gas fractions, thought to be close analogues to high-z star forming galaxies (e.g. DYNAMO sample, Green et al., 2010), have clumps a few hundred parsecs in size (e.g. Fisher et al., 2017) so if a clumpy ISM is typical in star forming galaxies at cosmic noon, which appears to be the case, HARMONI should have the spatial resolution to resolve individual clumps.

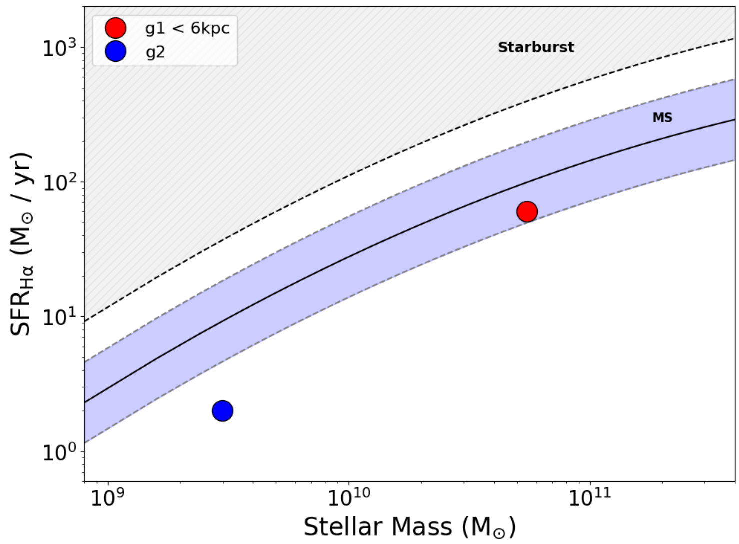

Figure 4.6: The location of g1 (red circle) and g2 (blue circle) on the stellar mass - SFR plane. The black line is the MS of Whitaker et al. (2014), with the blue region showing the typical MS scatter of 0.3 dex. The grey region shows the location of starburst galaxies. Error-bars are not included on the plot as the error in SFR is roughly equivalent to the size of the data points, due to the high S/N, and the stellar mass is taken directly from the simulation.

4.4.2 Star Formation

As discussed in Section 1.2, Hα emission can be used to infer the 'instantaneous' star formation occurring in a galaxy. To estimate the SFR from the Hα emission line, I extract an integrated spectrum from an aperture of 6 kpc in radius, centred on the peak of the continuum. I sum over all spaxels within this radius to get a single flux value per wavelength bin. I then fit a single component Gaussian, plus a constant to account for the continuum, to the emission line and integrate the area of this Gaussian to find the total Hα flux emitted by g1, and hence the luminosity. To calculate the SFR I then use the conversion factor of Murphy et al. (2011b), given in Equation 2.1, to get an $\mathrm{SFR}_{\mathrm{H}\alpha} = 60 \pm 4\ \mathrm{M}_\odot\ \mathrm{yr}^{-1}$. Although this is higher than the true SFR of 38 $\mathrm{M}_\odot\ \mathrm{yr}^{-1}$, it is on the MS at z = 2.2, and correctly classifies the galaxy as a normal star forming galaxy (Figure 4.6).

I also placed an aperture on g2, evaluated the SFR and placed it on the M_* - SFR plane. g2's SFR is below the MS as it spirals into g1 (the same

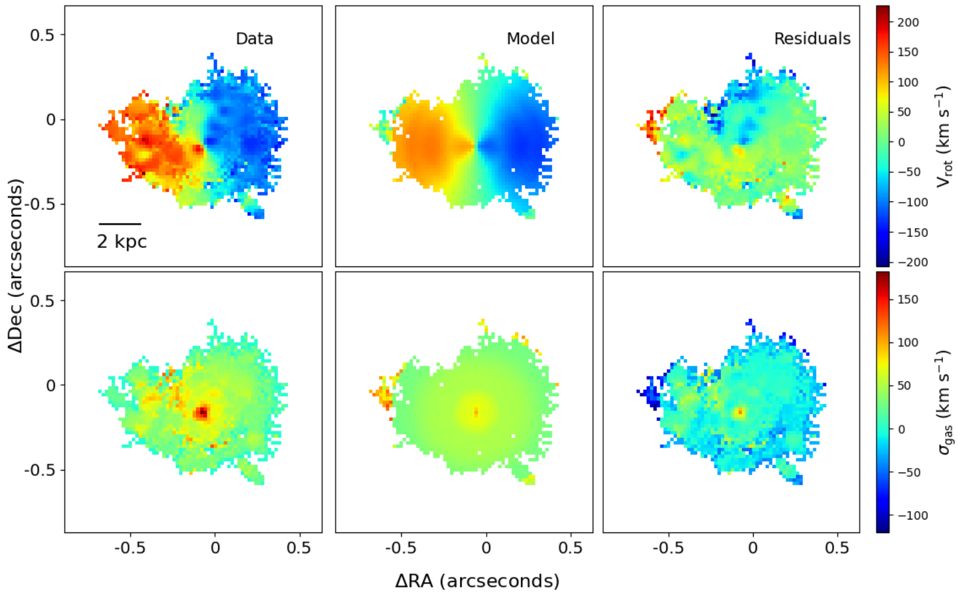

Figure 4.7: Moment maps from the mock observations and the best-fit rotating disk model. **Top left:** The observed 1st moment map. **Top middle:** 1st moment map from the best-fit model. **Top right:** The residual velocity field. **Bottom left:** The observed 2nd moment map. **Bottom middle:** The best-fit 2nd moment map. **Bottom right:** The residual velocity dispersion.

position with respect to the MS is found if I take the intrinsic SFR from the simulation), which is suggestive of environmental effects inhibiting star formation (e.g. Wetzel et al., 2013).

4.4.3 Kinematics

To test if the Hα emission line from LCARS correctly encodes the underlying physical condition of the ISM, the kinematics need to be extracted and compared to the intrinsic values. To fit a kinematic model to the Hα line, I used the ^{3D}BAROLO code, which has previously been described in Section 3.4.4.

I set the x and y positions to be the peak of the continuum and set the radial velocity to zero. The PA and inclination were set to the known values from LCARS, which are 90° and 20° respectively. The systematic velocity was set to zero, having specified in ^{3D}BAROLO that the rest wavelength equals the Hα emission line and that the galaxy is located at a redshift of 2.2. I left the V_{rot} and σ_{gas} as free parameters for the algorithm to find the best fit.

As in Section 3.4.4, I used the SEARCH algorithm to mask the galaxy from the background, with an initial 5σ cut across all channels and then included all adjoining 3σ regions within the mask. I selected a ring width of $0.06''$ to allow ~ 2 resolution elements across each ring. I experimented with differing ring sizes and the differing ring widths agreed within error to the $0.06''$ selection.

^{3D}BAROLO also allows the user to specify whether they want to fit kinematics to the galaxy as a whole, or just the approaching or receding half of the galaxy, and then assuming mirror symmetry. The rotation curve of the galaxy is reasonably symmetric, but I get a better match to NewHorizon when fitting the approaching side (discussed in Section 4.4.4). All other settings, not mentioned here, were left as default.

To calculate errors I ran ^{3D}BAROLO an additional ten times, keeping all best fit parameters constant, and allowing one at a time to vary, and I also varied which side of the galaxy to fit. The standard deviation of the best fit parameters across all these runs gave the errors in each ring.

The results of the best fit are given in Figures 4.7 and 4.8, and the fitted kinematics closely matched the true values, as will be discussed in Section 4.4.4.

4.4.4 Recovery of Kinematic Structure

Figure 4.9 shows the V_{rot} from the best fit model overlaid on the intrinsic rotation curve and velocity dispersion extracted from NewHorizon. The black line shows the mass weighted average rotational velocity of the gas in every cell within g1, in the NewHorizon simulation, with respect to the centre of mass of the galaxy. The grey shaded region shows the 1σ deviation from the mean value in that radial bin, at a scale of ~ 100 pc. As an aside, the best fit ^{3D}BAROLO errors appear smaller than the grey regions in Figures 4.9 and 4.10 as they are the statistical error on the fit, as described in the previous section, whereas the scatter on the intrinsic values is taken directly from the simulation. The main galaxy is covered by hundreds of

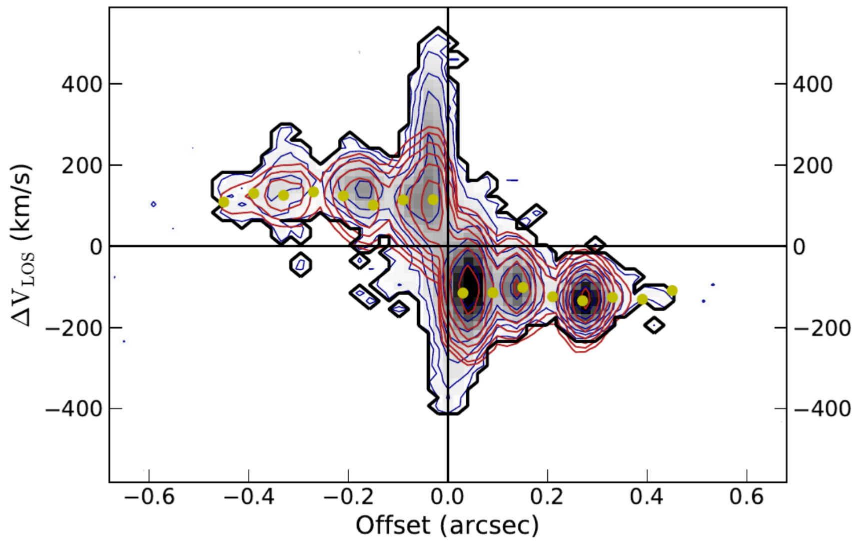

Figure 4.8: Position velocity diagram (output by ^{3D}BAROLO) along the major kinematic axis for the Hα mock observed cube with no dust extinction. The y-axis shows the projected rotational velocity and is denoted V_{los}. The black contours show the observed galaxy, with the red overlaid contours representing the ^{3D}BAROLO best fit model. The yellow points are the V_{rot} calculated for each ring in the model disk. Signatures of fast moving gas in the centre of the disk, with projected velocities up to $\sim$ 500 km s^{-1}, are clearly visible.

thousands of cells (the 30 kpc $\times$ 30 kpc FOV of my cube is composed of $\sim$ 27 million NewHorizon cells), and each cell has a bulk velocity and velocity dispersion. Due to the large number of data points per radial bin and NewHorizon's ability to resolve all non-circular flows and deviations from the mean gas dispersion on $<$ 100 pc scales, this gives a large intrinsic scatter for V_{rot} and σ_{gas}. Also, stellar feedback is implemented in the simulation and NewHorizon can resolve outflows from star forming regions within the galaxy disk. In a galaxy with an SFR $\sim$ 40 $M_{\odot}$ yr^{-1}, there are many star forming regions throughout the disk, and these can also increase the scatter of the intrinsic kinematics.

It is evident the kinematics extracted from the mock HARMONI simulation match the intrinsic rotational velocity and velocity dispersion. As mentioned in the previous section, I forced the best fit model to the approaching side. Fitting to both sides simultaneously led to some rings having a V_{rot} over 400 km s^{-1}. This is due to some non-circular flows affecting the best fit rotational velocity and pushing it to higher values. There is some low density gas moving at high velocities within

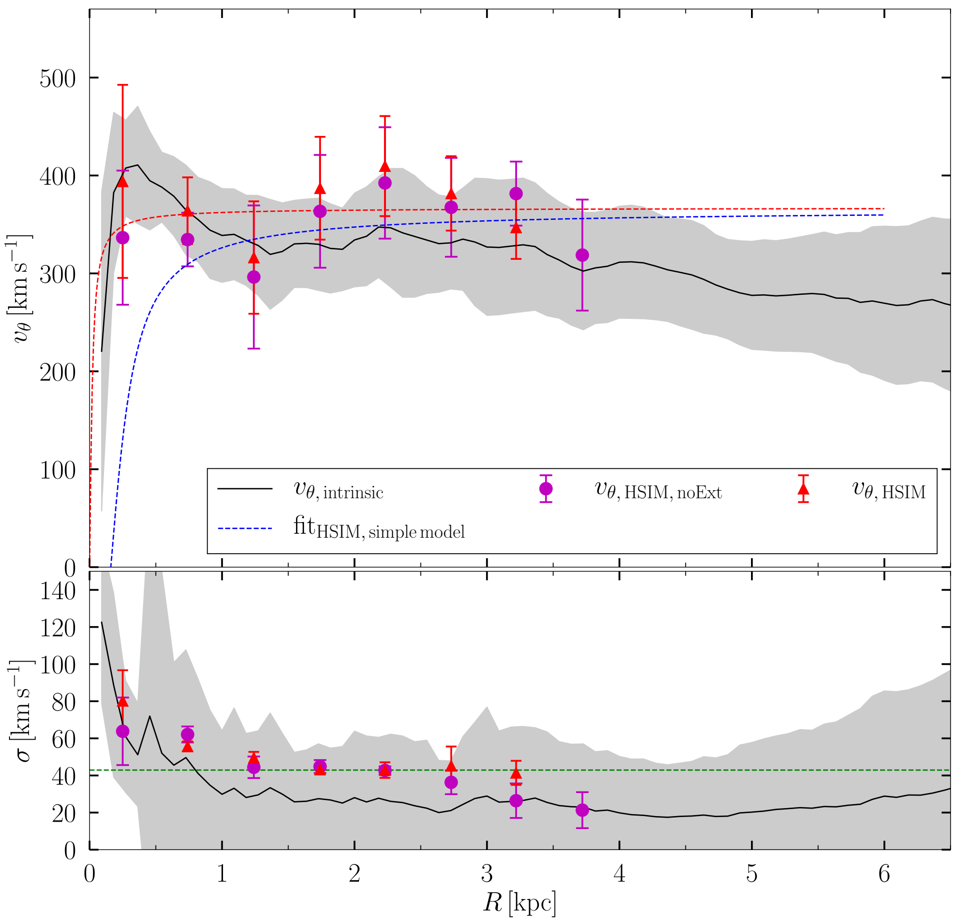

Figure 4.9: Top: The rotational velocity radial profile with the solid black line showing the intrinsic curve for g1. **Bottom:** Velocity dispersion radial profile for g1. The red and purple points show the values found by ^{3D}BAROLO for the observed cubes with and without dust, respectively. The red dashed line shows an arctan fit to the ^{3D}BAROLO red data points, while the blue dashed line shows an arctan fit directly to the 1st moment map (Figure 4.5). The shaded region represents one standard deviation from the intrinsic curve. This figure taken directly from G22, where the paper uses v_θ and σ as opposed to V_{rot} and σ_{gas} that I use in this thesis.

the disk, caused by outflows from stellar feedback. As there is no dust attenuation, some of these 'bubbles' of high velocity are biasing the fit. In any case, if I fit both sides the V_{rot} is $\sim$ 400 km s^{-1} rather than $\sim$ 350 km s^{-1}, and it still matches the intrinsic velocity within error (a typical V_{rot} error in each ring is 50 km s^{-1}). Also, as the galaxy has an inclination of 20°, a difference of 20 km s^{-1} in the line of sight velocity between two rings leads to a de-projected difference of $\sim$ 60 km s^{-1}, so if the galaxy was a little more edge on, these higher velocity regions wouldn't skew the fit to the same extent.

Referring back to Section 2.4.4 the ratio of V_{rot} / σ_{gas} can be used to aid classification of a galaxy's interaction state. As I use multiple rings to fit the kinematic model I use a flux weighted sum, like in Cappellari (2016), to find a single V_{rot} / σ_{gas} value for each galaxy:

$$\left(\frac{V_{\rm rot}}{\sigma_{\rm gas}}\right)^2 = \frac{\sum_i^N F_{\rm n} V_{\rm rot,n}^2}{\sum_i^N F_{\rm n} \sigma_{\rm gas,n}^2} \tag{4.3}$$

where N is the number of rings and F_n is the flux surface density in each ring found by ^{3D}BAROLO. The resulting V_{rot} / σ_{gas} = 6 ± 1.6, which shows g1 is strongly rotation dominated. The radial V_{rot} / σ_{gas} is plotted in Figure 4.10, which shows the galaxy gets more rotationally dominated with increasing radius. This suggests that the star forming regions in the disk are simply orbiting the galaxy at the circular velocity. Even the centre of the galaxy, with the highest σ_{gas}, has a V_{rot} / $\sigma_{gas} > 1$, and these kinematic signatures are suggestive of star formation occurring throughout the galaxy due to secular internal processes.

I use the best fit values from the outer ring to calculate the dynamical mass via Equation 2.6. I calculate the mass at 3.25 kpc, where the S/N is good enough to constrain the fit, and note that the $k_{eff} \approx 1$ and $V_{rms} \approx V_{rot}$ at a radius of 3.25 kpc due to the $V_{rot} \gg \sigma_{gas}$. I find a $M_{dyn} = 1.1 \pm 0.2 \times 10^{11}$ $M_{\odot}$, which is in excellent agreement to the intrinsic value of 8×10^{10} $M_{\odot}$ taken from the simulation. The galaxy is also baryon dominated, as opposed to dark matter dominated inside 6 kpc (see Table 4.1), which is similar to what I found for my U/LIRG sample in Chapter 2.

Although I don't explicitly look at inflows or outflows in this research, the PV diagram in Figure 4.8 shows signatures of an outflow. If inflows and outflows are ubiquitous in the high-z universe, as they appear to be in local U/LIRGs (e.g. Perna et al., 2021), then HARMONI will have the sensitivity to observe these.

The results in this section establish that LCARS correctly captures the underlying state of the ISM in the mock spectra, so mock observations from this pipeline can become an excellent tool for testing HARMONI's limits, in terms of spaxel scale, S/N etc., across a wide range of galaxy masses and luminosities at cosmic noon.

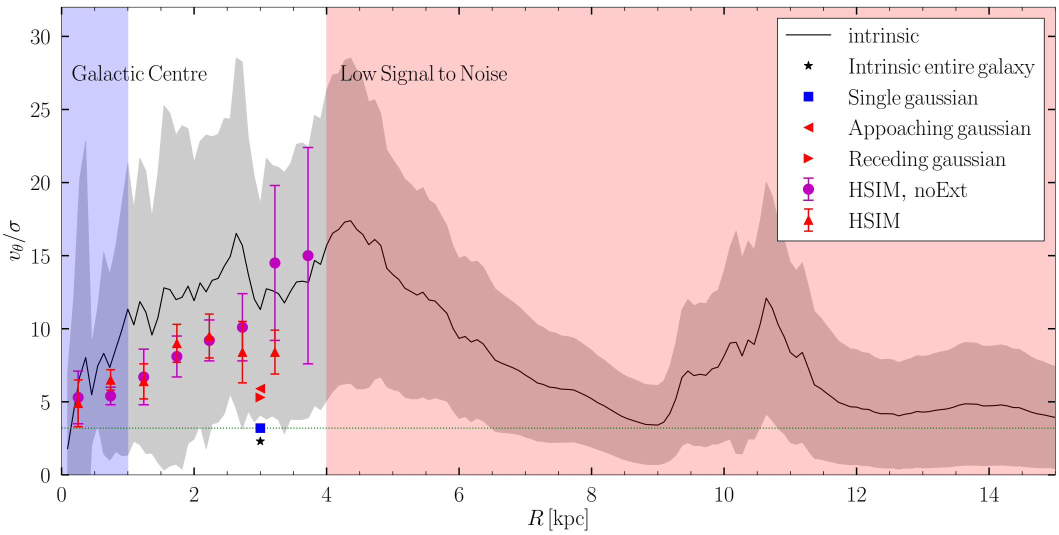

Figure 4.10: Radial profile of the dynamical ratio. The black line shows the intrinsic profile, with the grey shaded region showing the 1σ deviation. Red and purple points show the values found by ^{3D}BAROLO for the observed cubes with and without dust, respectively. The four data points with no error bars show the value of the dynamical ratio calculated on galaxy-wide scales (see Section 4.6.2), and as these values are independent of radius they are placed at 3 kpc by choice. The dotted green line shows the criteria threshold for a merger discussed in Section 2.4.4. The blue shaded region indicates g1's central 1 kpc and the shaded red region shows where g1 didn't have the requisite S/N to fit kinematics. This figure is taken directly from G22, where the paper uses v_θ and σ as opposed to V_{rot} and σ_{gas} that I use in this thesis.

4.5 Addition of Dust

While the cube with no extinction is a good test case, real galaxies contain dust, which affects the estimated SFR and may lead to an incorrect determination of the kinematics and morphology of a galaxy. As explained in Section 4.3.2, dust is added to LCARS cubes by assuming a column of dust between the emitting region and the observer, and the column density of dust is a function of the dust to gas phase metallicity ratio. The ratio was set to 1%, and this ratio was chosen as it gives a galaxy wide A_V of $\sim$ 0.9 mag, which allows the study of how moderate dust obscuration impacts recovery of the true properties of g1. As mentioned in Section 4.3.2, the dust to gas phase metallicity selection is an arbitrary choice applied in the LCARS pipeline and the user can scale it if they want to study environments with more or less dust.

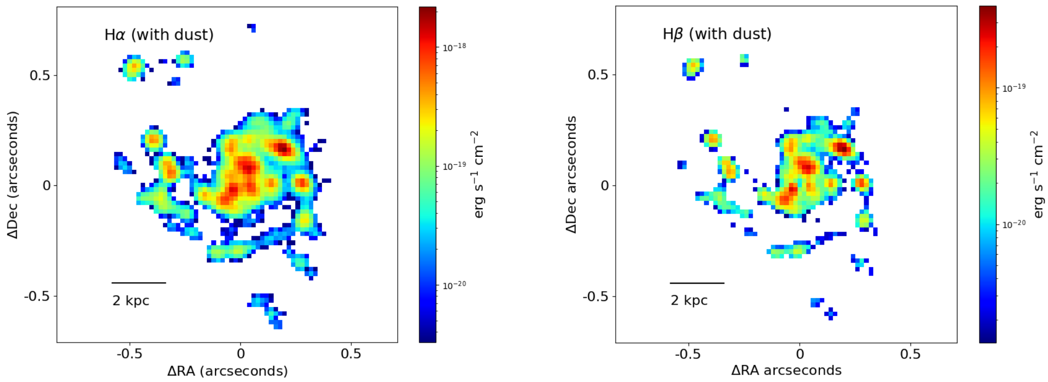

Figure 4.11: Left: Intensity map of the Hα emission line for g1 with dust included. **Right:** Intensity map of the Hβ emission line with dust included. Using the same method as the dust-free cubes, I performed a continuum subtraction and made a 5σ cut on each channel. A scale bar is shown in the bottom left of both plots for reference. I once again note that I am using two different colour scalings.

4.5.1 Star Formation

The flux ratio of emission lines is often used to correct for dust and find the intrinsic luminosity of a given emission line. A common method involves taking the ratio of Hα to Hβ, as these are relatively bright rest frame optical lines and their intrinsic flux ratio is set by quantum mechanics. To correct for dust, and find the intrinsic luminosity of Hα, I use the prescription of Domínguez et al. (2013):

$$L_{\mathrm{H}\alpha(\mathrm{int})} = L_{\mathrm{H}\alpha(\mathrm{obs})}\ 10^{0.4A_{\mathrm{H}\alpha}} = L_{\mathrm{H}\alpha(\mathrm{obs})}\ 10^{0.4k(\lambda)E(B-V)} \tag{4.4}$$

where

$$A_{H\alpha} = 3.3 \pm 0.80\ \mathrm{E(B-V)} \tag{4.5}$$

and

$$E(B-V) = \frac{2.5}{k(\lambda_{\mathrm{H}_\beta}) - k(\lambda_{\mathrm{H}_\alpha})} log_{10}\left[\frac{(H\alpha/H\beta)_{\mathrm{obs}}}{(H\alpha/H\beta)_{\mathrm{int}}}\right] \tag{4.6}$$

where $\mathrm{L}_{\mathrm{H}\alpha(\mathrm{int})}$ and $\mathrm{L}_{\mathrm{H}\alpha(\mathrm{obs})}$ are the intrinsic and observed luminosities, $\mathrm{A}_{\mathrm{H}\alpha}$ is the extinction at the wavelength of Hα and k(λ) is the value of the extinction curve at a given wavelength. The (Hα / Hβ)$_{\mathrm{int}}$ ratio equals 2.86, for case B recombination, as calculated from quantum mechanics (e.g. Osterbrock and Ferland, 2006). I use a Fitzpatrick (1999) attenuation curve to be consistent with the extinction curve used in LCARS which gives pre-factors of 2.5 / (k($\lambda_{\mathrm{H}_\beta}$) - k($\lambda_{\mathrm{H}_\alpha}$) = 1.5. Once again I extract an Hα and Hβ integrated spectrum inside a radius of 6 kpc, fit a single Gaussian to the emission line and integrate beneath the curve to get a flux for both lines. This gives us a dust corrected $\mathrm{SFR}_{\mathrm{H}\alpha}$ = 62 ± 15 $\mathrm{M}_\odot$ yr^{-1}, with the large errors arising from the error in the $\mathrm{A}_{\mathrm{H}\alpha}$ in Equation 4.5. This is in agreement with the $\mathrm{SFR}_{\mathrm{H}\alpha}$ = 60 ± 4 $\mathrm{M}_\odot$ yr^{-1} found in the cube without dust, showing that I can recover the true $\mathrm{SFR}_{\mathrm{H}\alpha}$ when correcting for dust using the H_β emission line.

If, hypothetically, I only had a K-band observation (Hβ is in the H-band at z = 2.2) and no other method of correcting for dust, I would get an uncorrected $\mathrm{SFR}_{\mathrm{H}\alpha}$ = 32 ± 2 $\mathrm{M}_\odot$ yr^{-1}, signifying that approximately 50% of the SFR is 'missing' without accounting for dust, i.e. the unobscured SFR is 50% of total SFR. If this were a real galaxy this 'missing' SFR should approximately equal the dust obscured SFR calculated from the IR SED, as the total SFR of a galaxy is equal to the unobscured SFR plus the dust obscured SFR. In this case, the hypothetical $\mathrm{SFR}_{\mathrm{IR}}$ is roughly 30 $\mathrm{M}_\odot$ yr^{-1}, and this would make g1 a LIRG. Following the same logic, I can estimate the spatial distribution of the dust obscured SFR by subtracting the LCARS cube with dust from the LCARS cube without dust, and this is shown in Figure 4.12.

4.5.2 Kinematics

Now that I have demonstrated the addition of dust doesn't impact the SFR estimates, any biases introduced by dust into the kinematic fit need to be checked. I fit a $^{\mathrm{3D}}$BAROLO model to the cube with dust, using the same procedure as the cube without extinction, and the best fit kinematics are overlaid on the intrinsic values in Figure 4.9. The results match both the intrinsic kinematics and the values found in the non-extinct cube. The only difference is the S/N only allowed 7 rings to be fitted, as opposed to the 8 rings in the non-dust observations, and I fit both sides of the galaxy simultaneously (as a reminder I fit the approaching side in the

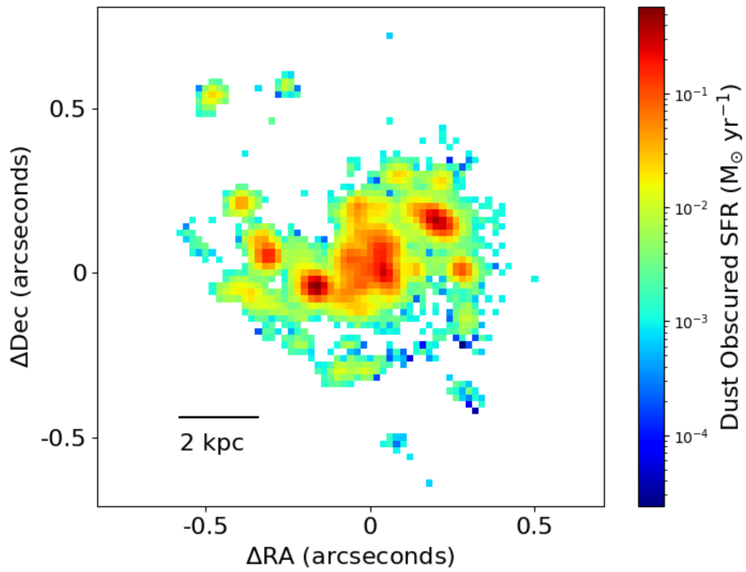

Figure 4.12: An estimate of the dust obscured SFR by subtracting the Hα cube with dust from Hα cube without dust. The resulting flux, is the flux that has been attenuated by the screen of dust model implemented in LCARS. This flux was converted to an SFR using the method explained in Section 4.4.2.

non-dust cube). Some bubbles of high velocity gas, that forced the best fit V_{rot} higher when fitting both sides in the dust free cube, have been attenuated by the dust. As the observations with dust are more realistic, this reinforces that fitting a model disk to HARMONI observations can recover the intrinsic kinematics.

From the best fit model I get a V_{rot} / σ_{gas} = 5.8 ± 1.2 matching that of the dust free dynamical ratio. I find a M_{dyn} = 9.6 ± 2.0 × 10^{10} $M_\odot$ which is in agreement with the intrinsic value and the dust free observed value.

4.6 Discussion

4.6.1 An Interacting Galaxy Can Have Similar Properties to an Isolated Galaxy

Despite being an interacting system, with the two galaxies having a separation of ∼ 10 kpc, and a mass ratio of 20:1, g1's observed properties are consistent with that of an isolated galaxy. It has a disk-like morphology, with a V_{rot} / σ_{gas} ∼ 6 consistent with that seen in isolated disks. The 1st and 2nd moment maps display a clumpy structure and spiral arms, but no clear signatures of disturbed kinematics. If I were to observe this system with a seeing limited resolution and/or poorer sensitivity than HARMONI it would be difficult to infer if this was an interacting system. It is on the MS (Figure 4.6) and has relatively extended regions of star formation observed out to a radius of $\sim$ 4 kpc. I don't observe tidal tails or other telltale signs of an ongoing merger (e.g. Veilleux et al., 2002, Kartaltepe et al., 2010).

It may be that interacting systems and minor mergers are ubiquitous at cosmic noon, but if a galaxy retains its disk like structure and ordered rotation, it is very difficult to categorize them as interacting. For example, in Chapter 2, I found $\sim$ 40% of MS luminous IR galaxies have disk like properties based on their dynamical ratio. Using the methodology of Section 2.4.4 the HARMONI mock observation would be classified as isolated, so it seems likely at least one of my KMOS sample may be undergoing a minor merger or interaction and would be reclassified as such if high spatial resolution observations were available.

It can also be argued that if below a certain mass ratio interactions don't have an impact on a galaxy's structure or SFR, then misclassifying a system as an isolated disk (or vice versa) doesn't impact our understanding of the triggers of star formation. E.g. merger/interaction induced star formation only becomes important above a certain mass ratio threshold, as below this threshold minor interactions only cause a small perturbation to the SFR, which is driven by internal steady state processes. With the new generation of telescopes, starting with JWST, providing much greater spatial resolution and/or sensitivity, this is a topic that will become increasingly relevant in the coming years.

4.6.2 Observables in the High-z Universe

It is often ambiguous which σ_{gas} to use when calculating the dynamical ratio, and various definitions seem to be used throughout the literature. For example, instead of the flux weighted $\mathrm{V_{rot}}$ / σ_{gas} that I used in Section 4.4.4, I could fit a functional form to the radial values of $\mathrm{V_{rot}}$ and σ_{gas}, and calculate the dynamical ratio from the asymptotic values (i.e. $\mathrm{V_{rot}}$ / σ_0), or I could use the σ_{gas} from the best fit Gaussian profile to the Hα emission line. I could use a similar method to Section 2.4.4 and use a redshift re-scaled velocity dispersion to compare to the local universe. What is clear is that there is no one definition of V_{rot} / σ_{gas} and when comparing samples from across the literature, it is often not comparing like with like. Also, even for my resolved dynamical ratio, plotted in Figure 4.10, each ring is $\sim$ 500 pc in diameter, so I am not probing the smallest scales on which star formation happens. Applying a stability criterion, such as V_{rot} / σ_{gas}, can indicate a disk is stable at large scales, but the disk can be turbulent and unstable on much smaller scales (e.g. Agertz et al., 2015), so measures of disk stability should be treated with care.

But, whichever of the above methods I choose I always get V_{rot} / σ_{gas} > 2.5, with the lowest value of $\sim$ 2.5 for the σ_{gas} taken from the best fit Gaussian profile. Irrespective of the method, I wouldn't misclassify the galaxy as dispersion dominated, so it seems V_{rot} / σ_{gas} can be useful to classify late type from early type galaxies, and possibly major mergers, but I cannot rule in or out interactions and minor mergers, and more sophisticated indicators are required. In Chapter 5 I will look at a range of indicators to see which, if any, can be used to differentiate between different stages in a galaxy's evolution.

Another caveat, when fitting kinematics and using the resulting information to gain insight, is I am implicitly assuming the luminosity accurately traces the underlying distribution of mass. Inflows and outflows driven by feedback from star formation can cause local pockets of Hα in the disk to move ahead or behind the circular velocity of the galaxy. If these inflows correspond to low density, high velocity structures which have low mass but a strong photon weighting, this can bias the fit and make it difficult to get an accurate V_{rot} for a galaxy. This is especially relevant at high-z as disks are more turbulent (e.g. Übler et al., 2017) and normal star forming galaxies have an SFR an order of magnitude higher than the local universe (e.g. Speagle et al., 2014), with associated feedback, assuming it scales with SFR.

I mentioned in Section 4.4.3 that I found a better match to the intrinsic V_{rot} by fitting the approaching side, as although there are perturbations, the disk had

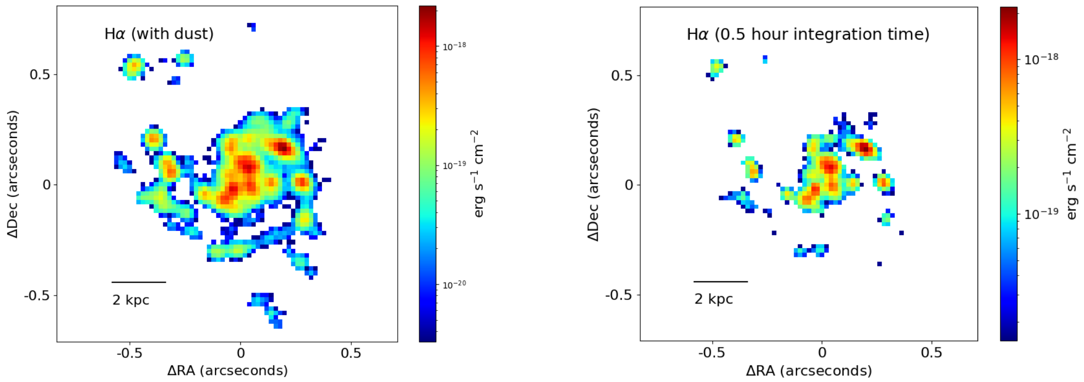

Figure 4.13: Left: Intensity map of the Hα emission line for g1 with dust included for the 10 hour integration time, with a 5σ cut on each channel. **Right:** Intensity map of the Hα emission line for g1 with dust included for an 0.5 hour integration time, with a 5σ cut on each channel.

a relatively smooth velocity field. The receding side of the disk had more regions deviating from the intrinsic V_{rot}. This can be seen in the top left plot in Figure 4.7, where clumps can be seen in the 1st moment map deviating from a smooth circular velocity. At lower spatial resolution, these perturbations can be smoothed out, making a parametric kinematic model easier to fit. Overall, fitting to both sides, as opposed to the approaching side, only shifts the inferred de-projected V_{rot} by a few 10s of km s^{-1}, so would still be a good match to the intrinsic rotation curve. But care must be taken when fitting a model to a more perturbed disk, and I will explore this in more depth in the next chapter.

4.6.3 Integration Time

As mentioned in Section 4.3.3, I have deliberately used long integration times (5 - 10 hours) for these observations, to maximize the S/N in the outer disk without having to re-bin data. I re-did the mock data cubes with integration times of 30 minutes for the cube with dust, and the analysis in this chapter is broadly replicable at these integration times. The uncorrected SFR$_{H\alpha}$ is 31 $\pm$ 2 $M_\odot$ yr^{-1} and the dust corrected SFR$_{H\alpha}$ is 69 $\pm$ 17 $M_\odot$ yr^{-1}, within a 6 kpc radius aperture centred on the peak of the continuum, which matches the 10 hour integration

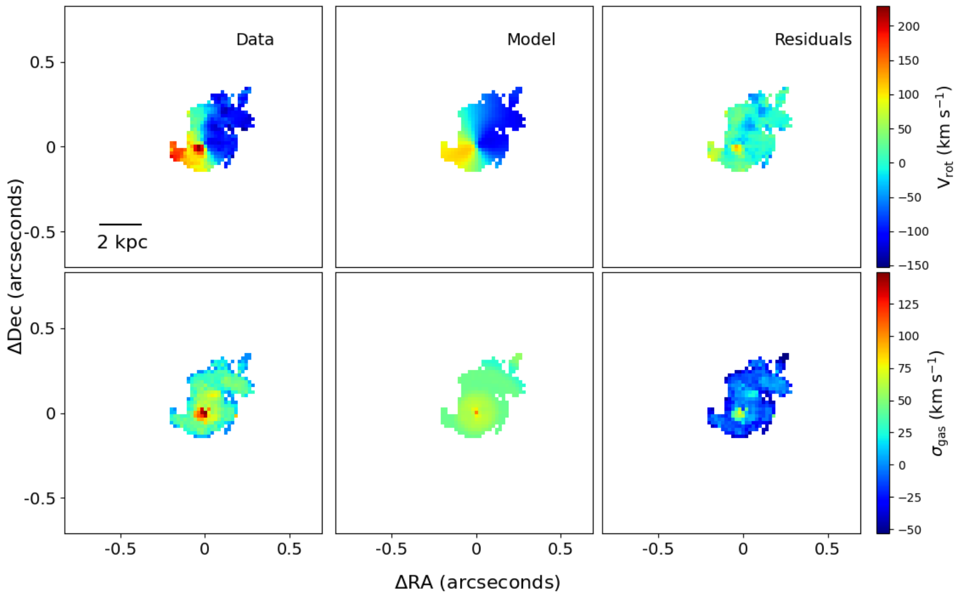

Figure 4.14: Moment maps from the 0.5 hour mock observations, with dust, and the best-fit rotating disk model. **Top left:** The observed 1st moment map. **Top middle:** 1st moment map from the best-fit model. **Top right:** The residual velocity field. **Bottom left:** The observed 2nd moment map. **Bottom middle:** The best-fit 2nd moment map. **Bottom right:** The residual velocity dispersion.

observation. The clumpy nature of star formation is also evident in the shorter observation time, as seen in Figure 4.13.

The kinematics appear accurate out to ~ 2.5 kpc before the S/N drops off, which can be seen in Figure 4.14. I recover a V_{rot} / σ_{gas} of ~ 6, which matches the dynamical ratio calculated from the higher S/N cube. The PA differs if I don't force the fit, as most of the high S/N regions lie off the major kinematic axis. This doesn't change any kinematics results but if comparing the kinematic PA with a hypothetical PA derived from fitting from optical photometry, for example HST ACS imaging, one may conclude the kinematic PA is offset from the optical disk inclination by ~ 20° (e.g. Rodrigues et al., 2017 did this type of analysis with HST and KMOS data).

Depending on the science goal, determining kinematics out to ~ 2.5 kpc may be sufficient. If the outer regions of the disk need to be explored, for example to check if rotation curves stay flat or decrease with increasing radii at high-z (e.g. Lang et al., 2017, Genzel et al., 2020), then longer integration times may be required. I didn't push the analysis to shorter observation times or re-bin the data, for example with Voroni binning (Cappellari and Copin, 2003), to try to recreate the kinematics, as the aim of this research was to check if the intrinsic properties of high-z galaxies are imprinted on their spectra. The threshold at which the analysis breaks down is outside the scope of this chapter and left for future work.

4.7 Conclusion

This chapter used a state of the art new pipeline to explore whether it is possible to accurately recover the properties of a high-z galaxy using the HARMONI spectrograph. Mock observations of the Hα and Hβ emission lines were constructed, and I applied various analysis techniques used throughout the literature to reveal:

1. The morphology of the observed Hα emission line closely resembles the map of stars formed in the past 10 Myr taken directly from the NewHorizon simulation. I found an $\mathrm{SFR}_{\mathrm{H}\alpha}$ of 60 $\pm$ 4 $\mathrm{M}_{\odot}$ yr^{-1} in the cube without dust, and this inferred SFR correctly places the galaxy on the MS.

2. The kinematics found by fitting a model to the Hα emission line were consistent with the asymptotic $\mathrm{V}_{\mathrm{rot}} \sim 360$ km s^{-1} and $\sigma_{\mathrm{gas}} \sim 30$ km s^{-1}. I found a dynamical ratio of $\sim$ 6 and a $\mathrm{M}_{\mathrm{dyn}} = 1.1 \pm 0.2 \times 10^{10}$ $\mathrm{M}_{\odot}$ which are in agreement with the intrinsic values.

3. The addition of moderate dust obscuration does not affect the recovery of the underlying properties of the galaxy, which is important as star forming galaxies at z $\sim$ 2 are dust enshrouded. I get a dust corrected $\mathrm{SFR}_{\mathrm{H}\alpha}$ of 62 $\pm$ 15 $\mathrm{M}_{\odot}$ yr^{-1}, dynamical ratio of 5.8 $\pm$ 1.2 and $\mathrm{M}_{\mathrm{dyn}} = 9.6 \pm 2.0 \times 10^{10}$ $\mathrm{M}_{\odot}$ when analysing the cubes with dust.

4. Despite being an interacting galaxy, g1 displays observational signatures consistent with being an isolated disk. This suggests that an interacting

pair of galaxies with mass ratios of 20:1 may be difficult to infer at high-z without deep high spatial resolution observations.

5. The results in this chapter are broadly replicable in an integration time of 30 minutes in the cube with dust. Depending on the science goal, HARMONI will be able to observe a target in minutes and will push our understanding of the internal structure of star forming galaxies at cosmic noon.

I have established that HARMONI observations can adequately capture the underlying global properties of a massive star forming galaxy at cosmic noon, and the exceptional spatial resolution allows the internal structure of a MS galaxy to be studied at this epoch. LCARS, in addition to HSIM, provides an excellent new tool for testing models of the high-z universe. It will allow us to probe what phenomena will be possible for HARMONI to observe, and allow testing of new analysis tools before HARMONI first light. Now that I have shown the pipeline encodes the underlying state of the galaxy, in the next chapter I will build on this and look for observables that can help discriminate between different stages of a galaxy's evolution.

They were so close to each other that they preferred death to separation.

—Gabriel Garcia Marquez *One Hundred Years of Solitude*

5

Observational Signatures of a Minor Merger at Cosmic Noon

Contents

This chapter will be submitted as: L. Hogan, K. Grisdale, D. Rigopoulou, N. Thatte, M. Pereira-Santaella, J. Devriendt, A. Slyz, I. García-Bernete. *On the Viability of Determining Galaxy Properties from Observations II: Observational Signatures of a Minor Merger at Cosmic Noon*, in prep.

5.1 Introduction

Key to translating future high spatial resolution observations into knowledge of the high-z universe is not only determining how a galaxy's properties are encoded into its spectral lines, but how do these observational signatures change as a galaxy interacts with its environment. We need to know which observables allow us to deduce a galaxy's SFH and surmise what observables are degenerate with multiple underlying properties of a galaxy.

In this chapter, I will tackle these issues by building on the analysis and results of Chapter 4. I will present further mock HARMONI observations of a z $\sim$ 2 star forming galaxy and track how the observational signatures change as the galaxy undergoes a minor merger. This work will help interpret future HARMONI observations and aid in translating the information from spatially resolved emission lines back to the underlying state of the ISM and star formation.

As well as testing observables, I will also try to gain insight on questions posed in Chapters 2 and 3, such as: how do minor mergers affect the dynamical ratio?, can minor mergers at cosmic noon be missed by observations?, how is the SFE linked to interaction stage?

Much of this thesis has examined the suggested bi-modality of star formation, the story of mergers versus steady state processes, and their link to the MS, starbursts and the transition region. This topic has so far been explored by observational data, presented in the previous chapters, so simulated galaxies and mock observations will offer a different way of approaching this subject and offer new insight.

5.2 Mock Observations

As the galaxy pair described in Chapter 4 evolved through cosmic time in NewHorizon, a third galaxy approached with a low impact factor and underwent a head on collision, as g2 was continuing to inspiral into g1. Taking advantage of this serendipitous minor merger, I now study three snapshots of the system over the

Table 5.1: Properties of the galaxy selected from NewHorizon.

	Snapshot 1		Snapshot 2		Snapshot 3	
Object	< 6kpc[1]	< 15kpc[2]	< 6kpc	< 15kpc	< 6kpc	< 15kpc
$\log(M_\star / M_\odot)$[3]	10.74	10.77	10.88[a]	10.93	10.82	10.95
$\log(M_{gas} / M_\odot)$[4]	10.28	10.34	10.34	10.68	10.36	10.70
SFR [$M_\odot$ yr^{-1}][5]	38	40	34	40	198	209

[1] Within a radius of 6 kpc centred on the peak of the continuum of g1, the main galaxy.
[2] The full FOV of the LCARS cube is approximately 30 kpc, so a radius of 15 kpc captures the entire system.
[3] Stellar mass.
[4] Gas mass.
[5] Average star formation rate in the previous 10 Myr.
[a] The $M_\star$ within the 6kpc radius aperture is greatest in snapshot 2, as the infalling satellite, g3, is within the aperture in snapshot 2, whereas it falls outside the aperture in the other two snapshots.

course of this merger. The first snapshot is the one described in the previous chapter, and I will still refer to both galaxies as g1 and g2. This snapshot counts as the pre-merger phase as although g1 and g2 are interacting, g1's properties are consistent with that of an isolated disk, as discussed in Section 4.6.1. The second snapshot occurs $\sim$ 400 Myr after snapshot 1, when g1 is undergoing a direct collision with a third galaxy (g3) with a mass ratio of $\sim$ 4:1, and the nuclei are separated by $\sim$ 2 kpc (g2 is still inspiraling, but as in the first snapshot it appears to have a negligible impact on g1). The third snapshot is taken when g3 has just made its first pass through g1 and the two nuclei are separated by $\sim$ 7 kpc. These three snapshots allow mock HARMONI observations of a minor merger to be made, and help determine the observational signatures of three different stages of a merger. Just to be clear, although this is a three body interaction, g2 appears to be having very little impact on the system, so it is effectively a two body interaction (g1 and g3), and throughout this chapter when I discuss the merger I am referring to g1 and g3 only, unless g2 is explicitly mentioned.

Once again, each snapshot is passed through LCARS to compute the Hα emission line and its underlying continuum, both with and without dust. I then create mock HARMONI observations of all three snapshots using HSIM. All details are

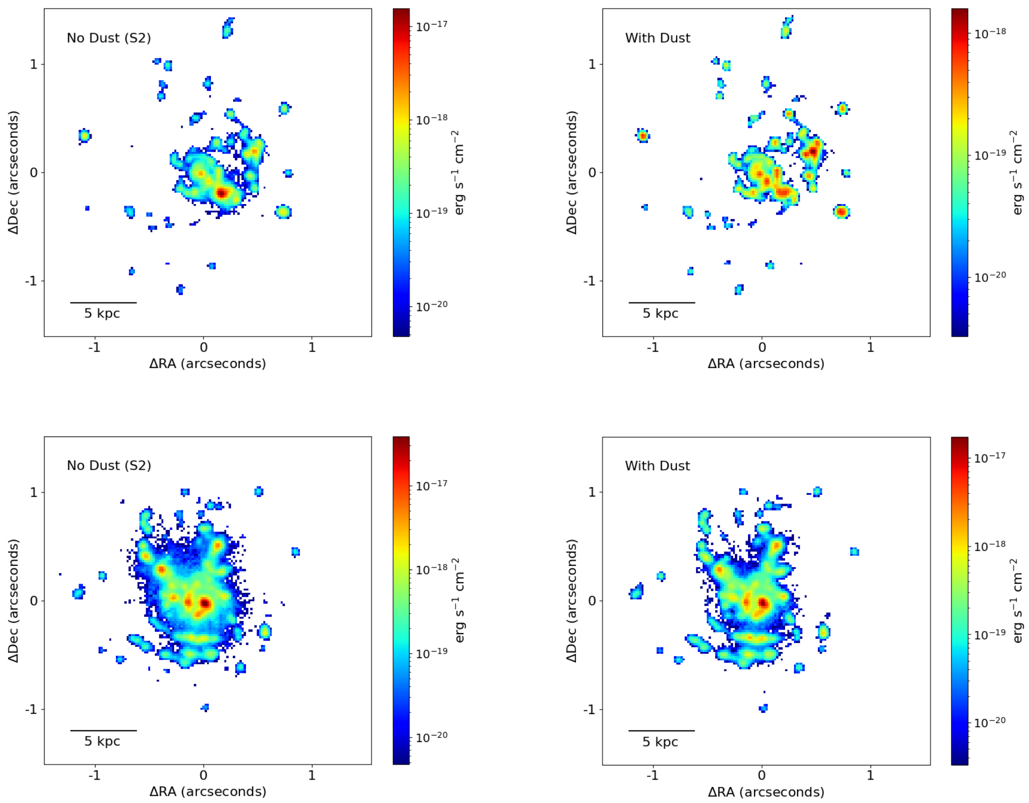

Figure 5.1: Left column: Continuum subtracted intensity maps of the Hα emission line in the observed cube without dust for snapshot 2 (top) and snapshot 3 (bottom). **Right column:** Continuum subtracted intensity maps of the Hα emission line in the observed cube with dust included (snapshot 1 comparison is in Figure 4.11). All maps use a 5σ cut and a scale bar is shown in the bottom left of all plots for reference. The general morphology is similar with and without dust, with the main difference being the brightest Hα clumps are more heavily attenuated than the fainter regions, and some inter clump emission is below the S/N threshold.

the same as in Section 4.3.3 and I include the same HSIM parameters again for easy reference in Table 5.2. As in Chapter 4, all three snapshots were placed at z = 2.2.

One of the LCARS products is a continuum only cube with the same spectral coverage as the emission line cube. In addition to the Hα mock observations, I mimic the continuum that would be observed on either side of the emission line in a K-band observation (1.951 - 2.469 μm, R = 7104). Instead of stitching together multiple continuum cubes until the spectral window of the continuum cube matched that of the entire K-band, I increased the exposure time in HSIM. Each continuum cube's spectral window is $\sim$ 4% the width of the K-band (cube: 0.021 μm, K-band:

Table 5.2: HSIM settings used for the mock observations.

Parameter	Setting
Integration Time	900s
Number of Integrations (without extinction)	20
Number of Integrations (with extinction)	40
Band	K
Spaxel Scale	20 × 20 mas
Adaptive Optics Mode	LTAO
Atmospheric Seeing	0.57″
Airmass	1.1
Moon Illumination	0
Telescope Temperature	280 K
Atmospheric Differential Refraction	True
Detector Systematics	False
Jitter	3 mas
Noise Seed	10

0.52 μm), so if I assume a roughly constant continuum I would expect ~ 25 times as many continuum photons if observed in the K-band, i.e. it would take 25 of the continuum cubes stitched together to cover the K-band. Therefore, I observe the continuum cube for 25 times longer than the Hα mock observation, by changing the number of integrations. All settings, except for the number of integrations, were kept the same as the Hα mock observations (Table 5.2).

For full disclosure, snapshot 2 was run with an updated version of LCARS, with the previous version used to run to snapshot 1 and snapshot 3. This update made slight changes to how LCARS processes the metal lines and no changes were made to how LCARS treats hydrogen. As I only use the hydrogen emission lines and the underlying continuum, the analysis, results and conclusions in this chapter will not change when snapshot 1 and snapshot 3 are processed through the new pipeline, albeit the absolute values may change slightly.

5.3 Analysis

In Chapter 4, I revealed that the mock IFS cubes captured the intrinsic properties of the underlying galaxy. In this chapter, I will no longer compare each observable to the intrinsic values taken directly from NewHorizon, as continually saying the observations and intrinsic values agree within error adds no further information to my results. Unless otherwise explicitly stated, the observed intensity maps, kinematics, SFR etc. agree with the simulated data. The goal of this chapter is to treat all three snapshots as if they were real observations and investigate what I can infer from the observables.

To reiterate, the first snapshot takes place around 400 Myr before the other two snapshots (see Figure 4.2), and snapshots 2 and 3 are only separated by $\sim$ 30 Myr. Throughout this chapter I will be plotting observables from the three snapshots and I space all three snapshots equally on the plots. These should not be interpreted as a rate of change between the three snapshots, and the plots just show how the observables have changed between all three.

5.3.1 Moment Maps

I made intensity maps of both the continuum and Hα emission, for cubes with and without dust. The intensity maps of the Hα lines are created using the methodology outlined in Section 4.4.1. For the continuum maps I integrated across all channels in the continuum only cubes to get a value in units of erg s^{-1} cm^{-2} arcsecond^{-2} and then divided this by the width of the cube to get the continuum value in units of erg s^{-1} cm^{-2} μm^{-1} arcsecond^{-2}. The maps are shown in Figures 5.2, 5.1 and 5.3. As a proviso, the continuum cube contains no emission lines and if this were a full K-band mock observation I would need to mask channels with emission lines first, before integrating the cube. Therefore, the S/N in a map from a continuum plus emission line cube would differ than those presented here (it would also depend on the spectral shape across the K-band in a real observation).

Qualitatively, as with snapshot 1, the Hα in snapshot 2 and snapshot 3 shows a clumpy structure, in both the dust and non-dust maps, with most star formation taking place within a few bright clumps. The main difference between the cubes with and without dust is some flux from the diffuse inter clump regions is below the S/N threshold, and the contrast between bright and faint regions is less pronounced

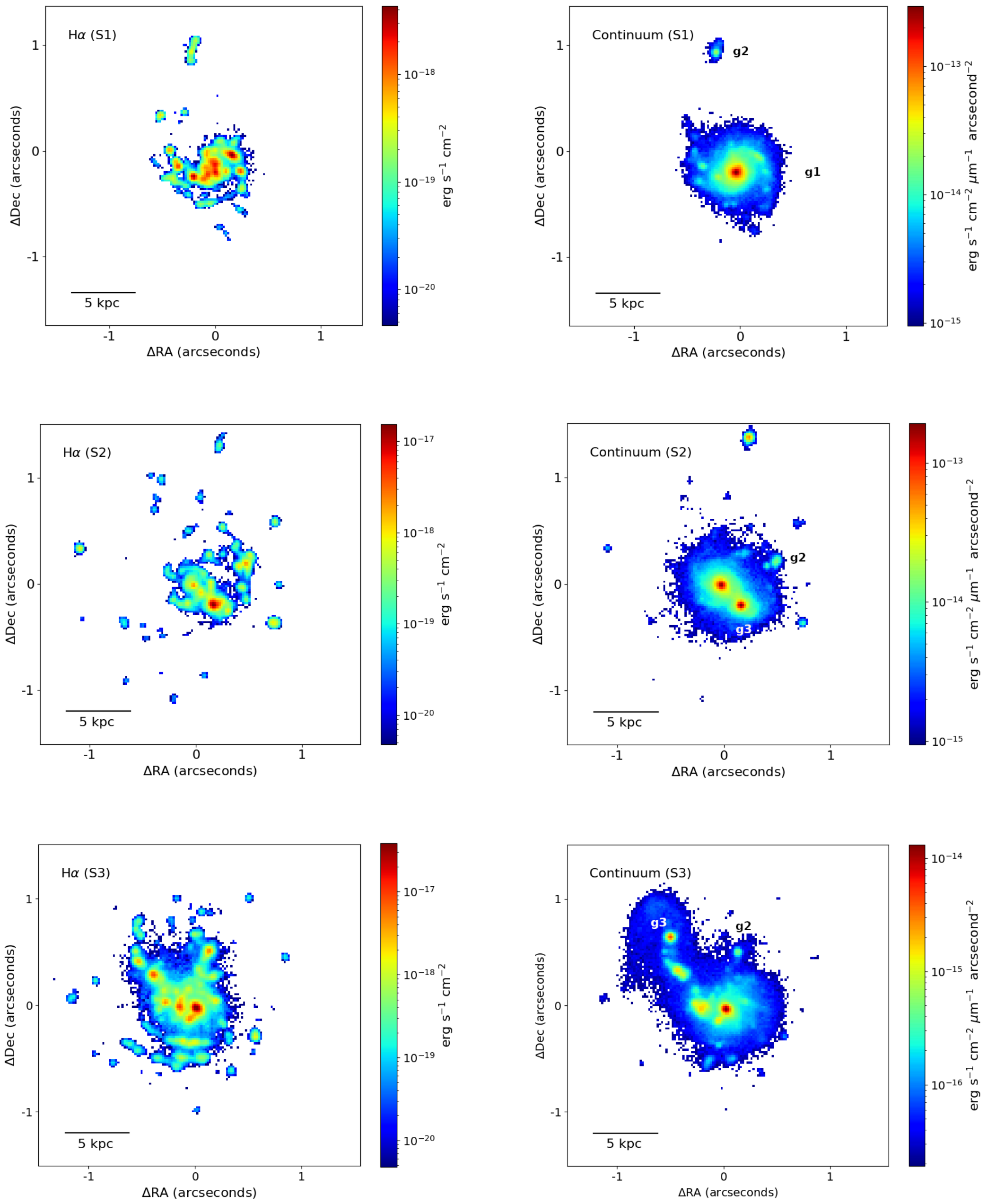

Figure 5.2: Left column: Continuum subtracted intensity map of the Hα emission line in the observed cube without dust for snapshot 1 (top), snapshot 2 (middle) and snapshot 3 (bottom). **Right column:** Intensity map of the optical continuum in the same FOV as the left column. All maps use a 5σ cut, and a scale bar is shown in the bottom left of all plots for reference. The intensity maps are centred on g1, and g2 can be seen at the top of snapshot 1, and it appears within g1's disk in snapshot 2 and snapshot 3. g3 doesn't appear in snapshot 1 and is the second nucleus to the south in snapshot 2. In snapshot 3 it has passed through g1's disk and is located at the north-most peak in snapshot 3's continuum map.

due to the dust more heavily attenuating the brighter regions in comparison to the fainter emission.

For the dust and dust-free continuum, the morphology is similar in snapshot 1 and snapshot 3. As with the Hα maps, the main difference is the contrast between bright and faint regions is less pronounced. Snapshot 2 displays the largest difference, with the southern nucleus (g3) being much more heavily attenuated by dust than the northern nucleus. In both snapshot 2 and snapshot 3, the g2 nucleus appears within the disk of g1, albeit its nucleus is faint compared to the nuclei of g1 and g3. All three galaxies are marked on the maps shown in Figure 5.2.

Looking at both Hα and continuum maps, the spiral arm structure is clear in snapshot 1. In snapshot 2, the continuum nuclei are co-spatial with the strongest regions of Hα emission, with the southern nucleus (g3) being brighter in Hα. In snapshot 3, g3 has passed through the disk of g1, and is now located to the north of g1, causing a clear asymmetry in the Hα and continuum intensity maps.

5.3.2 Kinematics

It is expected that a merger would perturb the observed kinematics, so once again I fit a kinematic model to all the snapshots, and use the same method described in Section 4.4.3 As in the previous chapter, I only focus on the main galaxy, g1. Snapshot 1's kinematics have already been presented in Chapter 4.

For snapshot 2 I fit the receding side, as g3 is in-falling at the approaching side. This fit is only constrained within ~ 2.5 kpc as the S/N is not adequate beyond this radius at the receding side. I set the inclination to 35°, as this was the value input into LCARS, and let ^{3D}BAROLO select the best PA. This snapshot is difficult to model as g1 appears to be rotationally dominated, although the ordered rotation is disturbed in the approaching side of the disk, due to the impact of g3. Also, g3's own kinematics are superimposed on top of g1, and is causing a huge spike in the velocity dispersion in the region surrounding the infalling nucleus (see Figures 5.9 and 5.4). And, although its effect is small compared to g3, g2's kinematics is also superimposed to the northwest of g1. I attempted fitting both sides while

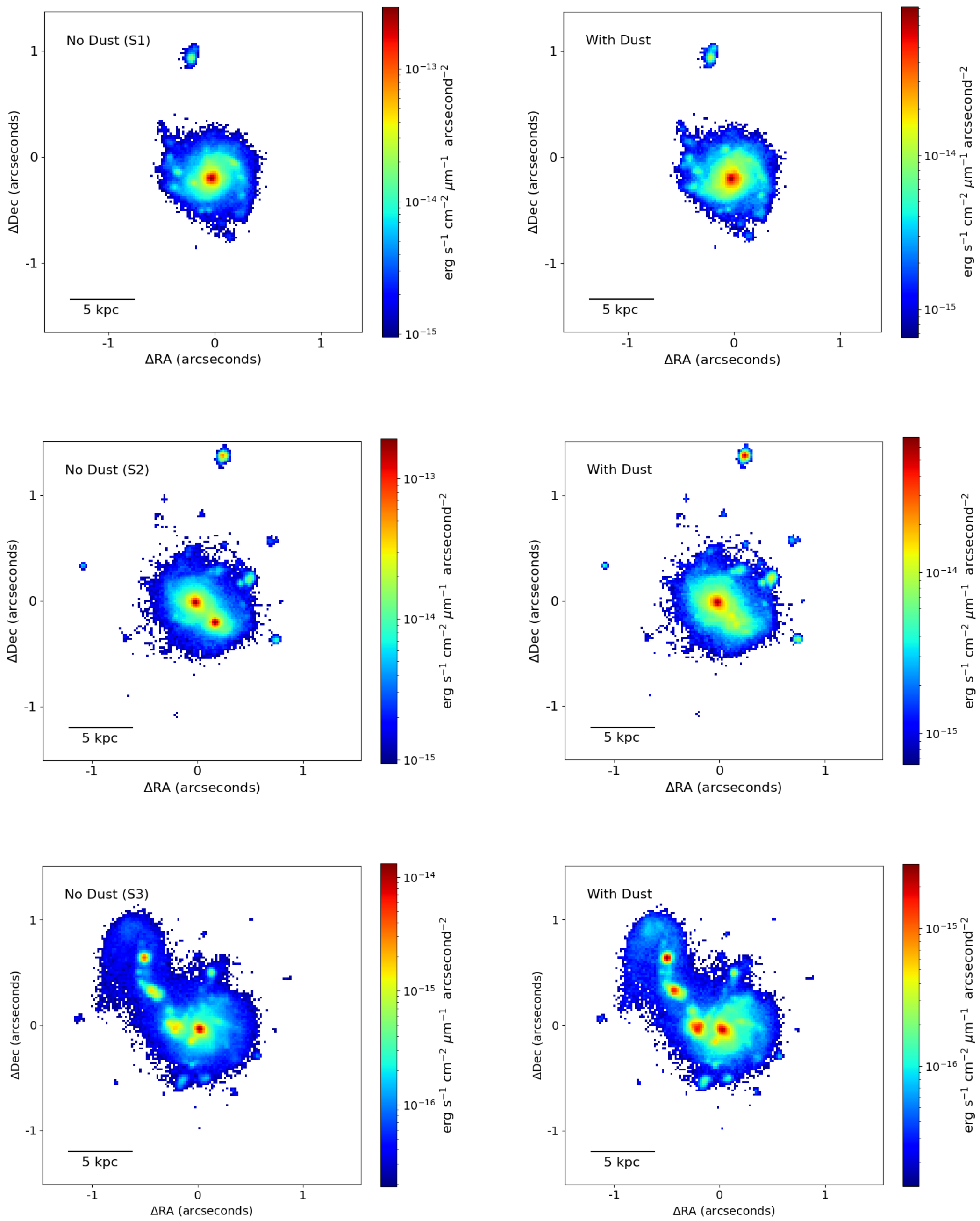

Figure 5.3: Left column: Intensity map of the optical continuum in the HSIM cube without dust for snapshot 1 (top), snapshot 2 (middle) and snapshot 3 (bottom). **Right column:** Intensity map of the optical continuum for the cubes with dust included. All maps use a 5σ cut, and a scale bar is shown in the bottom left of all plots for reference. Snapshot 1 and snapshot 3 have a similar morphology with and without dust, with just the contrast between the brightest and less bright clumps changing. In snapshot 2 the second nucleus begins to disappear and if there was a higher dust to gas phase metallicity ratio, it would be difficult to conclude that this was a merging galaxy based on just rest frame optical photometry.

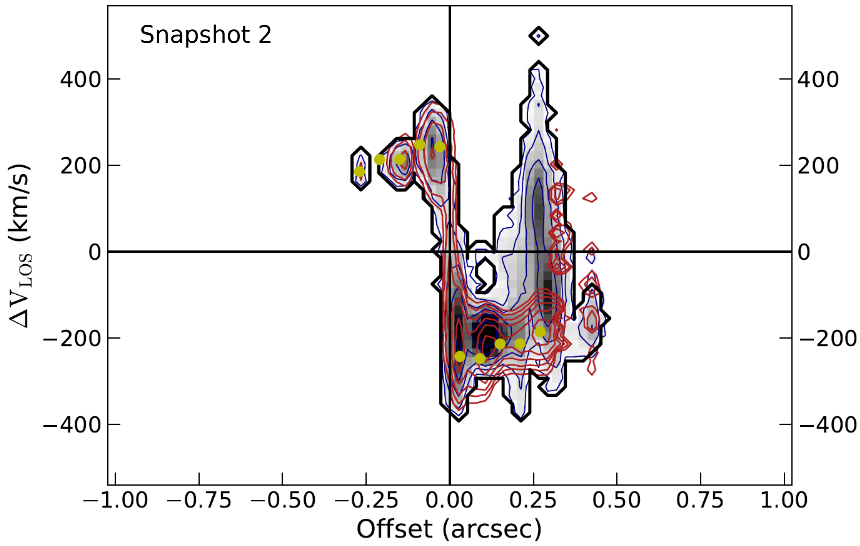

Figure 5.4: Position velocity diagram (output by ^{3D}BAROLO) along the major kinematic axis for the mock observed cube with dust included. The black contours show the observed flux, with the red overlaid contours representing the ^{3D}BAROLO best fit model. The yellow points are the V_{rot} calculated for each ring in the model disk.The y-axis shows the projected rotational velocity and is denoted V_{LOS}. g1 shows a clear rotation, with the infalling g3 causing a disturbance at $\sim 0.3''$. The best fit model was truncated $\sim 0.25''$ to prevent g3 from biasing the fit of g1's disk. The reasoning behind fitting a model rotating to an ongoing minor merger disk is discussed in Section 5.4.1.

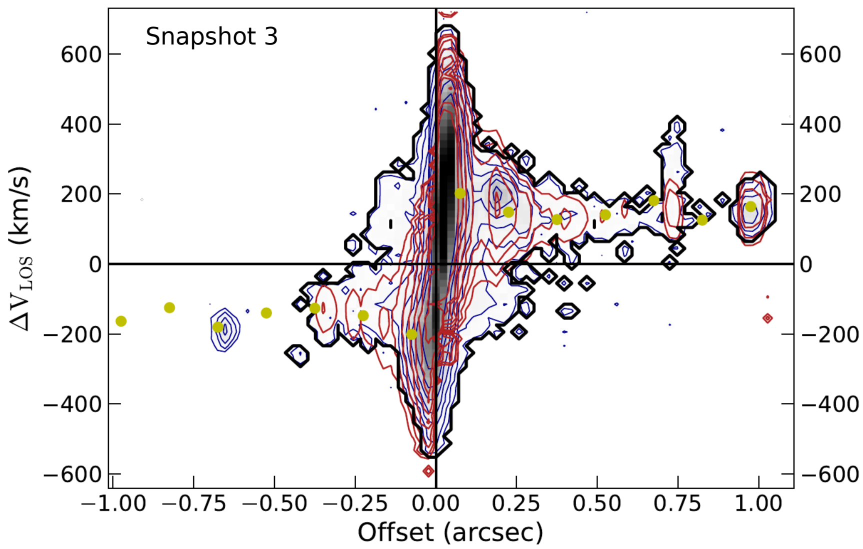

Figure 5.5: The description of the figure is the same as in Figure 5.4. This PV plot shows signatures of a perturbed rotating disk. There is clear evidence of fast moving gas at the centre of the galaxy, which corresponds to a compact region of high SFR.

truncating the model at ~ 1.5 kpc, and the results are similar to fitting the receding side only, with the V_{rot} differing by ~ 40 km s^{-1} and σ_{gas} differing by ~ 5 km s^{-1}. Trying to fit both sides simultaneously beyond this radius means the ^{3D}BAROLO model breaks down, as axial symmetry no longer holds.

Snapshot 3 was fit to both the approaching and receding side simultaneously. The inclination was set to 25° (directly from LCARS), the best fit PA was left to the algorithm, and the ring size was selected to be $0.16''$. In this snapshot, g3 has passed through and perturbed g1's disk, as seen in the top left of Figure 5.7. The larger ring width was selected to give a smoother kinematic fit, as a narrower ring increased the variance in the best fit V_{rot} and σ_{gas}. Allowing the radial velocity parameter to be a free parameter also improved the fit. This gave the rings a radial velocity of between -20 km s^{-1} and 20 km s^{-1} (with one outlier of ~ 100 km s^{-1}) which had the effect of damping the variance in V_{rot} so that the ring with the lowest velocity went from 294 to 311 km s^{-1} and the ring with the highest velocity went from 378 to 364 km s^{-1} in the cubes without dust (there was a similar outcome for the cube with dust). The PV plot in Figure 5.5 shows signatures of a disturbed rotating disk with a large dispersion, and fast moving gas in the centre of the disk where the central starburst is taking place.

As in Chapter 4, the kinematics in the cubes with and without dust agree within error for snapshots 2 and 3, so I only include the maps from the cubes with dust included in Figures 5.6 and 5.7. I also use the same method for error analysis, running ^{3D}BAROLO an additional ten times, keeping all best fit parameters constant while allowing one at a time to vary, and I then calculated the standard deviation of each parameter from these ten runs.

Snapshot 2 and snapshot 3 have been challenging to fit and the best fits contain large residuals, as shown in Figures 5.6 and 5.7. Kinematic modelling algorithms generally assume some form of axial symmetry and a smooth disk, and do not suit high spatial resolution observations where the internal structure has large deviations from a smooth ring (e.g. ^{3D}BAROLO) or a parametric model (e.g. GalPak^{3D}). Inspection of the 0th, 1st and 2nd moment maps show that the

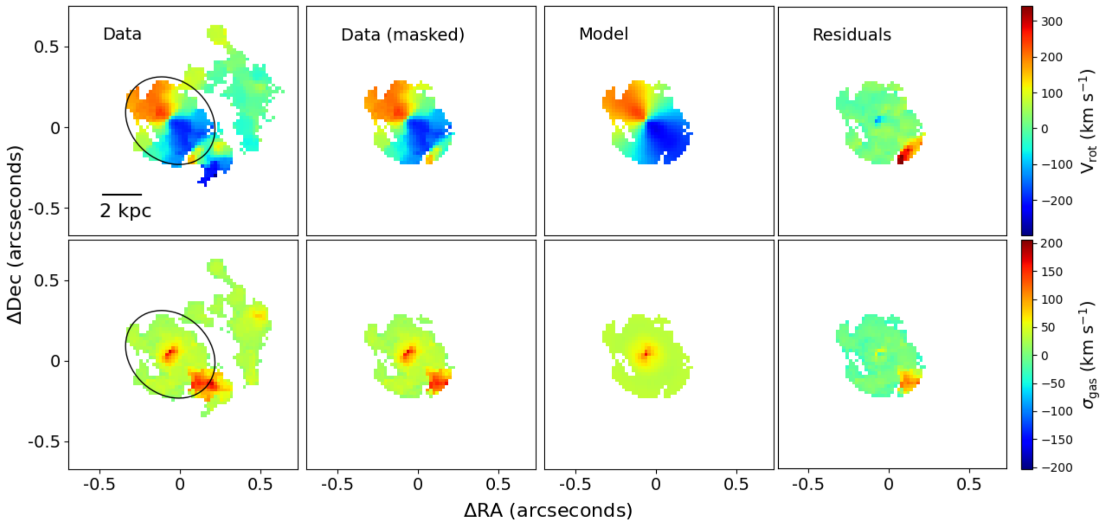

Figure 5.6: Moment maps from the mock observations and best-fit rotating disk model from the observations with dust included. **Top left:** The observed 1st moment map. **Top 2nd from left:** The observed 1st moment map masked at a radius of $\sim$ 2.5 kpc from the centre of g1, the region in which I confined the ^{3D}BAROLO model. This area of this mask is equal to the ellipse plotted in the leftmost column. **Top 2nd from right:** 1st moment map from the best-fit model. **Top right:** The residual velocity field. **Bottom left:** The observed 2nd moment map. **Bottom 2nd from left:** The observed 2nd moment map masked at a radius of $\sim$ 2.5 kpc. **Bottom 2nd from right:** The best-fit 2nd moment map. **Bottom right:** The residual velocity dispersion.

galaxy is perturbed from a simple disk yet also display signatures of a rotating disk (see also the PV diagrams in Figures 5.4 and 5.5). While an axisymmetric kinematic model that assumes ordered rotation is not a perfect fit to the data, it is a good first order approximation. Much of our current observations of the high-z universe have small scale perturbations smoothed out due to seeing limited resolution, or larger beam sizes, so a smooth axisymmetric model works well (in theory ALMA can achieve the 20 mas resolution of HARMONI, but a 20 mas beam size would require long observation times to achieve even a moderate S/N for a typical FIR emission line flux in a normal star forming galaxy at high-z, making these observations impractical).

For real observations, the PA and inclination would have to be determined from a galaxy's morphology and its intensity maps. I used the 'Fit Kinematic PA' code implemented in Krajnovic et al. (2006) and Cappellari et al. (2007) to test the

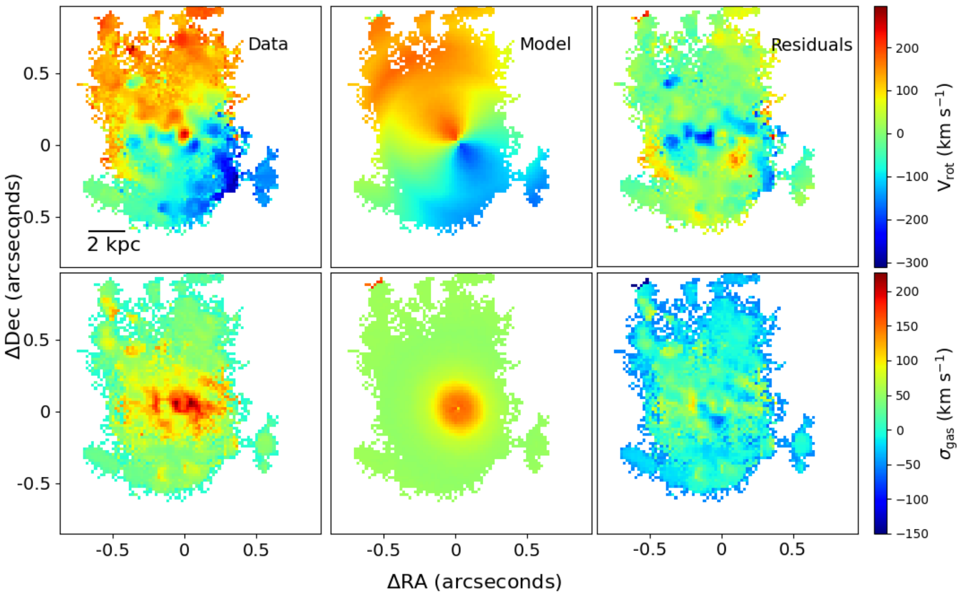

Figure 5.7: Moment maps from the mock observations and best-fit rotating disk model for the observations with dust included. **Top left:** The observed 1st moment map. **Top middle:** 1st moment map from the best-fit model. **Top right:** The residual velocity field. **Bottom left:** The observed 2nd moment map. **Bottom middle:** The best-fit 2nd moment map. **Bottom right:** The residual velocity dispersion.

robustness of my results, and this algorithm agreed with the PA of my best fit model. In general, finding an inclination in a real observation is challenging. Using a Sérsic model, with the Sérsic index as a free parameter, in GALFIT (Peng et al., 2010), I can get an inclination within 10° of the known inclination, so setting the inclination to the known value from LCARS does not bias my results.

5.3.3 Morphology

Clumps

It is clear from the Hα intensity maps of the three snapshots that the galaxies host clumpy star formation. To quantify the size and number of clumps I used the method of Lenkic et al. (2021), in which they studied the clumpy nature of local turbulent disks which are thought to be local analogues to MS galaxies at cosmic noon (Green et al., 2014). This method uses an 'unsharpening' masking technique which removes low-frequency components from the intensity map so that the clumpy structure, which correspond to high spatial frequencies, is enhanced. First, the intensity map is convolved with a Gaussian kernel with a FWHM of 15 pixels to produce a smoothed map. A sharpened image is then produced by blending the original and smoothed maps via:

$$Sharpened = original + (original - smoothed) \times constant \tag{5.1}$$

where the constant determines the lightness or darkness of the edge borders. An edge in image analysis is defined as a rapid variation in the intensity of neighbouring pixels, i.e. high spatial frequencies, and the lightness and darkness refers to the steepness of the gradient of the intensity. I chose a constant value of 15 as per the method of Lenkic et al. (2021).

I then apply a clump finding algorithm to the sharpened images shown in the top row of Figure 5.8. As in Lenkic et al. (2021), I use the blob_log algorithm in scikit-image Python package (Walt et al., 2014). This algorithm uses the Laplacian of Gaussian method, which first convolves an image with a Gaussian filter and then takes the Laplacian of this image. This method elicits a strong response for clumps in an image, as the peak of each clump is a local maxima. The response is maximized when the size of the Gaussian filter is similar to the size of the clump, so the algorithm finds clumps by cycling through a range of kernel sizes, with the maximum, minimum and step size specified by the user.

I impose that clumps must have a minimum of a 3σ enhancement above the sharpened image background and a minimum diameter of 4 pixels so that each clump has at least two spatial resolution elements. Therefore, the minimum standard deviation of the Gaussian kernel is $2/\sqrt{2}$ (maximum response occurs at the zeros of the Laplacian of a Gaussian where the radius = $\sqrt{2}\sigma$[1]). I assume a maximum diameter of 12 pixels to let the algorithm search for kpc size clumps, and I vary the Gaussian kernel in steps of 0.05. The clumps found by the algorithm are plotted in Figure 5.8.

[1] $\nabla^2 \, e^{-r^2/2\sigma^2} \propto (r^2 - 2\sigma^2)e^{-r^2/2\sigma^2}$

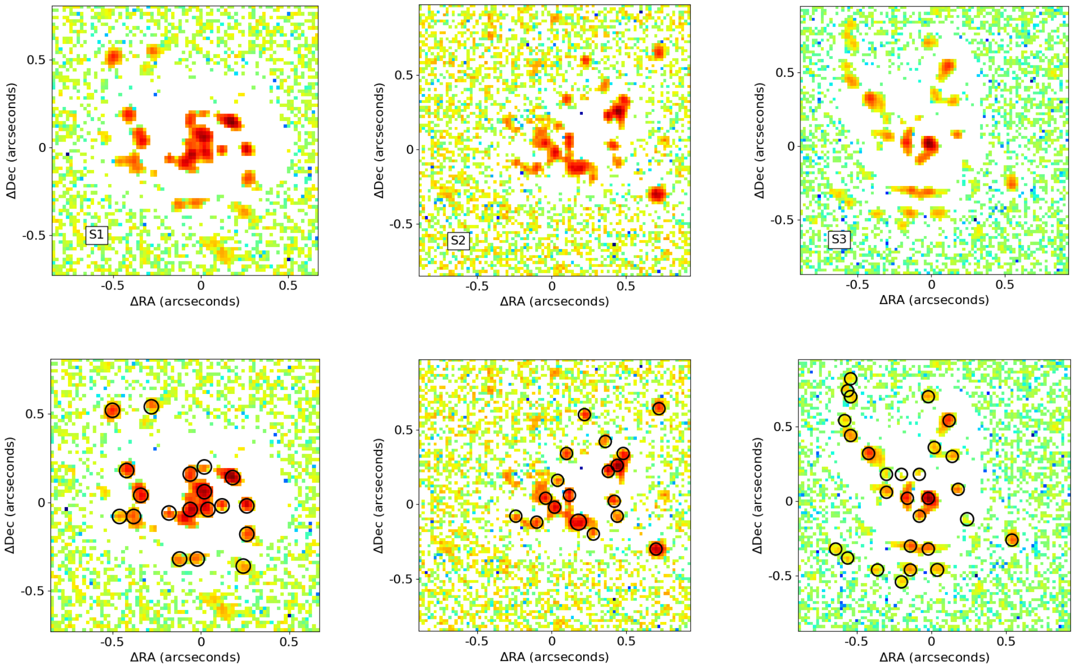

Figure 5.8: Top row: The sharpened Hα maps of g1 with dust included, used to identify Hα clumps, for all three snapshots. These are created using the methodology outlined in Section 5.3.3. **Bottom row:** The circles show the individual clumps found by the clump finding algorithm described in 5.3.3.

Non-parametric Morphology

The morphology of a galaxy is often investigated by fitting analytical models to the surface brightness, and using the parameters of this model to categorize a galaxy, e.g. half-light radius, Sérsic index, axis ratio. Non-parametric methods do not use a fixed functional form and can more easily capture small scale and irregular structure that can be associated with merging and interacting systems (e.g. Förster Schreiber et al., 2011, Baes et al., 2020).

The Gini co-efficient, introduced in Abraham et al. (2003), is a measure of the uniformity of the flux distribution within in the intensity maps of a galaxy. It can take a value between 0 and 1, with G = 0 denoting a constant flux across all pixels and G = 1 indicates that all the flux arises from a single pixel. The Gini co-efficient is defined as

$$G = \frac{1}{\bar{f} N_{pix}(N_{pix}-1)} \sum_{i}^{N_{pix}} (2i - N_{pix} - 1) f_i \qquad (5.2)$$

where $\bar{f}$ is the mean flux in the sky subtracted pixel, N_{pix} is the total number of pixels in the image and f_i is the sky subtracted flux in the i'th pixel. The pixels must also be sorted in order of increasing flux.

The M_{20} indicator (Lotz et al., 2004) is a measure of the second order moment of the brightest 20% of the intensity maps versus the total second order moment of the light distribution. The total second order moment is calculated as

$$M_{tot} = \sum_{i}^{N_{pix}} f_i[(x_i - x_c])^2 + (y_i - y_c])^2] \tag{5.3}$$

where f_i and N_{pix} are defined as above, x_i and y_i are the pixel location, and x_c and y_c are the centroid of the light distribution, which I determined from the centre of the continuum map. The second order moment of the brightest 20% is found by

$$M_{bright} = \sum_i M_i, \text{ while } \sum_i f_i < 0.2 f_{tot} \tag{5.4}$$

where f_{tot} is the total flux arising from the galaxy. M_{20} is then defines as

$$M_{20} = log_{10}\left(\frac{M_{bright}}{M_{tot}}\right) \tag{5.5}$$

The M_{20} indicator is sensitive to bright off-centre structures, so is helpful to identifying merger signatures such as multiple nuclei.

The asymmetry index quantifies the rotational symmetry/asymmetry of the light distribution in a galaxy. It is calculated by rotating the intensity map by 180° and subtracting it from the original map:

$$A = \frac{\sum_{i,j} |f_{i,j} - f_{i,j}^{180}|}{\sum_{i,j} | f_{i,j}|} \tag{5.6}$$

where $f_{i,j}$ is the flux from the i,j'th pixel in the original map and $f_{i,j}^{180}$ is the i,j'th pixel in the rotated map.

Applying these non-parametric models requires care, as the inclusion of sky pixels or the inclusion/exclusion of low surface brightness features can systematically increase or decrease the values calculated in the non-parametric models (e.g. Lotz et al., 2004). When comparing the non-parametric models between my three snapshots I have ensured the same integration time for all three snapshots and the same S/N cut, so that the same surface brightness threshold is used in all three, in order to mitigate the effect of any systematic differences between the three snapshots.

5.4 Results

5.4.1 Kinematic Signatures of a Minor Merger

Figure 5.9 shows the evolution of $\sigma_{\rm gas}$ in the three snapshots taken during the course of the minor merger. In snapshot 1, the $\sigma_{\rm gas}$ peaks in the centre of the galaxy, and most of the disk has a low $\sigma_{\rm gas}$. In snapshot 2, the in-falling nucleus is driving a region of high $\sigma_{\rm gas}$, although much of the disk on the opposite side of g1 remains settled with similar $\sigma_{\rm gas}$ values to snapshot 1. In snapshot 3, $\sigma_{\rm gas}$ is clearly higher in the centre of g1 than in the other snapshots. Taking a simple average over all spaxels in g1 for each snapshot, I find a $\sigma_{\rm gas}$ of 44 km s^{-1} in snapshot 1, 51 km s^{-1} in snapshot 2 and 68 km s^{-1} in snapshot 3. This indicates that although g1 remains rotationally dominated throughout the minor merger, the $\sigma_{\rm gas}$ does increase. These maps are fully in agreement with the $\sigma_{\rm gas}$ measured from fitting the emission line with a single Gaussian, with the $\sigma_{\rm gas}$ going from 145 km s^{-1}, to 134 km s^{-1} and finally 190 km s^{-1} in the non-extinguished cube, and 126 km s^{-1}, to 128 km s^{-1} and 186 km s^{-1} in the cubes with dust.

I have the requisite information to check how the $V_{\rm rot}$ / $\sigma_{\rm gas}$ changes through the three snapshots, and to check if the dynamical ratio can be used to infer the merger status of a galaxy. I use the flux weighted method described in Section 4.4.4 for combining the $V_{\rm rot}$ and $\sigma_{\rm gas}$ values found in each ring of the best fit model, and the results are plotted in Figure 5.10. Snapshot 3 could be fitted out to a larger radius than 6 kpc, but to be consistent with the other two snapshots, I only applied the $V_{\rm rot}$ / $\sigma_{\rm gas}$ calculation to rings $\leq$ 6 kpc.

Both the cubes with and without dust follow a similar trend, with the dynamical ratio decreasing from pre to post g3 perihelion. The dynamical ratio for the cubes without dust goes from 6 $\pm$ 1.6, to 7.9 $\pm$ 6.9 and then 2 $\pm$ 0.5 in the three

Table 5.3: Observed properties of the three snapshots.

Snapshot	$SFR_{H\alpha}$ [1]	V_{rot}	σ_{gas}	V_{rot} / σ_{gas}(Model) [4]	V_{rot} / σ_{gas} [5]	G [6]	M_{20} [7]	A [8]	τ_{dep} [9]	f_{gas} [10]
	$M_\odot$ yr^{-1}	km s^{-1}	km s^{-1}						Myr	
Without Dust										
1	60 ± 4	335 ± 53	56 ± 13	6.0 ± 1.6	4.8	0.61	-2.39	0.36	323 ± 22	0.35
2	75 ± 1	368 ± 49	47 ± 40	7.9 ± 6.2	1.5	0.59	-1.17	0.85	289 ± 4	0.28
3	243 ± 11	337 ± 63	170 ± 23	2.0 ± 0.5	1.3	0.64	-0.96	1.01	94 ± 4	0.35
With Dust										
1	32 ± 2	378 ± 55	65 ± 9	5.8 ± 1.2	4.8	0.54	-2.09	0.40	-	-
2	28 ± 1	396 ± 47	44 ± 13	9.0 ± 5.3	2.7	0.49	-1.72	0.63	-	-
3	120 ± 5	442 ± 42	129 ± 13	3.4 ± 0.5	1.8	0.58	-0.72	1.00	-	-

[1] g1's uncorrected star formation rate < 6kpc radius in the cube without dust extinction.
[2] Flux weighted de-projected rotational velocity from the ^{3D}BAROLO model, see Equation 4.3.
[3] Flux weighted velocity dispersion from the ^{3D}BAROLO model, see Equation 4.3.
[4] Ratio of the de-projected rotational velocity to the velocity dispersion from the ^{3D}BAROLO model.
[5] Dynamical ratio calculated from the flux weighted average of each spatial bin, as discussed in Section 5.4.1.
[6] Gini co-efficient
[7] Second order moment of the brightest 20% of the pixels in the galaxy versus the total second order moment of the light distribution.
[8] Asymmetry
[9] Depletion time. Same value for cubes with and without dust.
[10] M_{gas} / $M_\star$ inside a 6 kpc radius centred on the peak of the continuum in g1. Same value for cubes with and without dust. No errors as these values come directly from the simulation.

snapshots, respectively. The values for the mock observations with dust are 5.8 $\pm$ 1.2, 9 $\pm$ 2.8 and 3.4 $\pm$ 0.5.

Snapshot 2 appears to have a higher dynamical ratio, albeit with huge errors, due to fitting a truncated model disk to an ongoing minor merger. This shows the V_{rot} / σ_{gas} indicator is not appropriate to use in this snapshot, as g3 is only $\sim$ 2 kpc from the centre of g1 so the kinematics of g1 and g3 are superimposed (see leftmost column in Figure 5.6). Fitting a simple axisymmetric disk model is not adequate to disentangle two galaxies superimposed on each other. As discussed in Section 5.3.2 the model was fit to the $\sim$ 2.5 kpc around the centre of g1, so the V_{rot} / σ_{gas} is only tracing the inner region of g1 which is still strongly rotationally supported, as g3 hasn't perturbed the central region of g1 yet. Therefore, I am not comparing like with like in the three snapshots, as in snapshot 1 and snapshot 3 I am calculating a V_{rot} / σ_{gas} value for the entire galaxy (as far as S/N allows).

To place the three galaxies on an equal footing, I again use Equation 4.3 to get a flux weighted V_{rot} / σ_{gas}. But instead of calculating this quantity for the n radial rings in the best fit model disk, I now take n to be each spatial bin, i.e. I calculate a V_{rot} / σ_{gas} for each pixel in the 1st and 2nd moment maps and then compute a flux weighted sum. I take the inclination corrected $V_{rot,n}$ from each bin in the observed 1st moment maps (top left column in Figures 4.7, 5.6 and 5.7) and I use all values in snapshot 2, not just those inside the region in which I fitted the model disk. Likewise, $\sigma_{gas,n}$ was taken from the observed 2nd moment maps (bottom left column in Figures 4.7, 5.6 and 5.7). I then use the flux from the intensity maps for the weighting and plug all these values into Equation 4.3. This method ensures I can use all values in snapshot 2 and compare each galaxy equally, in that all spatial bins above the S/N threshold inside 6 kpc are used. The results are shown in Figure 5.11.

I should note that the $V_{rot,n}$ is not corrected for bins being off the major kinematic axis[2], which means I am calculating a lower $V_{rot,n}$ for all bins off the major kinematic axis. But, as the intrinsic V_{rot} is $\sim$ 350 - 400 km s^{-1} in all three

[2] $V_{los,obs} = V_{rot,int} \cos(\theta) \sin(i)$, where i is the inclination and θ is the angle between the major kinematic axis and the vector connecting a given spatial bin to the centre of the galaxy.

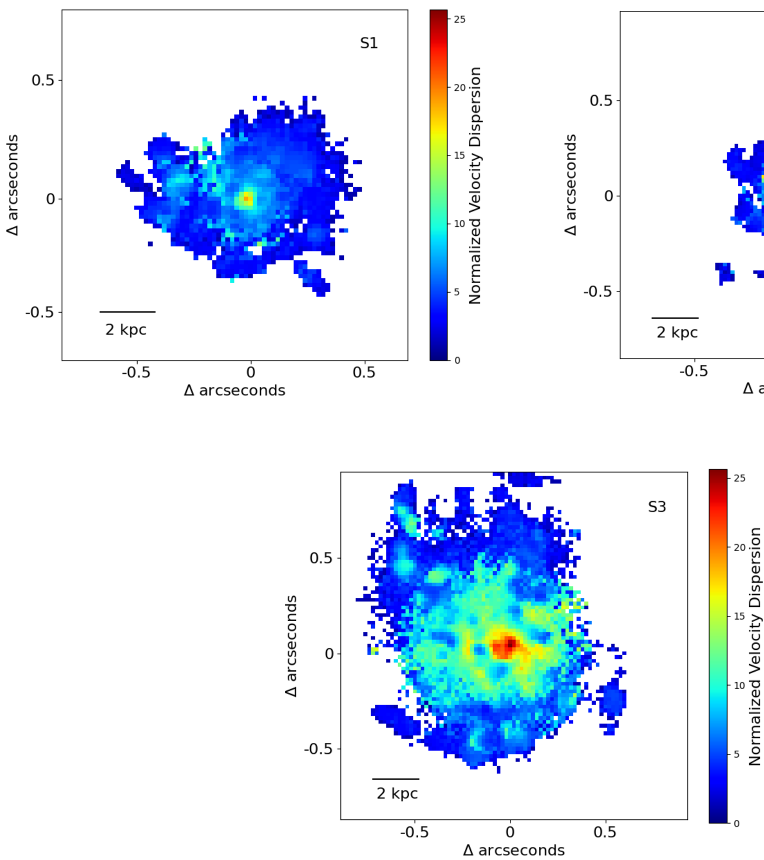

Figure 5.9: The evolution of the velocity dispersion from snapshot 1 (**top left**), to snapshot 2 (**top right**) and finally snapshot 3 (**bottom**). The three maps are normalized to the lowest σ_{gas} value found across the 3 maps, and all three have the same colour scaling. The average σ_{gas} increases from snapshot 1, through snapshot 2 to snapshot 3 showing the minor merger increased the observed σ_{gas}. These are from the dust free cube, but the cubes with dust look similar, with the difference being some diffuse low σ_{gas} regions are below the S/N cut.

snapshots, and I am using the same 6 kpc radius region in all calculations, it follows that the correction would be similar in all three snapshots, and this wouldn't change the decreasing trend of the dynamical ratio. A possible drawback of this method is that it is sensitive to S/N as the outer regions of a galaxy tend to be more rotation dominated, and these would be down-weighted in a flux weighted sum, and could be below the noise threshold. Cappellari (2016) limit the calculation to a region inside one effective radius, but in an observation like snapshot 2 and snapshot 3, it is difficult to define an effective radius, due to the presence of multiple nuclei. Also, correcting for $\cos(\theta)$ will become an issue when comparing

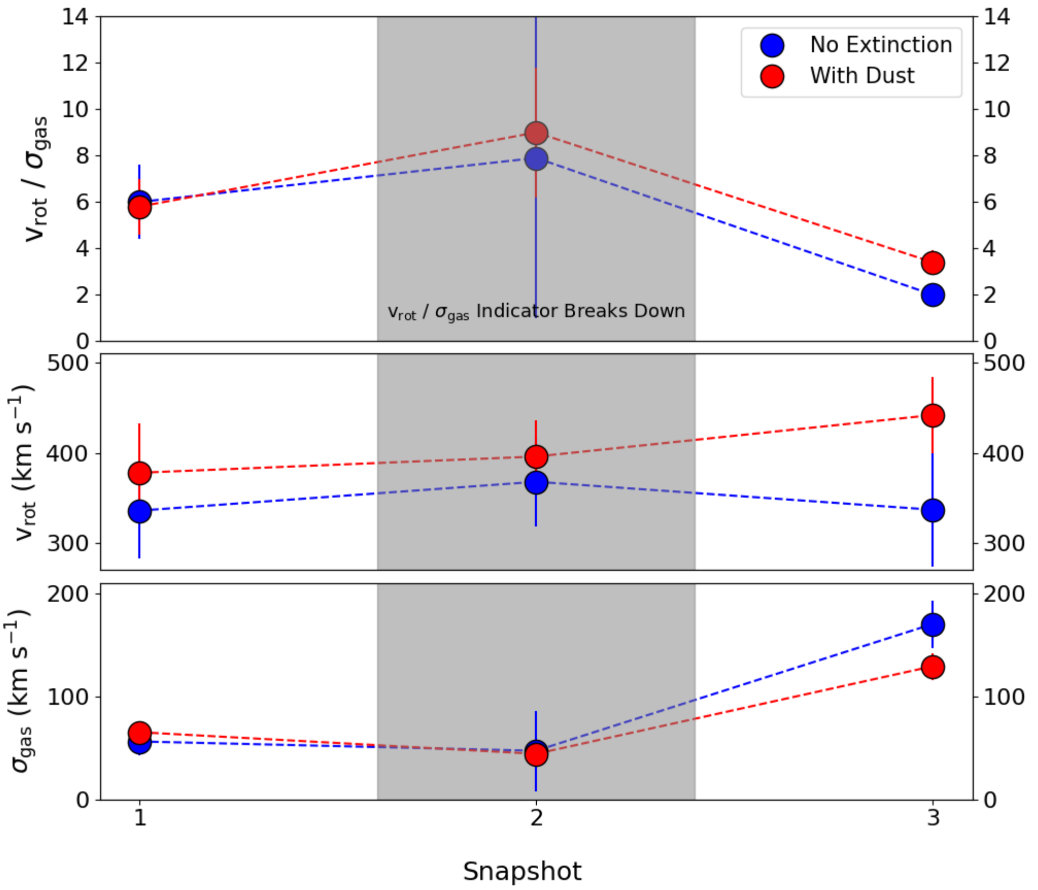

Figure 5.10: Top: The evolution of the dynamical ratio for the three snapshots, with similar trends found for the cubes with and without dust. **Middle:** The flux weighted V_{rot} used to calculate the dynamical ratio. **Bottom:** The flux weighted σ_{gas} used to calculate the dynamical ratio. The V_{rot} / σ_{gas} decreases from the pre-merger phase in snapshot 1 to snapshot 3, when g3 has passed through the disk of g1. The minor merger perturbs g1's disk and increases σ_{gas}, yet g1 remains rotationally dominated. The dynamical ratio breaks down in snapshot 2 as the kinematics of both g1 and g3 are superimposed in the line of sight and an axisymmetric parametric model cannot capture the complex kinematics.

a sample of galaxies. This will be difficult, as dividing by a small number ($\cos(\theta)$ approaches zero around the minor kinematic axis) can cause slight perturbations in the circular velocity to blow up.

Dust seems to bias the dynamical ratio in both the methodologies I have used. This is due to the cubes with dust having a systematically higher V_{rot} / σ_{gas} than the cubes without dust, as a lot of high σ_{gas} regions are co-spatial with high SFR regions which tend to have higher dust column densities. Consequently, these

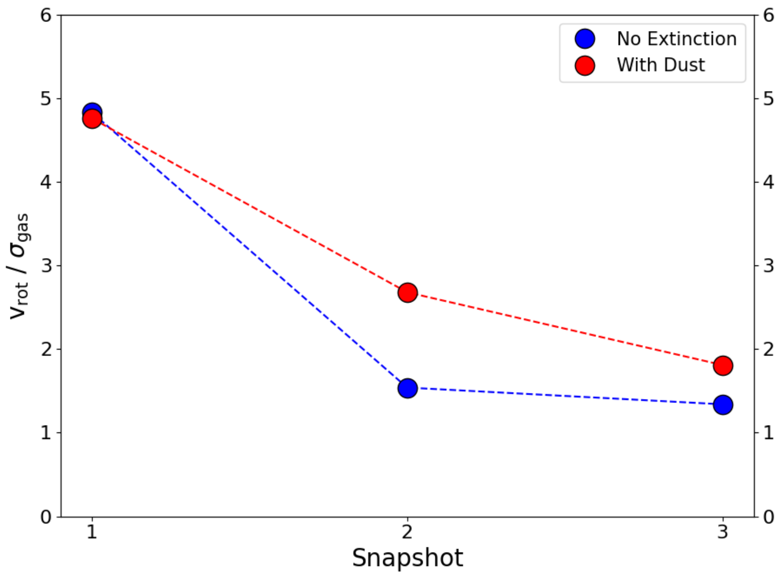

Figure 5.11: The evolution of the dynamical ratio for the three snapshots, using the flux weighted ratio of V_{rot} / σ_{gas} taken from each spatial bin within 6 kpc. Using this method, the dynamical ratio doesn't break down in snapshot 2, and the dynamical ratio monotonically decreases as the minor merger progresses.

regions are heavily attenuated and down-weighted to a greater extent than more quiescent star forming regions with less σ_{gas}. If this was a much dustier system, e.g. having a dust attenuation equivalent to the KMOS galaxies in Chapter 2, the V_{rot} / σ_{gas} may be driven to higher values.

Referring back to Section 4.6.2, different measures of σ_{gas} have been used throughout the literature and each have their merits. The differing definitions mentioned in that section all reveal the galaxy to be rotationally dominated, with the calculated V_{rot} / σ_{gas} > 2 for snapshot 3 irrespective of which method I use, with V_{rot} / σ_{gas} > 2.5 for both snapshot 1 and snapshot 2. If I use the σ_{gas} from the outer regions of the disk ($\approx \sigma_0$ as the outer rings are approaching an asymptotic value), V_{rot} / σ_{gas} > 5 for snapshot 3 and > 10 for snapshot 1 and snapshot 2.

One consistent result amongst the methods is that V_{rot} / σ_{gas} decreases between snapshot 1 and snapshot 3, as shown in Figures 5.10 and 5.11. This is due to the rise in the velocity dispersion as the minor merger proceeds, clearly seen in the bottom two panels in Figure 5.10 and also the maps in Figure 5.9. The V_{rot} doesn't change

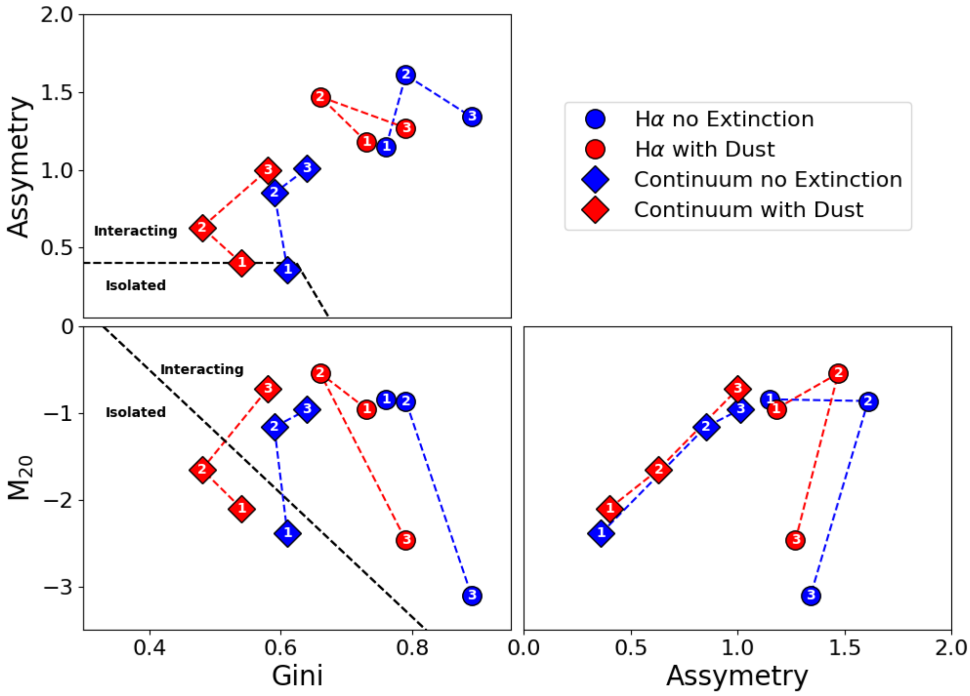

Figure 5.12: The non-parametric morphology indicators: Gini co-efficient, asymmetry index and the M_{20} indicator, plotted against each other for the three snapshots. The red data points correspond to the cubes with dust, and the blue data points are from the dust free observations. I have used the same methodology on the continuum (diamonds) and Hα (circles) maps. The dashed lines show threshold values for isolated versus mergers calculated by Lotz et al. (2008). The indicators calculated from the continuum show clear tracks from isolated to interacting, although snapshot 2's dust observation is misclassified in the M_{20} - Gini parameter space (the second nucleus is strongly attenuated by dust, see Figure 5.3). This figure shows the indicators break down when applied to my Hα maps.

as much, in relative terms, across all snapshots, so it is the rise in σ_{gas} that causes the decrease on the dynamical ratio.

5.4.2 Evolution of Morphology During a Minor Merger

Photometry has been used to classify galaxies since the time of HST, and it is important to check if the thresholds used to differentiate between a minor merger and an isolated galaxy (e.g. Lotz et al., 2008) will also hold in high spatial resolution HARMONI observations. The advantage of using cubes with and without dust is that I can use the cubes without dust to ensure non-parametric indicators are classifying each snapshot correctly, before checking how dust affects this categorization.

I apply the indicators listed in Section 5.3.3 to the continuum maps, as these indicators are usually performed on photometry in optical filters which are similar to my continuum observations (results are given in Table 5.3). I also apply them to the Hα maps, as non-parametric morphology indicators have been successfully used on high spatial resolution CO observations in the local universe (e.g. Davis et al., 2022), so it is worth exploring if Hα at high-z could also be used to classify a galaxy (the H_2 - SFR relations can break down on scales of 100 pc or less as CO and Hα peaks don't overlap, e.g. Schruba et al., 2010, so the comparison is not quite like with like). There has been some work done on applying these indicators to emission lines at high-z (e.g. Förster Schreiber et al., 2011, Guaita et al., 2015) but nothing that will match the resolution and sensitivity of HARMONI.

Firstly, I plot the Gini, M_{20} and asymmetry indicators against each other and use the threshold values of Lotz et al. (2008) to divide the M_{20} - G and G - A parameter spaces into isolated galaxies versus mergers, and this is shown in Figure 5.12. Lotz et al. (2008) calculated these thresholds from simulated SDSS observations and although they are calibrated for galaxies at $z < 1$, these thresholds correctly identify my non-dust observations as isolated or mergers, where I assume g1 in snapshot 1 being categorized as isolated is correct, as all other indicators classify it as isolated (see discussion in Section 4.6.1). To classify mergers from asymmetry alone, a threshold of $A > 0.35$ has been suggested by Conselice (2003) based on local mergers and the same threshold was used by Wilkinson et al. (2022) to find the merger fraction of post starburst galaxies. Lotz et al. (2004) utilized $A > 0.4$ as the criteria for local ULIRGs and this is the value I adopt as my threshold, as it gives the correct classification for all three snapshots.

For the cubes with dust, the G - A parameter space, and asymmetry alone, also correctly categorizes the three snapshots. But, even though the G - A is correctly classifying snapshot 2 as a merger, the cube with dust is closer to the isolated box than the dust free observation. Likewise, the asymmetry in snapshot 2 has a lower value, so the level of dust obscuration does bias the indicators. The M_{20} - G indicator incorrectly deduces snapshot 2 to be an isolated galaxy for the cube with dust. This is due to dust attenuating the second nucleus (g3) as can be seen in Figure 5.3. Just to reiterate, the 1% ratio of dust to gas phase metallicity that I am using gives a moderate dust obscuration, and yet the morphology indicators are affected. In future work, the ratio needs to be increased to similar levels as observed in the U/LIRGs in Chapter 2, and check how a larger column density of dust modifies the morphological indicators.

As can be seen in Figure 5.8, g1 retains its clumpy star forming structure throughout the course of the minor merger, with the number of star forming clumps increasing in snapshot3. The Hα non-parametric morphology indicators break down, and do not correctly classify the snapshots, due to this clumpy composition of the Hα emission. The asymmetry in Hα deviates from the continuum values, as it is unlikely two Hα clumps will coincide when an image is rotated by 180°. M_{20} and the Gini co-efficients differ between Hα and continuum due to the many bright off centre clumps observed in Hα.

As I have only observed one merger, from only one line of sight per snapshot, more work is needed to calibrate high-z morphology indicators, including increasing the sample size of mergers, and getting multiple viewing angles per merger.

5.4.3 Evolution of SFR

As outlined in Section 4.4.2, the $SFR_{H\alpha}$ for g1 in the three snapshots is found by applying the conversion factor of Murphy et al. (2011b) to the integrated Hα flux extracted from an aperture 6 kpc in radius. I get an intrinsic $SFR_{H\alpha}$ of 60 $\pm$ 4 $M_\odot$ yr^{-1}, 75 $\pm$ 1 $M_\odot$ yr^{-1} and 243 $\pm$ 10 $M_\odot$ yr^{-1} in snapshot 1, snapshot 2 and snapshot 3 respectively, signifying that a minor merger increases the instantaneous star formation within a galaxy. This is plotted in Figure 5.13. If I had chosen an aperture twice the radius, the $SFR_{H\alpha}$ for the three snapshots would only be higher by 6 $M_\odot$ yr^{-1}, 12 $M_\odot$ yr^{-1} and 26 $M_\odot$ yr^{-1} respectively, so the trend remains the same.

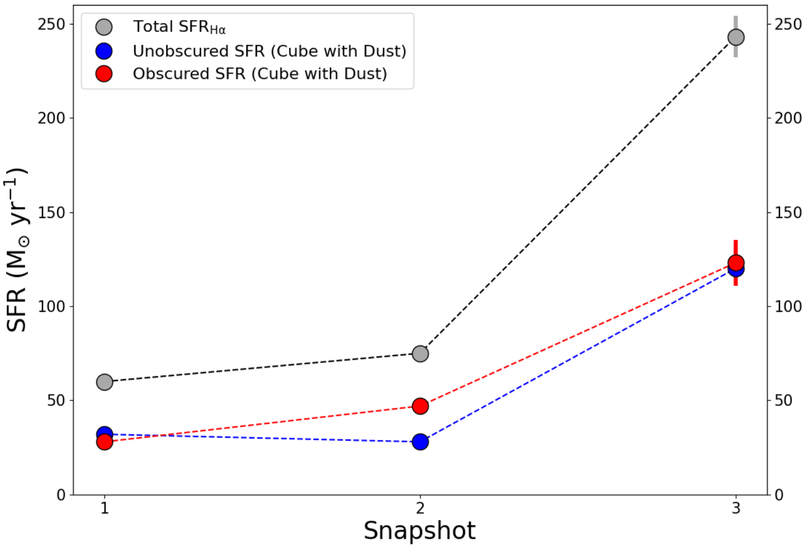

Figure 5.13: The evolution of the SFR across the 3 snapshots. The grey data points represent the total SFR as calculated from the Hα cube without dust, and using the Hα - SFR conversion factor from Equation 2.1. The blue data points show the uncorrected SFR taken from the Hα cube with dust included, and is a proxy for the unobscured SFR. The red points are the dust obscured SFR which is the difference between unobscured SFR and total SFR. This plot shows the relative fraction of obscured SFR is greatest in snapshot 2, as the burst of star formation occurring around the infalling nucleus is heavily dust obscured. Error bars are not visible for snapshot 1 and snapshot 2 as they are roughly the size of the data points.

Observationally, it has been found that local mergers can form compact star forming regions and in these regions optical indicators of the SFR, can be orders of magnitude lower than the SFR calculated from the IR SED (e.g. Rodríguez-Zaurín et al., 2011). With these results in mind, I can check how the dust obscured SFR changes throughout the three snapshots, calculated using the same method as Section 4.5.1. I find a similar trend to the unobscured SFR, with dust obscured SFR (the hypothetical SFR$_{IR}$ discussed in Section 4.5.1) of $\sim$ 28 $M_\odot$ yr^{-1}, 47 $M_\odot$ yr^{-1} and 123 $M_\odot$ yr^{-1} in the snapshot 1, snapshot 2 and snapshot 3 respectively.

While I stress that the pipeline does not include radiative transfer of the dust, I can estimate an IR luminosity for each snapshot by assuming both radiative transfer balance and that all radiation absorbed by the dust would be re-emitted in the IR if these were real galaxies. That being the case, the dust obscured

SFR calculated in the previous paragraph can be used as a proxy for the SFR_{IR}. By using the L_{IR} - SFR_{IR} conversion factor of Murphy et al. (2011b) I find that snapshot 1 would be a low luminosity LIRG, with a $\log(L_{IR} / L_{\odot}) \sim 11.3$, whereas snapshot 3 is a high luminosity LIRG with $\log(L_{IR} / L_{\odot}) \sim 11.9$. This agrees with the known properties of local LIRGs, where increasing IR luminosity is linked to mergers and interactions (e.g. Kartaltepe et al., 2010, Larson et al., 2016). Once again, I reiterate that Hα and L_{IR} trace different age ranges of recently formed stars, so the L_{IR} is just a rough approximation.

It is interesting to note a burst of star formation occurs around the in-falling nucleus (g3) during snapshot 2 and not in the centre of g1. An $SFR_{H\alpha}$ of 25 $\pm$ 1 $M_{\odot}$ yr^{-1} is found in a 1 kpc diameter centred on the g3 nucleus, which accounts for one third of the SFR in this snapshot. A central starburst doesn't occur in g1 until snapshot 3, which suggests there is a lag between the initial impact of g3 and an increase in the SFR of g1. This central starburst has an $SFR_{H\alpha}$ of 71 $\pm$ 2 $M_{\odot}$ yr^{-1} in the central 1kpc region.

The starburst regions in snapshot 2 and snapshot 3 seem to be heavily attenuated based on the difference of $SFR_{H\alpha}$ with and without dust, with snapshot 2's burst of star formation decreasing from 25 $\pm$ 1 $M_{\odot}$ yr^{-1} to 2 $\pm$ 0.05 $M_{\odot}$ yr^{-1} and snapshot 3's going from 71 $\pm$ 1 $M_{\odot}$ yr^{-1} to 27 $\pm$ 1 $M_{\odot}$ yr^{-1}, if uncorrected for dust extinction. Using the same arguments as in the previous paragraph, these 1 kpc regions would have a LIRG like luminosity. Also, these regions of high SFR are relatively compact, similar to the star forming regions in local U/LIRGs, which have sizes of 0.3 - 2 kpc (e.g. Alonso-Herrero et al., 2006, Pereira-Santaella et al., 2018).

Using the $M_{\star}$ taken from NewHorizon I place the three snapshots on the $M_{\star}$ - SFR plane and find that all three snapshots appear within the scatter of the MS (see Figure 5.14) despite undergoing a minor merger. I also placed g2 on the $M_{\star}$ - SFR, and its SFR is below the MS as it spirals into g1 (I do not include g2 data points for snapshot 2 and snapshot 3 as g2 and g1 have coalesced in these snapshots). These results will be further discussed in Section 5.5.1.

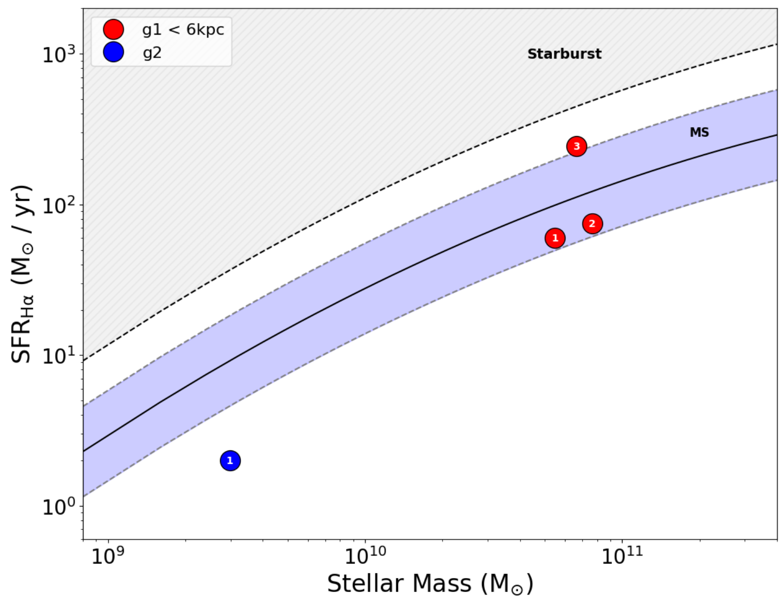

Figure 5.14: The location of g1 (red circles) and g2 (blue circle) on the stellar mass - SFR plane. The number inside each circle shows which snapshot each data point corresponds to. The black line is the MS of Whitaker et al. (2014), with the blue region showing the typical MS scatter of 0.3 dex. The grey region shows the location of starburst galaxies. Despite the increase in SFR as g1 undergoes a minor merger, it still remains within the scatter of the MS. g2, which is inspiralling around g1, shows an SFR below the MS, which is suggestive of its star formation being inhibited as it spirals into g1. g2 is only included for the first snapshot, as it has coalesced with g1 in the latter two snapshots. Note $M_\star$ for g1 is larger in snapshot 2, as the 6 kpc radius aperture covers both g1 and g3 (see Table 5.1.) Error bars are not included on the plot as the error in SFR is roughly equivalent to the size of the data points, due to the high S/N, and the stellar mass is taken directly from the simulation. g3 doesn't appear, as it isn't possible to isolate both its SFR and stellar mass in either snapshot 2 or snapshot 3.

5.4.4 SFE and Gas Fraction

As outlined in Section 1.4, both SFE and gas fraction increase with distance above the MS and remain approximately constant along the MS, and these findings have been observed to hold up until at least cosmic noon.

Taking the $M_\star$ and M_{gas} directly from the NewHorizon simulation, I calculate the SFE and gas fraction, $f_{gas} \equiv M_{gas} / M_\star$, for both the 6 kpc aperture and the total FOV of the cube, and I will refer to the full FOV as the system. As a reminder, the FOV contains only g1 and g2 in snapshot 1, whereas the other two snapshots contain g1, g2 and g3. The evolution of the SFE and the f_{gas} is plotted in Figures

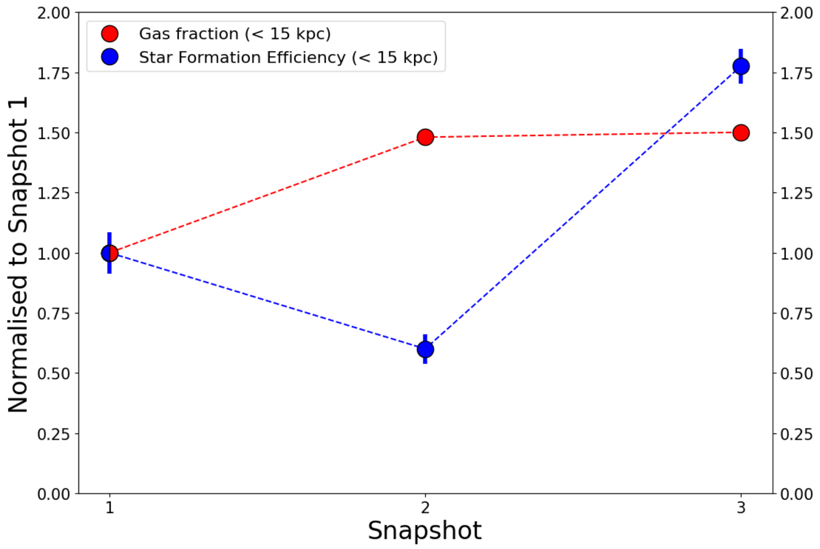

Figure 5.15: The evolution of the SFE and gas fraction, M_{gas} / $M_{\star}$, within a radius of 15 kpc centred on the continuum peak of g1 (the mock observations have a FOV of $\sim$ 30 kpc). Snapshot 1 includes just g1 and g2 in the aperture, whereas snapshot 2 and snapshot 3 contain all three galaxies. The gas fraction increases in snapshot 2 due to g3 entering the system, and then remains roughly constant. The SFE decreases in snapshot 2 due to the increase in gas mass, without a proportional increase in star formation, and the SFE then increases in snapshot 3 as g1 undergoes a burst of star formation due to the impact of g3. Error bars are not visible on some data points as they are smaller than the data points.

5.15 and 5.16. For the system, I find that f_{gas} increases between snapshot 1 and snapshot 2, as g3 enters the system, and then broadly remains constant between snapshot 2 and snapshot 3. The SFE decreases between snapshot 1 and snapshot 2 as the increased M_{gas} has not yet been converted into a higher SFR.

For the 6 kpc radius aperture centred on g1, the f_{gas} remains relatively constant across all three snapshots and the SFE is similar between snapshot 1 and snapshot 2. In snapshot 3, after g3 has passed through the disk of g1, the SFE increased by a factor of $\sim$ 3 above both snapshot 1 and snapshot 2. This shows that it is the SFE that is driving the burst of star formation in g1 due to the impact of the minor merger.

It is not until snapshot 3 that the SFE and SFR increases, but the disturbance in morphology is evident in snapshot 2. This suggests a lag between a morphological

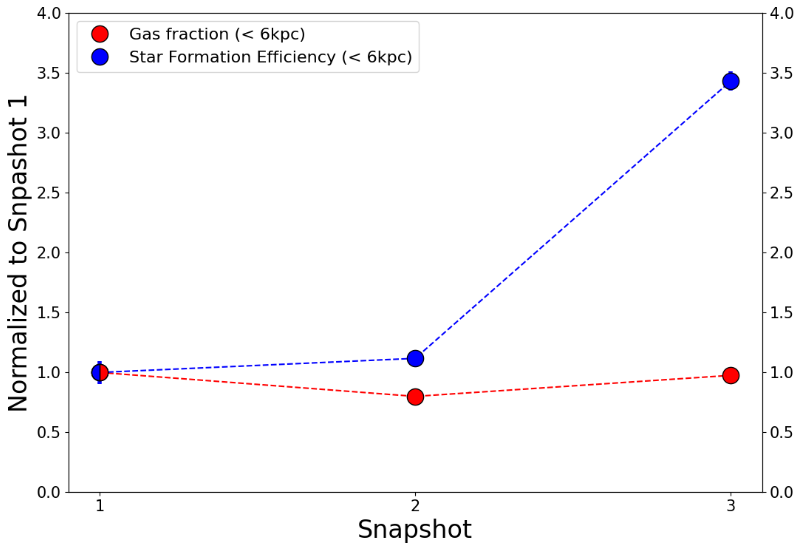

Figure 5.16: The evolution of the SFE and gas fraction within a radius of 6 kpc centred on the continuum peak of g1, which I define as the maximum extent of g1 in snapshot 1 (see Section 4.4). The gas fraction stays relatively constant throughout all the snapshots, but the SFE increased by a factor of three between snapshot 2 and snapshot 3. This suggests that the increase in SFR between snapshot 2 and snapshot 3 is powered by an increased SFE and not an increased gas fraction. Error bars are not visible on some data points as they are smaller than the data points.

indicator that a minor merger is taking place and an SFR/SFE indicator of a merger taking place.

It should be noted that the M_{gas} I use is taken from NewHorizon and doesn't differentiate between molecular or atomic gas, so the SFE and f_{gas} calculated in this chapter cannot be directly compared to observations of galaxies at high-z, which often uses molecular gas when calculating these properties (f_{gas} has been defined in terms of M_{mol} / $M_{\star}$ in the previous observational chapters of this thesis).

5.4.5 Evolution of Dust Obscuration

I use two proxies to infer the dust obscuration and its evolution in the three snapshots. The first proxy for the column density of dust is the ratio of the continuum in the cube with dust to the continuum in the cube with no extinction. Taking both extremes, a ratio of one tells us that there has been no extinction, so no dust is in the line of sight, whereas a ratio of zero means the stellar light has

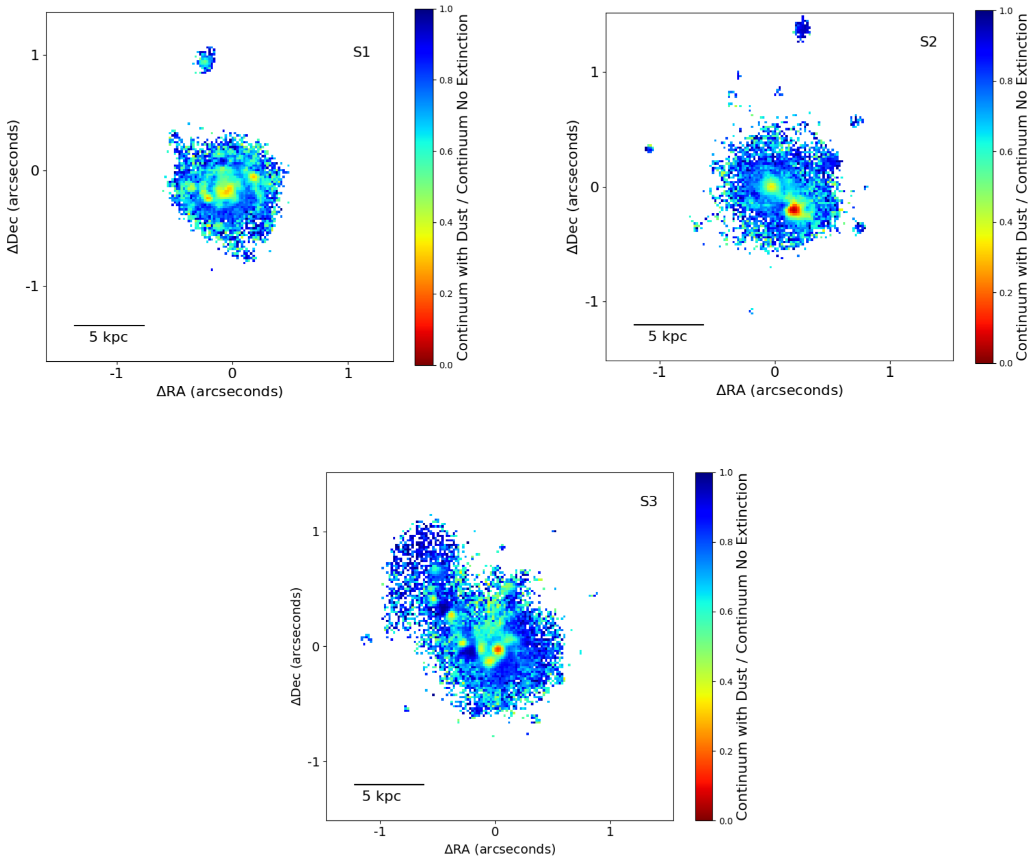

Figure 5.17: The ratio of continuum with dust to continuum without dust, which is a proxy for the dust column density, for snapshot 1 (**top left**), snapshot 2 (**top right**) and snapshot 3 (**bottom**). A value of zero means all the continuum flux has been attenuated and infers a high dust column density, whereas a ratio of one denotes there is no dust in the line of sight. For snapshot 1 and snapshot 3, the peak of the dust is co-located with the peak of g1's continuum, whereas in snapshot 2 the peak of the dust is co-located with the in-falling g3 nucleus and is ~ 2 kpc from the continuum peak of g1. The most attenuated region across all three snapshots is located around the infalling g3 nucleus in snapshot 2.

been fully attenuated and implies a large column density of dust. Mapping this ratio, see Figure 5.17, allows a deduction of the distribution of the dust and regions of high opacity. The second proxy is taking the SFR from the cube with dust away from the SFR calculated from the cube with no extinction. This difference gives us the obscured star formation, and a larger obscured star formation implies a greater column density of dust.

To reiterate, in all three snapshots the dust to gas phase metallicity is held at a constant 1%, so the three snapshots are directly comparable. The most heavily obscured region is the in-falling g3 nucleus, and its corresponding burst of star formation, in snapshot 2 with up to 95% of the continuum photons attenuated in the centre of the nucleus. The second most dust obscured region is the star forming region in the nucleus of g1 in snapshot 3, with up to 90% attenuation.

I was conservative with the choice of 1% dust to gas phase metallicity ratio. For example, Richardson et al. (2020) generated mock HARMONI observations of a $z \sim 1.5$ star forming galaxy, with an SFR of 3 $M_\odot$ yr^{-1} and assumed an 8% ratio. Taking the ratio of unobscured star formation to the total SFR I get ≈ 0.5 which is much higher than the ratio of ≈ 0.1 measured in the KMOS galaxies in Chapter 2, and in future work the effect of a higher dust to gas phase metallicity ratio will be explored.

As in Figure 4.12, I can get the spatial location of the dust obscured SFR by subtracting the cube with dust from the non attenuated cube, and the dust obscured SFR for snapshot 2 and snapshot 3 is plotted in Figure 5.18. These maps demonstrate the obscured star formation has a clumpy structure with the regions of highest obscured star formation being around the g3 nucleus in snapshot 2 and the g1 nucleus in snapshot 3, similar to the unobscured star formation, in Figure 5.1.

Clumpy structure has been observed in the dust continuum (e.g. Hodge et al., 2019), although a smooth dust continuum has also been observed in galaxies with clumpy structure in optical images (e.g. Hodge et al., 2016, Cheng et al., 2020). LCARS doesn't include radiative transfer of the dust, but as a crude proxy for an ALMA image I smoothed the obscured SFR maps (Figure 5.18) with a Gaussian kernel that mimics a $0.2''$ beam width, and present these in Figure 5.19. It is clear that much of the clumpy structure seen in the dust obscured SFR maps has been smoothed out, but in the absence of proper treatment of radiative transfer of dust in LCARS to create realistic mock ALMA observations of the dust continuum, I will not explore this topic further.

High-z observations have found offsets between the dust continuum, and UV and Hα emission (e.g. Chen et al., 2017, Cochrane et al., 2021) and snapshot 2 is likely to display similar properties if it happened to be observed by ALMA (a proxy

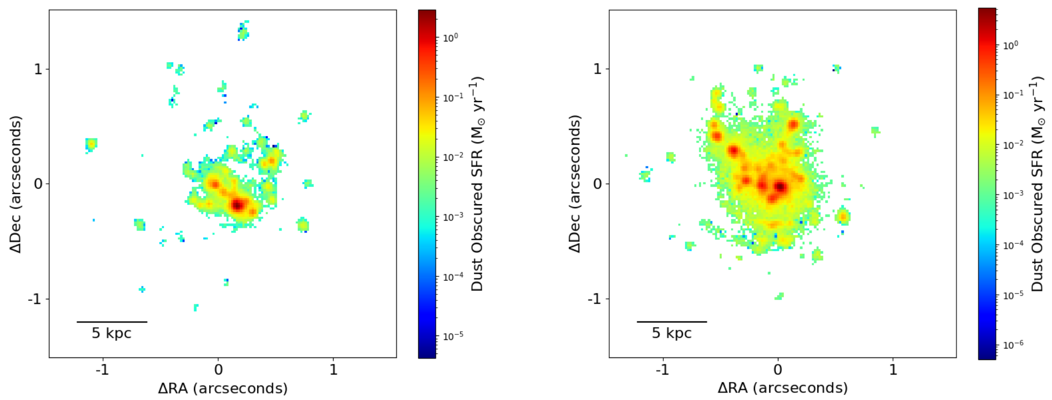

Figure 5.18: An estimate of the dust obscured SFR for snapshot 2 (**left**) and snapshot 3 (**right**) by subtracting the Hα cube with dust from Hα cube without dust and converting this flux to an SFR using the method explained in Section 4.4.2.

for an ALMA image is shown in Figure 5.19). The peak of the dust continuum is located at the nucleus of g3 and the peak of Hα in the attenuated cube is co-located with the nucleus of g2, due to little dust attenuation at this location. The peak of the optical continuum is located at the nucleus of g1. Therefore, the observed peaks in the dust, optical and Hα maps are all offset in snapshot 2, and it could be that some offsets observed in the high-z universe, if not found to be systematic, may be an ongoing merger.

5.5 Discussion

5.5.1 Minor Mergers and the Main Sequence

From the three snapshots, it appears that the burst of star formation after a minor merger is not sufficient to push a galaxy above the MS and into the starburst regime, as seen in Figure 5.14. For its $M_\star$, an SFR of ~ 450 $M_\odot$ yr^{-1} is needed for g1 to be classified as a starburst. For g1 the f_{gas} remains broadly constant throughout the minor merger, whereas the SFE increases after g3 passes through its disk, so it may be that an increase in SFE is a necessary, but not sufficient condition, for a galaxy to become a starburst, which I suggested in Chapter 3. If g1's f_{gas} doubled, while keeping the same SFE, it would become a starburst galaxy. As this chapter only studies one minor merger within the NewHorizon simulation, a larger sample

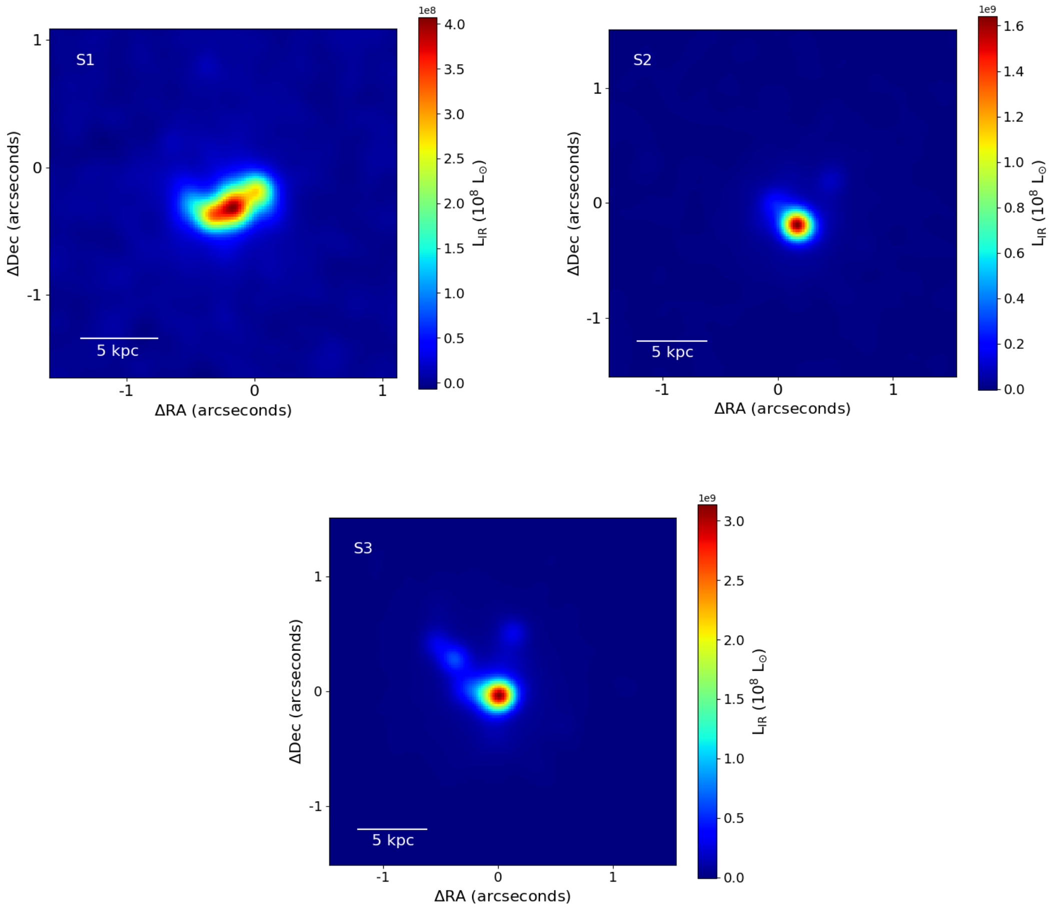

Figure 5.19: The dust obscured SFR for snapshot 1 (**top left**), snapshot 2 (**top right**) and snapshot 3 (**bottom**) convolved with a Gaussian kernel to mimic a 0.2″ beam width achievable with ALMA. Note these are not mock ALMA observations, just the HSIM output convolved with a Gaussian, and using L_{IR} as opposed to a flux from a given spectral window.

is needed to deduce what happens in other minor mergers and this would help us infer what are the necessary conditions for a starburst to occur.

Previous research by Di Matteo et al. (2007) used two simulated galaxies to test a range of impact parameters and alignment of angular momenta in mergers and found that on average galaxies that pass too close together at first perihelion had the lowest burst of star formation and the NewHorizon minor merger may be showing a similar effect.

Perret et al. (2014) and Fensch et al. (2017) ran a series of non-cosmological simulations, using two galaxies, and found that mergers did not elevate the SFR due to an already saturated star formation in gas rich turbulent disks at high-z. These simulated galaxies had a clumpy morphology similar to my mock observations, and it may be that a sufficiently turbulent ISM keeps a galaxy within the scatter of the MS throughout a minor merger. Renaud et al. (2022) and Segovia-Otero et al. (2022), using a cosmological zoom-in simulation of a Milky Way-like galaxy, found that a major merger only boosts a galaxy into the starburst phase if the galaxy has already formed a settled, non-clumpy, disk, as a turbulent ISM reduces the fraction of gas that can be compressed into dense enough regions to form stars.

5.5.2 Can Ongoing Minor Mergers be Mistaken for Disk Galaxies in Current High-z Observations?

Observing the high-z universe usually involves a trade-off between spatial resolution and S/N. Due to the comparatively low surface brightness of MS galaxies at $z > 2$ very high spatial resolution observations at cosmic noon are often limited to either bright objects, lensed objects or small sample sizes (in comparison to the large surveys mentioned in Section 1.7). There have been some Hα studies of un-lensed normal star forming galaxies at this epoch with AO instruments such as SINFONI and the Keck OH-Suppressing Infrared Integral Field Spectrograph (OSIRIS), which typically have a spatial resolution of $\sim$ 1 - 2 kpc at $z \sim 2$ (e.g. Law et al., 2009, Swinbank et al., 2012, Genzel et al., 2014, Espejo Salcedo et al., 2021). The largest of these observing programs is the SINS/zC-SINF Survey (Förster Schreiber et al., 2018) with 35 objects.

The main conclusions of these studies are the confirmation of a higher σ_0 in star forming galaxies at cosmic noon and a clumpy ISM seems to be present. The fraction of disks versus mergers seem to vary depending on the methodology. For example, Molina et al. (2017) find 60 % of galaxies may be mergers at $z \sim 2$ based on kinemetry, whereas Förster Schreiber et al. (2018) classify up to 70% to be rotating disks, using multiple criteria similar to KMOS^{3D} (Wisnioski et al., 2015). Espejo Salcedo et al. (2021) concluded that 20% of their sample of 10 galaxies are mergers, with another 20% inconclusive.

The number AO observed targets is smaller than those carried out on seeing limited instruments, so much of our knowledge of MS galaxies in the high-z universe comes from seeing limited studies with spatial resolution $> 0.5''$, such as my U/LIRG sample in Chapter 2, the KMOS^{3D} survey (Wisnioski et al., 2015) or the MOSDEF survey (Kriek et al., 2015). Even for excellent observing conditions the PSF will be $\approx 0.5''$, which corresponds to a spatial resolution of ~ 4 kpc at z = 2, so it is difficult to disentangle two nuclei very close together and asymmetries in the observed flux can get smeared out.

It is also clear that sample selection and methodology play a role in mergers versus isolated disks (from both the literature and my work in this thesis) so larger samples at higher spatial resolution will help tackle this problem. HARMONI will play a key role, being able to achieve spatial resolution on the order of 100 - 200 pc at high-z and its huge collecting area will provide greater sensitivity than current instruments, ensuring it will take much shorter integration times to observe an object.

It is worth referring back to SWIRE5, which has two peaks in its dust continuum and an asymmetric flux in its SDSS I-band and CO(3-2) emission (Figures 3.10 3.15), and SWIRE7, which has a tentative double peak in its SDSS I-band image (Figure 3.15). These are located at z $\sim$ 0.4 so have better spatial resolution than equivalent galaxies at cosmic noon for a given beam size, yet their merger status is still not conclusive. These potential mergers were even classified as isolated disks based on the dynamical ratio from seeing limited instruments, and it would have been very difficult to classify them otherwise prior to the data I present in Chapter 3. Observational studies have established an increase in merger rate with redshift and that minor mergers are more common (e.g. Lotz et al., 2011, Duncan et al., 2019) so it is likely that there are more minor merging pairs at cosmic noon that have been missed.

It is worth remembering that snapshot 2 and snapshot 3 are snapshots of a three body merger, albeit I have been ignoring g2 as it is making comparatively little impact on g1. At the 20 mas scale, it is almost impossible to say this is a three body merger and be able to tell g2 apart from a clump. It is the brightest clump in the dust attenuated cube, but doesn't have an impact on the velocity maps as it is dominated by the kinematics of g1 and g3. There is a slight peak in σ_{gas} in the 2nd moment map co-located with it nucleus (see small peak in top right of snapshot 2 map in Figure 5.9), but without prior knowledge it would not be strong evidence of a third nucleus in the map; albeit it may be that a particular sight line or different spatial resolution would make a three body merger appear more obvious.

To add context to this discussion, it is useful to compare my simulated galaxies to the Milky Way, the Large Magellanic Cloud (LMC) and Small Magellanic Cloud (SMC). The total mass of the LMC has been estimated as $\sim 2 \times 10^{11}$ M$_\odot$ (e.g. Erkal et al., 2019, Shipp et al., 2021) and assuming the Milky Way has a total mass of $\sim 10^{12}$ M$_\odot$ this is comparable to the 4:1 mass ratio of g1 and g3. The LMC is located at a distance of 50 kpc from the Milky Way and it is estimated it will merge with the Milky Way in around 2 Gyr (Cautun et al., 2019), so it is not an exact analogous scenario for my merger. The SMC is estimated to have a total mass of $\sim 6.5 \times 10^9$ M$_\odot$ and is located at a distance of 60 kpc from the Milky Way (Bekki and Stanimirovic, 2009), so although not an exact match for the mass ratio of 20:1 between g1 and g2, it is a similar order of magnitude. As the exact effect the Megellanic Clouds have on the Milky Way, and vice versa, is still an open topic, these two examples highlight the difficulty of disentangling mergers versus isolated galaxies at high-z, and uncovering the impact minor mergers have on star formation.

Finally, I wish to emphasize that although I focused on kinematic signatures, such as the dynamical ratio, there are a variety of other metrics that can be applied, and tested, to check if they can differentiate between disturbed and regular morphology/kinematics at cosmic noon. Stability analysis such as the Toomre Q parameter (defined in Section 3.5.2) is often applied to high-z star forming galaxies (e.g. Genzel et al., 2011). But, Agertz et al. (2015) have demonstrated that the scale chosen when calculating the stability criteria will affect the apparent stability of a disk, so further studies are required to check if a metric such as Toomre Q can be applied at the 100 pc scales probed by HARMONI. Tools such as kinemetry

(Krajnovic et al., 2006), a method that quantifies the asymmetry in the V_{rot} or σ_{gas} maps, may provide a good method to identify ongoing minor mergers, and kinemetry has been used in conjunction with non-parametric morphology indicators to distinguish various merger phases (McElroy et al., 2022). Recently developed tools include the Radon Transform (a set of line integrals through an image at different orientations and offsets from the origin, Stark et al., 2018), which has been successfully applied to stellar kinematics to identify mergers (Nevin et al., 2021) and may be worth exploring in gas kinematics at cosmic noon. These are just some examples of the many metrics in the literature that have used to try establish ordered versus disturbed kinematics, and there is huge scope for future research into identifying which kinematic signatures are the best classifiers of mergers versus isolated disks in the high-z universe.

5.6 Conclusion

This chapter has built on the work presented in Chapter 4, and explored the observational signatures of a minor merger as they would appear if observed by HARMONI. This type of research is important and necessary as the next generation of observatories allow us to probe higher spatial resolutions at ever greater redshifts. It is vital to understand how different objects, in different stages of their evolution, will appear in HARMONI if we want to correctly infer what we are observing. I chose three snapshots of a star forming galaxy in different stages of interaction, and the results were as follows.

1. I made mock observations, of the Hα line and underlying continuum, of a simulated minor merger at z $\sim$ 2. These were composed of three snapshots: the first snapshot in the pre-merger phase, and two snapshots ($\sim$ 400 Myr after snapshot 1) either side of the first perihelion of the minor merging galaxy.

2. A minor merger increases the SFR by a factor of ~ 3, but it appears a minor merger is not a sufficient condition for a galaxy to be boosted into the starburst regime.

3. The increase in SFR seems to be caused by an increase in SFE as the gas fraction remains approximately constant in g1, across the three snapshots.

4. The dynamical ratio decreases over the course of the minor merger, yet is consistent with g1 being a rotation dominated object even after the initial impact of g3. The result holds even when using different methodologies for calculating the dynamical ratio. This suggests that V_{rot} / σ_{gas}, without further information such as morphology, is not a good indicator to use to disentangle whether a galaxy is in the process of a minor merger. The drop in V_{rot} / σ_{gas} is due to the increase in σ_{gas} through the three snapshots.

5. The addition of moderate dust attenuation affects the morphology indicators, albeit the galaxy would still be correctly classified as merging. The non-parametric indicators break down when applied to the Hα line emission.

New tools or indicators may need to be developed to characterize galaxies at high-z. Indicators that give one value for a galaxy, e.g. V_{rot} / σ_{gas}, are very valuable in seeing limited data, but once the internal structure of a galaxy is resolved these indicators may be unrepresentative of the small scale structure, e.g. the gas in a galaxy could be globally stable against collapse, but be gravitationally unstable on small scales (e.g.Agertz et al., 2015), so one value cannot capture the full picture. Simple axisymmetric kinematic models may need to be modified if asymmetric disks are the norm. High resolution mock observations, with realistic small scale physics, will be a huge help in pushing this research forward in the coming years.

Ithaka gave you the marvelous journey.
Without her you wouldn't have set out.
She has nothing left to give you now.

And if you find her poor, Ithaka wont have fooled you.
Wise as you will have become, so full of experience,
youll have understood by then what these Ithakas mean.

— C. P. Cavafy *Ithaka*

6 Conclusion

Contents

6.1 Summary of Results

This thesis began by posing various open questions in the field of galaxy evolution. The overarching theme of these questions, and this thesis, was investigating the rate at which galaxies form stars, and trying to establish what mechanisms may modulate this process. I used (ultra) luminous infrared galaxies to probe these topics, as this subpopulation of galaxies is vigorously forming stars, and can be observed in both the local and high-z universe. U/LIRGs are excellent astrophysical objects for testing our best theories of galaxy evolution, and for pushing the current understanding of the field. For example, if the hypothetical CO dark ULIRG, discussed in Section 3.5.3, is proved correct in follow up observations this would require new theories of the ISM in star forming galaxies. Likewise, how the properties of U/LIRGs evolve from comic noon to the local universe provide strong constraints for cosmological and extra-galactic simulations. I will firstly summarize the findings of this thesis before bringing all the results together and discuss what insight this gives into cosmic star formation and galaxy evolution.

In Chapter 2 I showed that major mergers are not a necessary condition to drive the high observed SFRs. Many of my sample of U/LIRGs show properties that closely resemble those of the normal star forming population, such as two thirds being on the MS, their metallicities being in agreement with the MZR and at least 40% having disk like kinematics, although I cannot rule out minor mergers. Compared to local U/LIRGs, my z $\sim$ 2 sample are less dust obscured and most do not display signatures of major mergers, so the properties of the U/LIRG population have changed over the past 10 Gyr and local U/LIRGs are not necessarily analogues for their high-z counterparts.

In Chapter 3 I explore U/LIRGs at z $\sim$ 0.4, where they extend from the MS to the starburst region of the $M_\star$ - SFR parameter space. I study a sub-sample of U/LIRGs that appear to be in transition between these two modes of star formation and find that it is an increase in SFE, as opposed to gas fraction, that is pushing the sample towards the starburst regime at this epoch. All the galaxies in my sample seem to be undergoing an interaction, so interactions appear to be responsible for the boost in SFE. In the galaxies that have CO(3-2) emission line data, all show signatures of a rotating disk, so these galaxies may be in an early stage of interaction, which explains why their SFE falls between MS and starbursts. I find preliminary evidence of a CO dark ULIRG which merits follow up observations.

Chapter 4 uses a new pipeline, called LCARS, for adding photons to hydrodynamical cosmological simulations, and I show that the underlying properties of a simulated galaxy can be correctly extracted from a HARMONI mock observation of the Hα emission line, both with and without dust attenuation. LCARS and HSIM will be powerful tools for testing what can be observed at cosmic noon with HARMONI, and investigate whether these observables can differentiate between the different intrinsic properties of a galaxy, such as: can high spatial resolution observations always correctly reveal if a galaxy is merging or isolated?, is the ISM clumpy or smooth at 100 pc scales?

Chapter 5 uses LCARS to process three snapshots of a regular star forming galaxy undergoing a minor merger at z $\sim$ 2. I investigate how the observational signatures change throughout the three snapshots, and show that a galaxy's position on the MS is not always a reliable indicator of a merging versus non-merging galaxy. Neither is V_{rot} / σ_{gas}, although the dynamical ratio has decreased in snapshot 3 due to the increase in σ_{gas}. I deduce that the SFE, as opposed to gas fraction, is driving the boost in SFR as the minor merger progresses. The morphology indicators are affected by dust, but are still useful to categorize the galaxy correctly under moderate dust attenuation. I conclude that high spatial resolution HARMONI observations may uncover minor mergers at cosmic noon that can be missed by seeing limited observations.

6.2 What Can Luminous IR Galaxies Tell Us About Galaxy Evolution?

Bringing all the results in this thesis together, I now offer some insight that they provide into cosmic star formation. In the local universe, galaxies with a huge SFR are invariably being powered by merger induced star formation. But high-z galaxies with a similar SFR can be driven by internal steady state processes, and major mergers are not a necessary condition for galaxies with SFRs of 100s of $M_{\odot}$ yr^{-1}. Combining both the observational and simulation data presented in this thesis, a gas rich turbulent disk is sufficient to drive the SFR seen in a MS disk galaxy at high-z, despite secular processes in the local universe being unable to reach these SFRs. Therefore, similar processes drive star formation in the local and high-z universe, and as they are applied to gas rich disks the SFR is subsequently scaled up, i.e. normal star forming galaxies can have SFR in the hundreds of solar masses per year, and major mergers can have an SFR in the thousands.

In Chapters 3 and 5 it appears that an increased gas fraction also requires a simultaneous boost in SFE to substantially increase the SFR. At z $\sim$ 0.4, my sample, MS LIRGs and starburst ULIRGs have similar M_{mol}, but the ULIRGs have a higher SFE than my transitioning sample, which in turn has a higher SFE than the LIRGs. Likewise for my mock observations, the gas fraction has increased in snapshot 2, but it is not until the SFE increases in snapshot 3 that the SFR increases by roughly a factor of three. More research will be needed on this topic, but it may be a larger gas fraction primes the galaxy for a burst of star formation, and is a necessary condition, but it requires an increase in SFE, from a process such as a galaxy interaction, to push the SFR higher.

Galaxies are complex objects, and trying to classify them is not trivial. U/LIRGs form a subpopulation based on their L_{IR}, yet two galaxies of equal L_{IR} can differ in most of their properties, e.g. merger versus isolated, MS versus starburst, different SFE etc. Properties are not always transitive, e.g. isolated disks have high dynamical ratios yet a large V_{rot} / σ_{gas} does not always mean a galaxy is isolated, as seen in the minor merger analysed in Chapter 5. A single indicator is not sufficient, in many cases, to say what is the underlying state of the system and multiple indicators are necessary to break this degeneracy. But even if we have multiple indicators, it may still be ambiguous how a galaxy should be categorized. For example, if a galaxy is in an interacting system, but all indicators are consistent with it being isolated, then for all intents and purposes it is an isolated galaxy as the minor galaxy partner does not seem to impacting its star formation, or kinematics, at the time of observation. In snapshot 1 the mass ratio of the two galaxies is 20:1, yet g1 has the properties observed in isolated disks, so including it in the class of isolated disks seems to be the more appropriate choice, as the drivers of star formation are the same as those seen in isolated disk galaxies. If I happened to observe snapshot 1 with a FOV that didn't include g2, it would be difficult to infer g2 was there.

The apparent dichotomy between merger driven SFRs versus star formation from internal steady state processes, or the apparent bi-modality of SFE, may be an oversimplification. In general, starbursts have a higher SFE than star forming galaxies, but in Chapter 3 I showed how a subpopulation of galaxies tends to fall between these two modes, and the appearance of two distinct modes may in part be driven by using two extreme α_{CO} values, a ULIRG-like α_{CO} and a Milky Way-like α_{CO}.

As the spatial and spectral resolution of observations is improved by a new generation of telescopes, the importance of mock observations will increase, as they will allow us to make mock observations of galaxies in various states, and new indicators can be tested to see if degeneracies with current observables can be broken. Axisymmetric kinematic models may need to be tweaked to account for disks at high-z being more turbulent and clumpy, which may affect the fit. For example, in the simulations I resolve pockets of Hα emission moving faster and slower than the circular velocity due to star formation feedback, and these can skew a kinematic fit, especially if the pockets are located along the major kinematic axis and/or have a high S/N.

This thesis has shown the importance of multiple emission lines and observations by a variety of instruments to get a full picture of a galaxy. The sample in Chapter 3.8 had previously been studied in single dish CO, [CII] 158 μm, Hα and optical continuum observations, and yet SWIRE5 could never have been classified as a possible merger prior to the NOEMA observations, In fact, it was selected for the NOEMA observation proposal precisely because all previous observations had shown it to be an isolated disk, and it could act as a reference point for the known mergers that were selected for the CO(3-2) NOEMA observations. I still do not have enough information to say if SWIRE7 is a CO dark object, showing the necessity of observing multiple tracers and diagnostics of ISM conditions.

6.3 Future Work Arising from this Thesis

The results of this thesis have suggested new questions and avenues of research. Two immediate objectives would be to perform follow up observations to determine if SWIRE7 is a CO dark ULIRG, and confirm that SWIRE5 is undergoing a merger. SWIRE7 will require another emission line to confirm the inferred redshift. The [CI] J=1-0 492 GHz emission line would be a good candidate as it would enable the use of an additional method to predict the M_{mol} (e.g. Papadopoulos et al., 2004) while also allowing confirmation of the redshift. For SWIRE5, deep high spatial resolution imaging is needed from instruments such as the HST ACS, or NIRCam on JWST, to get the required $0.1''$ spatial resolution to further explore its dynamical status.

For the LCARS/HSIM research, we need to check how increasing the ratio of metals locked up in dust versus gas phase metallicity will change the indicators in Chapter 5. For example, snapshot 2 may be classified as isolated if the second nucleus (g3) is very heavily extinguished. Also, we can select another snapshot a couple of hundred Myr after snapshot 3 to investigate whether the σ_{gas} remains elevated after the minor merger or if it has it decreased to levels close to snapshot 1.

As LCARS can be applied to any object from a RAMSES simulation, we can make mock observations of additional high-z targets. This will allow us to check how various objects will appear in HARMONI observations, and how this changes as a function of spaxel scale, integration time and observing conditions. We can continue to explore observational signatures and find which are the best observables to understand the underlying properties of a given object.

We can also do follow up observations of the sample of U/LIRGs discussed in Chapter 2.2 and try to get higher spatial resolution, with an instrument such as the Enhanced Resolution Imager and Spectrograph (ERIS) or wait for the ultra high spatial resolution of HARMONI. This allows us to establish if any contain hidden minor mergers and whether some U/LIRGs are misclassified due to kinematics being fitted to seeing limited observations.

6.4 Final Thoughts

One of the pioneers of the stream of consciousness literary technique was my fellow countryman James Joyce, and I will end this thesis with some idle thoughts on my astrophysics journey as it comes to a close. We have entered an interesting period in astrophysics, and science more broadly. The public's scepticism in the scientific method appears to be growing, despite the undoubted success of scientific breakthroughs in alleviating the damage caused by the Covid-19 virus. And yet, this may all change as we are entering a new age of discovery in astrophysics with the recent launch of JWST, and upcoming observatories such as the ELT and the Square Kilometre Array. I started my physics undergraduate studies in 2012, and in the decade since researchers have made major breakthroughs such as confirming gravitational waves, imaging a black hole and discovering thousands of new exoplanets. In the coming years and decades many of the open questions explored in this thesis will be answered, but progress in physics has a Hydra-like quality, and solving a given problem invariably posits many deeper questions. More than most branches of physics, progress in astrophysics is hugely driven by observation rather than theory. Puzzling observations crop up with regularity and overturn our understanding of the universe, for example, the discovery of dark energy in the 1990s. It will be fascinating to see what unknown unknowns will be uncovered in the near future by the next generation of cutting edge observatories, and how these will overthrow some of our current best theories. Some of the assumptions I made when analysing the high-z universe in this thesis may turn out to be incorrect, but in the words of Hegel, "The owl of Minerva spreads its wings only with the falling of the dusk."

This thesis opened with the importance of astronomy in how civilizations view themselves. The motion of the planets helped justify Newton's view of a clockwork universe, which helped kick-start the Age of Reason. General Relativity impacted philosophy, art and literature throughout the 20th century. New astrophysical discoveries in the future will no doubt bleed into culture and continue to shape how we think about ourselves and our place in the Universe.

Appendices

You're still here? It's over...go home...go!

— Ferris Bueller *Ferris Bueller's Day Off*

A
Supplementary Material

Contents

A.1 Radio Imaging

As outlined in Section 1.8.2, a radio interferometer can be used to measure a set of complex visibilities, V(u,v), in the uv plane which is the sampled Fourier transform of the sky brightness, T(x,y). To create a map of the sky brightness, we need to Fourier transform the calibrated complex visibilities, but as Fourier transforms are computationally expensive, a fast Fourier transform (FFT) is performed instead. This is done by re-gridding the irregular uv sampling onto a regular 2D grid.

As is evident in Figure A.1, the density of uv points is not constant across the grid. Therefore, while performing the FFT, the visibilities on different baselines can be re-weighted, tapered and re-sampled to change the angular resolution and

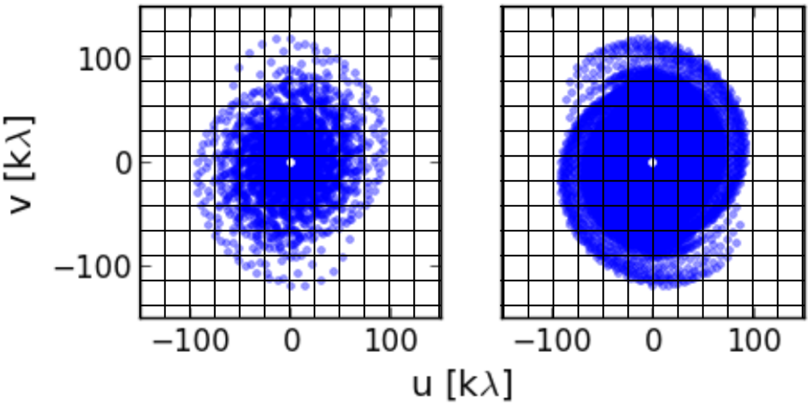

Figure A.1: An example of re-gridding the uv plane from Figure 1.11 (adapted from Avison and George, 2013) in order to perform an FFT. This figure demonstrates how re-gridding an irregular uv sampling with a regular grid leads to a non-uniform number of visibilities per grid sampling, and typically shorter baselines are better sampled than long baselines.

the noise in the final map. Common weightings used to account for differences in the density of sampling are:

- Natural Weighting: W(u,v) = 1/σ(u,v), where σ(u,v) is the noise of a visibility. This weighting maximizes S/N with a trade-off in spatial resolution, as it gives a poorer beam shape than other weightings.
- Uniform Weighting: W(u,v) = 1/ρ(u,v), where ρ(u,v) is the density of sampled points in a re-gridded region. This gives the best angular resolution, but decreases the point source sensitivity.
- Robust Weighting: A combination of natural and uniform weighting, which has an adjustable parameter that scales between -2 and 2, with natural = 2 and uniform = -2.

Once the FFT has been computed it produces a 'dirty image', T_D(x,y), which is the Fourier transform of the re-gridded V(u,v). At this point a non-linear, iterative deconvolution process is run ('cleaning') to interpolate and extrapolate the sampling of V(u,v) into un-sampled regions, to fill in the uv plane. This process also removes artefacts from the image. The cleaning routine works by assuming the sky brightness is made up of a number of point sources. The clean algorithm starts with the dirty map and identifies the brightest pixel in the image. It adds this point to a clean component list. This peak is then multiplied by the 'dirty beam' (Fourier transform of the sampling function described in Section 1.8.2) and a scaling factor, and taken away from the dirty map to leave a residual map. The brightest peak is found in this residual map and the previous steps are continually repeated until a stopping criterion is met, e.g. all peaks above a certain multiple of the noise are found, or all peaks above a certain percentage of the brightest point in T_D(x,y) are found. A clean image is then made by convolving the clean components with a clean beam (Gaussian fitted to the dirty beam) and this map should be a truer representative of the sky brightness.

A.2 HSIM

Here, I provide an overview of the steps HSIM performs when creating a mock HARMONI observation. Full technical details of these steps are provided in Zieleniewski et al. (2015).

The algorithm requires a 3D FITS cube with two spatial and one spectral dimension as an input. The FITS header needs to contain all the relevant information about the object, such as spatial and spectral sampling, flux units etc. The user then specifies the required observing setup, such as the AO mode, integration time etc., and these settings are listed in Table 4.2. Once the input cubes and settings have been specified, the following steps are performed.

A.2.1 Line Spread Function

The spectral resolution is degraded to the output resolution of the selected grating in HSIM. This is done by convolving with a line spread function of width:

$$\Delta\lambda_{\rm lsf} = \sqrt{(\Delta\lambda_{\rm out})^2 - (\Delta\lambda_{\rm in})^2} \tag{A.1}$$

where $\Delta\lambda_{\rm out}$ is the resolution of the chosen grating and $\Delta\lambda_{\rm in}$ is the resolution of the input cube. The spectral dimension of the cube is then sampled by the algorithm with a minimum of two bins per FWHM. If $\Delta\lambda_{\rm out} < \Delta\lambda_{\rm in}$ the user can choose whether to apply no convolution or to convolve with $\Delta\lambda_{\rm out}$ instead of $\Delta\lambda_{\rm lsf}$.

A.2.2 Atmospheric Refraction

The effect of atmospheric differential refraction is added to the cube, which causes a shift in each wavelength channel. After re-binning the cube, which is the next step in the pipeline, each wavelength channel is shifted back to mimic a data reduction pipeline.

A.2.3 PSF Convolution and Spatial Re-binning

Each wavelength channel is convolved with an AO PSF, with the PSF being a function of wavelength and seeing. The pipeline generates AO PSFs at 1 mas sampling and then performs the PSF convolution at 0.1 times the output spatial scale. If the input data cube is coarser than this sampling, it is interpolated to ensure flux conservation. After applying the PSF convolution, the cube is then re-binned to the output spatial scale, ensuring flux conservation.

A.2.4 Background and Throughput

The background and instrument throughput, is generated by incorporating the effects of sky, telescope, instrument and detector. The telescope is assumed to have a grey-body emission.

A.2.5 Noise

Poisson noise from the object, sky and telescope background is added. Dark current and detector read noise is also added to the cube.

A.2.6 Output Files

Upon applying each of the above steps, HSIM outputs multiple cubes including a fully reduced data cube (mimicking a cube after it has passed through a data reduction pipeline), a background cube and noise free cubes for both background and object.

A.3 KMOS Parent Sample

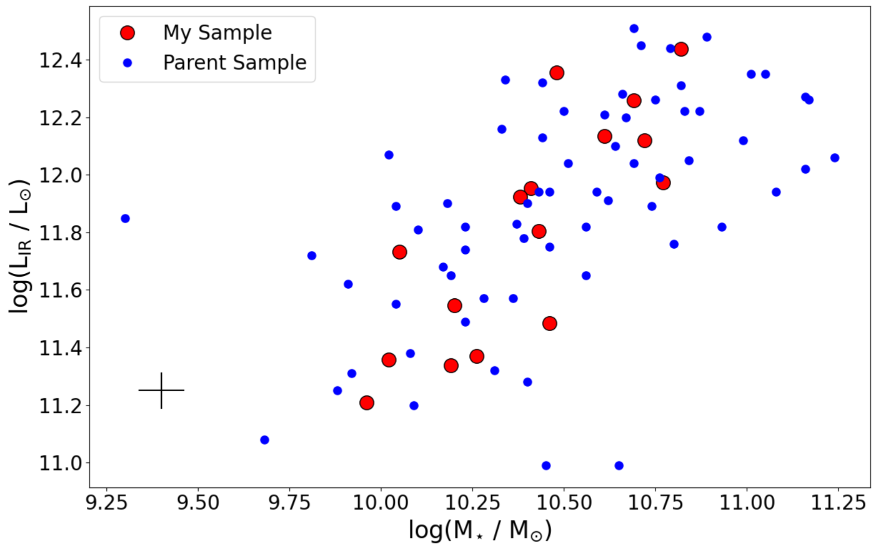

Figure A.2: The IR luminosity versus stellar mass of the parent sample from which my KMOS targets were selected (see Section 2.2.1 for details). The L_{IR} and $M_\star$ for both my sample and the parent sample, excluding my galaxies, is taken from ZFOURGE (Straatman et al., 2016), and not from Table 2.3. This is to ensure no systematic differences in the L_{IR} and $M_\star$, as the analysis in Chapter 2 uses newer photometry and a slightly different method to calculate the L_{IR} and $M_\star$. Two of my KMOS sample didn't have a L_{IR} or $M_\star$ in ZFOURGE, so there are only 16 data points. It can be seen my KMOS targets are a representative subsample of the parent sample. I assume a 15% error on all values, and the magnitude of these errors is shown in the bottom left corner.

A.4 Comparison of GalPak^{3D} to Observed Maps

In this section, I show a comparison of the observed KMOS maps to maps from the best fit model from GalPak^{3D}. I include an example galaxy for both my KMOS sample and the supplemental sample that are representative, in terms of S/N, of both these samples.

Many of the total sample that did not converge in GalPak^{3D} had velocity fields that didn't show an obvious single gradient or had very large velocity dispersions, but here I also include a galaxy with an observed gradient that didn't converge in GalPak^{3D}. This should convince the reader that although GalPak^{3D} uses an MCMC approach that always tries to converge to a model for a given dataset, it doesn't just automatically converge to a disk model because there is a hint of a gradient.

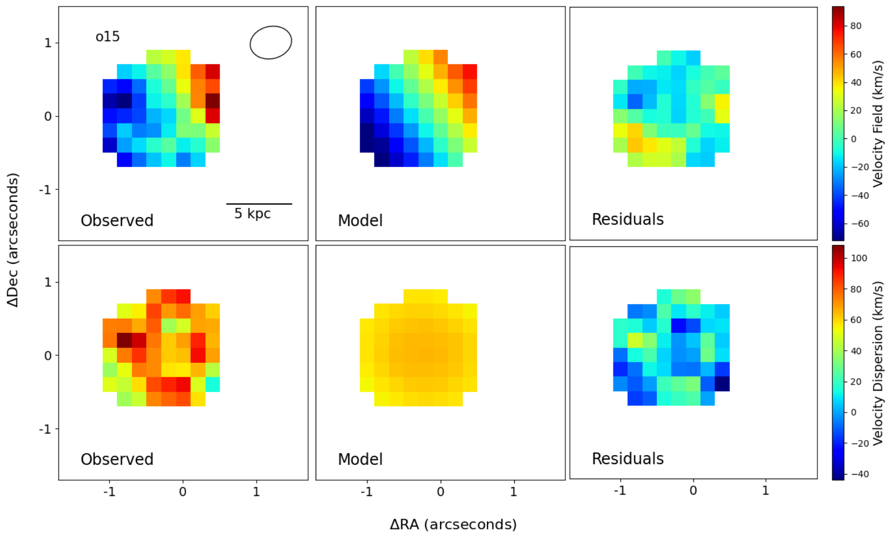

Figure A.3: Moment maps from the KMOS observation of o15 and the best-fit rotating disk model found by GalPak^{3D}. **Top left:** The observed 1st moment map (projected). **Top middle:** 1st moment map from the convolved best-fit model (projected). **Top right:** The residual velocity field. **Bottom left:** The observed 2nd moment map. **Bottom middle:** The convolved best-fit 2nd moment map. **Bottom right:** The residual velocity dispersion. The PSF is shown in the top right corner, with the physical scale given in the bottom right corner. Note, these maps have a different mask to the maps in Figures 2.2 and 2.5, due to low S/N in spaxels of the outer disk giving poor Gaussian fits in the observed moment maps. Therefore, these outer spaxels are excluded.

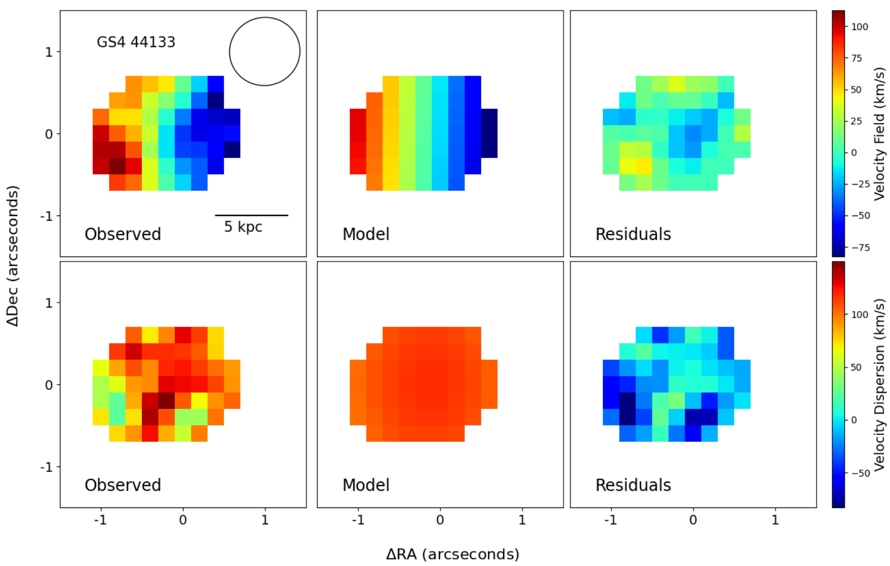

Figure A.4: Description the same as Figure A.3, except for GS4 44133 of the supplemental sample.

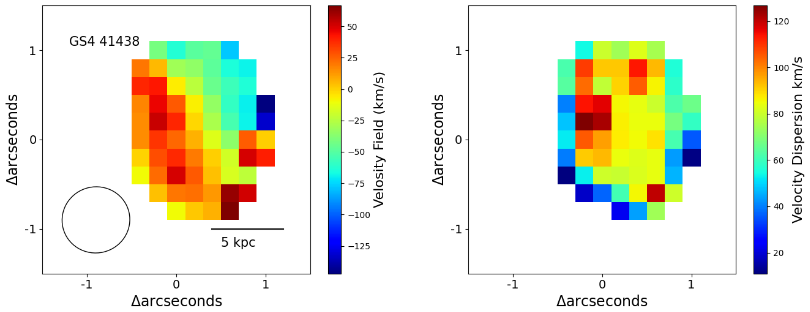

Figure A.5: Left: The observed 1st moment map (projected) for GS4 41438. **Right:** The observed 2nd moment map. This galaxy didn't converge for all the model parameters in GalPak^{3D} as it couldn't converge to a value for either the rotational velocity or the turnover radius. The PSF is shown in the bottom left corner, with the physical scale given in the bottom right corner.

References

Abraham, R. G., S. van den Bergh, and P. Nair (2003). "A New Approach to Galaxy Morphology. I. Analysis of the Sloan Digital Sky Survey Early Data Release". In: *The Astrophysical Journal* 588, pp. 218–229.

Agertz, O., A. B. Romeo, and K. Grisdale (2015). "Characterizing gravitational instability in turbulent multicomponent galactic discs". In: *Monthly Notices of the Royal Astronomical Society* 449, pp. 2156–2166.

Aghanim, N., Y. Akrami, F. Arroja, et al. (2020). "Planck 2018 results. I. Overview and the cosmological legacy of Planck". In: *Astronomy & Astrophysics* 641, A1.

Alonso-Herrero, A., M. García-Marín, A. Monreal-Ibero, et al. (2009). "PMAS optical integral field spectroscopy of luminous infrared galaxies - I. The atlas". In: *Astronomy & Astrophysics* 506, pp. 1541–1562.

Alonso-Herrero, A., G. H. Rieke, M. J. Rieke, et al. (2006). "Near-Infrared and Star-forming Properties of Local Luminous Infrared Galaxies". In: *The Astrophysical Journal* 650, p. 835.

Avison, A. and S. J. George (2013). "A graphical tool for demonstrating the techniques of radio interferometry". In: *European Journal of Physics* 34, pp. 7–17.

Baes, M., A. Nersesian, V. Casasola, et al. (2020). "Nonparametric galaxy morphology from UV to submm wavelengths". In: *Astronomy & Astrophysics* 641, A119.

Baldwin, J. A., M. M. Phillips, and R. Terlevich (1981). "Classification Parameters for the Emission-Line Spectra of Extragalactic Objects." In: *Publications of the Astronomical Society of the Pacific* 93, p. 5.

Bauermeister, A., L. Blitz, A. Bolatto, et al. (2013). "The EGNoG Survey: Molecular Gas in Intermediate-Redshift Star-Forming Galaxies". In: *The Astrophysical Journal* 768, p. 132.

Behrendt, M, M Schartmann, and A Burkert (2019). "The possible hierarchical scales of observed clumps in high-redshift disc galaxies". In: *Monthly Notices of the Royal Astronomical Society* 488, pp. 306–323.

Bekki, K. and S. Stanimirovic (2009). "The total mass and dark halo properties of the Small Magellanic Cloud". In: *Monthly Notices of the Royal Astronomical Society* 395, pp. 342–350.

Belfiore, F., R. Maiolino, K. Bundy, et al. (2018). "SDSS IV MaNGA - sSFR profiles and the slow quenching of discs in green valley galaxies". In: *Monthly Notices of the Royal Astronomical Society* 477, pp. 3014–3029.

Bellocchi, E., S. Arribas, and L. Colina (2016). "Distinguishing disks from mergers: Tracing the kinematic asymmetries in local (U)LIRGs using kinemetry-based criteria". In: *Astronomy & Astrophysics* 591, A85.

Bellocchi, E., S. Arribas, L. Colina, et al. (2013). "VLT/VIMOS integral field spectroscopy of luminous and ultraluminous infrared galaxies: 2D kinematic properties". In: *Astronomy & Astrophysics* 557, A59.

Bertelli, G., A. Bressan, C. Chiosi, et al. (1994). "Theoretical isochrones from models with new radiative opacities". In: *Astronomy & Astrophysics Supplement Series* 106, pp. 275–302.

Béthermin, M., E. Daddi, G. Magdis, et al. (2015). "Evolution of the dust emission of massive galaxies up to $z = 4$ and constraints on their dominant mode of star formation". In: *Astronomy & Astrophysics* 573, A113.

Bigiel, F., A. Leroy, F. Walter, et al. (2008). "The Star Formation Law in Nearby Galaxies on Sub-Kpc Scales". In: *The Astronomical Journal* 136, pp. 2846–2871.

Bigiel, F., A. K. Leroy, F. Walter, et al. (2011). "A Constant Molecular Gas Depletion Time in Nearby Disk Galaxies". In: *The Astrophysical Journal* 730, p. L13.

Bisbas, T. G., E. F. van Dishoeck, P. P. Papadopoulos, et al. (2017). "Cosmic-ray Induced Destruction of CO in Star-forming Galaxies". In: *The Astrophysical Journal*, p. 90.

Blanton, M. R., M. A. Bershady, B. Abolfathi, et al. (2017). "Sloan Digital Sky Survey IV: Mapping the Milky Way, Nearby Galaxies, and the Distant Universe". In: *The Astronomical Journal* 154, p. 28.

Bolatto, A. D., M. Wolfire, and A K. Leroy (2013). "The CO-to-H2 Conversion Factor". In: *Annual Review of Astronomy & Astrophysics* 51, pp. 207–268.

Bouché, N., H. Carfantan, I. Schroetter, et al. (2015). "GalPak3D: A Bayesian Parametric Tool for Extracting Morphokinematics of Galaxies from 3D Data". In: *The Astronomical Journal* 150, p. 92.

Bruzual, G. and S. Charlot (2003). "Stellar population synthesis at the resolution of 2003". In: *Monthly Notices of the Royal Astronomical Society* 344, pp. 1000–1028.

Buat, V., L. Ciesla, M. Boquien, et al. (2019). "Cold dust and stellar emissions in dust-rich galaxies observed with ALMA: a challenge for SED-fitting techniques". In: *Astronomy & Astrophysics* 632, A79.

Buat, V., N. Oi, S. Heinis, et al. (2015). "Dust attenuation up to $z \simeq 2$ in the AKARI North Ecliptic Pole Deep Field". In: *Astronomy & Astrophysics* 577, A141.

Burnham, A. D., C. M. Casey, J. A. Zavala, et al. (2021). "The Physical Drivers of the Luminosity-Weighted Dust Temperatures in High-Redshift Galaxies". In: *The Astrophysical Journal* 910, p. 89.

Calzetti, D., L. Armus, R. C. Bohlin, et al. (2000). "The Dust Content and Opacity of Actively Star-forming Galaxies". In: *The Astrophysical Journal* 533, pp. 682–695.

Cappellari, M. (2016). "Structure and Kinematics of Early-Type Galaxies from Integral Field Spectroscopy". In: *Annual Review of Astronomy & Astrophysics* 54, pp. 597–665.

Cappellari, M. and Y. Copin (2003). "Adaptive spatial binning of integral-field spectroscopic data using Voronoi tessellations". In: *Monthly Notices of the Royal Astronomical Society* 342, pp. 345–354.

Cappellari, M., E. Emsellem, R. Bacon, et al. (2007). "The SAURON project - X. The orbital anisotropy of elliptical and lenticular galaxies: revisiting the $(V/\sigma, \varepsilon)$ diagram with integral-field stellar kinematics". In: *Monthly Notices of the Royal Astronomical Society* 379, pp. 418–444.

Carilli, C.L. and F. Walter (2013). "Cool Gas in High-Redshift Galaxies". In: *Annual Review of Astronomy & Astrophysics* 51, pp. 105–161.

Casey, C. M., D. Narayanan, and A. Cooray (2014). "Dusty Star-Forming Galaxies at High Redshift". In: *Physics Reports* 541, pp. 45–161.

Cautun, M., A. J. Deason, C. S. Frenk, et al. (2019). "The aftermath of the Great Collision between our Galaxy and the Large Magellanic Cloud". In: *Monthly Notices of the Royal Astronomical Society* 483, pp. 2185–2196.

Chabrier, G. (2003). "Galactic Stellar and Substellar Initial Mass Function". In: *Publications of the Astronomical Society of the Pacific* 115, pp. 763–795.

Chen, C., J. A. Hodge, I. Smail, et al. (2017). "A Spatially Resolved Study of Cold Dust, Molecular Gas, H ii Regions, and Stars in the z = 2.12 Submillimeter Galaxy ALESS67.1". In: *The Astrophysical Journal* 846, p. 108.

Chen, Z., G. Fang, Z. Lin, et al. (2021). "Dust Temperature of Compact Star-forming Galaxies at z ∼ 13 in 3D-HST/CANDELS". In: *The Astrophysical Journal* 906, p. 71.

Cheng, C., E. Ibar, I. Smail, et al. (2020). "A kpc-scale resolved study of unobscured and obscured star-formation activity in normal galaxies at z = 1.5 and 2.2 from ALMA and HiZELS". In: *Monthly Notices of the Royal Astronomical Society* 499, pp. 5241–5256.

Chomiuk, L. and M. S. Povich (2011). "Toward a Unification of Star Formation Rate Determinations in the Milky Way and Other Galaxies". In: *The Astronomical Journal* 142, p. 197.

Clements, D. L., C. Pearson, D. Farrah, et al. (2018). "HERUS: the far-IR/submm spectral energy distributions of local ULIRGs and photometric atlas". In: *Monthly Notices of the Royal Astronomical Society* 475, pp. 2097–2121.

Clements, D. L., W. J. Sutherland, R. G. McMahon, et al. (1996). "Optical imaging of ultraluminous IRAS galaxies: how many are mergers?" In: *Monthly Notices of the Royal Astronomical Society* 279, pp. 477–497.

Cochrane, R. K., P. N. Best, I. Smail, et al. (2021). "Resolving a dusty, star-forming SHiZELS galaxy at z=2.2 with HST, ALMA and SINFONI on kiloparsec scales". In: *Monthly Notices of the Royal Astronomical Society* 503, pp. 2622–2638.

Combes, F. (2018). "Molecular gas in distant galaxies from ALMA studies". In: *Astronomy & Astrophysics Review* 26, p. 5.

Combes, F., S. García-Burillo, J. Braine, et al. (2011). "Galaxy evolution and star formation efficiency at 0.2 < z < 0.6". In: 528, A124.

— (2013). "Gas fraction and star formation efficiency at z < 1.0". In: *Astronomy & Astrophysics* 550, A41.

Condon, J. J. and S. M. Ransom (2016). *Essential Radio Astronomy.* Princeton: Academic Press.

Conselice, C. J. (2003). "The Relationship between Stellar Light Distributions of Galaxies and Their Formation Histories". In: *The Astrophysical Journal Supplement Series* 147, p. 1.

Contini, T., B. Epinat, N. Bouché, et al. (2016). "Deep MUSE observations in the HDFS. Morpho-kinematics of distant star-forming galaxies down to 10^8 $M_\odot$". In: *Astronomy & Astrophysics* 591, A49.

Cortese, L., J. Fritz, S. Bianchi, et al. (2014). "PACS photometry of the Herschel Reference Survey far-infrared/submillimetre colours as tracers of dust properties in nearby galaxies". In: *Monthly Notices of the Royal Astronomical Society* 440, pp. 942–956.

Cowie, L. L., J. González-López, A. J. Barger, et al. (2018). "A Submillimeter Perspective on the GOODS Fields (SUPER GOODS). III. A Large Sample of ALMA Sources in the GOODS-S". In: *The Astrophysical Journal* 865, p. 106.

D'Amato, Q., R. Gilli, C. Vignali, et al. (2020). "Dust and gas content of high-redshift galaxies hosting obscured AGN in the Chandra Deep Field-South". In: *Astronomy & Astrophysics* 636, A37.

Daddi, E., M. Dickinson, G. Morrison, et al. (2007). “Multiwavelength Study of Massive Galaxies at z $\sim$ 2. I. Star Formation and Galaxy Growth”. In: *The Astrophysical Journal* 670, pp. 156–172.

Daddi, E., D. Elbaz, F. Walter, et al. (2010). “Different Star Formation Laws for Disks Versus Starbursts at Low and High Redshifts”. In: *The Astrophysical Journal Letters* 714, p. L118.

Dalgarno, A. and R. A. McCray (1972). “Heating and Ionization of HI Regions”. In: *Annual Review of Astronomy & Astrophysics* 10, p. 375.

Davé, R., D. Anglés-Alcázar, D. Narayanan, et al. (2019). “SIMBA: Cosmological simulations with black hole growth and feedback”. In: *Monthly Notices of the Royal Astronomical Society* 486, pp. 2827–2849.

Davies, R. I., A. Agudo Berbel, E. Wiezorrek, et al. (2013). “The Software Package for Astronomical Reductions with KMOS: SPARK”. In: *Astronomy & Astrophysics* 558, A56.

Davis, T. A., J. Gensior, M. Bureau, et al. (2022). “WISDOM Project – X. The morphology of the molecular ISM in galaxy centres and its dependence on galaxy structure”. In: *Monthly Notices of the Royal Astronomical Society* 512, pp. 1522–1540.

Decarli, R., M. Aravena, L. Boogaard, et al. (2020). “The ALMA Spectroscopic Survey in the HUDF: Multi-band constraints on line luminosity functions and the cosmic density of molecular gas”. In: *The Astrophysical Jourbal* 902, p. 110.

Dekel, A., Y. Birnboim, G. Engel, et al. (2009). “Cold streams in early massive hot haloes as the main mode of galaxy formation”. In: *Nature* 457, pp. 451–454.

Dekel, A. and A. Burkert (2014). “Wet disc contraction to galactic blue nuggets and quenching to red nuggets”. In: *Monthly Notices of the Royal Astronomical Society* 438, pp. 1870–1879.

Delvecchio, I., C. Gruppioni, F. Pozzi, et al. (2014). “Tracing the cosmic growth of supermassive black holes to z $\sim$ 3 with Herschel”. In: *Monthly Notices of the Royal Astronomical Society* 439, pp. 2736–2754.

Di Matteo, P., F. Combes, A.-L. Melchior, et al. (2007). “Star formation efficiency in galaxy interactions and mergers: a statistical study”. In: *Astronomy & Astrophysics* 468, pp. 61–81.

Di Teodoro, E. M. and F. Fraternali (2015). “3D BAROLO: a new 3D algorithm to derive rotation curves of galaxies”. In: *Monthly Notices of the Royal Astronomical Society* 451, pp. 3021–3033.

Díaz-Santos, T., L. Armus, V. Charmandaris, et al. (2017). “A Herschel/PACS Far-infrared Line Emission Survey of Local Luminous Infrared Galaxies”. In: *The Astrophysical Journal* 846, p. 32.

Domínguez, A., B. Siana, A. L. Henry, et al. (2013). “Dust extinction from Balmer decrements of star-forming galaxies at $0.75<z<1.5$ with HST/WFC3 spectroscopy from the WISP survey”. In: *The Astrophysical Journal* 763, p. 145.

Dopita, M. A., L. J. Kewley, R. S. Sutherland, et al. (2016). “Chemical abundances in high-redshift galaxies: a powerful new emission line diagnostic”. In: *Astrophysics and Space Science* 361, p. 61.

Dowell, C. D., A. Conley, J. Glenn, et al. (2013). “HerMES: Candidate High-Redshift Galaxies Discovered With HERSCHEL/SPIRE,” in: *The Astrophysical Journal* 780, p. 75.

Downes, D. and P. M. Solomon (1998). “Rotating Nuclear Rings and Extreme Starbursts in Ultraluminous Galaxies”. In: *The Astrophysical Journal* 507, p. 615.

Draine, B. T. (2003). “Interstellar Dust Grains”. In: *Annual Review of Astronomy & Astrophysics* 41, pp. 241–289.

Draine, B. T. and A. Li (2007). “Infrared Emission from Interstellar Dust. IV. The Silicate-Graphite-PAH Model in the Post-Spitzer Era”. In: *The Astrophysical Journal* 657, pp. 810–837.

Drew, P. M., C. M. Casey, A. Cooray, et al. (2020). “Three Dusty Star-forming Galaxies at z $\sim$ 1.5: Mergers and Disks on the Main Sequence”. In: *The Astrophysical Journal* 892, p. 104.

Dubois, Y., R. Beckmann, F. Bournaud, et al. (2021). “Introducing the NewHorizon simulation: galaxy properties with resolved internal dynamics across cosmic time”. In: *Astronomy & Astrophysics* 651, A109.

Dubois, Y., J. Devriendt, A. Slyz, et al. (2010). “Jet-regulated cooling catastrophe”. In: *Monthly Notices of the Royal Astronomical Society* 409, pp. 985–1001.

Dubois, Y., C. Pichon, C. Welker, et al. (2014). “Dancing in the dark: galactic properties trace spin swings along the cosmic web”. In: *Monthly Notices of the Royal Astronomical Society* 444, pp. 1453–1468.

Duncan, K., C. J. Conselice, C. Mundy, et al. (2019). “Observational Constraints on the Merger History of Galaxies since z 6: Probabilistic Galaxy Pair Counts in the CANDELS Fields”. In: *The Astrophysical Journal*, p. 110.

Dunne, L., H.L. Gomez, E. da Cunha, et al. (2011). “Herschel-ATLAS: rapid evolution of dust in galaxies over the last 5 billion years”. In: *Monthly Notices of the Royal Astronomical Society* 417, pp. 1510–1533.

Dunne, L., S. J. Maddox, C. Vlahakis, et al. (2021). “Dust continuum, CO, and [C I] 1-0 lines: self-consistent H2 mass estimates and the possibility of globally CO-dark galaxies at z = 0.35”. In: *Monthly Notices of the Royal Astronomical Society* 501, pp. 2573–2607.

Elbaz, D., M. Dickinson, H. S. Hwang, et al. (2011). “GOODS-Herschel: an infrared main sequence for star-forming galaxies”. In: *Astronomy & Astrophysics* 533, A119.

Elbaz, D., R. Leiton, N. Nagar, et al. (2018). “Starbursts in and out of the star-formation main sequence”. In: *Astronomy & Astrophysics* 616, A110.

Elmegreen, B. G. and D. M. Elmegreen (2006). “Observations of Thick Disks in the Hubble Space Telescope Ultra Deep Field”. In: *The Astrophysical Journal* 650, p. 644.

Epinat, B., L. Tasca, P. Amram, et al. (2012). “MASSIV: Mass Assembly Survey with SINFONI in VVDS. II. Kinematics and close environment classification”. In: *Astronomy & Astrophysics* 539, A92.

Erkal, D., V. Belokurov, C. F. P. Laporte, et al. (2019). “The total mass of the Large Magellanic Cloud from its perturbation on the Orphan stream”. In: *Monthly Notices of the Royal Astronomical Society* 487, pp. 2685–2700.

Espejo Salcedo, J. M., K. Glazebrook, D. B. Fisher, et al. (2021). “Multi-resolution angular momentum measurements of z $\sim$ 1.5-2 star-forming galaxies”. In: *Monthly Notices of the Royal Astronomical Society* 509, pp. 2318–2338.

Fan, L., S.F. Jones, Y. Han, et al. (2017). “The SCUBA-2 850 m Follow-up of WISE-selected, Luminous Dust-obscured Quasars”. In: *Publications of the Astronomical Society of the Pacific* 129, p. 124101.

Farrah, D., C. J. Lonsdale, D. W. Weedman, et al. (2008). “The Nature of Star Formation in Distant Ultraluminous Infrared Galaxies Selected in a Remarkably Narrow Redshift Range”. In: *The Astrophysical Journal* 677, p. 957.

Fensch, J., F. Renaud, F. Bournaud, et al. (2017). “High-redshift major mergers weakly enhance star formation”. In: *Monthly Notices of the Royal Astronomical Society* 465, pp. 1934–1949.

Ferland, G. J., R. L. Porter, P. A. M. van Hoof, et al. (2013). “The 2013 Release of Cloudy”. In: *Revista Mexicana de Astronomia y Astrofisica* 49, pp. 137–163.

Ferreira, L., N. Adams, C. J. Conselice, et al. (2022). “Panic! at the Disks: First Rest-frame Optical Observations of Galaxy Structure at z > 3 with JWST in the SMACS 0723 Field”. In: *The Astrophysical Journal* 938, p. L2.

Fisher, D.B., K. Glazebrook, R.G. Abraham, et al. (2017). “Connecting Clump Sizes in Turbulent Disk Galaxies to Instability Theory”. In: *The Astrophysical Journal* 839, p. L5.

Fitzpatrick, E.L. (1999). “Correcting for the Effects of Interstellar Extinction”. In: *Publications of the Astronomical Society of the Pacific*, p. 63.

Forbes, J. C., M. R. Krumholz, A. Burkert, et al. (2014). “Balance among gravitational instability, star formation and accretion determines the structure and evolution of disc galaxies”. In: *Monthly Notices of the Royal Astronomical Society* 438, pp. 1552–1576.

Förster Schreiber, N. M., R. Genzel, N. Bouché, et al. (2009). “The SINS Survey: SINFONI Integral Field Spectroscopy of z ∼ 2 Star-Forming Galaxies”. In: *The Astrophysical Journal* 706, pp. 1364–1428.

Förster Schreiber, N. M., A. Renzini, C. Mancini, et al. (2018). “The SINS/zC-SINF Survey of $z \sim 2$ Galaxy Kinematics: SINFONI Adaptive Optics−assisted Data and Kiloparsec-scale Emission-line Properties”. In: *The Astrophysical Journal Supplement Series* 238, p. 21.

Förster Schreiber, N. M., A. E. Shapley, R. Genzel, et al. (2011). “Constraints on the Assembly and Dynamics of Galaxies. II. Properties of Kiloparsec-scale Clumps in Rest-frame Optical Emission of z ∼ 2 Star-forming Galaxies”. In: *The Astrophysical Journal* 739, p. 45.

Franco, M., D. Elbaz, L. Zhou, et al. (2020). “GOODS-ALMA: The slow downfall of star-formation in z = 2-3 massive galaxies”. In: *Astronomy & Astrophysics* 643, A30.

Freudling, W., M. Romaniello, D. M. Bramich, et al. (2013). “Automated data reduction workflows for astronomy. The ESO Reflex environment”. In: *Astronomy & Astrophysics* 559, A96.

Freundlich, J., F. Combes, L. J. Tacconi, et al. (2019). “PHIBSS2: survey design and z = 0.5 - 0.8 results. Molecular gas reservoirs during the winding-down of star formation”. In: *Astronomy & Astrophysics* 622, A105.

Galliano, F., M. Galametz, and A. P. Jones (2018). “The Interstellar Dust Properties of Nearby Galaxies”. In: *Annual Review of Astronomy & Astrophysics* 56, pp. 673–713.

Gao, Y. and P. M. Solomon (2004). “The Star Formation Rate and Dense Molecular Gas in Galaxies”. In: *The Astrophysical Journal* 606, pp. 271–290.

García-Burillo, S., F. Combes, A. Usero, et al. (2015). “High-resolution imaging of the molecular outflows in two mergers: IRAS 17208-0014 and NGC 1614”. In: *Astronomy & Astrophysics* 580, A35.

Geach, J. E., I. Smail, S. M. Moran, et al. (2011). "On the Evolution of the Molecular Gas Fraction of Star-Forming Galaxies". In: *The Astrophysical Journal Letters* 730, p. L19.

Geen, S., P. Hennebelle, P. Tremblin, et al. (2016). "Feedback in Clouds II: UV photoionization and the first supernova in a massive cloud". In: *Monthly Notices of the Royal Astronomical Society* 463, pp. 3129–3142.

Genzel, R., N. M. Förster Schreiber, P. Lang, et al. (2014). "The SINS/zC-SINF Survey of z $\sim$ 2 Galaxy Kinematics: Evidence for Gravitational Quenching". In: *The Astrophysical Journal* 785, p. 75.

Genzel, R., S. Newman, T. Jones, et al. (2011). "The SINS Survey of $z \sim 2$ Galaxy Kinematics: Properties of the Giant Star-Forming Clumps". In: *The Astrophysical Journal* 733, p. 101.

Genzel, R., S. H. Price, H. Übler, et al. (2020). "Rotation Curves in z $\sim$ 1-2 Star-Forming Disks: Evidence for Cored Dark Matter Distributions". In: *The Astrophysical Journal* 902, p. 98.

Genzel, R., N. M. Förster Schreiber, H. Übler, et al. (2017). "Strongly baryon-dominated disk galaxies at the peak of galaxy formation ten billion years ago". In: *Nature* 543, pp. 397–401.

Genzel, R., L. J. Tacconi, F. Combes, et al. (2012). "The Metallicity Depedence of the CO $\rightarrow$ H2 Convsersion Factor in z $\geqslant$ 1 Star-Forming Galaxies". In: *The Astrophysical Journal* 746, p. 69.

Genzel, R., L. J. Tacconi, J. Gracia-Carpio, et al. (2010). "A study of the gas-star formation relation over cosmic time". In: *Monthly Notices of the Royal Astronomical Society* 407, p. 2091.

Genzel, R., L. J. Tacconi, D. Lutz, et al. (2015). "Combined CO and Dust Scaling Relations of Depletion Time and Molecular Gas Fractions with Cosmic Time, Specific Star-formation Rate, and Stellar Mass". In: *The Astrophysical Journal* 800, p. 20.

Graciá-Carpio, J., E. Sturm, S. Hailey-Dunsheath, et al. (2011). "Far-Infrared Line Deficits in Galaxies with Extreme L_{fir}/M_{H2} Ratios". In: *The Astrophysical Journal* 728, p. L7.

Green, A. W., K. Glazebrook, P. J. McGregor, et al. (2010). "High star formation rates as the origin of turbulence in early and modern disk galaxies". In: *Nature* 467, pp. 684–686.

Green, A. W., K. Glazebrook, P. J. McGregor, et al. (2014). "DYNAMO - I. A sample of Hα-luminous galaxies with resolved kinematics". In: *Monthly Notices of the Royal Astronomical Society* 437, p. 1070.

Griffin, M. J., A. Abergel, A. Abreu, et al. (2010). "The Herschel-SPIRE instrument and its in-flight performance". In: *Astronomy & Astrophysics* 518, p. L3.

Grisdale, K., L. Hogan, D. Rigopoulou, et al. (2022). "On the Viability of Determining Galaxy Properties from Observations I: Star Formation Rates and Kinematics". In: *Monthly Notices of the Royal Astronomical Society* 513, pp. 3906–3924.

Grisdale, K., N. Thatte, J. Devriendt, et al. (2021). "Predicting the Observability of Population III Stars with ELT-HARMONI via the Helium 1640 Å emission line". In: *Monthly Notices of the Royal Astronomical Society* 501, pp. 5517–5537.

Guaita, L., J. Melinder, M. Hayes, et al. (2015). "The Lyman alpha reference sample: IV. Morphology at low and high redshift". In: *Astronomy & Astrophysics* 576, A51.

Gulkis, S. and I. de Pater (2003). “Radio Astronomy, Planetary”. In: *Encyclopedia of Physical Science and Technology (Third Edition)*. New York: Academic Press, pp. 687–712.

Guo, Y., M. Giavalisco, H.C. Ferguson, et al. (2012). “Multi-wavelength View of Kiloparsec-scale Clumps in Star-forming Galaxies at z $\sim$ 2”. In: *The Astrophysical Journal* 757, p. 120.

Gururajan, G., M. Bethermin, P. Theule, et al. (2022). “High resolution spectral imaging of CO(7-6), [CI](2-1), and continuum of three high-z lensed dusty star-forming galaxies using ALMA”. In: *Astronomy & Astrophysics* 663, A22.

Herrera-Camus, R., E. Sturm, J. Graciá-Carpio, et al. (2018). “SHINING, A Survey of Far-infrared Lines in Nearby Galaxies. II. Line-deficit Models, AGN Impact, [CII] - SFR Scaling Relations, and Mass - Metallicity Relation in (U)LIRGs”. In: *The Astrophysical Journal* 861, p. 95.

Hodge, J. A., I. Smail, F. Walter, et al. (2019). “ALMA Reveals Potential Evidence for Spiral Arms, Bars, and Rings in High-redshift Submillimeter Galaxies”. In: *The Astrophysical Journal* 876, p. 130.

Hodge, J. A., A. M. Swinbank, J. M. Simpson, et al. (2016). “Kiloparsec-scale Dust Disks in High-redshift Luminous Submillimeter Galaxies”. In: *The Astrophysical Journal* 833, p. 103.

Högbom, J. A. (1974). “Aperture Synthesis with a Non-Regular Distribution of Interferometer Baselines”. In: *Astronomy & Astrophysics Supplement Series* 15, p. 417.

Hopkins, A. M., A. J. Connolly, D. B. Haarsma, et al. (2001). “Toward a Resolution of the Discrepancy between Different Estimators of Star Formation Rate”. In: *The Astronomical Journal*, pp. 288–296.

Houck, J. R., D. W. Weedman, E. Le Floch, et al. (2007). “Spitzer Spectra of a 10 mJy Galaxy Sample and the Star Formation Rate in the Local Universe”. In: *The Astrophysical Journal* 671, p. 323.

Huang, J.-S., D. Rigopoulou, G. Magdis, et al. (2014). “HerMES: Spectral Energy Distributions of Submillimeter Galaxies at z $>$ 4”. In: *The Astrophysical Journal* 784, p. 52.

Hwang, H. S., D. Elbaz, G. Magdis, et al. (2010). “Evolution of dust temperature of galaxies through cosmic time as seen by Herschel”. In: *Monthly Notices of the Royal Astronomical Society* 409, pp. 75–82.

Iono, D., C. D. Wilson, M. S. Yun, et al. (2009). “Luminous Infrared Galaxies with the Submillimeter Array. II. Comparing the CO (3-2) Sizes and Luminosities of Local and High-Redshift Luminous Infrared Galaxies”. In: *The Astrophysical Journal* 695, p. 1537.

Johnson, H. L., C. M. Harrison, A. M. Swinbank, et al. (2018). “The KMOS Redshift One Spectroscopic Survey (KROSS): the origin of disc turbulence in z $\approx$ 1 star-forming galaxies”. In: *Monthly Notices of the Royal Astronomical Society* 474, pp. 5076–5104.

Kartaltepe, J. S., M. Dickinson, D. M. Alexander, et al. (2012). “GOODS-Herschel and CANDELS: The Morphologies of Ultraluminous Infrared Galaxies at z ~ 2”. In: *The Astrophysical Journal* 757, p. 23.

Kartaltepe, J. S., D. B. Sanders, E. Le Floc’h, et al. (2010). “A Multiwavelength Study of a Sample of 70 m Selected Galaxies in the COSMOS Field. II. The Role of Mergers in Galaxy Evolution”. In: *The Astrophysical Journal* 721, pp. 98–123.

Kennicutt, R. C. (1998). “Star formation in galaxies along the hubble sequence”. In: *Annual Review of Astronomy & Astrophysics* 36, pp. 189–231.

Kennicutt, R. C. and M. A. C. De Los Reyes (2021). “Revisiting the Integrated Star Formation Law. II. Starbursts and the Combined Global Schmidt Law”. In: *The Astrophysical Journal* 908, p. 61.

Kennicutt, R. C. and N. J. Evans (2012). “Star Formation in the Milky Way and Nearby Galaxies”. In: *Annual Review of Astronomy & Astrophysics* 50, pp. 531–608.

Kewley, L. J., M. A. Dopita, C. Leitherer, et al. (2013). “Theoretical Evolution of Optical Strong Lines across Cosmic Time”. In: *The Astrophysical Journal* 774, p. 100.

Kimm, T. and R. Cen (2014). “Escape Fraction of Ionizing Photons During Reionization: Effects due to Supernova Feedback and Runaway OB Stars”. In: *The Astrophysical Journal* 788, p. 121.

Kimm, T., H. Katz, M. Haehnelt, et al. (2017). “Feedback-regulated star formation and escape of LyC photons from mini-haloes during reionization”. In: *Monthly Notices of the Royal Astronomical Society* 466, pp. 4826–4846.

Kippenhahn, R., A. Weigert, and A. Weiss (2012). *Stellar structure and evolution*. 2nd ed. Berlin ; London: Springer.

Krajnovic, D., M. Cappellari, T. P. de Zeeuw, et al. (2006). “Kinemetry: a generalization of photometry to the higher moments of the line-of-sight velocity distribution”. In: *Monthly Notices of the Royal Astronomical Society* 366, pp. 787–802.

Kriek, M., A. E. Shapley, N. A. Reddy, et al. (2015). “The MOSFIRE Deep Evolution Field (MOSDEF) Survey: Rest-frame Optical Spectroscopy for $\sim$ 1500 H-selected Galaxies at $1.37 < z < 3.8$”. In: *The Astrophysical Journal Supplement* 218, p. 15.

Kroupa, P. (2001). “On the variation of the initial mass function”. In: *Monthly Notices of the Royal Astronomical Society*, pp. 231–246.

Krumholz, M. R., B. Burkhart, J. C. Forbes, et al. (2018). “A unified model for galactic discs: star formation, turbulence driving, and mass transport”. In: *Monthly Notices of the Royal Astronomical Society* 477, pp. 2716–2740.

Krumholz, M. R., A. K. Leroy, and C. F. McKee (2011). “Which Phase of the Interstellar Medium Correlates With the Star Formation Rate?” In: *The Astrophysical Journal* 731, p. 25.

Lagos, P., C. M. Baugh, C. G. Lacey, et al. (2011). “Cosmic evolution of the atomic and molecular gas contents of galaxies”. In: *Monthly Notices of the Royal Astronomical Society* 418, pp. 1649–1667.

Lamperti, I., A. Saintonge, M. Koss, et al. (2020). “The CO(32)/CO(10) Luminosity Line Ratio in Nearby Star-forming Galaxies and Active Galactic Nuclei from xCOLD GASS, BASS, and SLUGS”. In: *The Astrophysical Journal* 889, p. 103.

Lang, P., N. M. Förster Schreiber, R. Genzel, et al. (2017). “Falling outer rotation curves of star-forming galaxies at $0.6 < z < 2.6$ probed with KMOS^3D and SINS/ZC-SINF”. In: *The Astrophysical Journal* 840, p. 92.

Larson, K. L., D. B. Sanders, J. E. Barnes, et al. (2016). “Morphology and Molecular Gas Fractions of Local Luminous Infrared Galaxies as a Function of Infrared Luminosity and Merger Stage”. In: *The Astrophysical Journal* 825, p. 128.

Law, D. R., Charles C. Steidel, D. K. Erb, et al. (2009). “The Kiloparsec-scale Kinematics of High-redshift Star-forming Galaxies”. In: *The Astrophysical Journal* 697, pp. 2057–2082.

Le Floc'h, E., C. Papovich, H. Dole, et al. (2005). "Infrared Luminosity Functions from the Chandra Deep Field-South: The Spitzer View on the History of Dusty Star Formation at $0 \leq z \leq 1$". In: *The Astrophysical Journal* 632, p. 169.

Lee, N., K. Sheth, K. S. Scott, et al. (2017). "The fine line between normal and starburst galaxies". In: *Monthly Notices of the Royal Astronomical Society* 471, pp. 2124–2142.

Leitherer, C., D. Schaerer, J. D. Goldader, et al. (1999). "Starburst99: Synthesis Models for Galaxies with Active Star Formation". In: *The Astrophysical Journal Supplement Series* 123, p. 3.

Lenkic, L., A. D. Bolatto, D. B. Fisher, et al. (2021). "Giant Star Forming Complexes in High-z Main Sequence Galaxy Analogues: The Internal Structure of Clumps in DYNAMO Galaxies". In: *Monthly Notices of the Royal Astronomical Society* 506, pp. 3916–3934.

Leroy, A. K., F. Walter, K. Sandstrom, et al. (2013). "Molecular Gas and Star Formation in nearby Disk Galaxies". In: *The Astronomical Journal* 146, p. 19.

Liang, L., R. Feldmann, D. Kere, et al. (2019). "On the dust temperatures of high redshift galaxies". In: *Monthly Notices of the Royal Astronomical Society]* 489, pp. 1397–1422.

Lotz, J. M., P. Jonsson, T. J. Cox, et al. (2008). "Galaxy merger morphologies and time-scales from simulations of equal-mass gas-rich disc mergers". In: *Monthly Notices of the Royal Astronomical Society* 391, pp. 1137–1162.

Lotz, J. M., P. Jonsson, T. J. Cox, et al. (2011). "The Major and Minor Galaxy Merger Rates at $z < 1.5$". In: *The Astrophysical Journal* 742, p. 103.

Lotz, J. M., J. Primack, and P. Madau (2004). "A New Nonparametric Approach to Galaxy Morphological Classification". In: *The Astronomical Journal* 128, pp. 163–182.

Luhman, M. L., S. Satyapal, J. Fischer, et al. (2003). "The [C II] 158 Micron Line Deficit in Ultraluminous Infrared Galaxies Revisited". In: *The Astrophysical Journal* 594, pp. 758–775.

Madau, P. and M. Dickinson (2014). "Cosmic Star Formation History". In: *Annual Review of Astronomy & Astrophysics* 52, pp. 415–486.

Magdis, G. E., E. Daddi, M. Béthermin, et al. (2012a). "The Evolving Interstellar Medium of Star-Forming Galaxies Since $z = 2$ as Probed by Their Infrared Spectral Energy Distributions". In: *The Astrophysical Journal* 760, p. 6.

Magdis, G. E., E. Daddi, M. Sargent, et al. (2012b). "The Molecular Gas Content of $z = 3$ Lyman Break Galaxies: Evidence of a Non-Evolving Gas Fraction in Main-Sequence Galaxies at $z > 2$". In: *The Astrophysical Journal* 758, p. L9.

Magdis, G. E., D. Elbaz, H. S. Hwang, et al. (2010). "Herschel reveals a T_{dust}-unbiased selection of $z \sim 2$ ultraluminous infrared galaxies". In: *Monthly Notices of the Royal Astronomical Society* 409, pp. 22–28.

Magdis, G. E., D. Rigopoulou, G. Helou, et al. (2013). "Mid- to far-infrared properties of star-forming galaxies and active galactic nuclei". In: *Astronomy & Astrophysics* 558, A136.

Magdis, G. E., D. Rigopoulou, R. Hopwood, et al. (2014). "A Far-infrared Spectroscopic Survey of Intermediate Redshift (Ultra) Luminous Infrared Galaxies". In: *The Astrophysical Journal* 796, p. 63.

Magnelli, B., D. Elbaz, R. R. Chary, et al. (2011). "Evolution of the dusty infrared luminosity function from z = 0 to z = 2.3 using observations from Spitzer". In: *Astronomy & Astrophysics* 528, A35.

Magnelli, B., D. Lutz, A. Saintonge, et al. (2014). "The evolution of the dust temperatures of galaxies in the SFR-M_* plane up to z $\sim$ 2". In: *Astronomy & Astrophysics* 561, A86.

Maiolino, R. and F. Mannucci (2019). "De re metallica: the cosmic chemical evolution of galaxies". In: *The Astronomy & Astrophysics Review* 27, p. 3.

Maiolino, R., T. Nagao, A. Grazian, et al. (2008). "AMAZE. I. The evolution of the mass-metallicity relation at z > 3". In: *Astronomy & Astrophysics* 488, pp. 463–479.

Mannucci, F., G. Cresci, R. Maiolino, et al. (2010). "A fundamental relation between mass, star formation rate and metallicity in local and high-redshift galaxies". In: *Monthly Notices of the Royal Astronomical Society* 408, pp. 2115–2127.

Martig, M., F. Bournaud, R. Teyssier, et al. (2009). "Morphological Quenching of Star Formation: Making Early-Type Galaxies Red". In: *The Astrophysical Journal* 707, pp. 250–267.

Martin, G., S. Kaviraj, J. E. G. Devriendt, et al. (Nov. 2017). "The limited role of galaxy mergers in driving stellar mass growth over cosmic time". In: *Monthly Notices of the Royal Astronomical Society* 472, pp. L50–L54.

Maschmann, D. and A. Melchior (2019). "Ultimate merging at z $\sim$ 0.1". In: *Astronomy & Astrophysics* 627, p. L3.

Maschmann, D., A. Melchior, G. A. Mamon, et al. (2020). "Double-peak emission line galaxies in the SDSS catalogue. A minor merger sequence". In: *Astronomy & Astrophysics* 641, A171.

Mazzilli-Ciraulo, B., A.-L. Melchior, D. Maschmann, et al. (2021). "Two interacting galaxies hiding as one, revealed by MaNGA". In: *Astronomy & Astrophysics* 653, A47.

McElroy, R., C. Bottrell, M. H Hani, et al. (2022). "The observability of galaxy merger signatures in nearby gas-rich spirals". In: *Monthly Notices of the Royal Astronomical Society* 515, pp. 3406–3419.

McMullin, J. P., B. Waters, D. Schiebel, et al. (2007). "CASA Architecture and Applications". In: *Astronomical Data Analysis Software and Systems XVI* 376, p. 127.

Miettinen, O., I. Delvecchio, V. Smoli, et al. (2017). "An ALMA survey of submillimetre galaxies in the COSMOS field: Physical properties derived from energy balance spectral energy distribution modelling". In: *Astronomy & Astrophysics* 606, A17.

Miller, S. H., K. Bundy, M. Sullivan, et al. (2011). "The Assembly History of Disk Galaxies. I. The Tully-Fisher Relation to $z \simeq 1.3$ From Deep Exposures With DEIMOS". In: *The Astrophysical Journal* 741, p. 115.

Molina, J., E. Ibar, I. Smail, et al. (2019). "The kiloparsec-scale gas kinematics in two star-forming galaxies at z $\sim$ 1.47 seen with ALMA and VLT-SINFONI". In: *Monthly Notices of the Royal Astronomical Society* 487, pp. 4856–4869.

Molina, J., E. Ibar, A. M. Swinbank, et al. (2017). "SINFONI-HiZELS: the dynamics, merger rates and metallicity gradients of typical star-forming galaxies at z = 0.82.2". In: *Monthly Notices of the Royal Astronomical Society* 466, pp. 892–905.

Monreal-Ibero, A., S. Arribas, L. Colina, et al. (2010). "VLT-VIMOS integral field spectroscopy of luminous and ultraluminous infrared galaxies - II. Evidence for

shock ionization caused by tidal forces in the extra-nuclear regions of interacting and merging LIRGs”. In: *Astronomy & Astrophysics* 517, A28.
Moreno, J., P. Torrey, S. L. Ellison, et al. (2019). “Interacting galaxies on FIRE-2: the connection between enhanced star formation and interstellar gas content”. In: *Monthly Notices of the Royal Astronomical Society* 485, p. 1320.
Moreno, J., P. Torrey, S. L. Ellison, et al. (2021). “Spatially resolved star formation and fuelling in galaxy interactions”. In: *Monthly Notices of the Royal Astronomical Society* 503, pp. 3113–3133.
Muñoz, J. A. and S. Peng Oh (2016). “High-temperature saturation can produce the [CII] deficit in LIRGs and ULIRGs”. In: *Monthly Notices of the Royal Astronomical Society* 463, pp. 2085–2091.
Murphy, E. J., R.-R. Chary, M. Dickinson, et al. (2011a). “An Accounting of the Dust-Obscured Star Formation and Accretion Histories over the Last ~ 11 Billion Years”. In: *The Astrophysical Journal* 732, p. 126.
Murphy, E. J., J. J. Condon, E. Schinnerer, et al. (2011b). “Calibrating Extinction-Free Star Formation Rate Diagnostics With 33 GHz Free-Free Emission in NGC 6946”. In: *The Astrophysical Journal* 737, p. 67.
Murray, N. (2011). “Star Formation Efficiences and Lifetimes of Giant Molecular Clouds in the Milky Way”. In: *The Astrophysical Journal* 729, p. 133.
Muzzin, A., P. van Dokkum, M. Kriek, et al. (2010). “Well-sampled Far-infrared Spectral Energy Distributions of z ~ 2 Galaxies: Evidence for Scaled up Cool Galaxies”. In: *The Astrophysical Journal* 725, p. 742.
Nevin, R., L. Blecha, J. Comerford, et al. (2021). “Accurate Identification of Galaxy Mergers with Stellar Kinematics”. In: *The Astrophysical Journal* 912, p. 45.
Noeske, K. G., B. J. Weiner, S. M. Faber, et al. (2007). “Star Formation in AEGIS Field Galaxies since z = 1.1: The Dominance of Gradually Declining Star Formation, and the Main Sequence of Star-forming Galaxies”. In: *The Astrophysical Journal Letters* 660, p. L43.
Oliver, S. J., J. Bock, B. Altieri, et al. (2012). “The Herschel Multi-tiered Extragalactic Survey: HerMES”. In: *Monthly Notices of the Royal Astronomical Society* 424, pp. 1614–1635.
Onodera, M., C. M. Carollo, S. Lilly, et al. (2016). “ISM Excitation and Metallicity of Star-forming Galaxies at z $\simeq$ 3.3 from Near-IR Spectroscopy”. In: *The Astrophysical Journal* 822, p. 42.
Osterbrock, D. E. and G. J. Ferland (2006). “Astrophysics of gaseous nebulae and active galactic nuclei, 2nd Edition”. In.
Pan, H.-A., L. Lin, B.-C. Hsieh, et al. (2018). “The Effect of Galaxy Interactions on Molecular Gas Properties”. In: *The Astrophysical Journal* 868, p. 132.
Papadopoulos, P. P., W.-F. Thi, and S. Viti (2002). “Molecular Gas in Spiral Galaxies: A New Warm Phase at Large Galactocentric Distances?” In: *The Astrophysical Journal* 579, p. 270.
— (2004). “CI lines as tracers of molecular gas, and their prospects at high redshifts”. In: *Monthly Notices of the Royal Astronomical Society* 351, p. 147.
Park, M.-J., S. K. Yi, Y. Dubois, et al. (2019). “New Horizon: On the Origin of the Stellar Disk and Spheroid of Field Galaxies at z = 0.7”. In: *The Astrophysical Journal* 883, p. 25.
Pearson, W. J., L. Wang, M. Alpaslan, et al. (2019). “Effect of galaxy mergers on star formation rates”. In: *Astronomy & Astrophysics* 631, A51.

Pearson, W. J., L. Wang, P. D. Hurley, et al. (2018). “Main sequence of star forming galaxies beyond the Herschel confusion limit”. In: *Astronomy & Astrophysics* 615, A146.

Peng, C. Y., L. C. Ho, C. D. Impey, et al. (2010). “Detailed Decomposition of Galaxy Images. II. Beyond Axisymmetric Models”. In: *The Astronomical Journal* 139, pp. 2097–2129.

Pereira-Santaella, M., L. Colina, S. Garcia-Burillo, et al. (2018). “Spatially resolved cold molecular outflows in ULIRGs”. In: *Astronomy & Astrophysics* 616, A171.

Pereira-Santaella, M., L. Colina, S. García-Burillo, et al. (2021). “Are local ULIRGs powered by AGN? The sub-kpc view of the 220 GHz continuum. PUMA II”. In: *Astronomy & Astrophysics* 651, A42.

Pereira-Santaella, M., D. Rigopoulou, D. Farrah, et al. (2017). “Far-infrared metallicity diagnostics: Application to local ultraluminous infrared galaxies”. In: *Monthly Notices of the Royal Astronomical Society* 470, pp. 1218–1232.

Pereira-Santaella, M., D. Rigopoulou, G. E. Magdis, et al. (2019). “Optical Integral Field Spectroscopy of Intermediate Redshift Infrared Bright Galaxies”. In: *Monthly Notices of the Royal Astronomical Society* 486, p. 5621.

Perna, M., S. Arribas, L. Colina, et al. (2022). “The PUMA project. III. Incidence and properties of ionised gas disks in ULIRGs, associated velocity dispersion and its dependence on starburstiness”. In: *Astronomy & Astrophysics* 662, A94.

Perna, M., S. Arribas, M. Pereira Santaella, et al. (2021). “Physics of ULIRGs with MUSE and ALMA: The PUMA project I. Properties of the survey and first MUSE data results”. In: *Astronomy & Astrophysics* 646, A101.

Perret, V., F. Renaud, B. Epinat, et al. (2014). “Evolution of the mass, size, and star formation rate in high redshift merging galaxies - MIRAGE A new sample of simulations with detailed stellar feedback”. In: *Astronomy & Astrophysics* 562, A1.

Pettini, M and B. E. J. Pagel (2004). “[O III]/[N II] as an Abundance Indicator at High Redshift”. In: *Monthly Notices of the Royal Astronomical Society* 348, pp. L59–L63.

Pettini, M., A. E. Shapley, C. C. Steidel, et al. (2001). “The Rest-Frame Optical Spectra of Lyman Break Galaxies: Star Formation, Extinction, Abundances, and Kinematics”. In: *The Astrophysical Journal* 554, p. 981.

Piotrowska, J. M, A. F. L. Bluck, R. Maiolino, et al. (2020). “Towards a deeper understanding of the physics driving galaxy quenching inferring trends in the gas content via extinction”. In: *Monthly Notices of the Royal Astronomical Society: Letters* 492, pp. L6–L11.

Popesso, P., A. Concas, L. Morselli, et al. (2020). “The dust and cold gas content of local star forming galaxies”. In: *Monthly Notices of the Royal Astronomical Society* 496, pp. 2531–2541.

Popping, G., R. Decarli, A. W. S. Man, et al. (2017). “ALMA reveals starburst-like interstellar medium conditions in a compact star-forming galaxy at z $\sim$ 2 using [CI] and CO”. In: *Astronomy & Astrophysics* 602, A11.

Price, S. H., M. Kriek, G. Barro, et al. (2020). “The MOSDEF Survey: Kinematic and Structural Evolution of Star-forming Galaxies at 1.4 $\leq$ z $\leq$ 3.8”. In: *The Astrophysical Journal* 894, p. 91.

Price, S. H., M. Kriek, A. E. Shapley, et al. (2016). “The MOSDEF Survey: Dynamical and Baryonic Masses and Kinematic Structures of Star-forming Galaxies at 1.4 $\leq$ z $\leq$ 2.6”. In: *The Astrophysical Journal* 819, p. 80.

Renaud, F., F. Bournaud, K. Kraljic, et al. (2014). "Starbursts triggered by intergalactic tides andinterstellar compressive turbulence". In: *Monthly Notices of the Royal Astronomical Society* 442, pp. L33–L37.

Renaud, F., Á. Segovia Otero, and O. Agertz (2022). "The merger-starburst connection across cosmic times". In: *Monthly Notices of the Royal Astronomical Society* 516, pp. 4922–4931.

Reyes, M. A. C. de los and R. C. Kennicutt Jr. (2019). "Revisiting the Integrated Star Formation Law. I. Non-starbursting Galaxies". In: *The Astrophysical Journal* 872, p. 16.

Richardson, M. L. A., L. Routledge, N. Thatte, et al. (2020). "Simulating gas kinematic studies of high-redshift galaxies with the HARMONI integral field spectrograph". In: *Monthly Notices of the Royal Astronomical Society* 498, pp. 1891–1904.

Rigby, A. J., T. J. T. Moore, R. Plume, et al. (2016). "CHIMPS: the $^{13}CO/C^{18}O$ ($J = 3 \rightarrow 2$) Heterodyne Inner Milky Way Plane Survey". In: *Monthly Notices of the Royal Astronomical Society* 456, pp. 2885–2899.

Rigopoulou, D., R. Hopwood, G. E. Magdis, et al. (2014). "Herschel Observations of Far-infrared Cooling Lines in Intermediate Redshift (Ultra)-luminous Infrared Galaxies". In: *The Astrophysical Journal* 781, p. L15.

Rigopoulou, D., M. Pereira-Santaella, G. E. Magdis, et al. (2018). "On the Far-Infrared Metallicity Diagnostics: Applications to High-Redshift Galaxies". In: *Monthly Notices of the Royal Astronomical Society* 473, pp. 20–29.

Rigopoulou, D., H. W. W. Spoon, R. Genzel, et al. (1999). "A Large Mid-Infrared Spectroscopic and Near-Infrared Imaging Survey of Ultraluminous Infrared Galaxies: Their Nature and Evolution". In: *The Astronomical Journal* 118, p. 2625.

Rodighiero, G., E. Daddi, I. Baronchelli, et al. (2011). "The Lesser Role of Starbursts in Star Formation at z= 2". In: *The Astrophysical Journal* 739, p. L40.

Rodrigues, M., F. Hammer, H. Flores, et al. (2017). "Morpho-kinematics of $z \sim 1$ galaxies probe the hierarchical scenario". In: *Monthly Notices of the Royal Astronomical Society* 465, pp. 1157–1180.

Rodríguez Montero, F., R. Davé, V. Wild, et al. (2019). "Mergers, starbursts, and quenching in the SIMBA simulation". In: *Monthly Notices of the Royal Astronomical Society* 490, pp. 2139–2154.

Rodríguez-Zaurín, J., S. Arribas, A. Monreal-Ibero, et al. (2011). "VLT-VIMOS Integral Field Spectroscopy of Luminous and Ultraluminous Infrared Galaxies - III. The Atlas of the Stellar and Ionized Gas Distribution". In: *Astronomy & Astrophysics* 527, A60.

Rupke, D. S. N., S. Veilleux, and A. J. Baker (2008). "The Oxygen Abundances of Luminous and Ultraluminous Infrared Galaxies". In: *The Astrophysical Journal* 674.

Saintonge, A., D. Lutz, R. Genzel, et al. (2013). "Validation of the Equilibrium Model for Galaxy Evolution to $z \sim 3$ Through Molecular Gas and Dust Observations of Lensed Star-Forming Galaxies". In: *The Astrophysical Journal* 778, p. 2.

Sanders, D. B. and I. F. Mirabel (1996). "Luminous infrared galaxies". In: *Annual Review of Astronomy & Astrophysics* 34, pp. 749–792.

Sargent, M. T., M. Béthermin, E. Daddi, et al. (2012). "The Contribution of Starbursts and Normal Galaxies to Infrared Luminosity Functions at $z < 2$". In: *The Astrophysical Journal* 747, p. L31.

Sargent, M. T., E. Daddi, M. Béthermin, et al. (2014). "Regularity Underlying Complexity: A Redshift-Independent Description of the Continuous Variation of

Galaxy-Scale Molecular Gas Properties in the Mass-Star Formation Rate Plane". In: *The Astrophysical Journal* 793, p. 19.

Schmidt, M. (1959). "The Rate of Star Formation." In: *The Astrophysical Journal* 129, p. 243.

Schreiber, C., D. Elbaz, M. Pannella, et al. (2018). "Dust temperature and mid-to-total infrared color distributions for star-forming galaxies at $0 < z < 4$". In: *Astronomy & Astrophysics* 609, A30.

Schruba, A., A. K. Leroy, F. Walter, et al. (2010). "The Scale Dependence of the Molecular Gas Depletion Time in M33". In: *The Astrophysical Journal* 722, pp. 1699–1706.

Schruba, A., A. K. Leroy, F. Walter, et al. (2011). "A Molecular Star Formation Law in the Atomic-gas-dominated Regime in Nearby Galaxies". In: *The Astronomical Journal* 142, p. 37.

Scoville, N., K. Sheth, H. Aussel, et al. (2016). "ISM Masses and the Star Formation Law at z= 1 to 6: ALMA Observations of Dust Continuum in 145 Galaxies in the COSMOS Survey Field". In: *The Astrophysical Journal* 820, p. 83.

Segovia-Otero, Á., F. Renaud, and O. Agertz (2022). *VINTERGATAN IV: Cosmic phases of star formation in Milky Way-like galaxies.*

Shangguan, J., L. C. Ho, R. Li, et al. (2019). "Interstellar Medium and Star Formation of Starburst Galaxies on the Merger Sequence". In: *The Astrophysical Journal* 870, p. 104.

Shapley A, E., N. A. Reddy, M. Kriek, et al. (2015). "The MOSDEF Survey: Excitation Properties of $z \sim 2.3$ Star-Forming Galaxies". In: *The Astrophysical Journal* 801, p. 88.

Sharples, R., R. Bender, A. Agudo Berbel, et al. (2013). "First Light for the KMOS Multi-Object Integral-Field Spectrometer". In: *The Messenger* 151, pp. 21–23.

Shipp, N., D. Erkal, A. Drlica-Wagner, et al. (2021). "Measuring the Mass of the Large Magellanic Cloud with Stellar Streams Observed by S^5". In: *The Astrophysical Journal* 923, p. 149.

Simons, R. C., S. A. Kassin, G. F. Snyder, et al. (2019). "Distinguishing Mergers and Disks in High Redshift Observations of Galaxy Kinematics". In: *The Astrophysical Journal* 874, p. 59.

Simons, R. C., S. A. Kassin, J. R. Trump, et al. (2016). "Kinematic Downsizing at $z \sim 2$". In: *The Astrophysical Journal* 830, p. 14.

Solomon, P. M., D. Downes, S. J. E. Radford, et al. (Mar. 1997). "The Molecular Interstellar Medium in Ultraluminous Infrared Galaxies". In: *The Astrophysical Journal* 478. ADS Bibcode: 1997ApJ...478..144S, pp. 144–161.

Sommovigo, L., A. Ferrara, A. Pallottini, et al. (2022). "The REBELS ALMA Survey: cosmic dust temperature evolution out to $z \sim 7$". In: *Monthly Notices of the Royal Astronomical Society* 513, pp. 3122–3135.

Speagle, J. S., C. L. Steinhardt, P. L. Capak, et al. (2014). "A Highly Consistent Framework for the Evolution of the Star-Forming Main Sequence from z ~ 0-6". In: *The Astrophysical Journal Supplement Series* 214, p. 15.

Stacey, G. J., S. Hailey-Dunsheath, C. Ferkinhoff, et al. (2010). "A 158 μm [C II] Line Survey of Galaxies at $z \sim 1$-2: An Indicator of Star Formation in the Early Universe". In: *The Astrophysical Journal* 724, pp. 957–974.

Stark, D. V., K. A. Bundy, K. Westfall, et al. (2018). “SDSS-IV MaNGA: characterizing non-axisymmetric motions in galaxy velocity fields using the Radon transform”. In: *Monthly Notices of the Royal Astronomical Society* 480, pp. 2217–2235.

Stott, J. P., A. M. Swinbank, H. L. Johnson, et al. (2016). “The KMOS Redshift One Spectroscopic Survey (KROSS): dynamical properties, gas and dark matter fractions of typical z $\sim$ 1 star-forming galaxies”. In: *Monthly Notices of the Royal Astronomical Society* 457, pp. 1888–1904.

Straatman, C. M. S., L. R. Spitler, R. F. Quadri, et al. (2016). “The FourStar Galaxy Evolution Survey (ZFOURGE): ultraviolet to far-infrared catalogs, medium-bandwidth photometric redshifts with improved accuracy, stellar masses, and confirmation of quiescent galaxies to z ~ 3.5”. In: *The Astrophysical Journal* 830, p. 51.

Sutherland, Ralph S. and M. A. Dopita (1993). “Cooling Functions for Low-Density Astrophysical Plasmas”. In: *The Astrophysical Journal Supplement Series* 88, p. 253.

Sutter, J., D. A. Dale, K. Sandstrom, et al. (2021). “The Case for Thermalization as a Contributor to the [CII] Deficit”. In: *Monthly Notices of the Royal Astronomical Society* 503, pp. 911–919.

Swinbank, A. M., S. Dye, J. W. Nightingale, et al. (2015). “ALMA Resolves the Properties of Star-Forming Regions in a Dense Gas Disk at z $\sim$ 3”. In: *The Astrophysical Journal* 806, p. L17.

Swinbank, A. M., J. M. Simpson, Ian Smail, et al. (2014). “An ALMA survey of sub-millimetre Galaxies in the Extended Chandra Deep Field South: the far-infrared properties of SMGs”. In: *Monthly Notices of the Royal Astronomical Society* 438, pp. 1267–1287.

Swinbank, A. M., D. Sobral, Ian Smail, et al. (2012). “The properties of the star-forming interstellar medium at z = 0.84 - 2.23 from HiZELS: mapping the internal dynamics and metallicity gradients in high-redshift disc galaxies”. In: *Monthly Notices of the Royal Astronomical Society* 426, p. 935.

Symeonidis, M. and M. J. Page (2018). “What powers hyperluminous infrared galaxies at z $\sim$ 1 - 2?” In: *Monthly Notices of the Royal Astronomical Society: Letters* 479, pp. L91–L95.

Tacchella, S., C. M. Carollo, N. M. Förster Schreiber, et al. (2018). “Dust Attenuation, Bulge Formation, and Inside-out Quenching of Star Formation in Star-forming Main Sequence Galaxies at z $\sim$ 2”. In: *The Astrophysical Journal* 859, p. 56.

Tacconi, L. J., R. Genzel, A. Saintonge, et al. (2018). “PHIBSS: Unified Scaling Relations of Gas Depletion Time and Molecular Gas Fractions”. In: *The Astrophysical Journal* 853, p. 179.

Tacconi, L. J., R. Genzel, I. Smail, et al. (2008). “Submillimeter Galaxies at z ~ 2: Evidence for Major Mergers and Constraints on Lifetimes, IMF, and CO-H2 Conversion Factor”. In: *The Astrophysical Journal* 680, p. 246.

Tacconi, L. J., R. Genzel, and A. Sternberg (2020). “The Evolution of the Star-Forming Interstellar Medium Across Cosmic Time”. In: *Annual Review of Astronomy & Astrophysics* 58, pp. 157–203.

Tacconi, L. J., R. Neri, R. Genzel, et al. (2013). “PHIBSS: Molecular Gas Content and Scaling Rleations in z ~ 1 - 3 Massive, Main-Sequence Star-forming Galaxies”. In: *The Astrophysical Journal* 768, p. 74.

Tadaki, K., S. Belli, A. Burkert, et al. (2020). “Structural evolution in massive galaxies at z~2”. In: *The Astrophysical Journal* 901, p. 74.

Teyssier, R. (2002). "Cosmological hydrodynamics with adaptive mesh refinement - A new high resolution code called RAMSES". In: *Astronomy & Astrophysics* 385, pp. 337–364.

Thatte, N., M. Tecza, F. Clarke, et al. (2006). "The Oxford SWIFT integral field spectrograph". In: *Ground-based and Airborne Instrumentation for Astronomy*. Vol. 6269. SPIE, pp. 1135–1146.

Thatte, N. A., F. Clarke, I. Bryson, et al. (2014). "HARMONI: the first light integral field spectrograph for the E-ELT". In: *Ground-based and Airborne Instrumentation for Astronomy V*. Vol. 9147. International Society for Optics and Photonics, p. 914725.

Thornton, K., M. Gaudlitz, H. -Th. Janka, et al. (1998). "Energy Input and Mass Redistribution by Supernovae in the Interstellar Medium". In: *The Astrophysical Journal* 500, pp. 95–119.

Tiley, A. L., A. M. Swinbank, C. M. Harrison, et al. (2019). "The shapes of the rotation curves of star-forming galaxies over the last ≈10 Gyr". In: *Monthly Notices of the Royal Astronomical Society* 485, pp. 934–960.

Toomre, A. (1964). "On the gravitational stability of a disk of stars." In: *The Astrophysical Journal* 139, pp. 1217–1238.

Tremonti, C. A., T. M. Heckman, G. Kauffmann, et al. (2004). "The Origin of the Mass-Metallicity Relation: Insights from 53,000 Star-forming Galaxies in the Sloan Digital Sky Survey". In: *The Astrophysical Journal* 613, p. 898.

Turner, O. J., M. Cirasuolo, C. M. Harrison, et al. (2017). "The KMOS Deep Survey (KDS) - I. Dynamical measurements of typical star-forming galaxies at $z \simeq 3.5$". In: *Monthly Notices of the Royal Astronomical Society* 471, pp. 1280–1320.

Übler, H., N. M. Förster Schreiber, R. Genzel, et al. (2017). "The Evolution of the Tully-Fisher Relation between $z \sim 2.3$ and $z \sim 0.9$ with KMOS^{3D}". In: *The Astrophysical Journal* 842, p. 121.

Übler, H., S. Genel, A. Sternberg, et al. (2021). "The Kinematics and Dark Matter Fractions of TNG50 Galaxies at $z = 2$ from an Observational Perspective". In: *Monthly Notices of the Royal Astronomical Society* 500, pp. 4597–4619.

Übler, H., R. Genzel, E. Wisnioski, et al. (2019). "The Evolution and Origin of Ionized Gas Velocity Dispersion from $z \sim 2.6$ to $z \sim 0.6$ with KMOS^{3D}". In: *The Astrophysical Journal* 880, p. 48.

Valentino, F., E. Daddi, A. Puglisi, et al. (2020). "CO emission in distant galaxies on and above the main sequence". In: *Astronomy & Astrophysics* 641, A155.

Veilleux, S., D. -C. Kim, and D. B. Sanders (2002). "Optical and Near-Infrared Imaging of the IRAS 1 Jy Sample of Ultraluminous Infrared Galaxies. II. The Analysis". In: *The Astrophysical Journal Supplement Series* 143, pp. 315–376.

Vijarnwannaluk, B., M. Akiyama, M. Schramm, et al. (2022). *The Obscured Fraction of Quasars at Cosmic Noon*.

Walt, S. van der, J. L. Schönberger, J. Nunez-Iglesias, et al. (2014). "scikit-image: image processing in Python". In: *PeerJ* 2, e453.

Walter, F., C. Carilli, M. Neeleman, et al. (2020). "The Evolution of the Baryons Associated with Galaxies Averaged over Cosmic Time and Space". In: *The Astrophysical Journal*.

Wegner, M. and B. Muschielok (2008). "KARMA: the observation preparation tool for KMOS". In: *Advanced Software and Control for Astronomy II*. Vol. 7019. International Society for Optics and Photonics, 70190T.

Wetzel, A. R., J. L. Tinker, C. Conroy, et al. (2013). “Galaxy evolution in groups and clusters: satellite star formation histories and quenching time-scales in a hierarchical Universe”. In: *Monthly Notices of the Royal Astronomical Society* 432, pp. 336–358.

Whitaker, K. E., P. G. van Dokkum, G. Brammer, et al. (2012). “The Star Formation Mass Sequence Out to z= 2.5”. In: *The Astrophysical Journal* 754, p. L29.

Whitaker, K. E., M. Franx, J. Leja, et al. (2014). “Constraining the Low-Mass Slope of the Star Formation Sequence at $0.5 < z < 2.5$”. In: *The Astrophysical Journal* 795, p. 104.

Whiting, M. T. (2012). “DUCHAMP: a 3D source finder for spectral-line data”. In: *Monthly Notices of the Royal Astronomical Society* 421, pp. 3242–3256.

Wiklind, T., H. C. Ferguson, Y. Guo, et al. (2019). “Evolution of the Gas Mass Fraction of Progenitors to Todays Massive Galaxies: ALMA Observations in the CANDELS GOODS-S Field”. In: *The Astrophysical Journal* 878, p. 83.

Wilkinson, S., S. L. Ellison, C. Bottrell, et al. (2022). “The merger fraction of post-starburst galaxies in UNIONS”. In: *Monthly Notices of the Royal Astronomical Society* 516, pp. 4354–4372.

Wilson, C. D., G. R. Petitpas, D. Iono, et al. (2008). “Luminous Infrared Galaxies with the Submillimeter Array. I. Survey Overview and the Central Gas to Dust Ratio”. In: *The Astrophysical Journal Supplement Series* 178, p. 189.

Wisnioski, E., N. M. Förster Schreiber, M. Fossati, et al. (2019). “The KMOS^{3D} Survey: Data Release and Final Survey Paper”. In: *The Astrophysical Journal* 886, p. 124.

Wisnioski, E., N. M. Förster Schreiber, S. Wuyts, et al. (2015). “The KMOS^{3D} Survey: Design, First Results, and the Evolution of Galaxy Kinematics from $0.7 \leq z \leq 2.7$”. In: *The Astrophysical Journal* 799, p. 209.

Wolfire, M. G., D. Hollenbach, and C. F. McKee (2010). “The Dark Molecular Gas”. In: *The Astrophysical Journal* 716, pp. 1191–1207.

Wuyts, S., N. M. Förster Schreiber, E. Wisnioski, et al. (2016). “KMOS^{3D}: Dynamical Constraints on the Mass Budget in Early Star-Forming Disks”. In: *The Astrophysical Journal* 831, p. 149.

Zavala, J. A., C. M. Casey, S. M. Manning, et al. (2021). “The Evolution of the IR Luminosity Function and Dust-obscured Star Formation in the Last 13 Billion Years”. In: *The Astrophysical Journal* 909, p. 165.

Zieleniewski, S., N. Thatte, S. Kendrew, et al. (2015). “hsim: a simulation pipeline for the HARMONI integral field spectrograph on the European ELT”. In: *Monthly Notices of the Royal Astronomical Society* 453, pp. 3754–3765.